

Bregje Wilhelmina Maria de Wildt

Eindhoven University of Technology, The Netherlands

Copyright © 2022 by B.W.M. de Wildt

Cover design by Renée van den Berg

Printed by ADC Dereumaux

A catalogue record is available from the Eindhoven University of Technology Library

ISBN: 978-90-386-5582-6

This work is part of the research program TTW with project number TTW 016.Vidi.188.021, which is (partly) financed by the Netherlands Organization for Scientific Research (NWO). This research was also partly financially supported by the Gravitation Program “Materials Driven Regeneration”, funded by the Netherlands Organization for Scientific Research (024.003.013).

Financial support by the Netherlands society for Biomaterials and Tissue Engineering (NBTE) and the department of Biomedical Engineering of Eindhoven University of Technology for publication of this thesis is gratefully acknowledged.

Advancing tissue engineering of *in vitro* human bone models

PROEFSCHRIFT

Ter verkrijging van de graad van doctor aan de Technische Universiteit Eindhoven op
gezag van de rector magnificus, prof. dr. ir. F.P.T. Baaijens, voor een commissie
aangewezen door het College van Promoties, in het openbaar te verdedigen op vrijdag
4 november 2022 om 16:00 uur

door

Bregje Wilhelmina Maria de Wildt

geboren te Nijmegen

Dit proefschrift is goedgekeurd door de promotoren en de samenstelling van de promotiecommissie is als volgt:

Voorzitter:	prof. dr. M. Merkx
Promotoren:	dr. S. Hofmann prof. dr. K. Ito
Promotiecommissieleden:	prof. dr. C.V.C. Bouten prof. dr. G.C. Reilly (Sheffield University) prof. dr. ir. S.C.G. Leeuwenburgh (Radboud UMC) dr. A.D. Bakker (ACTA) dr. ir. D. Gawlitta (UMC Utrecht)

Het onderzoek dat in dit proefschrift wordt beschreven is uitgevoerd in overeenstemming met de TU/e Gedragscode Wetenschapsbeoefening.

Table of Contents

Chapter 1: General introduction.....	1
Part I: Towards tissue engineered <i>in vitro</i> models to evaluate human bone formation and regeneration.....	11
Chapter 2: From bone regeneration to three-dimensional <i>in vitro</i> models; tissue engineering of organized bone extracellular matrix	13
Chapter 3: Characterization of three-dimensional bone-like tissue growth and organization under influence of curvature and directional fluid flow	27
Chapter 4: Evaluating material-driven regeneration in a tissue engineered human <i>in vitro</i> bone defect model.....	55
Part II: Advancing tissue engineering of <i>in vitro</i> human bone remodeling models ...	87
Chapter 5: <i>In vitro</i> models of bone remodeling: a systematic review and map of available literature.....	89
Chapter 6: Human platelet lysate as alternative of fetal bovine serum for enhanced human <i>in vitro</i> bone resorption and remodeling.....	113
Chapter 7: Bioinspired silk fibroin mineralization for advanced <i>in vitro</i> bone remodeling models.....	151
Chapter 8: The impact of culture variables on human <i>in vitro</i> bone remodeling; a design of experiments approach.....	191
Chapter 9: General discussion.....	223
Bibliography	235
Summary	263
Publiekssamenvatting	266
Curriculum vitae	270
Scientific output.....	271
Dankwoord (Acknowledgement)	274

1

General introduction

Preface

Since the 1990s, bone tissue engineering has traditionally been focusing on developing grafts for patients with large bone defects, making use of scaffolds, progenitor cells, biochemical and biomechanical stimuli. By tuning these parameters, researchers have created bone-like tissues for transplantation. Before these grafts can be transplanted into humans, their ability to induce bone regeneration is routinely studied in animal experiments. Besides ethical concerns regarding the use of animal models, clinical translation of in animal experiments developed treatments is with a success rate of ~10% poor.

While engineered bone-like tissues proved of limited success for human bone regeneration, their development has advanced our ability to manipulate cells and engineer materials. To improve preclinical treatment development and to replace, reduce, and refine animal experiments, bone tissue engineering strategies are increasingly applied for the creation of *in vitro* models to study human bone in health and disease. This change in focus; from bone regeneration to *in vitro* models, has brought new challenges for researchers of which some are addressed in this thesis.

1.1 Bone in health and disease

As building blocks of the skeleton, bones have multiple mechanical and metabolic functions, that include providing structural support, maintaining mineral homeostasis and acid-base balance, serve as a reservoir for growth factors, and provide an environment for hematopoiesis (1). Within bones, two distinct structures can be identified: cortical or compact bone and trabecular or cancellous bone (**Figure 1.1A**). Although they have the same matrix composition, they differ in their porosity, three-dimensional (3D) structure, and metabolic activity (2,3). Cortical bone has a low porosity of 5% to 10% and is organized into cylindrical elements called osteons, providing resistance against compression, bending and torsion (2). Trabecular bone has a porosity of 50% to 90% and is organized into a network of trabeculae aligned to mechanical loads (2,4). Within these structures, bone tissue is composed of organic (*i.e.*, mainly collagen type I and a small portion of non-collagenous proteins), and inorganic (*i.e.*, carbonated hydroxyapatite) matrix organized at multiple hierarchical levels (5).

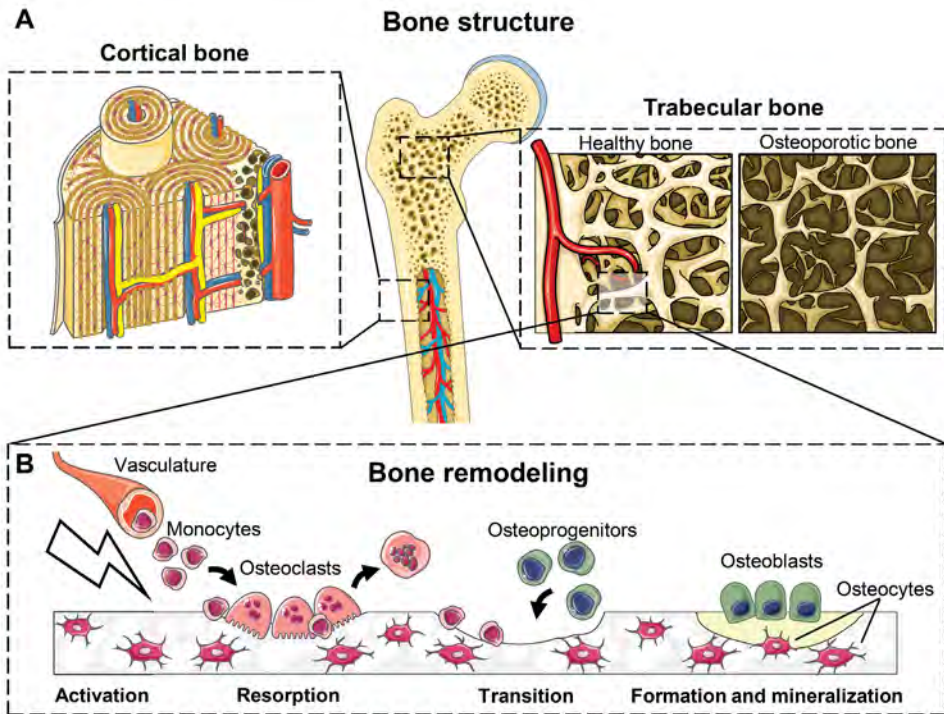


Figure 1.1. An overview of a long bone comprising of (A) cortical bone and trabecular bone. Trabecular bone has a high turnover rate; each year, 20% of the trabecular bone volume is remodeled. (B) Bone remodeling follows a specific sequence of events, starting with activation followed by resorption, transition, formation, and mineralization. Osteoclasts and osteoblasts and their progenitors are involved in this process which is regulated by osteocytes. The figure was created with Servier Medical Art, licensed under a Creative Common Attribution 3.0 Generic License (<http://smart.servier.com>, accessed on 15 July 2022).

Bone's mechanical and metabolic functions are maintained by the process of bone remodeling. A continuous process in which osteoclasts resorb bone and osteoblasts form bone, which is mainly regulated by osteocytes. It is believed that in the bone remodeling cycle, progenitor cells are typically attracted and activated by biomechanical or biochemical stimuli after which resorption of bone matrix by monocyte-derived osteoclasts starts. This phase is followed by a transition phase in which osteoclasts leave the bone surface, macrophages clean the surface, and osteoprogenitors or mesenchymal stromal cells are attracted. These osteoprogenitors subsequently differentiate into osteoblasts which produce new bone matrix, embed themselves in this matrix over time, and once this matrix mineralizes these osteoblasts differentiate towards osteocytes and obtain a more regulatory function in the remodeling process (6,7) (**Figure 1.1B**). As such, 20% of the trabecular bone volume is renewed each year (8). In the healthy situation, bone resorption and formation are coupled temporally and spatially, meaning

that resorbed bone volume is replaced by an equal volume of new bone. Uncoupling between resorption and formation can disturb their balance, leading to an absolute increase in bone mass in osteopetrosis and an absolute decrease in bone mass in osteopenia and osteoporosis (9). Osteoporosis is with a global prevalence of ~18% the most common bone remodeling pathology (10). Especially post-menopausal women are often affected with osteoporosis due to estrogen deficiency. The low bone mineral density associated with osteoporosis leads to fragile bones and therefore an increased fracture risk (11). Although osteoporosis itself is not lethal, mortality is a major risk following osteoporosis related hip fractures (12).

1.2 Bone regeneration

Bone tissue repair relies on a sequence of biological events, including inflammation, intramembranous and endochondral bone formation and coupled remodeling. Inflammation starts with the formation of a hematoma and the attraction of immune cells and progenitor cells (13). Subsequently, mesenchymal cells condensate and differentiate towards osteoblasts for intramembranous bone formation or towards chondrocytes to form a callus for endochondral bone formation. In parallel, cells that will form the new blood vessels are recruited and differentiated. As chondrocytes are further differentiated and/or undergo apoptosis, the cartilaginous callus undergoes mineralization. The newly formed bone and mineralized callus are over time remodeled into vascularized bone tissue by osteoclasts and osteoblasts (13). Due to bone's intrinsic capacity to remodel and regenerate, the majority of bone injuries or fractures heal without the formation of scar tissue (14). Nevertheless, in 2% – 5% of the defects, bone fails to bridge the gap resulting in a non-union, requiring intervention (15,16). In addition, intervention is also required for large bone defects caused by *e.g.*, tumor resection, infection or trauma, or in fractures where the regenerative process is impaired as for example in osteoporosis (14).

1.3 Bone tissue engineering

To facilitate bone regeneration of large osseous defects, bone tissue engineering has emerged since the 1990s (17). Traditionally, bone tissue engineering has been focusing on developing grafts making use of autologous or allogenic progenitor cells, biomaterials to facilitate 3D growth, and biochemical and biomechanical factors to stimulate osteogenic differentiation and bone-like tissue growth (**Figure 1.2**). To ensure successful regeneration, developed grafts should be biocompatible (*i.e.*, it should have the ability to perform with an appropriate host response) (17,18), bioactive, and mechanically stable while allowing for degradation and coupled remodeling (17). To

date, these bone-like tissues have proved to be of limited success for human bone regeneration. Nevertheless, their development has advanced our ability to manipulate cells and grow bone-like tissues in 3D. Bone tissue engineering is therefore increasingly also applied for the creation of 3D *in vitro* human bone models to enable the investigation of human bone physiology and pathology (19,20).

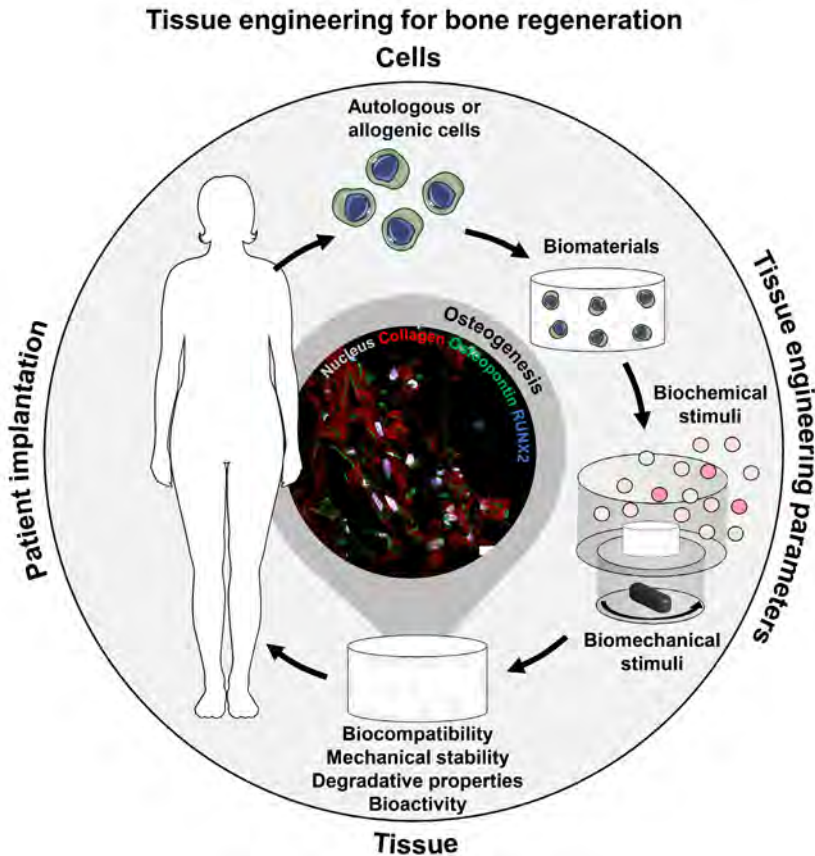


Figure 1.2. Traditional tissue engineering approach in which human autologous or allogenic cells are isolated and used to generate bone grafts using biomaterials, biochemical, and biomechanical stimuli. These stimuli typically lead to osteogenic differentiation and the creation of a bone-like extracellular matrix. Requirements for successful regeneration are biocompatibility, mechanical stability, degradative properties, and bioactivity. The figure was created with Servier Medical Art, licensed under a Creative Commons Attribution 3.0 Generic License (<http://smart.servier.com>, accessed on 15 July 2022).

1.4 The need for *in vitro* bone models

Currently, bone grafts and drugs for bone diseases like osteoporosis are, after simple two-dimensional (2D) *in vitro* cytocompatibility tests, routinely studied using animal

experiments (21). Despite animal studies being a crucial step in treatment safety and effectivity testing, the translation from *in vitro* to *in vivo* experiments has been poor (22). Moreover, with a success rate of around 8-10%, the subsequent clinical translation of *in vivo* animal studies is also poor (23,24). This poor translation is likely caused by their insufficient representation of the human physiology (25). Thus, both the translation from *in vitro* assessments to *in vivo* models and the translation from *in vivo* animal models to the human clinic need to be improved. To address these translational issues and improve preclinical treatment testing, advanced human *in vitro* bone models could be integrated into the preclinical graft testing routine (20,21,26).

From an ethical point of view, the use of animal experiments for medical research also is a frequent topic for debate (27,28). The current pace at which biomedical technologies, including bone grafts for regeneration, are being developed causes a significant burden on animal experiments (22). In 1959, guidelines for the use of animal experiments were published by Russel and Burch (29), introducing the principle of replacement, reduction and refinement of animal experiments (3Rs). As a consequence, many strategies to replace, reduce and refine animal experiments have been explored, including *in silico* (*i.e.*, computational simulations) bone remodeling or regeneration experiments (30,31), improved efficiency of *in vivo* animal experiments to study bone regeneration (32), human explant or *ex vivo* bone cultures to study bone regeneration (33), and the use of *in vitro* models or organoids for bone regeneration and remodeling (34,35).

1.5 Tissue engineering of *in vitro* bone models

In vitro bone models could thus facilitate the investigation of human bone physiology and pathology while addressing the principle of 3Rs. To create these *in vitro* models, the use of tissue engineering techniques has been proposed (19,20). This change in focus; from tissue engineering for bone regeneration to *in vitro* models, has brought new challenges for researchers (**Figure 1.3**). In terms of cells, often multiple cell types are required to model certain aspects of bone. For example, an *in vitro* model for bone remodeling would require at least a co-culture of osteoclasts and osteoblasts to allow for studying their cross-talk and coupling (36). Moreover, these cells need to be seeded in physiologically relevant seeding densities and ratios to enable this cross-talk through cell-cell contact and soluble factors (37). Thereby, as healthy human bone tissue for cell isolation is scarce, the use of primary progenitor cells is often needed since cell-lines are not able to capture all physiological aspects of primary cells (38). However, the use of primary cells also requires tight control over cell differentiation while the use of differentiation factors might disturb the natural cell cross-talk (7).

Tissue engineering of *in vitro* bone models for treatment development

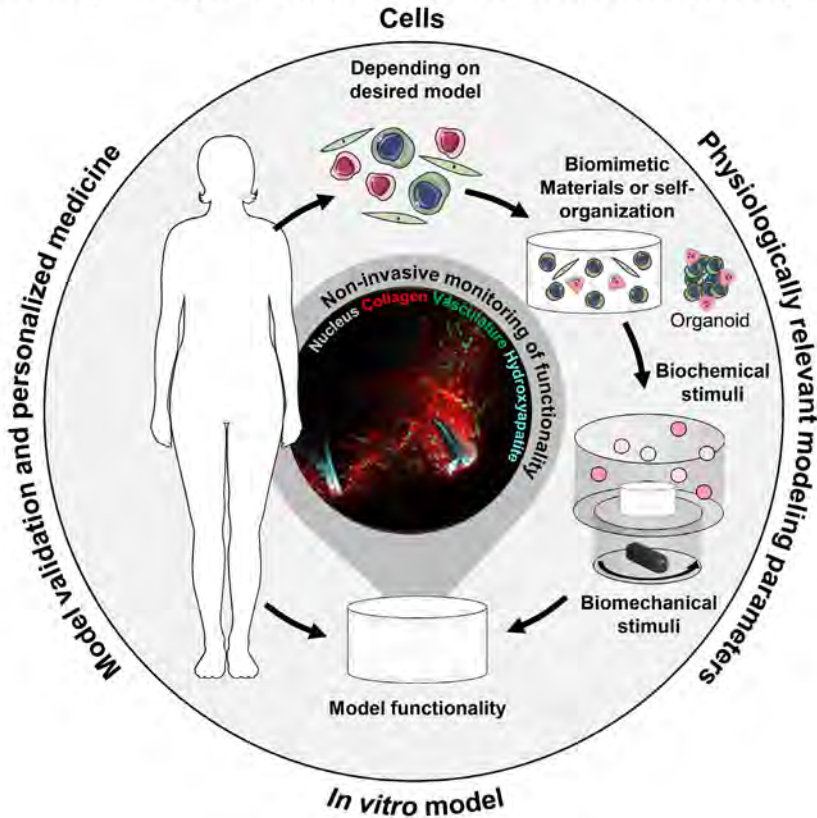


Figure 1.3. Tissue engineering approach to create 3D *in vitro* bone models. The use of cells, biomaterials, biochemical and biomechanical stimuli need to be reconsidered in terms of physiological relevance. In addition, model functionality is the most important outcome which should ideally be monitored over time non-invasively. Model functionality can be validated with the use of *in vivo* data or knowledge to enable translation. The figure was created with Servier Medical Art, licensed under a Creative Common Attribution 3.0 Generic License (<http://smart.servier.com>, accessed on 15 July 2022).

In terms of biomaterials and the engineered extracellular matrix (ECM), for *in vitro* bone models they should resemble the physiological bone ECM. For bone regeneration, this was often not imperative because of the bone's innate capacity to regenerate and remodel upon implantation. However, as changes in the bone ECM structure are often a hallmark of bone pathology (39–41), *in vitro* bone models that aim at studying the bone ECM under influence of treatments should be able to capture aspects of the physiological bone ECM in addition to the interactions of the cells with the ECM. Whether this improved biomimicry can be reached by using bioinspired materials or by letting the cells organize their niche, is yet to be investigated.

The use of biochemical and biomechanical stimuli should also be reconsidered for *in vitro* bone models (42). Tissue engineering for bone regeneration often involved optimization towards maximalization of collagen formation and mineralization by osteogenically differentiated mesenchymal stromal cells. As such, differentiation factor concentrations and mechanical loading conditions are optimized to support specific cell types, while in co-culture biochemical and biomechanical conditions need to be supportive for all cultured cell-types (43). Ideally, external biochemical stimulation is minimized to allow for the physiological cross-talk of the co-cultured cells (7).

While for bone regeneration purposes, tissue engineered constructs were often analyzed at the end-point of a culture to study bone-like ECM formation and osteogenesis, *in vitro* bone models require the monitoring of their functionality over time (42). Preferably, non-invasive methods are used to enable the evaluation of multiple time-points while reducing the culture burden and thereby facilitating high throughput analysis (7). Model functionality should subsequently be compared with human or animal *in vivo* knowledge and/or data for model validation and potentially result translation or extrapolation (44).

Taken together, the change in focus from tissue engineering for bone regeneration to *in vitro* models requires a major change in conception. More specifically, tissue engineering methods for the use of cells, biomaterials, biochemical, and biomechanical stimuli need to be refined, as well as the engineered construct analyses. Some of these challenges are addressed in this thesis.

1.6 Thesis outline

This introduction (**Chapter 1**) provides a general overview of the role of tissue engineering for bone regeneration and the potential of tissue engineering for *in vitro* models to study bone physiology and pathology. As the tissue engineering strategy is highly dependent on the to be modeled aspects of bone physiology and pathology, this thesis is divided into two parts. Part I focusses on tissue engineering of *in vitro* models to evaluate human bone formation and regeneration and part II focusses on tissue engineering of *in vitro* models to evaluate human bone remodeling.

Part I: Towards tissue engineered *in vitro* models to evaluate human bone formation and regeneration

One challenge for the development of *in vitro* models for bone formation is the creation of a bone-like tissue that resembles the physiological bone ECM. In **Chapter 2**, we (i) give recommendations on the ECM requirements for *in vitro* bone models, (ii) review

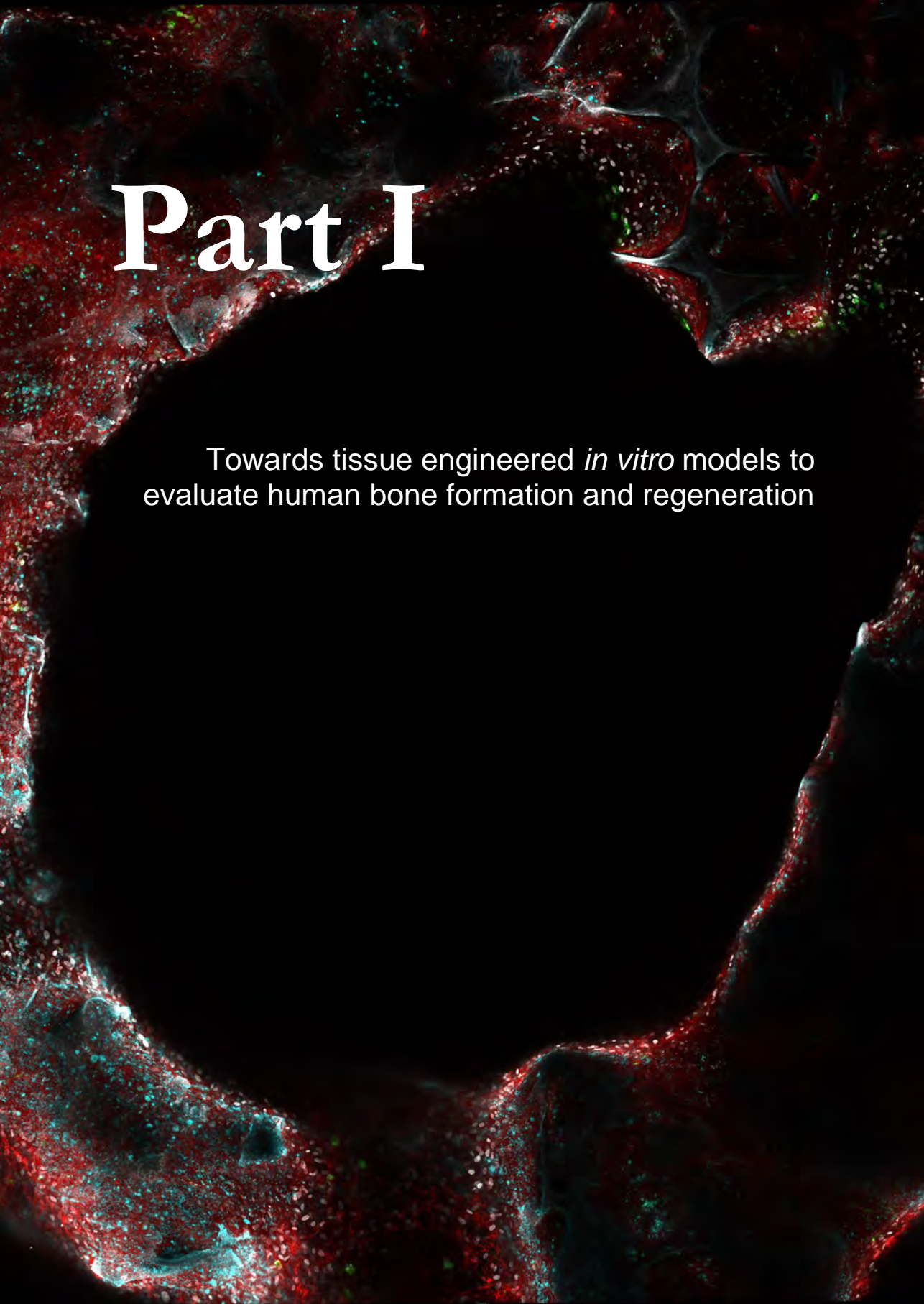
what has been achieved thus far, and (iii) suggest how this can be improved in future. One of these suggestions is the application of mechanical loading like directional fluid flow, which has been demonstrated to induce osteoblast alignment on 2D substrates. *In vivo*, cells and collagen are however aligned in 3D and often with surface concavities. In **Chapter 3**, we therefore aimed at characterizing cell and tissue growth and orientation in a 3D concave “critically sized” channel with and without the application of directional fluid flow. As full regeneration of the channel was indeed not accomplished in both static and dynamic cultures, we chose to use this critically sized defect model to enable the *in vitro* investigation of material-driven bone regeneration in **Chapter 4**. Graft vascularization is one the major challenges for successful bone regeneration *in vivo*. We therefore combined the *in vitro* bone defect model with a co-culture of mesenchymal stromal cells and endothelial cells. The engineered platform enabled to study the materials’ potential to induce migration, vascularization, and osteoinduction, which are crucial processes of bone regeneration.

Part II: Advancing tissue engineering of *in vitro* human bone remodeling models

To study healthy and pathological bone remodeling, *in vitro* models should at least include a co-culture of osteoclasts and osteoblasts. To perform these co-cultures, each lab develops their own protocol for the cell-culture and analyses methodology. As a consequence, current *in vitro* remodeling models face reproducibility and translational issues. To address this problem, we identified all co-cultures that have been described in literature before 2020 in **Chapter 5**. From these studies, differences in cell-culture methods (culture substrate, mechanical loading, cell sources, culture medium, seeding density and cell-ratio) and resorption/formation analyses methods were mapped systematically. For example, we identified the controversial fetal bovine serum (FBS) as common standard for these co-cultures. In **Chapter 6**, we therefore investigated whether FBS could be replaced by human platelet lysate (hPL) as a more physiologically relevant and xenogeneic-free medium supplement for *in vitro* human bone remodeling models. Another limitation of current *in vitro* bone remodeling models identified in **Chapter 5** is the lack of functional (*i.e.*, resorption and formation) outcome measures, and their spatiotemporal organization, which might be facilitated by the used of bioinspired materials. Inspired by collagen mineralization techniques, we developed a mineralized silk fibroin scaffold in **Chapter 7**. As a remodeling template, this scaffold facilitated the spatiotemporal investigation of both resorption by osteoclasts and formation by osteoblasts. In **Chapter 8**, we utilized the model described in **Chapter 7** to address the reproducibility and translational issues identified in **Chapter 5**. A design of experiments set-up was used to study the influence of tissue engineering parameters

including base medium, cell-ratio, hPL concentration, mechanical loading, osteogenic medium supplements, osteoclast medium supplements, and vitamin D3 on osteoclast-osteoblast co-cultures. With this study, we characterized the effect of these culture conditions on the remodeling balance and therefore also identified an optimal protocol for healthy balanced *in vitro* bone remodeling, using a tissue engineering approach.

In **Chapter 9**, the main findings of this thesis are presented and discussed, and potential future directions are described.

A fluorescence microscopy image of a tissue section. The image shows a complex, porous structure with a central dark void. The surrounding tissue is stained with red and green fluorescent markers, highlighting cellular structures and possibly mineral deposits. The red signal is more prominent, forming a dense network around the central void, while the green signal is more sparsely distributed. The overall appearance is that of a highly porous, interconnected biological or engineered structure.

Part I

Towards tissue engineered *in vitro* models to
evaluate human bone formation and regeneration

2

From bone regeneration to three-dimensional *in vitro* models; tissue engineering of organized bone extracellular matrix

This chapter is based on:

Bregje W. M. de Wildt^{1,2}, Sana Ansari^{1,2,3}, Nico A. J. M. Sommerdijk^{2,3}, Keita Ito^{1,2}, Anat Akiva^{2,3}, Sandra Hofmann^{1,2}

1. Orthopaedic Biomechanics, Department of Biomedical Engineering, Eindhoven University of Technology, Eindhoven, The Netherlands.
2. Institute for Complex Molecular Systems (ICMS), Eindhoven University of Technology, Eindhoven, The Netherlands.
3. Department of Chemical Engineering and Chemistry, Laboratory of Materials and Interface Chemistry and Centre for Multiscale Electron Microscopy, Eindhoven University of Technology, Eindhoven, The Netherlands.

Abstract

Traditionally, bone tissue engineering has been used for creating implants for bone regeneration, but recently it is increasingly applied to create 3D *in vitro* bone models to study bone physiology and pathology. For 3D *in vitro* bone models, the engineered extracellular matrix organization should resemble the *in vivo* physiological bone structure as this is often the hallmark in skeletal pathologies - an issue that has not been achieved yet. In this review paper, we define the extracellular matrix requirements for an optimal 3D *in vitro* model based on the most recent advances on bone structure. To meet these requirements, osteoclasts, osteocytes and mature osteoblasts should work together under physiological conditions, and the formed extracellular matrix should be analyzed and optimized at multiple length scales.

2.1 Introduction

Bones have remarkable mechanical properties thanks to their extraordinary extracellular matrix (ECM) composition and organization (45). To attain these mechanical properties, organic and inorganic matrix components are highly organized at multiple hierarchical levels (5), and continuously remodeled by osteoclasts (bone-resorbing cells), osteoblasts (bone-forming cells), and osteocytes (regulating cells) (46,47). During the last decades, researchers have attempted to mimic bone using a tissue engineering approach.

Traditionally, bone tissue engineering has been comprised of developing grafts for patients with large osseous defects, making use of scaffolds, progenitor cells, mechanical stimuli, and soluble factors. For bone regeneration, this approach was used in order to achieve constructs with osteogenic, osteoconductive, and osteoinductive properties (48). As such, tissue-engineered bone-like constructs can be able to induce regeneration, even if they fail to resemble the complex ECM structure of real human bone, thanks to bone's innate capacity to regenerate and remodel. Over the last years, bone tissue engineering is increasingly applied to develop 3D *in vitro* human bone models for drug testing, addressing the principle of 3Rs (reduction, refinement, replacement) (7,20). For 3D *in vitro* bone models, the engineered ECM structure should resemble the complex ECM structure of physiological human bone. This is particularly important for models aiming at mimicking bone pathologies where remodeling is affected, as in these situations the bone's ECM composition and organization, and thus its mechanical competence, is often changed (39). For example in osteogenesis imperfecta, the collagen network is more loosely woven and minerals appear smaller and disorganized, resulting in brittle bones (40). Another example is osteoporosis, where collagen fibrils were found to be less aligned and only partly mineralized in a mouse model, leading to fragile bones (41). To be able to mimic the ECM structure of these pathologies and to distinguish it from the healthy situation, the *in vitro* recreation of the healthy bone ECM structure should be accomplished first.

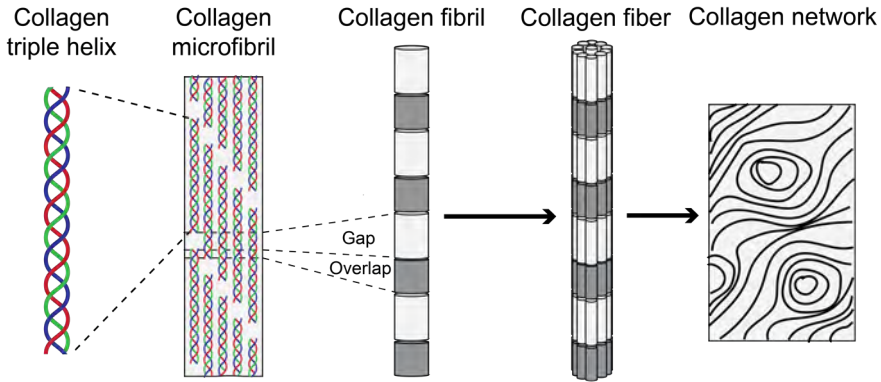
With this review paper, we attempt to define what to aim for in bone tissue engineering when creating 3D *in vitro* models representing healthy bone physiology. In this regard, we (i) characterize the physiological human *in vivo* bone structure, (ii) give recommendations on criteria for an *in vitro* model for physiological human bone, (iii) discuss what has been achieved thus far in meeting these criteria making use of bone tissue engineering, (iv) suggest how we might optimize the ECM structure for *in vitro* bone models to meet the proposed criteria in future, and (v) propose how these criteria should be assessed.

2.2 The organic matrix; a template for mineralization

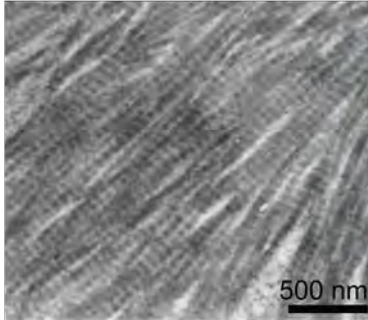
Bone ECM consists for ~30 to 40% of organic matrix that provides bone with toughness and elastic properties (46). The organic matrix is mainly composed of collagen type I molecules, produced by osteoblasts (46). These molecules form triple helices that can assemble into collagen microfibrils in a twisted and staggered arrangement, with a gap region between two consecutive molecules (49). Multiple collagen microfibrils can bundle into collagen fibrils, and in turn, multiple of these collagen fibrils can form a collagen fiber (**Figure 2.1A**). The orientation of these collagen fibers contributes to the mechanical competence of bone (50). More specifically, collagen networks that are aligned parallel to the load are better resistant to tension whereas collagen networks aligned perpendicular to the load are better resistant to compression (51,52). Collagen network density and fibril organization are important determinants for successful subsequent mineralization (53,54) (**Section 2.3**). Based on the organization of collagen, we can describe two extremes of bone structure organization (although more gradations can be made (5)): (i) the more immature woven bone with a disordered collagen fiber structure and loosely packed poorly oriented collagen fibrils, and (ii) the more mature lamellar bone with a dense network of parallel aligned collagen fibers within a lamella but with alternating orientation between lamellae (55). *In vivo*, woven bone is thought to be the primary formed bone by osteoblasts that rapidly secrete collagen which assembles into fibril bundles with little or no preferred orientation (5,56). Lamellar bone is formed upon bone remodeling; it is believed that osteoblasts array themselves in a polarized fashion along a surface, and secrete collagen fibrils onto the surface in a parallel orientation (56). A small portion of the organic matrix is composed of non-collagenous proteins (NCPs) (46), they are believed to play an important role in collagen fibril assembly and subsequent mineralization of these collagen fibrils (57,58). Together, the collagen network, individual collagen fibril organization, and NCPs form a template for mineralization and are thus a major determinant for the eventual ECM structure. Therefore, to resemble physiological bone in 3D *in vitro* bone models, the organic matrix should comprise of a highly dense and aligned collagen network at the micrometer scale and highly organized collagen fibrils at the nanometer scale (**Figure 2.1**). NCPs are instrumental in the collagen organization and facilitate its mineralization.

Organic matrix

A Collagen structure

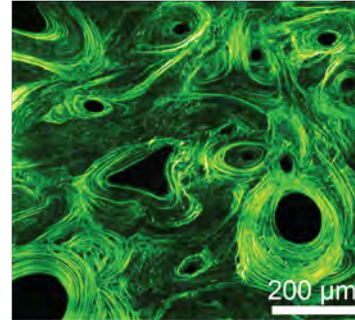


B Nanometer scale



Uniformly organized collagen fibrils

C Micrometer scale



Dense and aligned collagen network

Figure 2.1. The organic matrix should comprise of organized collagen fibrils on the nanometer scale and a highly dense and aligned collagen fiber network on the micrometer scale. **(A)** Simplified representation of the collagen structure at multiple hierarchical levels. **(B)** Electron microscopy image of rat cortical bone collagen fibrils *in vivo* showing a high level of organization (reprinted from Bone, 26:4, Kafantari et al., Structural alterations in rat skin and bone collagen fibrils induced by ovariectomy, 349-353, Copyright (2000), with permission from Elsevier). **(C)** Second harmonic generation image of human femoral cortical bone showing a dense and aligned collagen fiber network (reprinted from Sci. Rep., 7:3419, Genthal et al., Label-free imaging of bone multiscale porosity and interfaces using third-harmonic generation microscopy, Copyright (2017), open access).

For *in vitro* bone tissue engineering, collagen network density and orientation are not common outcome parameters. When visualized with conventional light microscopy, the collagen networks seen in *in vitro* engineered constructs are often at a low level of organization, which can in the best cases be characterized as similar to the immature woven bone. In addition, as these collagen networks are often only assessed at the

micrometer scale, it is unclear whether the individual collagen fibrils exhibit uniformly a high level of organization. Anatomic-level evaluation of collagen produced by osteoblasts *in vitro* and *in vivo* showed misfolded collagen proteins in the 2D *in vitro* situation (59). It was suggested that collagen protein folding could be improved by optimization of the culture conditions (59), emphasizing the importance of multiscale analysis when optimizing protocols that aim for the resemblance of *in vivo* bone structures. Moreover, although important for collagen fibril assembly and subsequent mineralization, the function of NCPs is often neglected in bone tissue engineering. When studies report expression and/or synthesis of NCPs such as osteocalcin and alkaline phosphatase, they often use it to demonstrate the differentiation of the progenitor cells towards the osteogenic lineage instead of reporting on their distribution in the matrix and functions.

In recent years, researchers have attempted to create lamellar-like collagen networks with and without the use of cells. These studies are based on the concept that collagen alignment can be induced by either collagen-producing cells, self-assembling collagen molecules, or selective collagen degradation (60). More specifically, osteoblasts may influence collagen orientation by: (i) exerting traction forces on their ECM (61), or (ii) by producing collagen parallel to their orientation, which can be guided by an oriented substrate (62,63), curvature (64,65), or mechanical stimuli like stretch and fluid flow (66,67) where cells align to the surface or the direction of the applied mechanical stimulus. Thus far, these techniques have led to orientation of collagen in only one direction instead of an alternating orientation between collagen layers as present in lamellar bone *in vivo*. To create acellular dense collagen networks with alternating orientations between different collagen layers, collagen densification techniques were used (53,68–70). These techniques are based on liquid crystal phasing of collagen; a physiological state between liquid and solid in which highly concentrated collagen molecules can arrange and assemble (71). In turn, such a dense and aligned collagen film can increase osteoblast proliferation and differentiation, and guide the cells to align in the direction of the substrate collagen (72). Under more physiological collagen concentrations, it has been demonstrated that collagen fibrils in solution can already align with the direction of flow in absence of cells (73). These aligned collagen fibrils were subsequently stabilized under physiological relevant strain (*i.e.*, mimicking the traction forces of fibroblasts on ECM) to form a highly oriented collagen fiber (73). ECM strain is not only important for the formation of oriented collagen fibers, it can also protect already existing fibrils against degradation that are oriented in the direction of the strain (74).

Although the above-mentioned studies provide insight into the mechanisms of collagen alignment in bone, translation to 3D *in vitro* tissue engineering remains challenging. Studies that made use of substrates were all performed in 2D and investigated cellular behavior over a short period of time, thus lacking spatial and temporal complexity. In addition, the use of collagen substrates to induce cell and collagen alignment in 3D is challenging, and degradation of these templates can result in collagen reorganization over time (75). Therefore, future studies should investigate the optimal parameters to create a dense aligned, possibly even lamellar-like, collagen network in 3D *in vitro* engineered constructs. For the assessment of collagen network density and alignment, micrometer scale imaging is appropriate, as these parameters require a relatively wide field of view. To investigate whether engineered collagen networks exhibit highly organized collagen fibrils, collagen networks should not only be assessed at the micrometer scale, but also at the nanometer scale. Furthermore, as NCPs play an important role in collagen fibril assembly and subsequent mineralization, they should be considered when aiming for improving these two aspects of bone ECM formation.

2.3 The inorganic matrix; controlling extrafibrillar and intrafibrillar mineralization

The inorganic matrix of bone comprises ~60 to 70% of the total bone ECM and contains mainly carbonated hydroxyapatite (46). *In vivo*, collagen mineralization appears inside and outside collagen fibrils, known as intrafibrillar and extrafibrillar mineralization, respectively (76,77). Mineralization starts when mineral precursors enter the collagen gap regions where hydroxyapatite crystals nucleate and orientate with their c-axes parallel to the long axis of collagen fibrils. As recently investigated, these minerals grow outside the dimensions of the single collagen fibril, forming a continuous pattern of intrafibrillar and extrafibrillar minerals (**Figure 2.2A**) (78). Together these minerals form *in vivo* an interconnected network (79), providing bone with mechanical rigidity and compressive strength (80). Therefore, to resemble physiological human bone in 3D *in vitro* bone models, the inorganic matrix should comprise of a highly mineralized collagen network with interconnected intrafibrillar and extrafibrillar minerals (**Figure 2.2**).

Mineral organization is thus highly complex, but unfortunately often not considered in bone tissue engineering. Instead, in bone tissue engineering, mineral deposition is often evaluated using calcium assays, calcium staining, or micro computed tomography. These techniques say something about mineral content, but not their specific size and location within the tissue, which are important for bone's mechanical functionality (45). It remains therefore unreported whether bone tissue-engineered construct really comprise

of a mineralized collagen network, and if so, whether these minerals are located within the collagen fibrils, aligned on the outside, or only precipitated within the extrafibrillar spaces.

Inorganic matrix

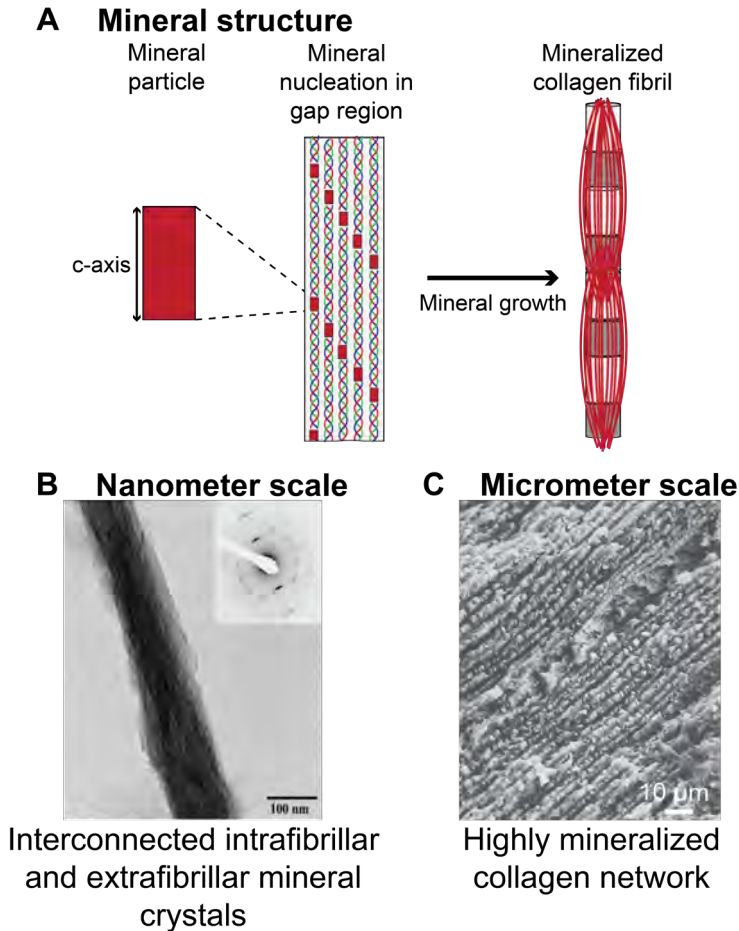


Figure 2.2. The inorganic matrix should comprise of a highly mineralized collagen network on the micrometer scale, and interconnected intra and extrafibrillar minerals on the nanometer scale. **(A)** Simplified representation of the mineral structure, location of nucleation, and mineral growth. **(B)** Transmission electron microscopy image of mineralized collagen fibril showing a high level of alignment of intrafibrillar and extrafibrillar minerals (reprinted from *Biomacromolecules*, 12:8, A.S. Deshpande et al., Primary Structure and Phosphorylation of Dentin Matrix Protein 1 (DMP1) and Dentin Phosphoprotein (DPP) Uniquely Determine Their Role in Biomineralization, 2933-2945, Copyright (2011), with permission from American Chemical Society). **(C)** Scanning electron microscopy image of rat long bone showing mineralized aligned lamellae (reprinted from *Acta Biomater.*, 10, Reznikov et al., Bone hierarchical structure in three dimensions, 3815-3826, Copyright (2014), with permission from Elsevier).

To improve *in vitro* mineralization of collagen, it is important to know what factors can influence mineralization and how we can apply them in bone tissue engineering. Biochemically, citrate infiltration of collagen fibrils might promote intrafibrillar mineralization (81). In addition, it is believed that citrate plays an important role in connecting individual mineral particles (82). Citrate might be provided by osteoblasts that attain the ability to produce it during differentiation from mesenchymal stromal cells (MSCs) (83,84). In addition, NCPs such as osteocalcin and osteopontin are believed to play an essential role in intrafibrillar crystal growth and crystal morphology (85). Of importance, *in vitro* mineralization might be influenced by fetal bovine serum (FBS), a nutritional serum supplement often used for bone tissue engineering. The chemical composition of FBS is often not provided and varies from batch to batch and among different brands. Some FBS types even induce mineralization in the absence of cells (86). In this way, mineral may already form before differentiating cells can take charge over their formation, which might lead to uncontrolled mineral precipitation. To enable cell-controlled mineralization, medium composition needs to be optimized. Although the actual FBS components that influence mineralization are not known, alkaline phosphatase and fetuin likely play a role (57). Both proteins are not only produced by osteoblasts but may also be present in FBS. More specifically, alkaline phosphatase can induce mineralization in the presence of calcium and the osteogenic culture supplement glycerophosphate (87), possibly leading to uncontrolled mineral precipitation in the extrafibrillar spaces.

The collagen network is likely important for mineralization. It not only functions as a passive template; collagen fibril organization can improve mineralization by providing confined spaces at gap regions. These spaces might guide the minerals into the collagen fibrils (54). Biomechanically, fluid shear stress can influence NCP expression/synthesis by osteoblasts (88), which will likely influence mineralization as well. As such, the magnitude of fluid flow induced shear stresses has been shown to be predictive of mineral formation and might direct MSCs to proliferate or become osteoblasts, associated with increased mineralization (89,90). These studies typically focus on mineral quantity instead of quality, thus whether these fluid shear forces only affect the amount of mineralization, or also mineral location with respect to the collagen fibrils as characterized by Reznikov et al., (2018) (78), should be investigated. To investigate whether engineered mineralized bone ECM exhibits a highly mineralized collagen network with interconnected intrafibrillar and extrafibrillar minerals, tissue engineered constructs and its individual mineralized collagen fibrils should be visualized at the nanometer scale.

2.4 The cells; a role for osteoclasts, mature osteoblasts, and osteocytes?

In vivo, organized bone matrices as characterized by Reznikov et al., 2014 (5) are only observed after remodeling which includes: (i) activation or recruitment of progenitor cells, (ii) resorption of mineralized matrix by osteoclasts, (iii) surface preparation for bone formation, and (iv) ECM deposition by osteoblasts, regulated by osteocytes (91). In contrast, the *in vitro* approach usually starts with the differentiation of progenitor cells (mostly MSCs) towards matrix-producing osteoblasts, ignoring the contribution of osteocytes and osteoclasts. These progenitor cells start producing collagen and alkaline phosphatase during the initial stages of osteogenic differentiation (92). This may lead to uncontrolled fibrillogenesis if no sufficient NCPs are produced at this stage, and, in the presence of serum supplemented medium, uncontrolled mineralization. Osteoblasts produce NCPs important for collagen fibril assembly and mineralization and develop the ability to produce citrate as they mature (83,92,93). In addition, it has been demonstrated that undifferentiated MSC-like cells exert less traction forces on their substrate than mature osteoblast-like cells (61), indicating that mature osteoblasts have a superior ability to organize their ECM. Therefore, osteoblast maturation will likely improve ECM formation and organization as well.

When osteoblasts get embedded in their matrix, they can become osteocytes. Osteocytes are thought to guide bone formation and resorption by regulating the activities of osteoclasts and osteoblasts and are therefore important for overall bone structure (47). Besides this regulation function, these cells produce proteins that are important for mineralization of collagen, for example the NCP dentin matrix protein 1 (DMP1) (47,94). Accordingly, osteocytes not only regulate overall bone structure, but they might also influence the ECM organization at the nanometer scale, and they should therefore be included in 3D *in vitro* models for bone.

Recently, several osteoclast derived factors were identified that may influence osteoblast differentiation and subsequent matrix formation (95,96). In addition, as osteoclasts appear to deposit osteopontin in their resorption pits *in vitro* (97), they might have an active role in guiding mineralization. Moreover, synthesis of osteomodulin, important for fibrillogenesis, seems to be coupled to osteoclasts *in vivo*, as its expression was reduced in osteoclast-deficient mice (93). Thus, integration of osteoclasts may not only be important for resorption of the initially formed poorly organized ECM, but it might also improve ECM production by osteoblasts. Although *in vitro* bone remodeling by (mature) osteoblasts, osteocytes, and osteoclasts is still in its infancy (as reviewed by Owen and Reilly, 2018 (7)), it might be the only way to achieve the formation of physiological bone ECM.

Cells play thus an important role in regulating the ECM organization by the factors they secrete. In turn, the ECM organization can influence the cellular behavior (**Figure 2.3**). For example, osteoclasts need a mineralized surface to form a proper actin ring to create a resorption pit. In addition, it is believed that osteoblasts *in vivo* only produce lamellar-like bone when they are in full contact with the solid substrate surface (56,98). Accordingly, tissue engineering of 3D highly organized ECM is complex as the most effective starting point, *i.e.*, use an organized scaffold (as described by Liu et al., 2016 (99)) or let the cells organize their niche, is yet to be investigated.

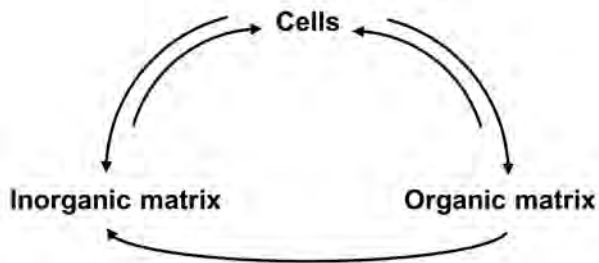


Figure 2.3. Organic bone matrix forms a template for the inorganic bone matrix. As such, osteoblasts, osteoclasts and osteocytes can control both organic and inorganic extracellular matrix organization via several pathways. However, they are in this process influenced by their own substrates. This complicates engineering of a 3D highly organized extracellular matrix as the most effective starting point is yet to be investigated.

Researchers have also attempted to improve osteogenesis by chondrogenic priming of progenitor cells (100). This strategy is based on endochondral ossification: the mechanism by which long bones develop *in vivo* where a cartilage template is formed, mineralized and subsequently replaced by woven bone. Endochondral ossification based bone tissue engineering could benefit bone regeneration as it may improve angiogenesis and remodeling *in vivo* (100). *In vitro*, chondrogenic priming might increase mineral content after subsequent osteogenic differentiation (101). Whether this method could improve bone remodeling *in vitro*, and thus potentially improve physiological bone formation is yet to be investigated.

2.5 Assessment of *in vitro* engineered bone-like structures

In bone tissue engineering, bone ECM components such as collagen, alkaline phosphatase, and minerals are often quantified and visualized at the micrometer scale to demonstrate osteogenesis. This might be enough for regeneration purposes, where, after implantation, the patient's own cells can contribute to remodeling. However, with the goal to develop *in vitro* bone models that resemble the complex ECM of *in vivo* bone,

additional structural assessments on both micrometer and nanometer scale are essential as explained in **Section 2.2** and **2.3**. In this regard, a multidisciplinary approach, in which bone biologists, material scientists, (bio)chemists and mechanical engineers work together, should be taken to improve the formation and assessment of 3D *in vitro* engineered bone models. Based on the discussed topics in previous sections, we suggest assessing the following outcome parameters and propose techniques to assess them (**Table 2.1**).

Table 2.1. Proposed outcome parameters and techniques to assess extracellular matrix organization.

Micrometer scale		Nanometer scale		
	Outcome	Techniques	Outcome	Techniques
Organic matrix	Collagen network orientation	PLM (102) PRS (102) pFTIR (102) pSHG (102) FM with DO algorithm (103)	Collagen fibril organization	AFM (102) TEM (102) FIB-SEM (102) SEM (102)
	Collagen network density	LM or FM and quantitative analysis		
Inorganic matrix	Mineral content	μ CT LM or FM and quantitative analysis EDS (104)	Mineral properties	XRD (105)
	Mineral location with respect to collagen network	Correlated LM or FM and SEM (106,107) Correlated LM and (SR) μ CT (108)	Mineral location with respect to collagen fibril	AFM (102) TEM (102)

Abbreviations: extracellular matrix (ECM), polarized light microscopy (PLM), polarized raman spectroscopy (PRS), polarized fourier transform infrared spectroscopy (pFTIR), polarized second harmonic generation (pSHG), fluorescence microscopy (FM), degree of orientation (DO), light microscopy (LM), micro-computed tomography (μ CT), energy dispersive X-ray spectroscopy (EDS), synchrotron micro-computed tomography (SR μ CT), atomic force microscopy (AFM), transmission electron microscopy (TEM), focused ion beam scanning electron microscopy (FIB-SEM), X- ray diffraction (XRD).

Especially the localization of minerals at the micrometer scale, and the collagen fibril, mineral property and location at the nanometer scale will require advanced techniques. Evaluation of collagen network orientation remains challenging, as techniques based on polarization require a dense collagen network which is not always achieved in bone tissue engineering, and which should be improved. As an alternative, fluorescent light microscopy images can be used in combination with a degree of orientation algorithm

(103). To assess whether the 3D *in vitro* bone model resembles physiological bone, these parameters should also be assessed in, and compared to 'real' physiological bone.

2.6 Conclusion

Taken together, with the purpose to create 3D *in vitro* bone models for studying bone related diseases and drug testing, tissue engineered ECM organization should resemble the *in vivo* physiological bone structure as this is often changed in pathological situations. We define the resemblance to the *in vivo* situation as a mineralized oriented dense collagen network with highly organized collagen fibrils and NCPs, allowing for intrafibrillar and organized extrafibrillar mineralization with interconnected mineral crystals. To compare the eventual ECM organization with the *in vivo* situation, researchers should consider assessing their *in vitro* bone models not only at the micrometer scale, but also on the nanometer scale. To recreate the complex *in vivo* situation, the initially formed disorganized ECM might need to be resorbed and osteocytes/mature osteoblasts should be allowed to take control of collagen fibrillogenesis and mineralization under conditions that simulate the physiological biochemical and biomechanical environment of bone.

Author contributions

B.d.W., N.S., A.A. and S.H. contributed to the conceptualization. B.d.W. and S.A. contributed to section 2.3 and 2.5. Other sections were written by B.d.W. B.d.W. and S.A. contributed to the preparation of the figures. All authors contributed to manuscript revision and approved the submitted version. A.A., N.S., K.I and SH contributed in the supervision. SH acquired main funding for this research.

Acknowledgement

We gratefully acknowledge the financial support for B.d.W. and S.H. by the research program TTW with project number TTW 016.Vidi.188.021, which is (partly) financed by the Netherlands Organization for Scientific Research (NWO). S.H. was also supported by the ERC Starting Grant REMOTE (Grant Agreement Number 336043). S.A. was supported by the Ministry of Education, Culture and Science (Gravitation Program 024.003.013). N.S. was supported by the ERC Advanced Investigator Grant COLMIN (Grant Agreement Number 788982). A.A. was supported by the Marie Curie Research Grants Scheme (Grant Agreement Number 794296) and was an awardee of the Weizmann Institute of Science–National Postdoctoral Award Program for Advancing Women in Science.

3

Characterization of three-dimensional bone-like tissue growth and organization under influence of curvature and directional fluid flow

This chapter is based on:

Bregje W.M. de Wildt^{1,2}, Feihu Zhao^{1,3}, Iris Lauwers¹, Bert van Rietbergen¹, Keita Ito^{1,2}, Sandra Hofmann^{1,2}

1. Orthopaedic Biomechanics, Department of Biomedical Engineering, Eindhoven University of Technology, The Netherlands.
2. Institute for Complex Molecular Systems, Eindhoven University of Technology, The Netherlands.
3. Biomedical Engineering, Zienkiewicz Centre for Computational Engineering, Faculty of Science and Engineering, Swansea University, United Kingdom.

Submitted

Abstract

The transition in the field of bone tissue engineering from bone regeneration to three-dimensional *in vitro* models has come with the challenge of recreating a dense and anisotropic bone-like extracellular matrix with cell culture. The creation of such an organized bone-like extracellular matrix has received little attention thus far. Although the mechanism by which bone extracellular matrix gains its structure is not fully understood, curvature (especially concavities), mechanical loading due to deformations or directional fluid flow, and osteocyte signaling have been identified as potential contributors. Here, guided by computational simulations, we evaluated three-dimensional cell and bone-like tissue growth and organization in a concave channel with and without directional fluid flow stimulation. Human bone marrow-derived mesenchymal stromal cells were seeded on donut-shaped silk fibroin scaffolds and stimulated to undergo osteogenic differentiation for 42 days statically or in a flow perfusion bioreactor. Constructs were investigated for cell distribution, and tissue growth and organization on day 14, 28, and 42. As a result, directional fluid flow was able to improve bone-like tissue growth but not organization. After 28 days of culture, when osteogenic differentiation was likely accomplished, cells tended to have a small preference for orientation in the tangential (*i.e.*, circumferential) direction of the channel. Based on our results supported by existing literature, we suggest that three-dimensional bone-like tissue anisotropy might be guided by curvature, while extracellular matrix production can be increased through the application of fluid shear stress. With this study, an initial attempt in three-dimensions was made to improve the resemblance of *in vitro* produced bone-like extracellular matrix to the physiological bone extracellular matrix.

3.1 Introduction

Bones have remarkable mechanical properties due to their extracellular matrix (ECM) composition and organization. To attain these properties, organic and inorganic matrix components are highly organized (109). In addition, bone structure is maintained and adapted through lifelong remodeling by osteoclasts (bone-resorbing cells), osteoblasts (bone-forming cells), and osteocytes (regulating cells) (46,47). Traditionally, bone tissue engineering methods (*i.e.*, making use of cells, scaffolds, biochemical and biomechanical stimuli) have been applied to recreate bone-like tissue *in vitro* for implantation and subsequent regeneration of large osseous defects. Because of bone's innate remodeling capacity, these implants may successfully induce regeneration, even if they fail to mimic the complex bone ECM structure. The recapitulation of the physiological bone ECM *in vitro* has received too little attention from researchers (110).

Tissue engineering strategies are nowadays increasingly applied for the creation of *in vitro* models of healthy or pathological bone, aiming at improving preclinical treatment development while addressing the principle of reduction, refinement, and replacement of animal experiments (3Rs) (7,19,20,111). Changes in bone's ECM composition and organization are characteristic for bone pathologies like osteoporosis, osteogenesis imperfecta, and bone metastasis (39–41,112). Therefore, *in vitro* models that aim at studying changes in bone ECM under the influence of treatments would benefit from improved control over organic matrix formation and subsequent mineralization (110,113). As the organic bone ECM with mainly collagen type I functions as a mineralization template (53), the improvement of collagen network organization and density may enhance the biomimicry of *in vitro* produced bone ECM. However, the mechanism by which collagen forms a dense anisotropic or lamellar network *in vivo* is poorly understood. It is well accepted that *in vivo* bone morphology and mass is regulated by osteocytes which sense interstitial fluid flow through their lacuna-canalicular networks (114). Recently, the anisotropy of the osteocyte lacuna-canalicular network has been correlated with the degree of apatite orientation in bone ECM, indicating a role for osteocytes in regulating ECM anisotropy (115). The preferred orientation of collagen producing osteoblasts could also be manipulated to stimulate anisotropic collagen formation. This might be accomplished by mechanical loading like cyclic stretch or directional fluid flow (66,67). These studies are however mainly performed in a controlled but simplified two-dimensional (2D) environment for a short period of time, not representative for the *in vivo* situation and ignoring tissue formation outcomes. In three-dimensional (3D) systems, fluid flow has been demonstrated to stimulate bone-like tissue growth including collagen formation (90,116,117). One challenge in these 3D environments is that both increased mass transport and wall shear stress (WSS) as a result of fluid flow could have an effect (88,113).

In addition to the application of external mechanical loading, substrate curvature could also induce cell organization (64), subsequent anisotropic collagen formation (65), and bone-like tissue growth (117–119). Bone-like tissue growth is especially stimulated in concavities with high curvatures (120). Cell and tissue anisotropy is then often observed in the tangential or circumferential direction of a pore (65). Thus, to promote *in vitro* bone-like tissue growth and anisotropy, fluid flow and curvature are likely two important factors. However, to our knowledge these two factors have not been evaluated together and therefore it is unclear which of the two factors dominates bone-like tissue growth and anisotropy.

Accordingly, in this study bone-like tissue growth and anisotropy were evaluated in a concave channel in a 3D silk fibroin (SF) scaffold statically or under influence of directional fluid flow. Osteogenically stimulated human bone marrow-derived mesenchymal stromal cells (hBMSCs) were used because of their ability to proliferate and differentiate into osteoblasts and osteocytes (116), making them an appropriate candidate for (personalized) *in vitro* bone models (121). As the cell response to fluid flow or curvature might change during osteogenic differentiation from mesenchymal stromal cell to osteocyte (88,120), tissue growth and organization were studied over a period of 42 days with intermediate time points at day 14 and day 28 (**Figure 3.1**). In addition, prior to experiments computational simulations were performed. Fluid flow patterns and fluid shear stress magnitude at the channel wall were simulated with a computational fluid dynamics (CFD) model to (i) determine the optimal bioreactor settings for osteogenesis and bone-like tissue formation, and (ii) ensure only fluid flow at the channel wall in the longitudinal direction (*i.e.*, direction of the flow) to minimize an effect of mass transport and flow in the radial (*i.e.*, into the scaffold) direction.

3.2 Materials and Methods

3.2.1 Scaffold fabrication

Bombyx mori L. silkworm cocoons were degummed by boiling them in 0.2 M Na₂CO₃ (S-7795, Sigma-Aldrich, Zwijndrecht, The Netherlands) for 1 h. Silk was dried and subsequently dissolved in 9 M LiBr (199870025, Acros, Thermo Fisher Scientific, Breda, The Netherlands), filtered, and dialyzed against ultra-pure water (UPW) for 36 h using SnakeSkin Dialysis Tubing (molecular weight cut-off: 3.5 K, 11532541, Thermo Fisher Scientific). Dialyzed SF solution was frozen at -80° C and subsequently lyophilized for 6 days. Lyophilized SF was dissolved in hexafluoro-2-propanol (003409, Fluorochem, Hadfield, UK) at a concentration of 17% (w/v) and casted in cylindrical scaffold molds filled with NaCl granules with a size of <200 μm as templates for the pores. Molds were covered and after 3 h, covers were removed from molds, and hexafluoro-2-propanol

was allowed to evaporate for 7 days whereafter β -sheets were induced by submerging SF-salt blocks in 90% MeOH for 30 min. SF-salt blocks were cut into discs of 3 mm height with a Accutom-5 (04946133, Struer, Cleveland, OH, USA). NaCl was dissolved from the scaffolds in ultra-pure water, resulting in porous sponges. These sponges were punched with a 9 mm diameter biopsy punch for the outer dimensions and a 3 mm diameter biopsy punch for the central channel with a fixed curvature of -0.67 mm^{-1} . The dimensions of the channel are based on previous research in which a 3 mm channel remained open over a period of 42 days (117), which is essential to enable studying the influence of directional fluid flow. Scaffolds were sterilized by autoclaving in phosphate buffered saline (PBS) at 121°C for 20 min.

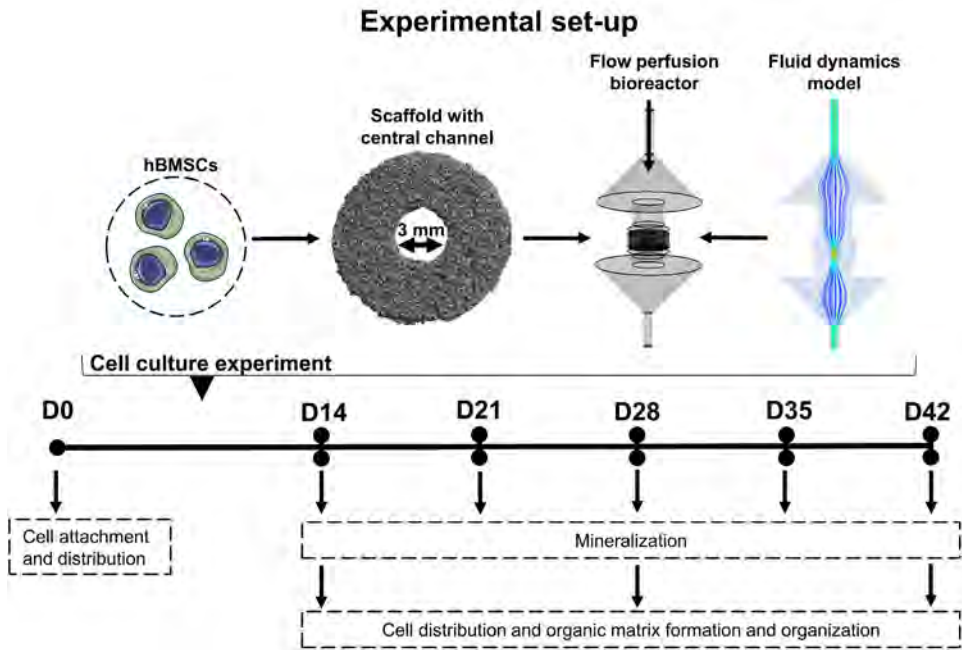


Figure 3.1. Experimental set-up of the study. hBMSCs were seeded on silk fibroin scaffolds with a central concave channel. Fluid flow was applied in longitudinal direction of the channel with a flow perfusion bioreactor of which the settings were determined with a computational fluid dynamics model. Cells were stimulated to undergo osteogenic differentiation over a period of 42 days with intermediate time points at day 14 and 28 to study cell distribution, and tissue growth and organization. Mineralization was checked weekly from day 14 onwards with non-destructive micro-computed tomography scanning. Abbreviations: human bone marrow derived stromal cells (hBMSCs), day (D). Cell images were modified from Servier Medical Art, licensed under a Creative Common Attribution 3.0 Generic License (<http://smart.servier.com/>, accessed on 8 July 2021).

3.2.2 Scaffold geometry

To obtain the detailed geometry of the scaffold, a micro-computed tomography scan (μ CT) was acquired with a μ CT100 imaging system (Scanco Medical, Brüttisellen, Switzerland). Scanning was performed for air-dried scaffolds with an isotropic voxel size of $3.9 \mu\text{m}$, energy level of 45 kVp, intensity of $200 \mu\text{A}$, integration time of 300 ms, and with twofold frame averaging. To reduce part of the noise, a constrained Gaussian filter was applied with a filter support of 1 and a filter width sigma of 0.8 voxel. Filtered images were segmented at a global threshold of 55% of the maximum grayscale value. Unconnected objects smaller than 50 voxels were removed through component labeling. A distance transformation function was used to determine the pore size distribution at four regions of interest (location S1, S3, S5, and S7 of **Figure 3.2A**).

3.2.3 Multi-scale computational fluid dynamics (CFD) model

Micro-scale: scaffold permeability calculation

As the region of interest was the scaffold's central channel, the porous region around the channel was homogenized using the permeability that was determined based on the reconstructed geometry from the μ CT scan as previously described (122). This was done to reduce the excessively high computational cost caused in modeling the irregular micro-struts of the porous SF scaffold. The homogenized scaffold permeability was determined based on the geometry of 8 representative volumetric elements (RVEs) with a diameter of $500 \mu\text{m}$ (> 4 times average pore size) and a height equal to the height of the scaffold (**Figure 3.2A**). The RVEs were selected from the total scaffold geometry that was reconstructed using Seg3D software (University of Utah, UT, USA). The fluid domain of RVEs was meshed using the same strategy as in (122) with global maximum and minimum element sizes of $20 \mu\text{m}$ and $0.2 \mu\text{m}$, respectively.

The RVEs' permeability was determined from Darcy's law (**Equation 3.1**):

$$Q = \frac{\kappa A}{\mu} \cdot \frac{\Delta p}{H} \quad (3.1)$$

Where Δp is the pressure drop over the scaffold height H determined by solving the CFD model for each RVE; Q is the prescribed flow rate, A the cross-sectional area to the flow, μ the dynamic viscosity of the culture medium ($\mu = 1.09 \text{ mPa}\cdot\text{s}$ for cell culture medium (123)), and κ the permeability.

In the CFD model, the medium flow was defined as incompressible Newtonian and described by the Navier-Stokes equation that was solved using the finite volume method (FVM). As a convergence criterion it was required that the root-mean-square residual

of the mass and momentum was smaller than a fixed threshold set at 10^{-4} . Calculations were done using ANSYS CFX (ANSYS, Inc., PA, USA).

Macro-scale: wall shear stress calculation

The macro-scale model representing the full scaffold and perfusion bioreactor domain was used for the fluid shear stress calculations on the scaffold channel wall (**Figure 3.2C**). In this macro-structural model, the scaffold region was homogenized and assigned a permeability calculated from the eight RVE micro-scale models. The region of the porous media (scaffold and newly formed tissue) was defined as a homogeneous porous media (**Figure 3.2C**), and described by Darcy's equation (**Equation 3.2**):

$$\begin{cases} \nabla \cdot \mathbf{q} = 0 \\ \frac{\mu}{\kappa} \mathbf{q} + \nabla p = 0 \end{cases} \quad (3.2)$$

where \mathbf{q} is the Darcy velocity and p the pressure.

The remaining central bioreactor channel without tissue formation was defined as free fluid (incompressible, Newtonian laminar flow), and described by the Navier–Stokes equations (**Equation 3.3**):

$$\begin{cases} \nabla \cdot \mathbf{v} = 0 \\ \frac{\partial \mathbf{v}}{\partial t} + \mathbf{v} \cdot \nabla \mathbf{v} = -\nabla p + \mu \nabla^2 \mathbf{v} \end{cases} \quad (3.3)$$

where \mathbf{v} is the fluid velocity vector.

The top and bottom surfaces of the porous media domain were defined as boundaries with continuity of mass flux, and the scaffold internal channel wall was defined as a non-slip wall boundary as it is assumed that there will be only minor fluid following across the wall. At the inlet of the CFD model, a constant flow rate of 1.5 mL/min was prescribed according to the experimental condition. At the outlet, a relative pressure of 0 Pa was applied. The macro-scale CFD model was meshed with 1,720,090 tetrahedral elements, solved by FVM using ANSYS CFX (ANSYS, Inc., PA, USA) and the same convergence criteria as for micro-scale model.

To check the assumption that only little fluid flows through the interface between the channel and the scaffold, a CFD model in which a scaffold with idealized cubic pore shape and uniform pore size, was utilized. As this model only served to support the assumptions made for the main macro-model as described above, details on this model can be found in the supplementary information (**Section Regularized element CFD model**).

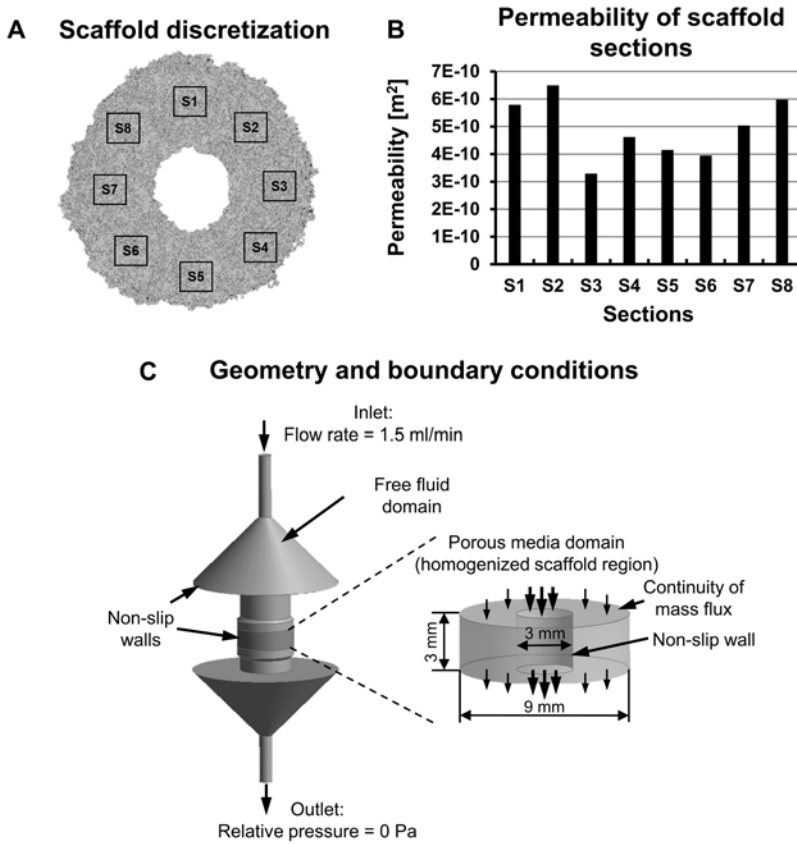


Figure 3.2. Multi-scale CFD model parameters. (A) Scaffold geometry was obtained with μ CT scanning whereafter the reconstructed scaffold was discretized into eight RVEs for permeability determination using the micro-model. (B) Calculated permeability of each scaffold RVE. (C) Geometry and boundary conditions of the CFD model. Abbreviations: computational fluid dynamics (CFD), representative volumetric element (RVE), micro-computed tomography (μ CT).

3.2.4 Cell experiment

hBMSC isolation, expansion and seeding

hBMSCs were isolated from human bone marrow (Lonza, Walkersville, MD, USA) and characterized for surface markers and multilineage differentiation, as previously described (124). hBMSCs were frozen at passage 4 with 5×10^6 cells/ml in freezing medium containing fetal bovine serum (FBS, BCBV7611, Sigma-Aldrich) with 10% DMSO and stored in liquid nitrogen until further use. Before experiments, hBMSCs were thawed, collected in high glucose DMEM (hg-DMEM, 41966, Thermo Fisher Scientific), seeded at a density of 2.5×10^3 cells/cm² and expanded in expansion medium containing hg-DMEM, 10% FBS (BCBV7611, Sigma-Aldrich), 1% Antibiotic

Antimycotic (anti-anti, 15240, Thermo Fisher Scientific), 1% Non-Essential Amino Acids (11140, Thermo Fisher Scientific), and 1 ng/mL basic fibroblastic growth factor (bFGF, 100-18B, PeproTech, London, UK) at 37 °C and 5% CO₂. After 7 days, cells were detached using 0.25% trypsin-EDTA (25200, Thermo Fisher Scientific) and seeded onto scaffolds at passage 5. Cells were seeded at a density of 5*10⁶ cells per scaffold and seeding was performed dynamically for 6 hours in 50 ml tubes on an orbital shaker at 150 RPM in osteogenic control medium (lg-DMEM (22320, Thermo Fisher Scientific), 10% FBS (SFBS, Bovogen, East Keilor, Australia and 1% anti-anti) (125). After seeding, scaffolds were kept in wells plates overnight to ensure proper attachment before flow was applied.

Bioreactor culture

hBMSC-loaded scaffolds were cultured in custom-made flow perfusion bioreactors as previously described (89). Scaffolds were cultured statically and dynamically for which a flow of 1.5 ml/min was applied, based on pre-simulations. Cells were stimulated to undergo osteogenic differentiation by providing osteogenic differentiation medium (osteogenic control medium with osteogenic supplements 10 mM β-glycerophosphate (G9422, Sigma-Aldrich), 50 μg/ml ascorbic acid-2-phosphate (A8960, Sigma Aldrich), and 100 nM Dexamethasone (D4902, Sigma-Aldrich)). For static bioreactors, 6 ml medium was supplied which was completely changed 3 times a week. For dynamic bioreactors, 12 ml medium was supplied of which only half of the volume could be replaced 3 times a week with double concentrated osteogenic supplements (*i.e.*, 20 mM β-glycerophosphate, 100 μg/ml ascorbic acid-2-phosphate, and 200 nM Dexamethasone) to keep the initial concentration of supplements constant. The bioreactor culture was maintained for 14, 28 or 42 days at 37 °C and 5% CO₂.

3.2.5 Cell construct analyses

Cell attachment

As cell attachment can be influenced by the cell experienced mechanical load (126), cell attachment was assessed at day 0 for a small subset of the samples ($N = 4$). These samples were cut in half and fixed in 2.5% glutaraldehyde in 0.1 M sodium cacodylate buffer (CB) for 4 h and then washed in CB. Samples were stained with 0.04% osmium tetroxide (75632, Sigma-Aldrich) in CB for 90 min and dehydrated with graded ethanol series (37%, 67%, 96%, 3 x 100%, 15 min each) followed by lyophilization. Samples were subsequently coated with 20 nm gold and imaging was performed in high vacuum, at 10 mm working distance, with a 10 kV electron beam (Quanta 600F, FEI, Eindhoven, The Netherlands).

Cell distribution visualization

Day 0, 14, 28 and 42 scaffolds ($N = 4$ scaffolds per condition per time point) were cut in half and soaked for 15 minutes in each 5% (w/v) sucrose and 35% (w/v) sucrose in PBS. Samples were embedded in Tissue Tek® (Sakura, Alphen aan den Rijn, The Netherlands) and quickly frozen with liquid N_2 . Cryosections were sliced in the vertical plane with a thickness of 5 μ m. Upon staining, sections were fixed for 10 minutes in 3.7% neutral buffered formaldehyde and washed twice with PBS. Sections were subsequently stained with 1 μ g/ml DAPI (D9542, Sigma-Aldrich) for 10 min and washed twice with PBS. Coverslips were mounted with Mowiol, tile scans were made with an epi-fluorescence microscope (Zeiss Axio Observer 7, 10x/0.3 EC Plan-Neofluor), and tile scans were stitched with Zen Blue software (version 3.3, Zeiss, Breda, The Netherlands).

Organic matrix growth visualization and quantification

To visualize collagen deposition, cryosections were prepared in two different planes (*i.e.*, the horizontal and vertical place, $N = 4$ scaffolds per condition, time point, and plane) and stained with Picrosirius Red. Sections were soaked in Weigert's Iron Hematoxylin (HT1079, Sigma-Aldrich) solution for 10 minutes, washed in running tap water for 10 minutes, and stained in 1% w/v Sirius Red (36,554-8, Sigma-Aldrich) in picric acid solution (36011, Sigma-Aldrich) for one hour. Subsequently, sections were washed in two changes of 0.5% acetic acid and dehydrated in one change of 70% and 96% EtOH, three changes of 100% EtOH, and two changes of xylene. Sections were mounted with Entellan (107961 Sigma-Aldrich). To capture the entire section, tile scans were made with a bright field microscope (Zeiss Axio Observer Z1, 10x/0.45 Plan-Apochromat objective). Tile scans were stitched with Zen Blue software (version 3.1, Zeiss). Tissue growth was quantified in the vertical plane and horizontal plane measuring the distance from outer scaffold boarder to outer cell/tissue boarder at 10 different locations in each plane using Fiji (127). The measured distances in the two planes were averaged for the average channel tissue ingrowth per sample.

To check whether the produced ECM was of a bone-like nature, cryosections ($N = 4$ scaffolds per condition per time point) were prepared and fixed as described above and stained with the bone ECM markers osteopontin and collagen type I (128,129). Briefly, sections were permeabilized in 0.5% Triton X-100 in PBS for 5 min and blocked in 10% normal goat serum in PBS for 30 min. Primary antibodies (osteopontin: 1:200, 14-9096-82, Thermo Fisher Scientific; collagen type I: 1:200, ab34710, Abcam, Cambridge, UK) were incubated overnight at 4 °C, secondary antibodies (osteopontin: Alexa 546, 1:200, A21123, Invitrogen Molecular Probes; collagen type I: Alexa 647, 1:200, A21246, Invitrogen Molecular Probes) were incubated with 0.1 μ g/ml DAPI for 1 h at room

temperature. Coverslips were mounted with Mowiol, and images were acquired with a laser scanning microscope (Leica TCS SP8X, 40x/0.95 HC PL Apo objective).

Biochemical content analyses

To quantify the biochemical content, lyophilized scaffolds ($N = 4$ per condition per time point) were weighted and digested overnight in papain digestion buffer (containing 100 mmol phosphate buffer, 5 mmol L-cysteine, 5 mmol EDTA and 140 $\mu\text{g}/\text{ml}$ papain (P4762, Sigma-Aldrich)) at 60 °C. DNA was quantified using the Qubit Quantification Platform (Invitrogen) with the high sensitivity assay, according to the manufacturer's instructions. Hydroxyproline content as a measure for collagen was quantified using a chloramine-T assay (130) with trans-4-hydroxyproline (H54409, Sigma-Aldrich) as reference. Absorbance values were measured at 550 nm using a plate reader (Synergy™ HTX, Biotek) and standard curve absorbance values were used to determine hydroxyproline content in the samples.

Matrix mineralization

Bioreactors were scanned and analyzed with a $\mu\text{CT}100$ imaging system weekly from day 14 to day 42. Scanning was performed at an isotropic nominal resolution of 17.2 μm , energy level of 45 kVp, intensity of 200 μA , integration time of 300 ms and with twofold frame averaging. To reduce part of the noise, a constrained Gaussian filter was applied with a filter support of 1 and a filter width sigma of 0.8 voxel. Filtered images were segmented to detect mineralization at a global threshold of 24% of the maximum grayscale value. Unconnected objects smaller than 30 voxels were removed through component labeling. Mineralized volume was computed for the total scaffold and the channel region using the scanner manufacturer's image processing language (IPL) (131).

Cell and tissue organization

A quarter of each scaffold ($N = 4$ per condition per time point) was fixed in 3.7% neutral buffered formaldehyde. Samples were washed in PBS, permeabilized for 30 min in 0.5% Triton X-100 in PBS and stained for 1 h with 0.1 $\mu\text{g}/\text{ml}$ DAPI, 100 pmol Atto 647-conjugated Phalloidin and 1 $\mu\text{mol}/\text{mL}$ CNA35-mCherry (132) to visualize cell nuclei, F-actin and collagen, respectively. Samples were subsequently washed and imaged in PBS. Z-stacks of the channel wall were acquired with a confocal laser scanning microscope (Leica TCS SP8X, 20x/0.40 HC PL Fluotar L objective). Z-stacks were deconvolved using the CLME deconvolution algorithm with the Batch Express function of Huygens Professional (version 20.04, Scientific Volume Imaging, The Netherlands). Cell nuclei at the channel wall were subsequently quantified after segmentation using the Huygens Object Analyzer tool (Scientific Volume Imaging) and normalized for the tissue volume. Z-stacks were converted to maximum intensity projections for presentation using Fiji (127). In addition, phalloidin maximum intensity

projections were used for cell orientation analyses using a previously described algorithm (103) in MATLAB (version 2019b, The MathWorks Inc., Natick, MA, USA). In short, the principal direction of each pixel with an actin fiber was derived after eigenvector decomposition of the Hessian matrix. A two-term Gaussian distribution (for bimodal distributions present in the data) was subsequently fitted to the derived actin fiber distribution per sample.

3.2.6 Statistical analyses

Statistical analyses were performed, and graphs were prepared in GraphPad Prism (version 9.3.0, GraphPad, La Jolla, CA, USA) and R (version 4.1.2) (133). Data were tested for normality in distributions and equal variances using Shapiro-Wilk tests and Levene's tests, respectively. When these assumptions were met, mean \pm standard deviation are presented, and to test for differences, a two-way ANOVA was performed followed by Tukey's post hoc tests with adjusted p-value for multiple comparisons. Other data are presented as median \pm interquartile range and were tested for a difference between static and dynamic with non-parametric Mann-Whitney U test for each time point with adjusted p-value for multiple comparisons. A p-value of <0.05 was considered statistically significant.

3.3 Results

3.3.1 Computational fluid dynamics simulation

From the μ CT analyses, a similar pore size distribution for four regions of interest was found with an average pore size of $103 \pm 40 \mu\text{m}$ (**Figure S3.1**). Based on the CFD model for the eight RVEs at the micro-scale, the average permeability of the whole scaffold was $4.92 \times 10^{-10} \text{ m}^2$ (**Figure 3.2B**). According to the macro-scale CFD model, the fluid shear stress at the channel wall was uniformly distributed along the longitudinal direction of the channel (*i.e.*, from top to bottom) with an average value of 10.62 mPa (maximum WSS = 20.67 mPa, minimum WSS = 9.33 mPa) (**Figure 3.3**). Moreover, from the CFD model with idealized cubic pore shape elements the average velocity along the channel was 1.2 mm/s, while the average velocity in the radial direction (*i.e.*, across the channel) was 2.3×10^{-3} mm/s (supplementary information, **Section Regularized element CFD model**). Thus, the fluid velocity along the channel was > 520 times higher than the fluid velocity in the radial direction, confirming the assumption that fluid flow through the interface can be neglected. Furthermore, the majority of the fluid flow went through the channel rather than through the scaffold region: the average z-component (*i.e.*, in longitudinal direction) of the fluid velocity vector was 1.20 mm/s in the channel compared to 0.16 mm/s in the scaffold region (**Figure S3.2**).

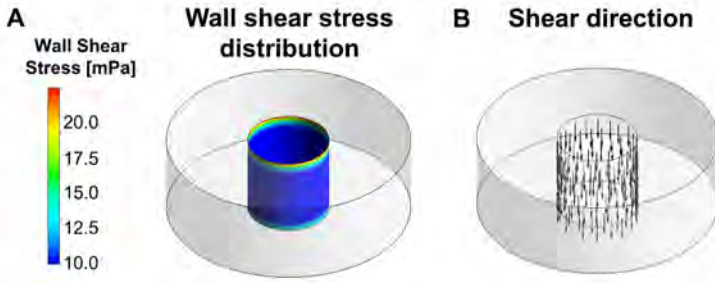


Figure 3.3. (A) Wall shear stress distribution on the inner channel wall of the scaffold. (B) The direction of the shear vector was uniform and in the longitudinal direction of the channel.

3.3.2 Cell attachment and distribution

After seeding, cells were found within the pores of the scaffold, in the scaffold and at the channel wall (**Figure 3.4A**). SEM revealed that cells at the channel wall bridged the scaffold pores (**Figure 3.4B**). The cells collectively covered the channel pores (**Figure S3.3**). Then, the influence of fluid flow on cell distribution and potentially on cell proliferation at the channel wall was evaluated. After 42 days, dynamically cultured samples seemed to have formed a thicker cell layer at the channel wall (**Figure 3.4C+D**). DNA content quantification of the entire scaffold revealed a time dependent decrease in DNA which was different for statically and dynamically cultured scaffolds (**Figure 3.4E**). When comparing the two culture conditions per time point, DNA content at day 28 was higher in statically cultured scaffolds than dynamically cultured samples (**Figure 3.4E**). Interestingly, DNA content tended to increase from day 0 to day 14 for both conditions, after which it decreased again to values of day 0 for dynamically cultured scaffolds after 28 days and for statically cultured scaffolds after 42 days. To check whether there was a difference in cell number at the scaffold channel wall between statically and dynamically cultured scaffolds, cell nuclei were counted from Z-stacks of the scaffold channel wall (**Figure 3.4F**). At the channel wall, no differences between statically and dynamically cultured scaffolds were found. This suggests that the observed thickening in cell layer is the result of ECM production by cells at the channel wall, rather than cell proliferation.

3.3.3 Organic matrix growth and mineralization

Collagen deposition was visualized in the horizontal and vertical plane (**Figure S3.4**). Vertical plane images revealed collagen formation after picosirius red staining through the entire scaffold for both statically cultured and dynamically cultured scaffolds (**Figure 3.5A** and **Figure S3.4** for more representative images).

Cell attachment and distribution

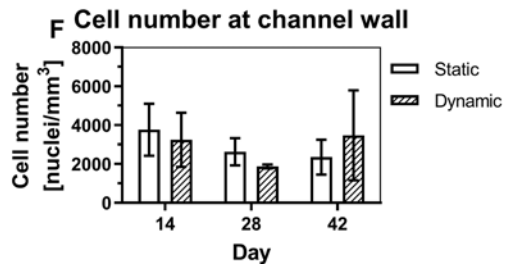
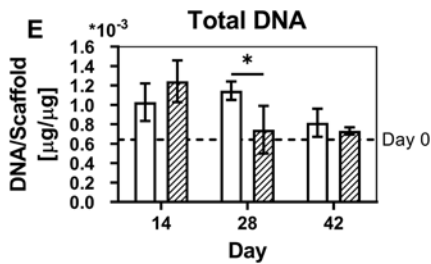
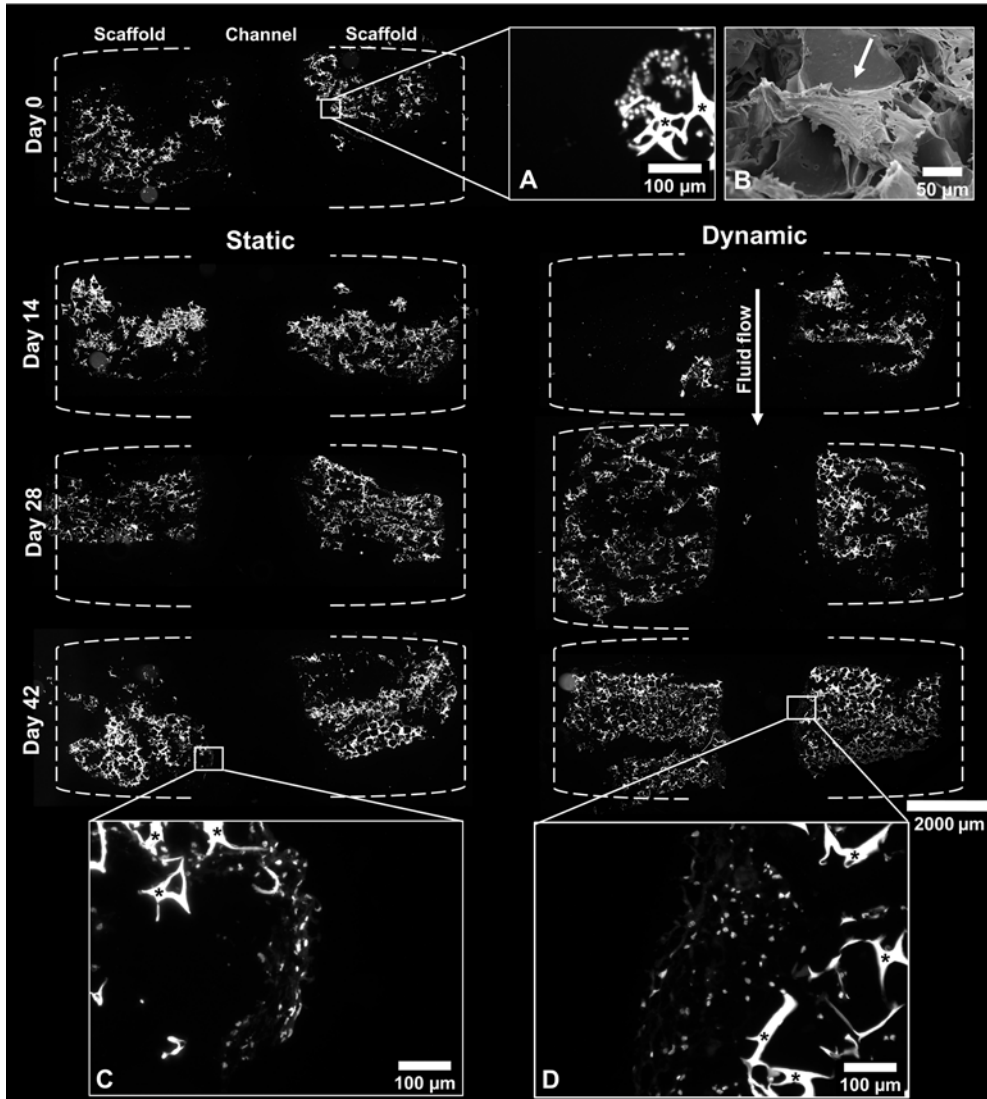


Figure 3.4. Cell distribution within the scaffold and attachment at the channel wall. (A) Scaffold vertical

plane sections in which cells and scaffold are visualized with nuclei (DAPI) staining and scaffold autofluorescence (triangular-like structures, indicated with an asterisk) of day 0 samples. **(B)** Cell attachment at day 0 visualized with scanning electron microscopy. **(C)** Cell layer at channel wall for statically cultured scaffolds and **(D)** dynamically cultured scaffolds. **(E)** Total DNA quantification, $p < 0.05$ for factor time and time x group interaction (Two-way ANOVA and Tukey's post hoc tests within each time point), and **(F)** cell count at the channel wall, n_s (Two-way ANOVA). Asterisks in graphs represent results of post hoc analyses ($*p < 0.05$)

Collagen content tended to increase with time, with most collagen visible at day 42 of culture for both groups. This was quantified by measuring the hydroxyproline content. Indeed, a time-dependent increase in hydroxyproline content was found (**Figure 3.5C**). This increase over time was however similar for statically and dynamically cultured constructs. When zooming in at the channel wall, dynamically cultured scaffolds tended to have a thicker layer of formed tissue than statically cultured scaffolds (**Figure 3.5B**). By measuring the thickness of this newly formed tissue in the vertical and horizontal plane, tissue growth at the channel wall could be quantified. Again, a time-dependent increase in tissue thickness was found (**Figure 3.5D**). At the channel wall, this time-dependent increase was different for statically and dynamically cultured scaffolds. Dynamically cultured scaffolds had a statistically significant thicker layer of tissue on day 42 at the channel wall than statically cultured scaffolds.

A positive immunohistochemical staining for collagen type I and osteopontin revealed that the formed ECM at the channel wall was of a bone-like character (**Figure S3.5**). On day 14, collagen type I and osteopontin were mostly present around the cells while on day 42 they were more distributed through the ECM for both statically and dynamically cultured scaffolds. Dynamically cultured scaffolds seemed to have a higher collagen density at the channel wall than statically cultured scaffolds (**Figure S3.5**).

Longitudinal μ CT monitoring allowed for visualization and quantification of matrix mineralization. From the 3D scans and their quantification, a clear increase in mineralization over time was observed for both groups (**Figure 3.6A+B**). Although non-significant, more mineralization seemed present in statically cultured scaffolds. As we were mostly interested in the scaffold channel wall, the scaffold channel volume was also analyzed for the presence of mineralization. Interestingly, at the channel wall differences between statically and dynamically cultured scaffolds could not be observed.

3.3.4 Cell and tissue organization

Over the culture period progression, no clear trend in cell and tissue organization was observed for statically and dynamically cultured scaffolds (**Figure 3.7A+C**). From the actin fiber distributions, no consistent influence of directional fluid flow was observed (**Figure 3.7B+D**). On day 28, cells tended to align more in the tangential or

circumferential direction of the channel for both statically and dynamically cultured scaffolds. This was however not consistent for all scaffolds in the dynamically cultured group.

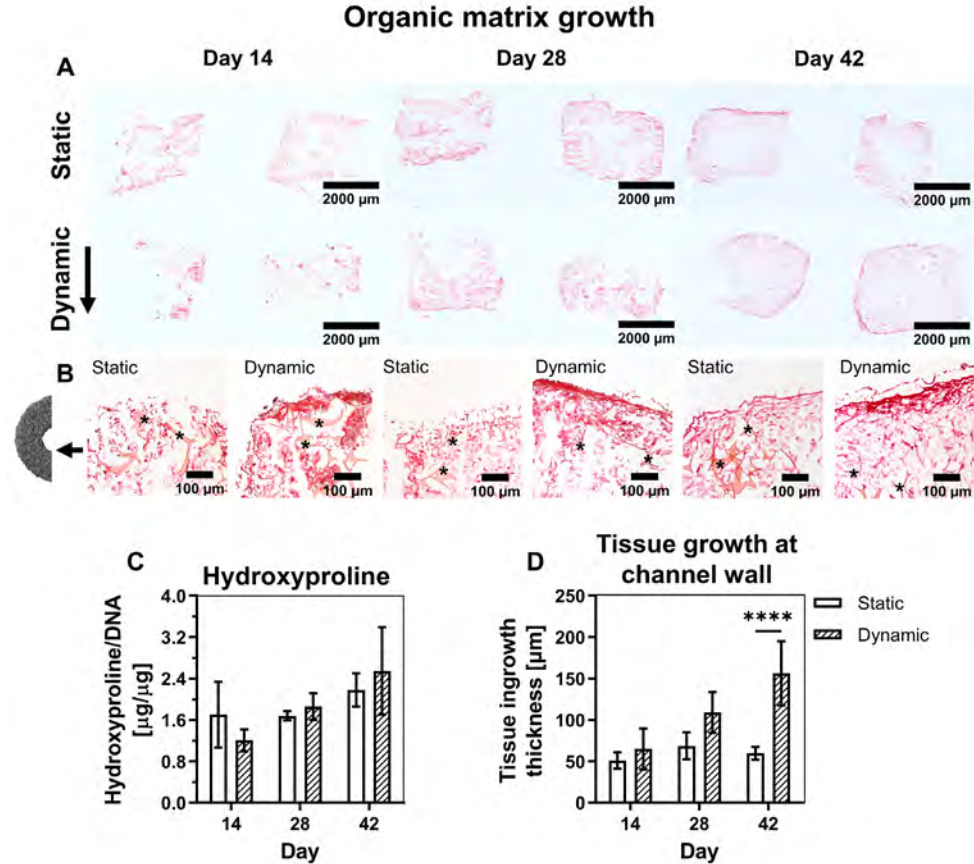


Figure 3.5. Visualization and quantification of organic matrix growth. **(A)** Micrographs of vertical plane sections stained for collagen (picrosirius red). **(B)** Micrographs of the channel wall of vertical plane sections stained for collagen. Scaffold is indicated with an asterisk **(C)** Hydroxyproline content quantification of the scaffold, $p < 0.05$ for factor time (Two-way ANOVA and Tukey's post hoc tests within each time point) **(D)** Tissue growth quantification at the channel wall, $p < 0.05$ for factor time, group, and time x group interaction (Two-way ANOVA and Tukey's post hoc tests within each time point). Asterisks in graphs represent results of post hoc analyses ($****p < 0.0001$).

3.4 Discussion

With the transition in the application of bone tissue engineering strategies from bone regeneration to 3D *in vitro* models, the challenge to create an organized bone ECM has been identified (110). The creation of an anisotropic and dense bone-like ECM has

received little attention and currently available studies were mainly (i) performed on 2D substrates over a short period of time, or (ii) did not include anisotropy as an outcome. Although the mechanism by which bone ECM gains its dense and organized structure is not fully understood, curvature (especially concavities), mechanical loading like directional fluid flow, and osteocyte signaling have been identified as potential contributors.

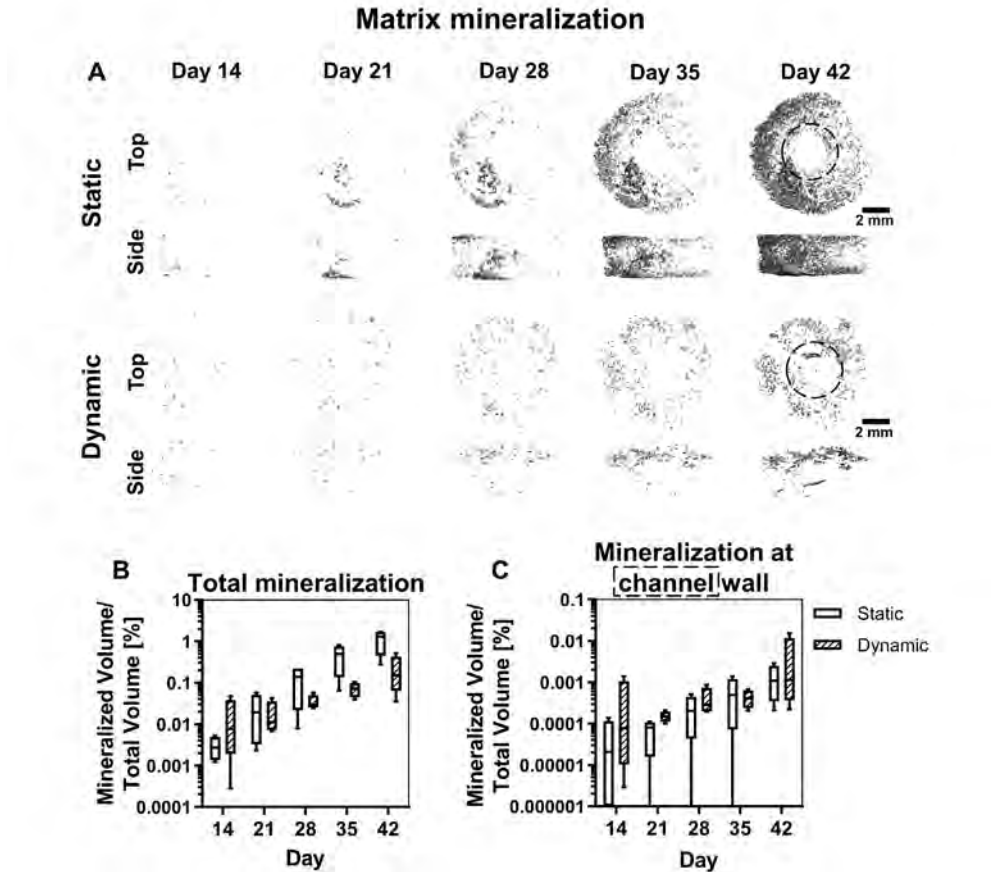


Figure 3.6. Mineralization over time obtained with μ CT-scanning. (A) Segmented μ CT scans of statically and dynamically cultured scaffolds from day 14 to day 42. (B) Mineralized volume of the entire scaffold obtained from μ CT scans, *ns* (Mann-Whitney U tests per time point with Bonferroni correction for multiple comparisons). (C) Mineralized volume around the channel volume obtained from μ CT scans, *ns* (Mann-Whitney U tests per time point with Bonferroni correction for multiple comparisons). Area highlighted with dashed line was analyzed to obtain mineralization at the channel wall. Abbreviations: micro-computed tomography (μ CT).

In this study, we aimed at evaluating 3D cell and tissue growth and organization in a concave channel with and without directional fluid flow stimulation over a period of 42

days to include the contribution of cell differentiation. As a result, directional fluid flow improved bone-like tissue growth but not organization. After 28 days of culture, when osteogenic differentiation of the cells was likely accomplished, they tended to have a small preference for orienting themselves in the tangential direction of the channel. Even when fluid flow was applied in the perpendicular direction, most samples showed cells with a preference for alignment in the tangential (*i.e.*, circumferential) direction of the channel which might be an effect of its curvature (65).

In this study, a CFD model was used to calculate the WSS magnitude and direction. The multiscale model allowed for the calculation of WSS magnitude over the entire channel wall for the highly irregular scaffold used in this study. With an average WSS of 10.62 mPa, mechanical stimulation was within the range of osteogenic and mineralization stimulation for human cells in a 3D environment, based on previous research (90,126). To enable this calculation, the assumption that fluid was only flowing in the longitudinal channel direction had to be made. To check whether this assumption was valid, a CFD model was applied on a simplified scaffold geometry comprising of uniform cubical elements as pores. From this model, the made assumption that fluid for generating mechanical stimulation only flows in the longitudinal channel direction seemed valid. In addition, most fluid went through the channel, indicating that within the scaffold culture conditions could be considered static (*i.e.*, limited mass transport). This might explain why the difference in collagen formation between statically and dynamically cultured scaffolds were only observed at the channel wall. Another assumption for determining the WSS on the cells was their attachment. Only if cells have a flat attachment to the channel wall, WSS on cells is comparable to the calculated WSS. When cells bridge pores, fluid flow not only induces shear but also strain (126). After seeding, cells indeed bridged the pores at the channel wall. As such, the calculated WSS magnitude might have been an underestimation of the by the cells experienced mechanical load. Cells also covered the channel wall already directly after seeding. It is expected that once they produce ECM, the irregular channel wall gets covered with a more homogeneous tissue layer in which cells experience less strain and are stimulated by mostly WSS (113). However, substantial tissue growth in the channel will likely also change the fluid flow induced shear stress (134). Thus, the fluid flow induced mechanical load is expected to change over time which hinders the interpretation of the obtained results and therefore is a limitation of the present study. In this study, tissue growth and mineralization were already monitored over the entire culture period. Future studies would benefit from including these tissue growth and mineralization parameters in their models to get a more realistic estimation of the change in stress over time and potentially adapt the input flow accordingly (113,135).

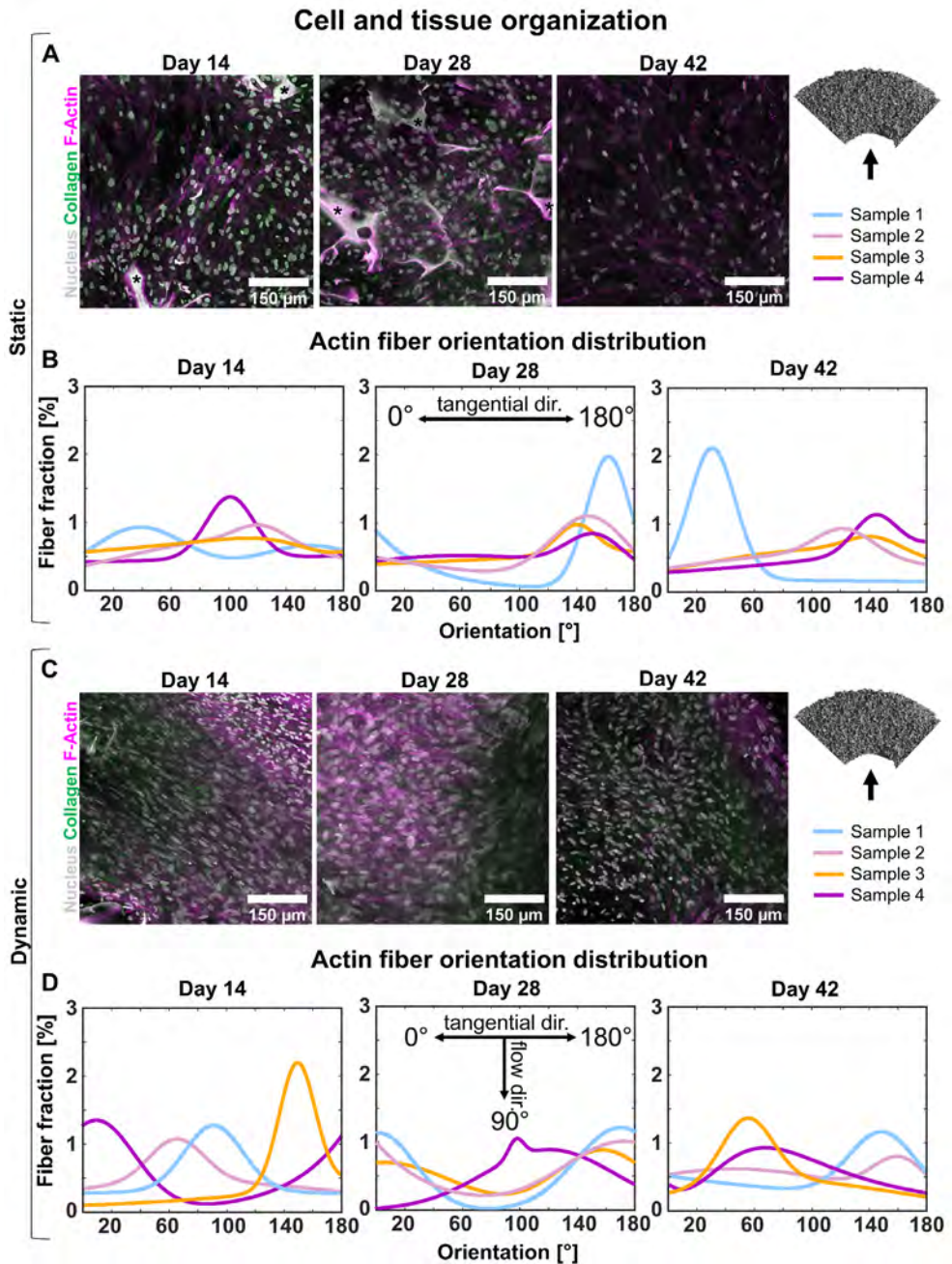


Figure 3.7. Cell and tissue organization analysis. (A) Deconvolved maximum intensity projections of Z-stacks obtained from the channel wall of statically cultured scaffolds. Tissues are stained for the nucleus (gray), collagen (green), and F-Actin (magenta). Scaffold is indicated with an asterisk. (B) Gaussian fit (2nd order) of actin fiber orientation distribution of statically cultured scaffolds relative to the tangential direction

of the channel and fluid flow. **(C)** Deconvolved maximum intensity projections of Z-stacks obtained from the channel wall of dynamically cultured scaffolds. Tissues are stained for the nucleus (gray), collagen (green), and F-Actin (magenta). **(B)** Gaussian fit of actin fiber orientation distribution of dynamically cultured scaffolds. Abbreviation: direction (dir.).

Interestingly, while other studies have reported increased mineralization under the influence of WSS (90,116), in our study an opposite effect was observed. Studies with a similar set-up have also found more mineralization in statically cultured scaffolds than dynamically cultured scaffolds (89,117). In the used perfusion bioreactor set-up, only half of the medium volume can be replaced whereas in statically cultured bioreactors all medium can be replaced. To account for this, osteogenic supplements were added in a double concentration under the assumption that they are either consumed or degraded before the next medium change. However, this way of medium replacement might also induce a difference between the groups in protein concentration derived from FBS or in soluble factors produced by the cells (136). Recently, the impact of alkaline phosphatase in FBS on mineralization has been shown (137). We therefore suggest that the difference in mineralization is attributed to the bioreactor system and its practical limitations, something that needs to be considered for future experiments using this bioreactor system. At the channel wall, differences in mineralization between statically and dynamically cultured constructs were absent. This suggests that in dynamically cultured constructs, mechanically stimulated cells at the channel wall contributed more to mineralization than cells within the scaffold that likely sensed no to limited shear stress.

In our effort to improve cell and tissue organization in 3D, directional fluid flow was applied in a concave channel. Fluid flow has been shown to stimulate cellular alignment in 2D (67), while (mainly concave) curvature has been shown to induce anisotropic collagen formation in 3D (65,120,138). By applying fluid flow in the longitudinal direction of a concave channel in a 3D scaffold, we attempted to identify the main driver of 3D cell and tissue organization. When cells were oriented in the longitudinal direction of the channel, curvature was considered to be neglectable, while if cells aligned in the tangential or circumferential direction, curvature was -0.67 mm^{-1} . Over the entire culture period, no clear influences of curvature nor directional fluid flow were observed. Only a small preference for the tangential direction (*i.e.*, the channel curvature) was observed after 28 days for both statically and dynamically cultured scaffolds. Fluid flow does not seem to have a consistent influence on cell and tissue organization in the presence of curvature in 3D. Reasons why the influence of curvature was limited in this study could be (i) the irregular channel wall, (ii) the differentiation state of the cells, and/or (iii) the channel diameter and thus the curvature magnitude. First, while in this scaffold, the smallest possible pores were produced to maximize the channel to pore size ratio,

scaffold pores might still have induced small and local changes in curvature which could have locally influenced initial cell orientation. This might also explain why after 28 days a small influence of curvature was visible, as once cells have formed a monolayer and produced their own ECM, curvature becomes a more dominant factor than scaffold properties (139). However, one would then also expect to see cell alignment in constructs cultured for 42 days which could not be detected in this study. Second, previous research has demonstrated that undifferentiated hBMSCs prefer to avoid curvature and would therefore align in the longitudinal direction of the channel (120). Therefore, cells might have changed their orientation during their differentiation process. Third, bone-like tissue growth is mainly stimulated with higher concavities (117). However, to avoid closing of the channel, which would have induced unpredictable flow patterns, a trade-off between curvature and channel diameter had to be made.

Recently, prostaglandin E2 signaling by osteocytes was identified as a potential inducer of osteoblast alignment (140). In this study, osteocytes might have been differentiated from hBMSCs but most likely only under influence of mechanical stimulation and towards the end of the culture period (116). The contribution of osteocytes to ECM anisotropy in bone complicates the investigation of organized ECM formation *in vitro*, as in our approach it requires long-term experiments. Osteoblast-osteocyte co-cultures might be performed to overcome this limitation. In addition, the field would benefit from controlled experiments in which multiple cues (*e.g.*, strain, fluid flow, curvature, presence of osteocytes) can be assessed in a high-throughput fashion. Such experiments could lead to the identification of the driving cues for bone ECM growth and anisotropy. Nevertheless, the here presented longitudinal characterization of cell and tissue growth and organization under influence of curvature in the absence and presence of directional fluid flow underlines the complexity of the *in vitro* creation of a dense and anisotropic bone-like ECM, which is desired for *in vitro* bone models (110).

3.5 Conclusion

In the present study, we presented a computationally informed 3D model for bone-like tissue growth. In our attempt to improve ECM density and anisotropy, cell organization and tissue growth were evaluated under influence of curvature with and without the application of directional fluid flow. Based on the results obtained within this study supported by existing literature, we believe that anisotropy in 3D might be guided by curvature while ECM growth can be improved with the application of WSS. As such, an attempt was made to improve the resemblance of *in vitro* produced bone-like ECM to the physiological bone ECM.

Author contributions

B.d.W., F.Z., I.L., K.I. and S.H. contributed to conception, methodology and design of the study. B.d.W. performed the experiments and analyzed the experimental results. F.Z. and I.L. performed the computational simulations. B.d.W. and F.Z. contributed to the figures presented in the manuscript. B.d.W. wrote the original draft of the manuscript. All authors contributed to manuscript revision and approved the submitted version. B.d.W., F.Z., B.v.R., K.I., and S.H. contributed in the supervision. S.H. acquired funding for this research.

Acknowledgement

This work is part of the research program TTW with project number TTW 016.Vidi.188.021, which is (partly) financed by the Netherlands Organization for Scientific Research (NWO).

Supplementary information

Scaffold pore size analysis

To determine the pore size and pore size distribution, the image background was filled with largest possible spheres of which the diameter was derived. From the micro-computed tomography (μ CT) analyses, a comparable pore size distribution for four regions of interest was found with an average pore size of $103 \pm 40 \mu\text{m}$ (**Figure S3.1**). The average pore size was used for the regularized element computational fluid dynamics (CFD) model (**Figure S3.2**).

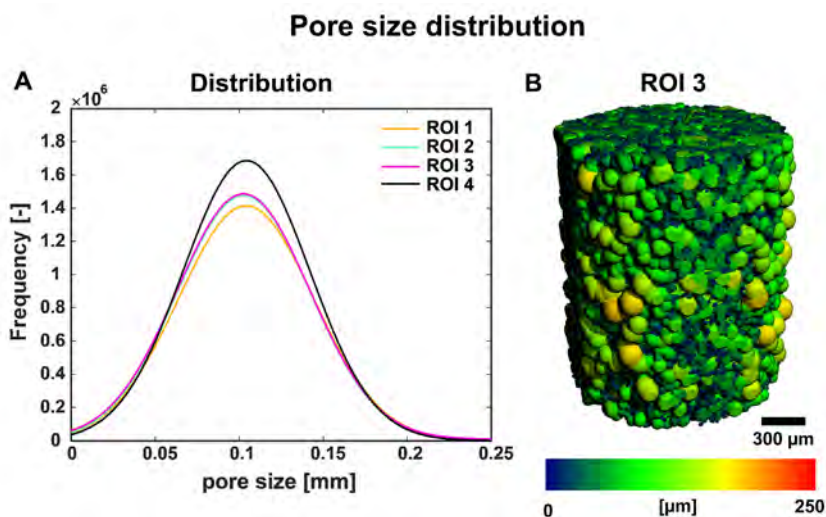


Figure S3.1. (A) Gaussian fits of pore size distributions of four different regions of interest (ROI) in the

scaffold. **(B)** Pore size distribution was obtained by filling the micro-computed tomography (μCT) scan background with largest possible sphere per pore.

Regularized element CFD model

In the macro-scale model, the assumption was made that no fluid flows through the interface of the channel and the scaffold. To check this assumption, a CFD model was evaluated in which a scaffold with idealized cubic pore shape, a porosity of 90% and a pore size of $103\ \mu\text{m}$ was used (**Figure S3.2A**). To save the computational costs, representative volumetric elements (RVEs) were modelled with the side faces set as periodic boundaries (**Figure S3.2A**). A fluid velocity of $393\ \mu\text{m/s}$ (corresponding to a flow rate of $1.5\ \text{ml/min}$) and a relative pressure of $0\ \text{Pa}$ were prescribed at the inlet and outlet (**Figure S3.2A**). The other surfaces (*i.e.*, struts surfaces) were defined as non-slip walls. The physical properties of flow, mesh strategy and convergence criteria were kept the same as those in the model described in **Section 3.2.3**.

It was found that average velocity along the channel (in Z direction in **Figure S3.2B**) was $1.2\ \text{mm/s}$, while the average velocity in the radial direction (*i.e.*, across the channel) was $2.3 \times 10^{-3}\ \text{mm/s}$. Thus, the fluid velocity along the channel is > 520 times higher than that the fluid velocity in the radial direction. Moreover, majority of the fluid flow went through the channel rather than through the scaffold region (*i.e.*, average Z -direction velocity magnitude = $1.20\ \text{mm/s}$ in channel vs $0.16\ \text{mm/s}$ in the scaffold region) (**Figure S3.2C**).

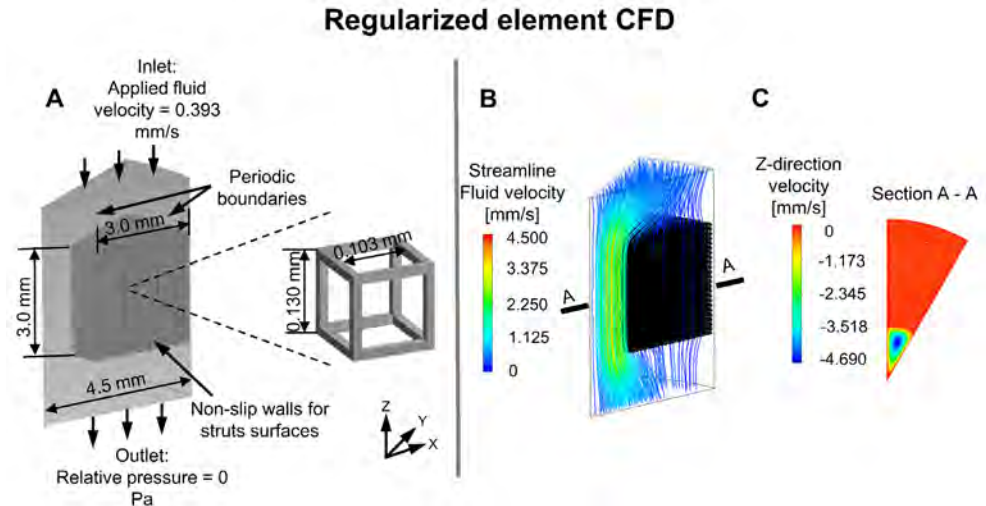


Figure S3.2. **(A)** One representative volumetric element (RVE) of computational fluid dynamics (CFD) model that is based on the scaffold assembled by repeating idealized cubic pore units. **(B)** Overall fluid velocity distribution within the channel and porous scaffold area. **(C)** Z -direction fluid velocity within the channel and porous scaffold (viewed from cross section A-A).

Supporting information on biological experiment

Cell attachment at the channel wall was assessed at day 0 with scanning electron microscopy. Cells at the channel wall seemed to bridge the scaffold pores and seemed to collectively cover the channel pores (**Figure S3.3**).

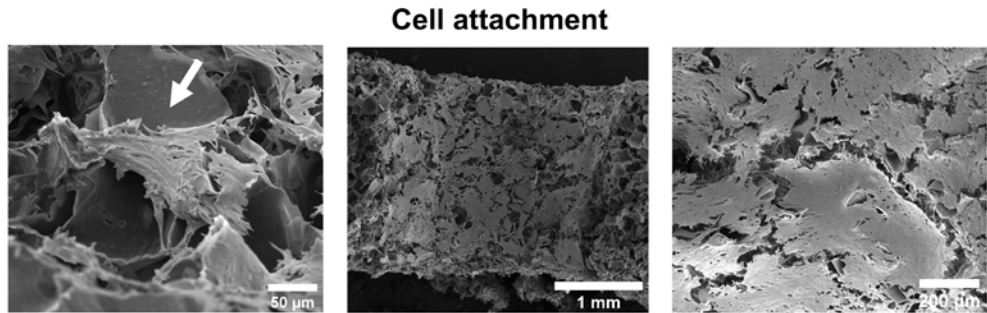


Figure S3.3. Cell attachment at day 0 visualized with scanning electron microscopy. White arrow indicates a cell bridging the scaffold pore.

To visualize collagen deposition, cryosections were prepared in two different planes ($N = 4$ scaffolds per condition, time point, and plane) and stained with Picrosirius Red. To capture the entire section, tile scans were made with a bright field microscope (**Figure S3.4**).

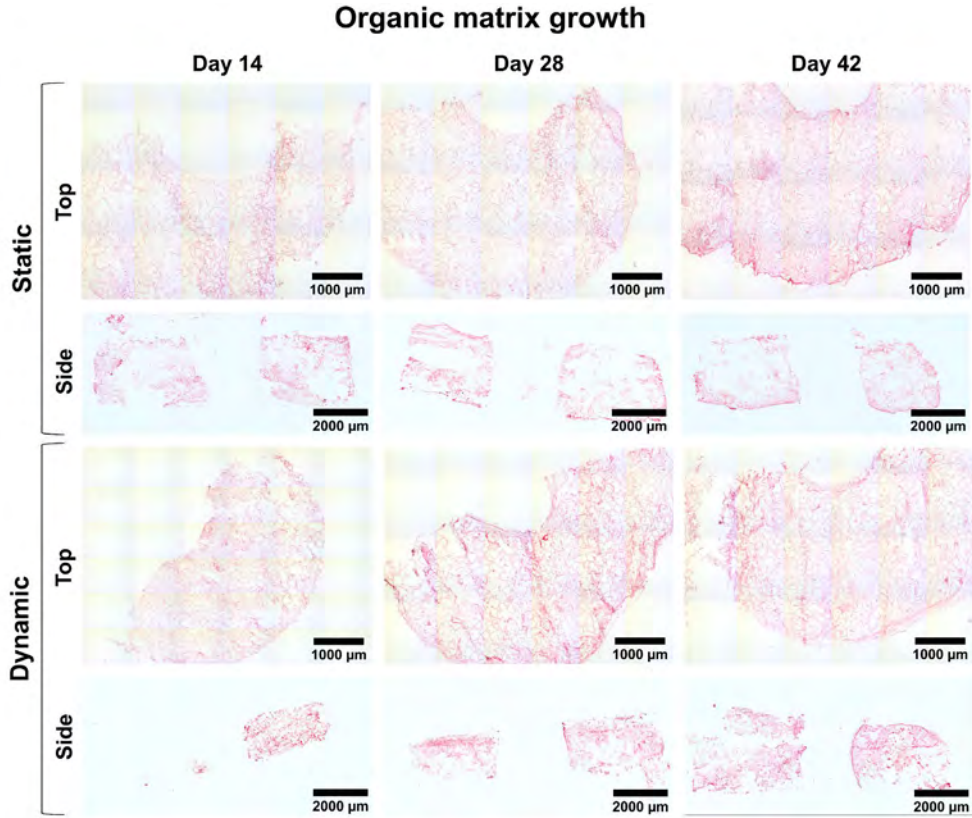


Figure S3.4. Micrographs of vertical plane and horizontal plane scaffold sections stained for collagen (picrosirius red). These images were used for tissue growth quantification.

To check whether the produced extracellular matrix was of a bone-like nature, cryosections ($N = 4$ scaffolds per condition per time point) were prepared and stained with the bone ECM markers osteopontin and collagen type I. A positive immunohistochemical staining for collagen type I and osteopontin revealed that the formed ECM at the channel wall was indeed of a bone-like character (**Figure S3.5**). On day 14, collagen type I and osteopontin were mostly present around the cells while on day 42 they were more distributed through the ECM for both statically and dynamically cultured scaffolds. Dynamically cultured scaffolds seem to have a higher collagen density at the channel wall than statically cultured scaffolds (**Figure S3.5C+F**).

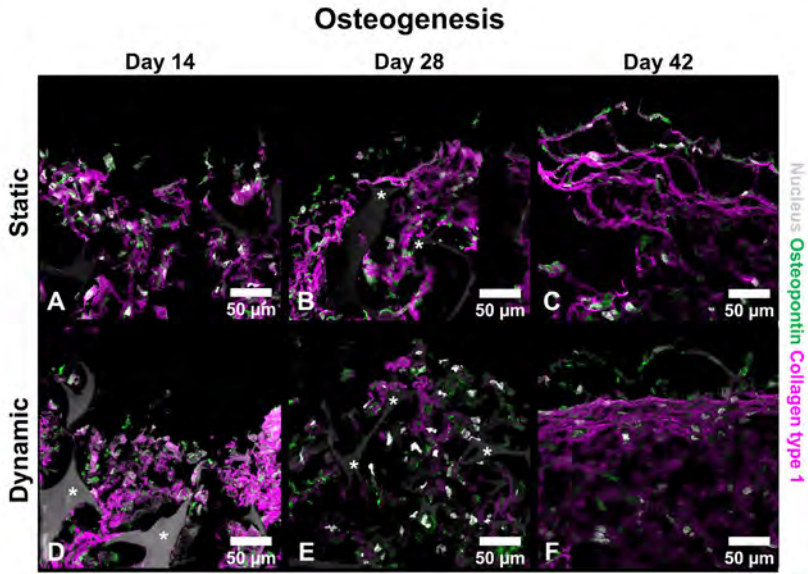


Figure S3.5. Osteogenic differentiation of hBMCSs over time. (A-F) Immunohistochemical analysis of sections for collagen type I (magenta), the nucleus (gray) and osteopontin (green). Asterisks indicate the scaffold. Abbreviations: human bone marrow-derived mesenchymal stromal cells (hBMSCs).

4

Evaluating material-driven regeneration in a tissue engineered human *in vitro* bone defect model

This chapter is based on:

Bregje W.M. de Wildt¹, Esther E.A. Cramer¹, Leanne S. de Silva^{2,3}, Keita Ito¹, Debby Gawlitta^{2,3}, Sandra Hofmann¹

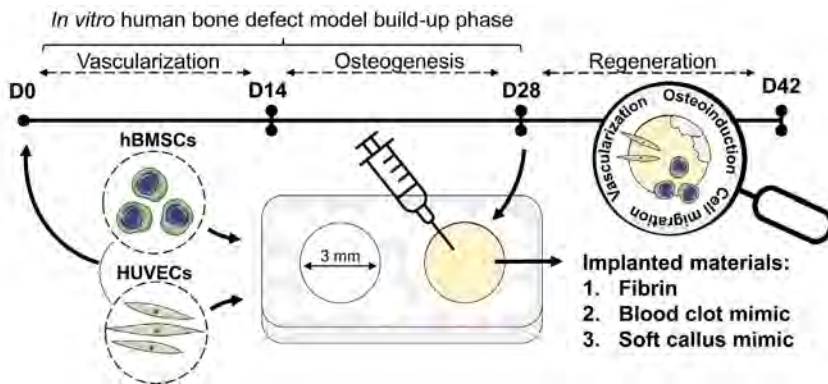
1. Orthopaedic Biomechanics, Department of Biomedical Engineering and Institute for Complex Molecular Systems (ICMS), Eindhoven University of Technology, Eindhoven, The Netherlands.
2. Department of Oral and Maxillofacial Surgery & Special Dental Care, University Medical Center Utrecht, Utrecht University, Utrecht, The Netherlands.
3. Regenerative Medicine Center Utrecht, Utrecht, The Netherlands

Submitted

Abstract

Advanced *in vitro* human bone defect models can contribute to the evaluation of materials for *in situ* bone regeneration, addressing both translational and ethical concerns regarding animal models. In this study, we attempted to develop such a model to study material-driven regeneration, using a tissue engineering approach. By co-culturing human umbilical vein endothelial cells (HUVECs) with human bone marrow-derived mesenchymal stromal cells (hBMSCs) on silk fibroin scaffolds with *in vitro* critically sized defects, the growth of vascular-like networks and three-dimensional bone-like tissue was facilitated. After a model build-up phase of 28 days, materials were artificially implanted and HUVEC and hBMSC migration, cell-material interactions, and osteoinduction were evaluated 14 days after implantation. The materials physiologically relevant for bone regeneration included a platelet gel as blood clot mimic, cartilage spheres as soft callus mimics, and a fibrin gel as control. Although the *in vitro* model was limited in the evaluation of immune responses, hallmarks of physiological bone regeneration were observed *in vitro*. These included the endothelial cell chemotaxis induced by the blood clot mimic and the mineralization of the soft callus mimic. Therefore, the present *in vitro* model could contribute to an improved pre-clinical evaluation of biomaterials while reducing the need for animal experiments.

Graphical abstract



4.1 Introduction

Bone is a highly vascularized and dynamic tissue with the capacity to regenerate without scar formation. Nevertheless, in 2% – 5% of the defects, the failure of bone to bridge the gap results in a non-union (15,16). Bone tissue engineering has been focusing on the development of implantable grafts to tackle such defects. While initially grafts were grown prior to implantation *in vitro* by making use of biomaterials, progenitor cells, and stimuli, current grafts are more often developed to be intelligent biomaterials for *in situ* regeneration, making use of the bone's innate capacity to regenerate upon implantation (141,142). After successful *in vitro* assessments, these grafts are routinely studied in animal models (143–145). Despite animal studies being a crucial step in elucidating material-host interactions, the translation from *in vitro* to *in vivo* experiments has been poor. The current pace at which materials are being developed causes a significant burden on animal experiments (22). Moreover, with a success rate of less than 10%, the subsequent clinical translation of *in vivo* animal models is also poor (23,24), which is likely caused by their insufficient representation of the human physiology (25). Thus, both the translation from *in vitro* assessments to *in vivo* models and the translation from *in vivo* animal models to the human clinic need to be improved. To address these translational issues and improve preclinical graft testing, advanced human *in vitro* bone defect models should be developed and integrated into the preclinical graft testing routine (20,21,26). For the creation of such *in vitro* models, traditional bone tissue engineering strategies can be applied (19).

While bone tissue engineering strategies have already been successfully applied for the creation of *in vitro* models for bone marrow (146), bone metastasis (147), woven bone (116) and bone remodeling (43), the development of human *in vitro* bone defect models for biomaterial testing is rarely explored (19,26). A tissue engineered defect model has previously been proposed, where authors created defects in silk fibroin (SF) scaffolds, seeded scaffolds with human bone marrow-derived mesenchymal stromal cells (hBMSCs), and studied tissue growth and mineralization in the defect area upon osteogenic differentiation (117). In another study, the *in vitro* evaluation of biomaterial-induced bone regeneration was analyzed using a fibrin matrix that was sandwiched between two human trabecular bone discs loaded with rabbit periosteal cells (35). Constructs were subsequently mechanically stimulated and histologically evaluated after 14 days of culture (35). Although they observed osteogenic differentiation of the periosteal cells under influence of mechanical loading, cell migration into the defect site was not detected.

Successful material-driven bone regeneration relies on a cascade of biological events, including: (i) inflammation and immunomodulation, (ii) progenitor cell migration and

differentiation, (iii) vascularization, (iv) osteoinduction, (v) implant remodeling (142). As such, models aiming at recapitulating material-driven bone regeneration *in vitro* should be able to capture such events. Especially the materials' ability to stimulate vascularization is of interest as this is crucial for successful fracture healing (148), and it is therefore the current major challenge in regenerative treatments of large bone defects (149).

In this study, we attempted to develop an *in vitro* human bone defect model to study material-driven regeneration, using a tissue engineering approach (**Figure 4.1A**). To enable the evaluation of a material's potential to stimulate vascularization, cell migration and osteoinduction, hBMSCs were co-cultured with human umbilical vein endothelial cells (HUVECs) to generate the bone compartment containing the defects (**Figure 4.1A**). In a three-dimensional (3D) microenvironment, HUVECs are capable of forming vascular networks in co-culture with hBMSCs; where hBMSCs function as supporting cells by surrounding vessel-like structures and providing angiogenic factors (150,151). In turn, endothelial cells support osteogenic differentiation by the secretion of factors like bone morphogenetic proteins (152). As a result, hBMSCs can additionally undergo osteogenic differentiation in the 3D space between the capillary-like network (153,154). To facilitate 3D growth of these cells, a SF scaffold was used with two *in vitro* critically sized defects of 3 mm in diameter, as based on previous experiments (117) (**Figure 4.1A**). First, the bone defect model was created by 14 days of culture to stimulate vascularization, followed by 14 days of culture to stimulate osteogenic differentiation and bone-like matrix formation (**Figure 4.1B**). At day 28, defects were filled with physiologically relevant graft materials, aiming at mimicking physiological bone regeneration for the validation of our model (**Figure 4.1C**). Implanted materials included a human platelet lysate gel as blood clot mimic, devitalized cartilage spheres as soft callus mimics (155), and a fibrin gel as control. By tracking the defect model with non-destructive confocal microscopy, the materials' potential to stimulate cell migration, vascularization and osteoinduction were evaluated.

4.2 Materials and Methods

4.2.1 Scaffold fabrication

Bombyx mori L. silkworm cocoons were degummed by boiling them in 0.2 M Na₂CO₃ (S-7795, Sigma-Aldrich, Zwijndrecht, The Netherlands) for 1 h. After drying, silk was dissolved in 9 M LiBr (199870025, Acros, Thermo Fisher Scientific, Breda, The Netherlands), filtered, and dialyzed against ultra-pure water (UPW) for 36 h using SnakeSkin Dialysis Tubing (molecular weight cut-off: 3.5 K, 11532541, Thermo Fisher Scientific). The dialyzed SF solution was frozen at -80° C and lyophilized for 7 days.

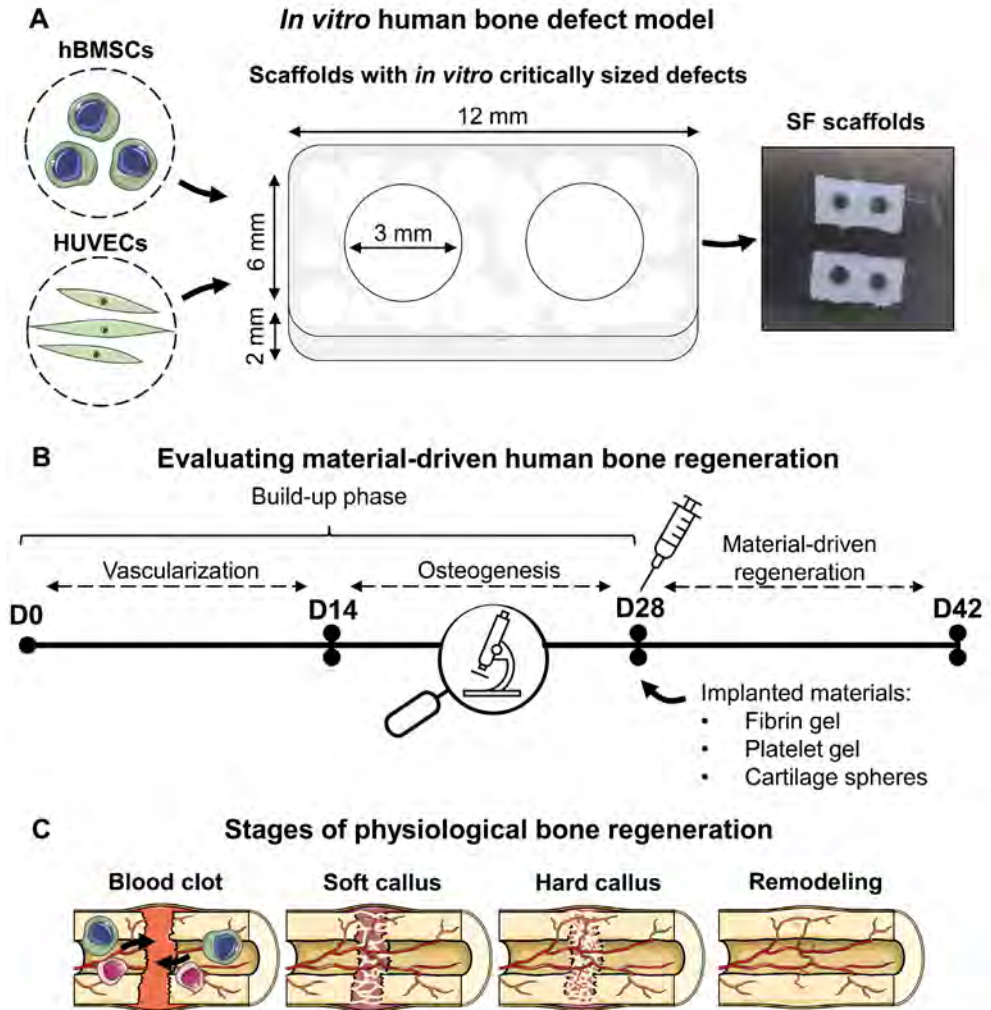


Figure 4.1. Experimental set-up of the presented study. **(A)** A co-culture of hBMSCs and HUVECs was performed on SF scaffolds with two critically sized defects. **(B)** To create the *in vitro* bone defect model, cells were first stimulated to form vascular-like networks for 14 days. hBMSCs were subsequently stimulated to undergo osteogenic differentiation and produce bone-like matrix for 14 days. After 28 days, materials were implanted, and regeneration was studied after an additional 14 days of culture (day 42). Fibrin gel, platelet gel as blood clot mimic, and cartilage spheres as soft callus mimics were implanted, aiming at capturing physiological stages of bone regeneration **(C)**. The figure was modified from Servier Medical Art, licensed under a Creative Common Attribution 3.0 Generic License (<http://smart.servier.com/>, accessed on 20 May 2022). Abbreviations: human bone marrow-derived mesenchymal stromal cells (hBMSCs), human umbilical vein endothelial cells (HUVECs), silk fibroin (SF), day (D).

Lyophilized SF was dissolved in hexafluoro-2-propanol (003409, Fluorochem, Hadfield, UK) at a concentration of 17% (w/v) and casted in scaffold molds containing NaCl granules with a size of 425-500 μm as template for the pores. Molds were covered to improve the SF blending with the granules. After 3 h, covers were removed from molds, and hexafluoro-2-propanol was allowed to evaporate for 7 days whereafter β -sheets were induced by submerging SF-salt blocks in 90% MeOH for 30 min. SF-salt blocks were cut into discs of 2 mm height with a Accutom-5 (04946133, Struer, Cleveland, OH, USA). NaCl was dissolved for 48 h from the scaffolds in UPW, resulting in porous sponges. These sponges were cut into scaffolds with a length of 12 mm and a width of 6 mm and provided with two central defects with a 3 mm diameter biopsy punch. The dimensions of the defects were based on previous research in which a 3 mm channel remained open over a period of 42 days (117). Scaffolds were sterilized by autoclaving in phosphate buffered saline (PBS) at 121° C for 20 min.

4.2.2 Cell culture experiments

hBMSC isolation, expansion and seeding

Mesenchymal stromal cells were isolated from human bone marrow (1M-125, Lonza, Walkersville, MD, USA, collected under their institutional guidelines and with informed consent) and characterized for surface markers and multilineage differentiation, as previously described (124). hBMSCs were frozen at passage 4 with 5×10^6 cells/ml in freezing medium containing fetal bovine serum (FBS, BCBV7611, Sigma-Aldrich) with 10% DMSO and stored in liquid nitrogen until further use. Before experiments, hBMSCs were thawed, collected in high glucose DMEM (hg-DMEM, 41966, Thermo Fisher Scientific), seeded at a density of 2.5×10^3 cells/cm² and expanded in expansion medium containing hg-DMEM, 10% FBS (BCBV7611, Sigma-Aldrich), 1% Antibiotic Antimycotic (anti-anti, 15240, Thermo Fisher Scientific), 1% Non-Essential Amino Acids (11140, Thermo Fisher Scientific), and 1 ng/ml basic fibroblast growth factor (bFGF, 100-18B, PeproTech, London, UK) at 37 °C and 5% CO₂. After 10 days at around 80% confluence, cells were detached using 0.25% trypsin-EDTA (25200, Thermo Fisher Scientific) and seeded onto scaffolds at passage 5. Cells were seeded at a density of 1×10^6 cells per scaffold and seeding was performed dynamically (125) for 6 hours in 50 ml tubes on an orbital shaker at 150 RPM in osteogenic control medium (low glucose-DMEM (lg-DMEM, 22320, Thermo Fisher Scientific), 10% FBS (SFBS, Bovogen, East Keilor, Australia) and 1% anti-anti). After seeding, scaffolds were transferred to 24-wells plates and kept overnight in endothelial cell growth medium-2 (EGM-2, CC-3162, Lonza). HUVECs were seeded the next day.

HUVEC expansion and seeding

Pooled primary green fluorescent protein (GFP) expressing HUVECs (GFP, Olaf Pharmaceuticals, Worcester, MA, USA) were expanded in EGM-2 with 3% extra FBS (FBS, BCBV7611, Sigma-Aldrich) to passage 8. After 5 days, HUVECs were detached using 0.25% trypsin-EDTA. Just before seeding, EGM-2 was removed from hBMSC-containing scaffolds. HUVECs were resuspended at a concentration of $1 \times 10^6/50 \mu\text{l}$, and cells were seeded with a $50 \mu\text{l}$ drop onto the hBMSC-containing scaffolds. Scaffolds were incubated at 37°C for 20 min to allow for cell attachment, whereafter 2 ml EGM-2 was added to the wells which is referred to as day 0 of the experiment.

hBMSC-HUVEC co-culture

Constructs ($N = 16$) were incubated for 42 days at 37°C and 5% CO_2 and initially provided with EGM-2 to allow for the development of vascular-like networks. After 14 days, when vascular-like structures were formed, medium was switched to osteogenic differentiation medium (osteogenic control medium with osteogenic supplements 10 mM β -glycerophosphate (G9422, Sigma-Aldrich), 50 $\mu\text{g}/\text{ml}$ ascorbic acid-2-phosphate (A8960, Sigma Aldrich), and 100 nM Dexamethasone (D4902, Sigma-Aldrich)) for the remaining culture period. During the whole experiment, medium was changed 3 times a week. On day 28, some scaffolds ($N = 4$) were sacrificed to assess osteogenic differentiation and mineralization. Other scaffolds were kept in culture for another 14 days.

Preparation of devitalized cartilage spheres

Cartilaginous spheres as soft callus mimics were grown from hBMSCs as previously described (155). Briefly, 20×10^6 hBMSCs were encapsulated in collagen type I gel droplets (4 mg/ml) (354249, Corning, New York, USA), according to the manufacturer's instructions. After gelation, samples were cultured in chondrogenic differentiation medium (hg-DMEM (31966, Thermo Fisher Scientific), 1% insulin-transferrin-selenium + premix (354352, Corning), 100 nM dexamethasone (D8893, Sigma-Aldrich), 50 $\mu\text{g}/\text{ml}$ ascorbic acid-2-phosphate, 100 units/ml of penicillin and 100 $\mu\text{g}/\text{ml}$ streptomycin (15140, Thermo Fisher Scientific), and 10 ng/ml transforming growth factor- β_1 (Peprotech). Spheres were cultured for 28 days. For the first 4 days, medium was refreshed daily and afterwards 3 times per week. After 28 days, spheres were devitalized by a mild procedure and stored frozen until use.

Material implantation

After 28 days of culture, three different materials were artificially implanted: (i) a human fibrin gel, (ii) a human platelet lysate gel as blood clot mimic, and (iii) two devitalized cartilage spheres as soft callus mimics. Just before implantation, medium was removed of all scaffolds. For the fibrin gel, fibrinogen (341576-M, Sigma-Aldrich) was mixed

with thrombin (T6884, Sigma-Aldrich) to a final concentration of 2.5 mg/ml fibrinogen and 0.2 U/ml thrombin. In each defect ($N = 4$ scaffolds and $N = 8$ defects), 50 μ l fibrin was pipetted, whereafter samples were incubated at 37 °C for 25 min to allow for polymerization of the gel. For the platelet gel, ELAREM™ matrix kit (MA30311) was used according to the manufacturer's instructions. A 10% ELAREM™ matrix solution was prepared in PBS to which 50 μ g/ml ELAREM™ accelerator was added. In each defect ($N = 4$ scaffolds and $N = 8$ defects), 50 μ l platelet gel was pipetted, whereafter samples were placed in the incubator at 37 °C for 2 min to allow for gelation. For the cartilage spheres, spheres were soaked for 5 min in lg-DMEM to allow for rehydration of the spheres. Meanwhile, fibrin gels were prepared and 25 μ l was implanted as described above. Before polymerization of the gel, two spheres per defect ($N = 4$ scaffolds and $N = 8$ defects) were dried with a sterile gauze and implanted. After implantation, a small droplet of fibrin gel was added on top of the spheres to fill the defect. Samples were incubated at 37 °C for 25 min to allow for polymerization of the gel. After proper gelation in all conditions, osteogenic differentiation medium was added, and defect regeneration was followed after an additional 14 days of culture.

4.2.3 *In vitro* model analyses

Live confocal microscopy

During the culture period, vascularization (day 4, 7, 11 and 14) ($N = 16$ scaffolds), bone-like matrix production (day 28) ($N = 4$ scaffolds), and cell migration (day 35 and 42) ($N = 4$ defects per condition) were visualized with microscopy. HUVECs were visualized by their GFP-label. Collagen, hydroxyapatite and hBMSCs were visualized with viable dyes from day 28 on. On day 27 (end-point samples), 34 and 41, samples were washed in lg-DMEM and samples were stained overnight at 37 °C in osteogenic control medium with 0.2 nmol/ml OsteoSense™ 680 (dissolved in PBS; NEV10020EX, PerkinElmer, Waltham, MA, USA) to visualize hydroxyapatite, and 1 μ mol/ml in-house made CNA35-mCherry (132) to visualize collagen. The next day, one droplet of NucBlue™ Hoechst 33342 (R37605, Thermo Fisher Scientific) was added per scaffold to visualize all cell nuclei and samples were incubated at 37 °C for 20 min. Samples were washed three times in lg-DMEM and provided with fresh osteogenic differentiation medium. Data were acquired on a confocal laser scanning microscope equipped with a multiphoton laser and incubation unit (Leica TCS SP8X, 10x/0.40 HC PL Apo CS2 objective). During imaging, samples were kept at 37 °C and 5% CO₂. To visualize cell nuclei, the multiphoton laser was used at $\lambda = 740$ nm to reduce cytotoxicity that can be induced by using violet light (156). To study the influence of staining on cell death, unstained and stained samples were additionally compared for their lactate dehydrogenase (LDH) release in the supernatant.

Micro-computed tomography (μ CT)

After 42 days, scaffold halves ($N = 4$ per condition) were fixed in 3.7% neutral buffered formaldehyde overnight. Samples were scanned and analyzed with a μ CT100 imaging system. Scanning was performed at an isotropic nominal resolution of 17.2 μ m, energy level of 45 kVp, intensity of 200 μ A, integration time of 300 ms and with twofold frame averaging. To reduce part of the noise, a constrained Gaussian filter was applied with filter support 1 and filter width sigma 0.8 voxel. Filtered images were contoured for the scaffold and its 3 mm diameter defect and segmented to detect mineralization at a global threshold of 24% of the maximum grayscale value. To further reduce noise, unconnected objects smaller than 30 voxels were removed through component labeling. Mineralized volumes were computed for the total scaffold and the defect region using the scanner manufacturer's image processing language (IPL) (131).

Biochemical content analysis

To quantify the biochemical content, scaffolds were cut in halves ($N = 4$ per condition) and their defect content was collected by punching with a 3 mm biopsy punch. Scaffolds and defects were lyophilized, dry weights of scaffolds were collected, and samples were digested overnight in papain digestion buffer (containing 100 mmol phosphate buffer, 5 mmol L-cysteine, 5 mmol EDTA and 140 μ g/ml papain (P4762, Sigma-Aldrich)) at 60 °C. DNA content of scaffolds and defects was quantified using the Qubit Quantification Platform (Invitrogen) with the high sensitivity assay, according to the manufacturer's instructions. Hydroxyproline content as a measure for collagen was quantified in scaffolds using a chloramine-T assay (130) with trans-4-hydroxyproline (H54409, Sigma-Aldrich) as reference. Absorbance values were measured at 550 nm using a plate reader (SynergyTM HTX, Biotek) and standard curve absorbance values were used to determine hydroxyproline content in the samples. Glycosaminoglycan (GAG) content of scaffolds was measured using a dimethyl methylene blue (DMMB) assay (157) with shark cartilage chondroitin sulfate (C4284, Sigma-Aldrich) as a reference. Absorbance was read at 540 nm and 595 nm using a plate reader. Absorbance values were subtracted from each other (540-595) and converted to GAG content using standard curve absorbance values.

(Immuno)histochemical analyses

Scaffold halves ($N = 4$ per condition) were prepared for cryosections by soaking them for 15 minutes in each 5% (w/v) sucrose and 35% (w/v) sucrose in PBS. Samples were embedded in Tissue Tek® (Sakura), quickly frozen with liquid N₂ and cryosections were prepared. Upon staining, sections were fixed in 3.7% neutral buffered formaldehyde and washed twice with PBS. To visualize collagen deposition, 5 μ m thick cryosections ($N = 4$ scaffolds per condition) were stained with Picrosirius Red. Sections were soaked in Weigert's Iron Hematoxylin (HT1079, Sigma-Aldrich) solution for 10 minutes,

washed in running tap water for 10 minutes, and stained in 1% w/v Sirius Red (36,554-8, Sigma-Aldrich) in picric acid solution (36011, Sigma-Aldrich) for one hour. Subsequently, sections were washed in two changes of 0.5% acetic acid and dehydrated in one change of 70% and 96% EtOH, three changes of 100% EtOH, and two changes of xylene. Sections were mounted with Entellan (107961 Sigma-Aldrich). To capture the entire sample, tile scans were made with a bright field microscope (Zeiss Axio Observer Z1, 10x/0.45 Plan-Apochromat objective). Tile scans were stitched with Zen Blue software (version 3.1, Zeiss).

To study osteogenic differentiation, 5 μm thick cryosections ($N = 2$ scaffolds per condition) were stained with 1 $\mu\text{g}/\text{ml}$ DAPI and antibodies for runt-related transcription factor-2 (RUNX2) and osteopontin. Collagen deposition was characterized by staining 5 μm thick cryosections ($N = 2$ scaffolds per condition) with 1 $\mu\text{g}/\text{ml}$ DAPI and a collagen type I antibody. To study the cell-material interactions and the supporting cell functionality of the hBMSCs, 30 μm thick cryosections ($N = 4$ scaffolds of the cartilage spheres group) were stained with 1 $\mu\text{g}/\text{ml}$ DAPI, 50 pmol Atto 488-conjugated Phalloidin (49409, Sigma-Aldrich) and antibodies for CD31 and α -smooth muscle actin. Briefly, sections were permeabilized in 0.5% Triton X-100 in PBS (5 min for 5 μm sections and 10 min for 30 μm sections) and blocked in 10% normal goat serum in PBS for 30 min. Primary antibodies were incubated overnight at 4 $^{\circ}\text{C}$ in 1% normal goat serum in PBS, secondary antibodies were incubated with DAPI and Phalloidin (if applicable) for 1 h at room temperature. Antibodies are listed in **Table S4.1**. Images of the osteogenic differentiation and collagen type I staining were acquired with an epi-fluorescence microscope (Zeiss Axio Observer 7, 20x/0.4 LD Plan-Neofluor objective), and tile scans were stitched with Zen Blue software (version 3.3, Zeiss, Breda, The Netherlands). Z-stacks of 30 μm thick sections to visualize cell-material interactions were acquired with a laser scanning microscope (Leica TCS SP8X, 40x/0.95 HC PL Apo objective). Z-stacks were converted to maximum intensity projections using Fiji (127).

LDH activity

To evaluate potential cytotoxic effects of implanted materials, LDH activity was measured in the culture medium supernatant on day 42 ($N = 4$ per condition). A 100 μl supernatant sample or NADH (10107735001, Sigma-Aldrich) standard was incubated with 100 μl LDH reaction mixture (11644793001, Sigma-Aldrich) in 96-wells assay plates. Absorbance was measured directly after the reaction mixture was added and after 30 min at 492 nm. LDH activity was calculated between the initial absorbance values and the absorbance values after 30 min reaction, using standard curve absorbance values.

Multiplex immunoassays

To evaluate the protein content in the culture medium supernatant on day 42 ($N = 4$ per condition), a total of 21 proteins as markers for cell migration, vascularization, remodeling and bone formation were quantified using multiplex immunoassays at the Multiplex Core Facility (MCF) of the Laboratory for Translational Immunology of the University Medical Center Utrecht, the Netherlands. Immunoassays were developed and validated by the MCF and based on Luminex xMap technology (Luminex, Austin, TX, USA) (158). Briefly, samples were incubated with MagPlex microspheres (Luminex) for 1 h at room temperature with continuous shaking, followed by 1 h incubation with biotinylated antibodies and 10 min incubation with phycoerythrin-conjugated streptavidin in high performance ELISA buffer (HPE, Sanquin, Hamburg, Germany). Data acquisition was performed with FLEXMAP 3D equipment in combination with xPONENT software (version 4.3, Luminex), and analyzed by 5-parametric curve fitting using Bio-Plex Manager software. Protein concentrations were normalized by converting them into *z*-scores (*i.e.*, the number of standard deviations from the overall sample average) and presented using Heatmapper (159).

4.2.4 Statistical analyses

Statistical analyses were performed, and graphs were prepared in GraphPad Prism (version 9.3.0, GraphPad, La Jolla, CA, USA) and R (version 4.1.2) (133). Data were tested for normality in distributions and equal variances using Shapiro-Wilk tests and Levene's tests, respectively. When these assumptions were met, mean \pm standard deviation are presented, and to test for differences, a one-way ANOVA was performed followed by Holm-Šidák's method with adjusted *p*-values for multiple comparisons. Other data are presented as median \pm interquartile range and were tested for differences with a non-parametric Kruskal-Wallis test followed by Dunn's tests with adjusted *p*-values for multiple comparisons. A *p*-value of <0.05 was considered statistically significant.

4.3 Results

4.3.1 Creation of a tissue engineered human *in vitro* bone defect model

By microscopically evaluating GFP-labeled HUVECs in co-culture with hBMSCs during the initial 14 days of culture, the development of vascular-like structures after 14 days under the influence of EGM-2 medium was confirmed (**Figure 4.2**). On day 4 and 7, HUVECs appeared more as single cells that attached to the scaffold wall concavities where they started to form circular-like networks. From day 11 onwards, clear vascular-like networks with a branched morphology were found which started forming tubular structures (**Figure 4.2**, white arrows). HUVECs and vascular-like structures appeared

throughout the whole scaffolds, which can be appreciated from the defect overview images (**Figure 4.2**).

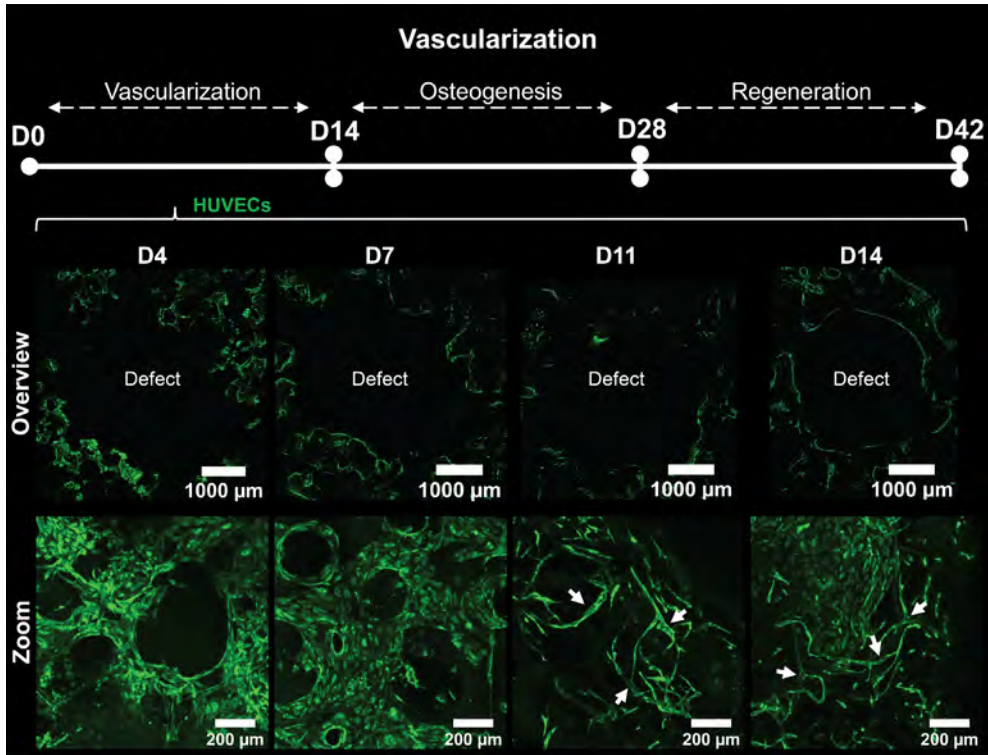


Figure 4.2. Microscopic evaluation of GFP-expressing HUVECs during the initial 14 days of culture to evaluate vascular-like network development. In the top panel, defect overview images are presented. At the bottom panel, close-up z-stack maximum intensity projection images are presented. White arrows indicate tubular vascular networks. Abbreviations: green fluorescent protein (GFP), human umbilical vein endothelial cells (HUVECs), day (D).

After 14 days, medium was switched to osteogenic differentiation medium to induce bone-like matrix formation and osteogenic differentiation of hBMSCs. Indeed, after an additional 14 days (*i.e.*, day 28 of culture) hBMSCs had produced a bone-like extracellular matrix as observed from the collagen and hydroxyapatite stainings (**Figure 4.3A**), which are the two main components of the bone extracellular matrix (106). Staining of samples did not induce additional cell death (**Figure S4.1**). The defect of the scaffolds remained unfilled, confirming its critical size for *in vitro* experiments. Both single HUVECs and HUVECs organized in vascular-like networks were observed after 28 days (**Figure 4.3A** and **Video S4.1**). The presence of single HUVECs indicates that some vascular-like networks might have regressed after the switch from endothelial growth medium to osteogenic differentiation medium. Mineralization of the bone

defect model was also confirmed by μ CT imaging, showing mineralized matrix throughout the whole scaffold (**Figure 4.3B**). By immunohistochemical analyses, collagen type I production was confirmed (**Figure 4.3C**). Osteogenic differentiation of hBMSCs was observed by the presence of the nuclear transcription factor RUNX2 and the non-collagenous protein osteopontin in the proximity of RUNX2 positive cells, as typical markers for osteogenesis (**Figure 4.3D**) (128). As a next step, materials were implanted into this bone-like defect model possessing vascular-like networks.

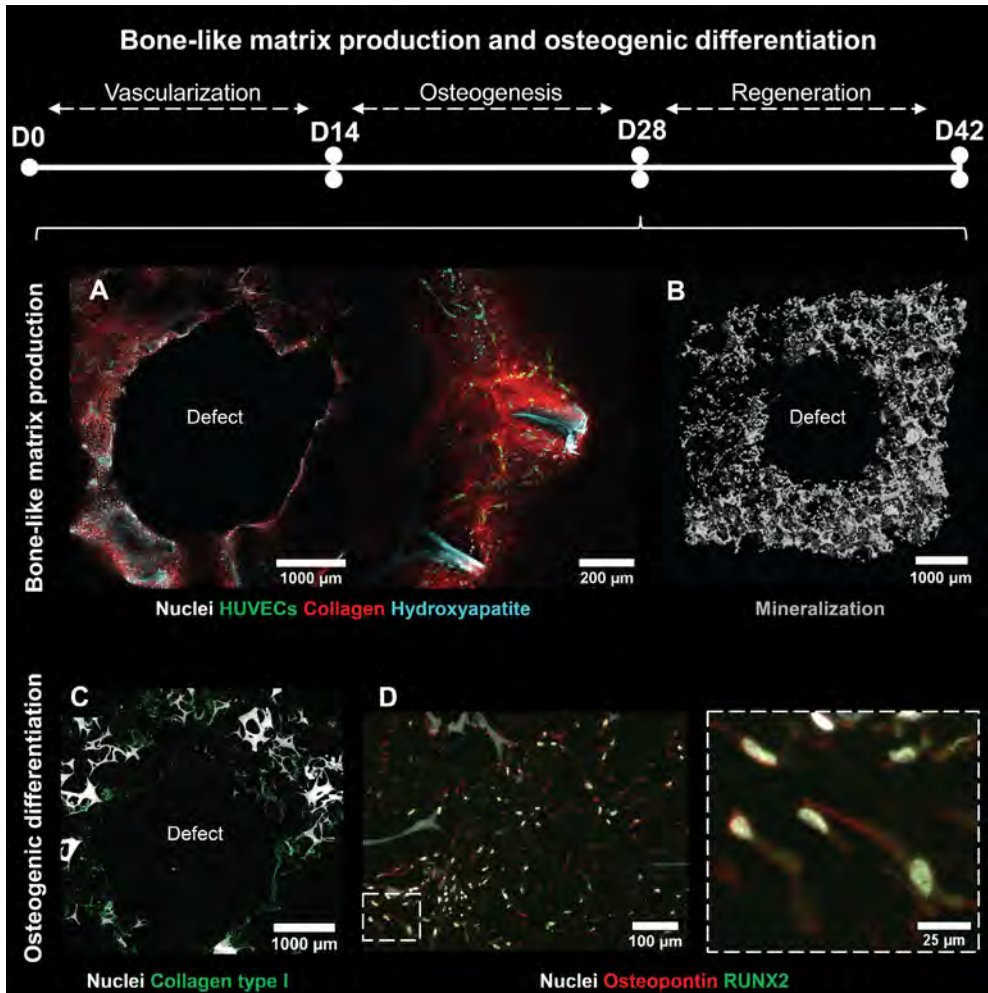


Figure 4.3. Evaluation of the osteogenesis phase after 28 days of culture. (A) Defect overview image (left) and close-up image (right) of viable construct containing GFP-expressing HUVECs (green) and stained for nuclei (gray), collagen (red), and hydroxyapatite (cyan). (B) μ CT reconstruction of scaffolds indicating mineralization through the whole defect model. (C) Collagen type I (green), (D) osteopontin (red), and RUNX2 (green) immunohistochemical analyses indicated osteogenic differentiation of the hBMSCs in the model. Abbreviations: green fluorescent protein (GFP), human umbilical vein endothelial cells (HUVECs),

day (D), micro-computed tomography (μ CT), runt-related transcription factor-2 (RUNX2), human bone marrow-derived mesenchymal stromal cells (hBMSCs).

4.3.2 Cell migration into the defect area upon material implantation

Upon material implantation, cell migration was microscopically evaluated on day 35 and 42. On day 35, defects implanted with fibrin gel or platelet gel showed little to no cell migration (**Figure 4.4A+B**). Only defects implanted with cartilage spheres showed clear migration of both HUVECs and (likely osteogenically differentiated) hBMSCs (**Figure 4.4C**), green cells and white nuclei, respectively) into the fibrin around the spheroids, already at day 35. Interestingly, HUVECs appeared to have migrated to the defect wall of defects implanted with platelet gel (**Figure 4.4B**). In contrast, this was not observed in defects implanted with fibrin (**Figure 4.4A**), indicating that the HUVECs require a chemical stimulus, likely present in the platelet gel, to migrate. These observations were confirmed after 42 days of culture. hBMSCs migrated to the implanted material in all conditions, but in defects implanted with platelet gel and cartilage spheres, also HUVECs migrated which was not observed in defects implanted with fibrin gel (**Figure 4.4D-F**, **Video S4.2-S4.4** and **Figure S4.2** for overview images). The migration of these cells appeared only in distinct areas (**Figure S4.2**), which could indicate the degradation or contraction of the implanted gels as observed before (33). Defects implanted with cartilage spheres remained stable over time. Cell migration of both hBMSCs and HUVECs was observed around the spheres and HUVECs even attached to the cartilage spheres (**Figure 4.4F** and **Video S4.4**).

4.3.3 Cell-material interactions

To evaluate the interactions of the cells with the implanted materials, cell culture medium supernatants of day 42 were analyzed for their protein content (after 2 days incubation with the samples). Protein concentrations were converted to Z-scores (*i.e.*, the normalized deviation from the average of all experimental groups) and color-coded for presentation (**Figure 4.5A**). Of importance, these proteins can either be secreted by the cells or be a product of material degradation. Interestingly, all 21 studied proteins were detected in the culture medium supernatants at concentrations above the concentration measured in control medium (*i.e.*, fresh osteogenic differentiation medium that has not been in contact with the cells) (**Table S4.2**). As such, proteins important for physiological bone regeneration can be captured with the presented bone defect model. Only sclerostin concentration in scaffolds implanted with platelet gel was at a similar level as the control medium (**Table S4.2**). In scaffolds implanted with fibrin gel and cartilage spheres, significantly more sclerostin was measured when comparing the concentrations of all experimental groups (**Table S4.2**). Sclerostin is known to inhibit bone formation and promote bone resorption by stimulating secretion of

receptor activator of nuclear factor kappa- β ligand (RANKL) by osteocytes (160). Indeed, RANKL was also significantly higher in scaffolds implanted with cartilage spheres than in scaffolds implanted with platelet gel (**Table S4.2**). Therefore, scaffolds implanted with cartilage spheres might be the most potent inducer of material degradation and remodeling. This was however not reflected in the ratio between RANKL and its inhibitor osteoprotegerin (OPG), which was similar among groups (**Figure 4.5B**).

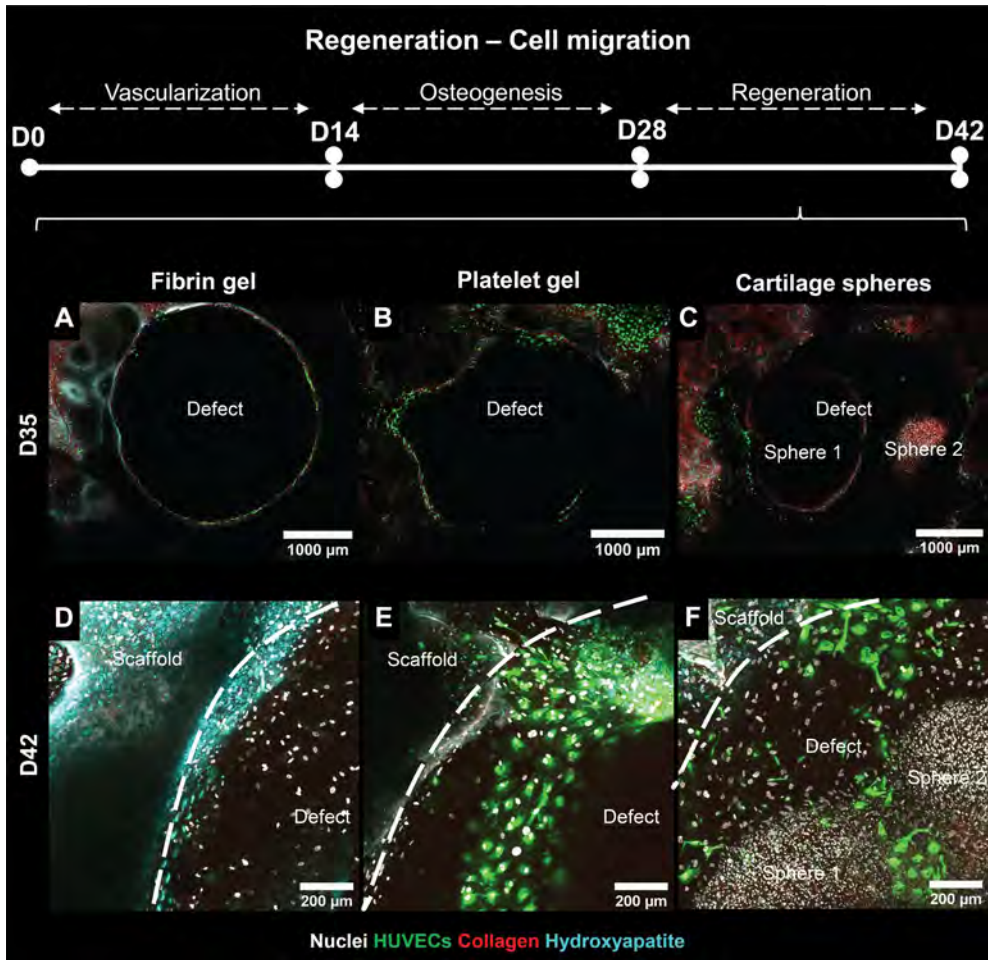


Figure 4.4. Evaluation of the regeneration phase of viable constructs after 35 days and 42 days of culture. Top panel presents defect overview images at day 35, bottom panel presents close-up z-stacks maximum intensity projection images at day 42 of culture of construct containing GFP-expressing HUVECs (green) and stained for nuclei (gray), collagen (red), and hydroxyapatite (cyan), implanted with (**A+D**) fibrin gel, (**B+E**) platelet gel, or (**C+F**) two cartilage spheres. Abbreviations: green fluorescent protein (GFP), human umbilical vein endothelial cells (HUVECs), day (D).

Other protein levels of interest were the concentrations of connective tissue growth factor (CTGF), vascular endothelial growth factor (VEGF), matrix metalloproteinase (MMP)-3 and MMP-9. The CTGF concentration, important for cell condensation during regeneration (161), tended to be lowest in scaffolds of which the defects were implanted with cartilage spheres where cell condensation might not be necessary because of the implanted soft callus mimic. In contrary, for vascularization important VEGF tended to have the highest concentration in scaffolds of which the defects were implanted with cartilage spheres. However, in the same condition the concentrations of other important factors for vascularization angiopoietin-1 and 2 tended to be relatively low. MMP-3, which is involved in the degradation of cartilage (162), and MMP-9, the in bone most abundant MMP also involved in endochondral ossification (163,164), tended to be relatively high in scaffolds of which defects were implanted with cartilage spheres. However, none of these concentrations differed significantly from the concentrations measured in the other conditions. LDH activity in the culture medium supernatant was measured as an indicator of material induced cytotoxicity. No significant differences were observed between the different materials (**Figure 4.5C**). Based on the attachment of HUVECs to the cartilage spheres, as observed in the cell migration evaluation (**Figure 4.4F**), the cell-material interaction was evaluated microscopically for this condition (**Figure 4.5D**). By staining for CD31 as an endothelial marker and α -smooth muscle actin as a mural cell marker, the co-effort of HUVECs and hBMSCs to induce cartilage sphere vascularization was studied. Both inside the bone defect (*i.e.*, in the scaffold) as around the sphere, α -smooth muscle actin was located around HUVECs, identified with CD31 (**Figure 4.5D**). However, α -smooth muscle actin did not appear co-located with the actin cytoskeleton. As such, hBMSCs might have lost their supporting cell functionality upon osteogenic differentiation. Only around the defect, cells were found with typical α -smooth muscle actin fibers, indicating that some hBMSCs were still capable of performing their supporting cell or pericyte-like cell functionality. In addition, by the absence of the endothelial marker CD31 around the spheres, also the attachment of hBMSCs to the spheres was confirmed by the layer of actin around them, which was not observed in non-implanted control spheres (**Figure 4.5D**). Infiltration of cells into the cartilage spheres was not observed.

4.3.4 Materials' osteoinductive properties

After 42 days of culture, scaffolds and defects were evaluated for their cell and extracellular matrix content. In the scaffold, no clear differences between groups were observed in the DNA, hydroxyproline (*i.e.*, a measure for collagen), and GAG content (**Figure 4.6A-C**).

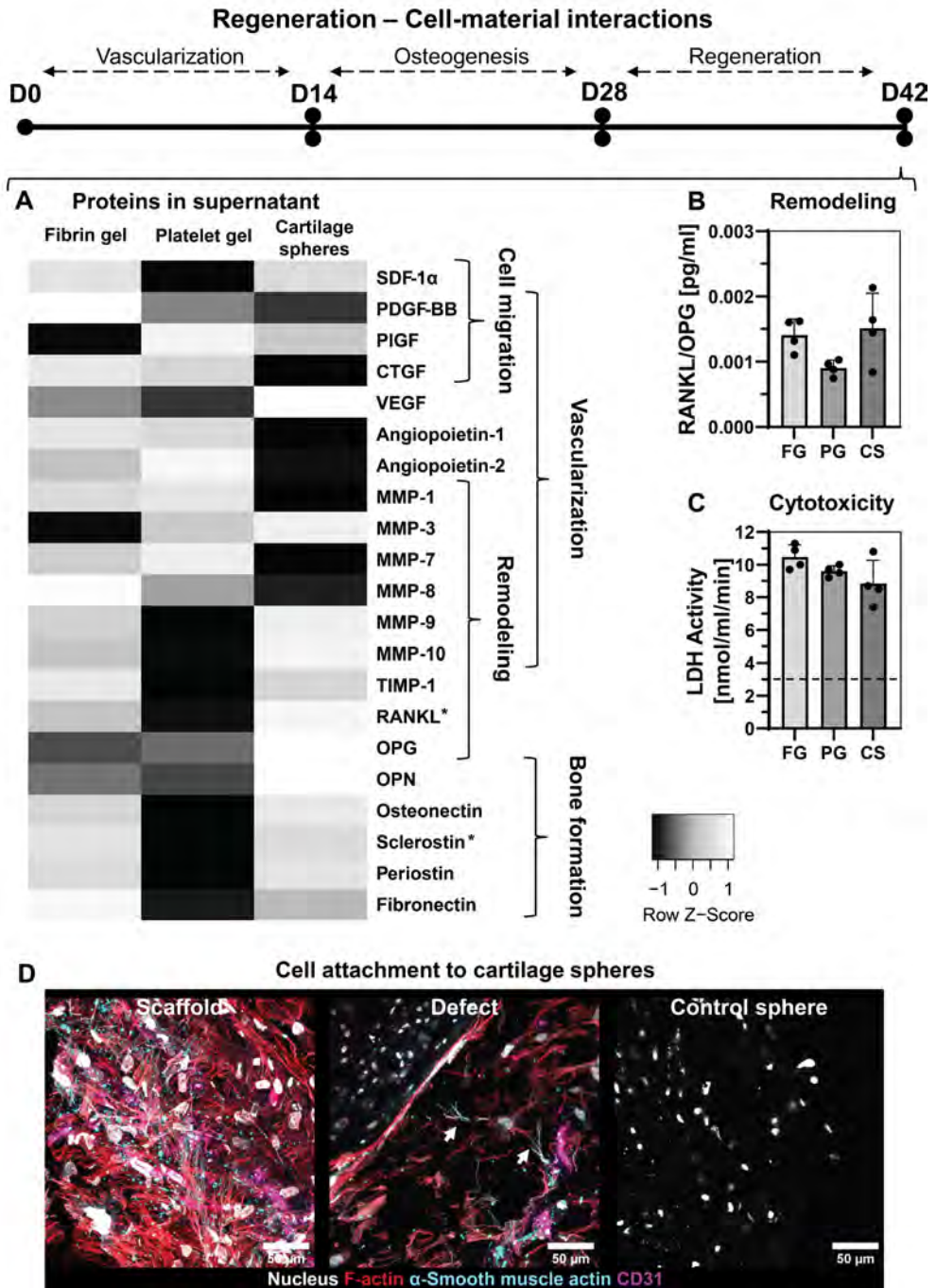


Figure 4.5. Evaluation of cell-material interactions after 42 days of culture (14 days post-implantation). (A) Multiplex immunoassays to measure proteins in cell supernatants, presented as z-scores (*i.e.*, the normalized

deviation from the average of all experimental groups). Concentration values were used for statistical comparisons, $p < 0.05$ for RANKL and sclerostin (One-way ANOVA and Holm-Šidák's post hoc tests), *ns* for other factors (Kruskal-Wallis tests for MMP-10, PIGF, MMP-3 and MMP-7, One-way ANOVAs for all other factors). **(B)** RANKL/OPG ratios in the culture medium supernatants, *ns* (One-way ANOVA). **(C)** Cytotoxicity measured by LDH activity in the supernatant. Dashed line represents concentration measured in control medium, *ns* (One-way ANOVA). **(D)** Z-stack maximum intensity projection images of sections stained for F-Actin (red), the nucleus (gray), endothelial cell marker CD31 (magenta) and supporting cell marker α -smooth muscle actin (cyan). White arrows point at locations where α -smooth muscle actin was co-localized with the actin cytoskeleton. Abbreviations: day (D), stromal derived factor (SDF), platelet derived growth factor (PDGF), placental growth factor (PIGF), connective tissue growth factor (CTGF), vascular endothelial growth factor (VEGF), matrix metalloproteinase (MMP), tissue inhibitor of metalloproteinase (TIMP), receptor activator of nuclear factor kappa- β ligand (RANKL), osteoprotegerin (OPG), osteopontin (OPN), lactate dehydrogenase (LDH).

By measuring the DNA content in the defects, cell migration into the defect was quantified. In defects implanted with fibrin and platelet gel, little DNA was measured (**Figure 4.6D**). Especially in defects implanted with platelet gel, DNA contents were low. In defects implanted with cartilage spheres, DNA content was much higher, likely caused by the presence of dead cartilage cells in the devitalized spheres. Interestingly, the measured DNA content in defects with implanted spheres tended to be lower than the measured DNA content in non-implanted control spheres. This suggests some degradation of implanted spheres. When visualizing collagen with picosirius red, migrated cells in the defects filled with fibrin gel produced collagen (**Figure 4.6E**), which was characterized as collagen type I (**Figure S4.3**). This produced matrix did however show almost no mineralization (**Figure 4.6I+K**). Matrix formation and mineralization in the defect was not observed in defects implanted with platelet gel (**Figure 4.6F+I+K**). In defects implanted with cartilage spheres, collagen formation was observed around the spheres (**Figure 4.6G**). In addition, mineralization of the cartilage spheres was observed (**Figure 4.6I+K**). When quantifying the overall mineralization in the scaffold and the defects, no significant differences were observed. However, outer scaffolds implanted with fibrin gel tended to have a higher mineralized volume than outer scaffolds implanted with platelet gel or cartilage spheres, whereas defects implanted with cartilage spheres tended to have a higher mineralized volume compared to defects implanted with fibrin or platelet gel. This was caused by mineralization of some cartilage spheres. For model validation, cartilage sphere mineralization in our *in vitro* model was compared to cartilage sphere mineralization *in vivo* 14 days after ectopic implantation in a rat model. *In vivo*, cartilage spheres were also partly mineralized on day 14 (**Figure S4.4**).

quantification as a measure for collagen in scaffolds, *ns* (One-way ANOVA). (C) GAG content in scaffolds, *ns* (Kruskal-Wallis test). (D) DNA quantification in defects, $p < 0.05$ (Kruskal-Wallis and Dunn's post hoc tests, $**p < 0.01$). (E-G) Collagen visualized by picosirius red. Asterisks mark the cartilage spheres. (H) Quantified and (I) visualized mineralization of constructs using μ CT, *ns* (One-way ANOVA). (J) Quantified and (K) visualized mineralization of defects using μ CT, *ns* (One-way ANOVA). Abbreviations: day (D), glycosaminoglycan (GAG), micro-computed tomography (μ CT).

4.4 Discussion

With the poor translation from *in vitro* assessments to *in vivo* models and clinical trials, there is a need for advanced *in vitro* models. For evaluation of materials for *in situ* or material-driven bone regeneration, where intelligent biomaterials make use of the bone's innate capacity to regenerate and remodel upon implantation, such *in vitro* models do not currently exist (26). This not only hinders clinical translation, but also leaves a significant burden on animal experiments (22). Novel bone defect models to evaluate material-driven bone regeneration and to address the replacement, reduction and refinement of animal experiments principle (3Rs) have been developed in the recent years. This includes *ex vivo* human bone explant cultures and multiple semi-orthotopic implantations of bovine bone explants in mice (32,33). These models allow for the evaluation of cell-material interactions of multiple cell types in their native environment. However, the multicellular environment also complicates unraveling cell-material interactions. Thereby, keeping bone explants viable over time outside the living body remains a challenge (21,165). Cell death in explants transplanted in a different host as described above may trigger a non-physiological regeneration/remodeling response. Instead, with the development of an *in vitro* bone defect model a bottom-up approach can be adopted. As such, the complexity of models can be adapted, depending on which cell-material interactions need to be elucidated. Here, we used a tissue engineering approach to create an *in vitro* human bone defect model that enabled the *in vitro* evaluation of the material's potential to stimulate vascularization, cell migration and osteoinduction.

A co-culture of HUVECs and hBMSCs was used to create a bone-like extracellular matrix with vascular-like structures. By using a SF scaffold with two *in vitro* "critically sized" defects (117), 3D tissue growth was facilitated around the defects. HUVECs were stimulated to form vascular-like structures in endothelial growth medium, using hBMSCs as supporting and osteogenic cells. These vascular-like structures indeed developed over a period of 14 days and showed a branching morphology towards the end of the vascularization phase (*i.e.*, from day 0 to day 14). Vascular-like structures were mostly maintained for an additional 14 days when osteogenic differentiation and bone-like matrix formation of hBMSCs was induced. Although the main focus was on

the defect during the regeneration phase (*i.e.*, from day 28 to day 42), some HUVEC-hBMSC networks had regressed at this stage, based on the fragmented α -smooth muscle actin staining as a supporting cell marker. In addition, one limitation of the presented study is the lack of quality assessment of the vascular network (166). Therefore, future experiments might further investigate functional properties like network connectivity and whether the vascular-like structures are indeed hollow and maybe even perfusable. Additionally, vasculature in physiological bone has, based on its location and presumably function, a distinct molecular identity (*i.e.*, a relative expression level of CD31 and endomucin) (167). Bone-specific vasculature markers were not assessed in our study. Moreover, during physiological bone regeneration, vascularization is also a result of angiogenesis from existing vasculature (168), while in our *in vitro* model HUVECs only migrated from likely immature networks in the scaffold. Nevertheless, a primitive endothelial network, osteogenic differentiation and bone-like matrix formation, including the formation of collagen type I, osteopontin, and hydroxyapatite, was established prior to the implantation of the biomaterials.

To improve the translation from *in vitro* assessments to *in vivo* models and clinical trials, standardized protocols for the analyses of treatments on all model levels should be implemented (169). This would allow comparison and potential extrapolation of experimental outcomes from different models (44). Established biomarkers could facilitate in these comparisons (169–171). For bone regeneration, commonly assessed biomarkers include *e.g.*, alkaline phosphatase, RUNX2, bone morphogenetic protein 2 and 7, osteopontin, osteocalcin, collagen type I, and vascular markers VEGF and CD31 (172). As bone regeneration also involves callus and woven bone remodeling, the regulators of bone turnover RANKL and OPG are relevant as well (172,173). In our effort to improve and allow *in vitro/in vivo* translation, some of these markers were evaluated. In addition to these markers, other factors that have been reported to be involved in cell migration, vascularization, remodeling, and bone formation were evaluated upon material implantation (**Table S4.2**). An apparent difference was found in markers representative for the inhibition of bone formation and the stimulation of bone resorption; sclerostin and RANKL, respectively (173). In scaffolds implanted with cartilage spheres, a higher level of sclerostin and RANKL was measured when compared to scaffolds implanted with platelet gel. *In vivo*, osteocytes can express sclerostin and RANKL in the absence of mechanical stimulation to regulate bone remodeling (174). Scaffolds that expressed sclerostin and RANKL might have been more matured. In these scaffolds, hBMSCs might have been embedded in their matrix and differentiated into osteocytes, which were stimulated to produce sclerostin and RANKL in the absence of mechanical loading. However, this needs to be confirmed by

the evaluation of morphological osteocyte characteristics and the localization of osteocyte markers (116).

While no clear differences in other biomarkers were observed, the presence of all markers in the culture medium supernatants allows for the evaluation of physiological processes in bone regeneration with the presented *in vitro* model. Most likely, measured protein concentrations represent the bulk expression from cells in the scaffold, rather than the expression of the limited number of cells that interacted with the materials. Nevertheless, our *in vitro* model was able to capture some physiological regeneration events. First, the chemotaxis needed to attract vasculature to the defect site was reflected by the model to some extent. While in the fibrin gel mostly hBMSCs migrated to the defect site, in the platelet gel and cartilage spheres conditions, also HUVECs migrated to the defect site. Second, *in vivo* bone regeneration includes soft callus mineralization (175), something that was also observed in our *in vitro* model. As such, the *in vitro* model presented in this study shows resemblance to some stages of physiological bone regeneration.

When comparing the obtained *in vitro* results to *in vivo* data, some similarities can be observed. It is well accepted that for *in vivo* bone defects, fibrin alone is incapable of inducing full regeneration (176,177). This was also observed in the present *in vitro* model which might be explained by its inability to attract vascularization. Further, recently, blood clots were used to regenerate mouse cranial defects (178). It was found that *in vivo* these blood clots were completely degraded 15 days after implantation (178). In parallel, after 14 days, blood clot mimics in the current study were mostly degraded even though in our study a blood clot mimic was used instead of a physiological blood clot. Furthermore, in this study, the implanted devitalized cartilage spheres showed initial mineralization after 14 days, similar to when implanted *in vivo* for 14 days. Previously, these devitalized cartilage spheres were already shown to stimulate subcutaneous endochondral bone formation and bone regeneration in critically sized long bone defects in rats (155). In these *in vivo* defects, complete bridging of the gap was already observed with μ CT 4 weeks after implantation (155). The successful mineralization seen *in vivo* and *in vitro* might be attributed to the presence of alkaline phosphatase in the spheres (155). However, cartilage spheres that were further differentiated into hypertrophic cartilage spheres and subsequently devitalized, containing higher levels of alkaline phosphatase, were less successful in defect regeneration *in vivo* (155). Thus, while *in vitro* mineralization might be mainly caused by the presence of alkaline phosphatase, *in vivo* there are likely a multitude of factors regulating mineralization and regeneration. While some similarities were observed, the major difference between *in vivo* and *in vitro* models is the lack of the initial inflammatory response in *in vitro* models.

Initial immune responses *in vivo* can be predictable for subsequent bone regeneration (179), which underlines the importance of the immune cells in bone regeneration. The immune system is highly complicated, featuring a multitude of cell types and interactions. Therefore, future studies should investigate which immune responses are predictive for bone regeneration and how these immune responses can be integrated into the *in vitro* model. The addition of monocytes and their subsequent macrophage and osteoclast differentiation might already allow for enhanced degradation of the materials which may, in case of the spheres, improve growth factor release from the spheres and vascular infiltration into the spheres.

Besides the lack of immune cells (*e.g.*, monocytes, macrophages and osteoclasts), vascular maturation and functionality in the presented *in vitro* model, the model also lacks the presence of adjacent tissues that influence bone regeneration *in vivo* (*e.g.*, periosteum, bone marrow, muscle tissue (180,181). Animal experiments are therefore still inevitable. Other limitations are the absence of mechanical loading and the presence of the xenogeneic FBS. Mechanical loading is a well-accepted regulator of bone remodeling (4), and *in vivo* mechanical loading was also shown to influence bone regeneration (182). Bioreactors could facilitate in this mechanical loading, which ideally allows for longitudinal microscopic evaluation and in which samples are easily accessible for staining and material implantation. To replace FBS, alternatives for HUVEC-hBMSC co-cultures like human platelet lysate or defined serum-free media need to be explored. Human platelet lysate was already demonstrated to support bone remodeling (183), while serum-free medium proved efficient for HUVECs co-cultured with human adipose tissue derived stromal cells (184).

4.5 Conclusion

Advanced *in vitro* human bone defect models could facilitate in the evaluation of materials for *in situ* bone regeneration, addressing both translational and ethical concerns regarding animal experiments. Here, we present such an *in vitro* model, which was used to implant physiologically relevant materials for bone regeneration including a fibrin gel, platelet gel as blood clot mimic, and cartilage spheres as soft callus mimics. Within this model, important hallmarks of *in situ* bone regeneration including cell migration, vascularization, and osteoinduction, were observed *in vitro*. These included the endothelial cell chemotaxis induced by the blood clot mimic and the mineralization of the soft callus mimic. As such, this *in vitro* model could contribute to improved pre-clinical evaluation while aiding to reduce the need for animal experiments.

Author contributions

B.d.W., E.C., D.G. and S.H. contributed to conception, methodology and design of the study. B.d.W. and E.C. performed the experiments and contributed to analyzing the experimental results. Cartilage spheres and *in vivo* data were provided by L.d.S. and D.G.. B.d.W. wrote the original draft of the manuscript. All authors contributed to manuscript revision and approved the submitted version. B.d.W. and S.H. acquired funding for this research.

Acknowledgement

We thank Dewy van der Valk for the transport of the cartilage spheres from Utrecht to Eindhoven. We thank the Multiplex Core Facility of the Laboratory for Translational Immunology of the University Medical Center Utrecht, the Netherlands, for the Luminex analysis. This work is part of the research program TTW with project number TTW 016.Vidi.188.021, which is (partly) financed by the Netherlands Organization for Scientific Research (NWO). This research was also financially supported by the Gravitation Program “Materials Driven Regeneration”, funded by the Netherlands Organization for Scientific Research (024.003.013).

Supplementary information

The antibodies that were used for immunofluorescent stainings are listed in **Table S4.1**.

Table S4.1. List of antibodies that were used in this study

Antigen	Supplier	Catalogue No.	Conjugate	Species	Dilution
RUNX2	Abcam	ab23981		Rabbit	1:500
Osteopontin	Thermo Fisher	14-9096-82		Mouse	1:200
Collagen type I	Abcam	Ab34710		Rabbit	1:200
CD31	Abcam	Ab37259		Mouse	1:100
α -Smooth muscle actin	Thermo Fisher	MA5-13188		Rabbit	1:500
Anti-rabbit IgG	Molecular Probes	A21246	Alexa-647	Goat	1:200
Anti-mouse IgG1	Molecular Probes	A21127	Alexa-555	Goat	1:200

Abbreviations: runt-related transcription factor 2 (RUNX2).

To study the influence of staining with OsteoSense™ 680, CNA35-mCherry and NucBlue™ Hoechst 33342 on cell death, unstained and stained samples were compared for their lactate dehydrogenase (LDH) release in the supernatant from day 40 to day 42 (Figure S1).

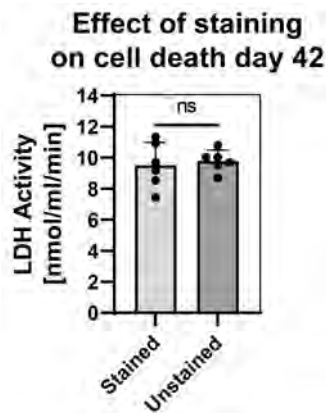


Figure S4.1. Potential staining-induced cell-death measured by LDH activity in the supernatant. Staining of samples did not induce additional cell death, *ns* (independent t-test).

On day 42 of the culture, cells had migrated to the implanted material in all conditions, but in defects implanted with fibrin gel, only hBMSCs migrated while in defects implanted with platelet gel both hBMSCs and HUVECs migrated (Figure S2). The migration of these cells appeared only in distinct areas. Defects implanted with cartilage spheres seemed to remain stable over time. In these defects, cell migration of both hBMSCs and HUVECs was observed by the presence of both cells around the spheres (Figure S2).

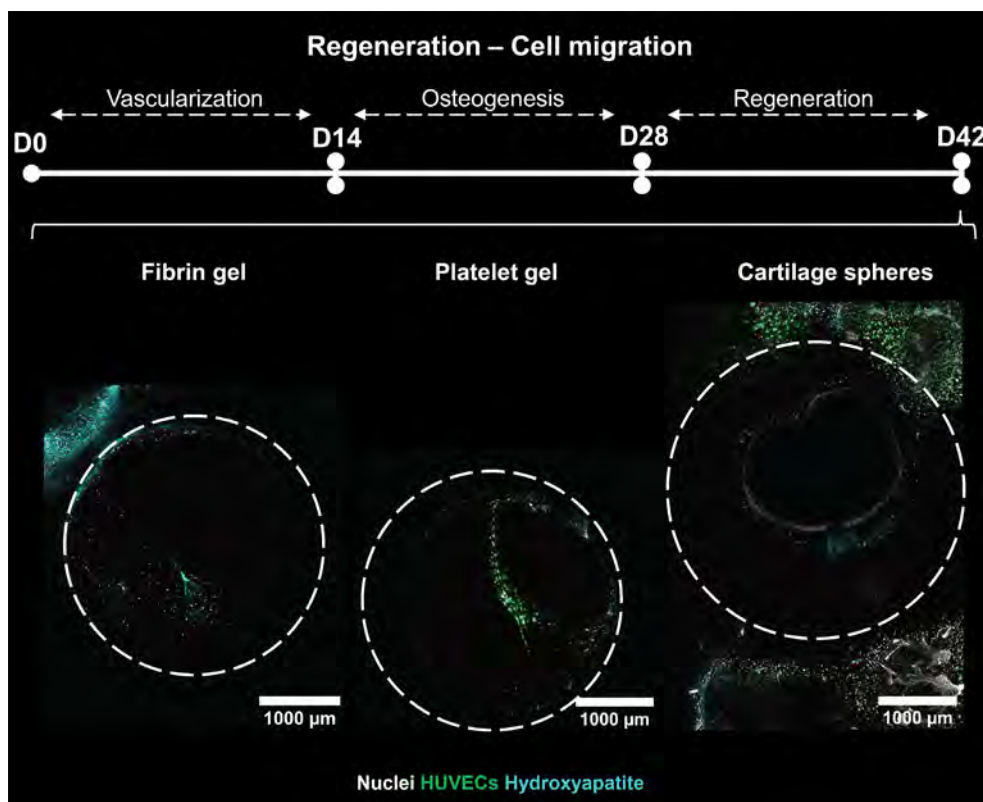


Figure S4.2. Evaluation of the regeneration phase of viable constructs. Images present defect overview images at day 42 of culture of constructs containing GFP-expressing HUVECs (green) and stained for nuclei (gray), and hydroxyapatite (cyan).

To evaluate the interactions of the cells with the implanted materials, culture medium supernatants of day 42 were analyzed for their protein content (**Table S4.2**).

Table S4.2. Evaluation of proteins relevant in for bone regeneration using multiplex immunoassays.

Analyte	Contribution to bone regeneration	Concentration in control medium (pg/ml)	Concentration in supernatant (pg/ml)
SDF-1 α	Important role in migration of MSCs, mainly in inflammation (185). Could support osteogenic differentiation and angiogenesis (186,187). Hypothesized to recruit osteoclast precursors (188).	71.9	FG: 372 \pm 46.4
			PG: 335 \pm 74.0
			CS: 370 \pm 49.9
PDGF-BB	Can enhance osteoclast differentiation of macrophage-like cells (189). Overexpression of PDGF-BB in MSCs can promote osteogenesis and angiogenesis (190).	16.4	FG: 43.5 \pm 11.2
			PG: 37.6 \pm 4.75
			CS: 35.8 \pm 1.42
PlGF ^o	Can recruit hematopoietic cells and stimulate the expression of pro-angiogenesis factors upon a fracture. Might influence osteogenic differentiation of MSCs and important for remodeling of healed fracture (191).	18.9	FG: 764 \pm 117
			PG: 782 \pm 161
			CS: 787 \pm 29.1
CTGF	Important for MSC condensation and chondrogenic differentiation during endochondral bone regeneration (161).	14.0	FG: 181 \pm 28.7
			PG: 179 \pm 18.4
			CS: 170 \pm 23.5
VEGF	Could enhance osteoclast survival and resorption (192,193). Could also recruit chondroclasts, osteoclasts and immune cells. Promotes vascularization and can promote osteogenic differentiation (152).	47.9	FG: 5.12*10 ³ \pm 1.29*10 ³
			PG: 4.83*10 ³ \pm 544
			CS: 5.98*10 ³ \pm 482
Angiopoietin -1	Can promote vascular integrity in regenerating vasculature (194).	979	FG: 10.5*10 ³ \pm 1.58*10 ³
			PG: 10.5*10 ³ \pm 2.32*10 ³

			CS: $9.91 \cdot 10^3 \pm 1.21 \cdot 10^3$
Angiopoietin -2	Can improve mineralization and angiogenesis in bone regeneration (195).	1.22*10 ³	FG: $5.09 \cdot 10^3 \pm 1.01 \cdot 10^3$
			PG: $5.72 \cdot 10^3 \pm 1.08 \cdot 10^3$
			CS: $4.24 \cdot 10^3 \pm 1.17 \cdot 10^3$
MMP-1	Most abundant collagenase in tissues, cleaves collagen, but its absence only leads to modest abnormalities in bone remodeling (163).	ND	FG: 785 ± 481
			PG: 802 ± 401
			CS: 655 ± 99.5
MMP-3 ^o	Involved in degradation of cartilage and the invasion of vasculature in osteoarthritis (162). Can cleave non-collagenous proteins (163).	96.3	FG: 294 ± 178
			PG: 424 ± 376
			CS: 454 ± 591
MMP-7 ^o	Can promote RANKL availability and cleave non-collagenous proteins. Might be crucial for proper bone regeneration (163).	445	FG: $9.18 \cdot 10^3 \pm 5.03 \cdot 10^3$
			PG: $10.4 \cdot 10^3 \pm 9.63 \cdot 10^3$
			CS: $7.62 \cdot 10^3 \pm 1.15 \cdot 10^3$
MMP-8	Seems to be crucial for proper bone regeneration (163).	41.9	FG: 155 ± 17.5
			PG: 142 ± 19.6
			CS: 133 ± 3.28
MMP-9	Most abundant MMP in bone, participates in osteoclast recruitment and the release of growth factors from the extracellular matrix (163). MMP9 is also involved in endochondral ossification (164).	228	FG: $1.04 \cdot 10^3 \pm 78.7$
			PG: 928 ± 125
			CS: $1.08 \cdot 10^3 \pm 33.1$
MMP-10 ^o	Might promote (pathological) calcification (196,197).	91.3	FG: 529 ± 38.1
			PG: 470 ± 22.2
			CS: 558 ± 81.2
TIMP-1	High affinity for MMP-9 (inhibition), important for osteogenic lineage commitment of MSCs (163).	101	FG: $18.9 \cdot 10^3 \pm 448$
			PG: $18.0 \cdot 10^3 \pm 664$
			CS: $18.8 \cdot 10^3 \pm 621$

RANKL	Typically expressed by cells from the osteogenic lineage, including MSCs, osteoblasts and osteocytes. Required for osteoclast differentiation (198).	ND	FG: 19.6 ± 3.64
			PG: 13.3 ± 3.80 #
			CS: 24.1 ± 4.43 #
OPG	Can prevent RANKL from binding to the RANK receptor on preosteoclasts, thereby inhibiting osteoclast differentiation (198,199).	$1.41 \cdot 10^3$	FG: $14.2 \cdot 10^3 \pm 3.56 \cdot 10^3$
			PG: $14.5 \cdot 10^3 \pm 2.41 \cdot 10^3$
			CS: $16.9 \cdot 10^3 \pm 3.71 \cdot 10^3$
Osteopontin	Instrumental for intrafibrillar mineralization and promotes osteoclast activation (200). Can promote osteoclast precursor migration (201).	321	FG: 716 ± 96.7
			PG: 713 ± 15.1
			CS: 737 ± 45.7
Osteonectin	Can promote bone formation and mineralization. Regulates collagen fibrillogenesis (202).	$1.27 \cdot 10^3$	FG: $42.7 \cdot 10^3 \pm 5.55 \cdot 10^3$
			PG: $35.6 \cdot 10^3 \pm 5.69 \cdot 10^3$
			CS: $44.0 \cdot 10^3 \pm 4.20 \cdot 10^3$
Sclerostin	Inhibits bone formation and osteogenesis, could stimulate RANKL secretion by osteocytes, thereby promoting osteoclast differentiation (160).	414	FG: 503 ± 36.5 *
			PG: 413 ± 41.0 # *
			CS: 496 ± 50.2 #
Periostin	Upregulated in response to bone injury. Is crucial for callus, cartilage and bone formation (203).	ND	FG: $61.0 \cdot 10^3 \pm 6.00 \cdot 10^3$
			PG: $56.8 \cdot 10^3 \pm 5.74 \cdot 10^3$
			CS: $61.3 \cdot 10^3 \pm 5.34 \cdot 10^3$
Fibronectin	Could inhibit osteoclastogenesis (204,205), but could enhance mature osteoclast activity and resorption (204). Could promote osteogenic differentiation and bone-like matrix formation of MSCs at low	$330 \cdot 10^3$	FG: $4.42 \cdot 10^6 \pm 621 \cdot 10^3$
			PG: $3.45 \cdot 10^6 \pm 456 \cdot 10^3$

	coating densities, and inhibit differentiation but promote proliferation at higher coating densities (206).		CS: $3.92 \times 10^6 \pm 758 \times 10^3$
--	---	--	--

Values represent mean \pm standard deviation or $^\circ$ median \pm interquartile range. Significant differences are indicated with: $\#^*p < 0.05$. Abbreviations: stromal derived factor (SDF), platelet derived growth factor (PDGF), placental growth factor (PIGF), connective tissue growth factor (CTGF), vascular endothelial growth factor (VEGF), matrix metalloproteinase (MMP), tissue inhibitor of metalloproteinase (TIMP), receptor activator of nuclear factor kappa- β ligand (RANKL), osteoprotegerin (OPG), osteopontin (OPN).

Collagen type I formation after 42 days was visualized in and around the defects using immunohistochemistry (Figure S2). Collagen type I formation was mainly visible in scaffolds implanted with fibrin gel or cartilage spheres (Figure S2).

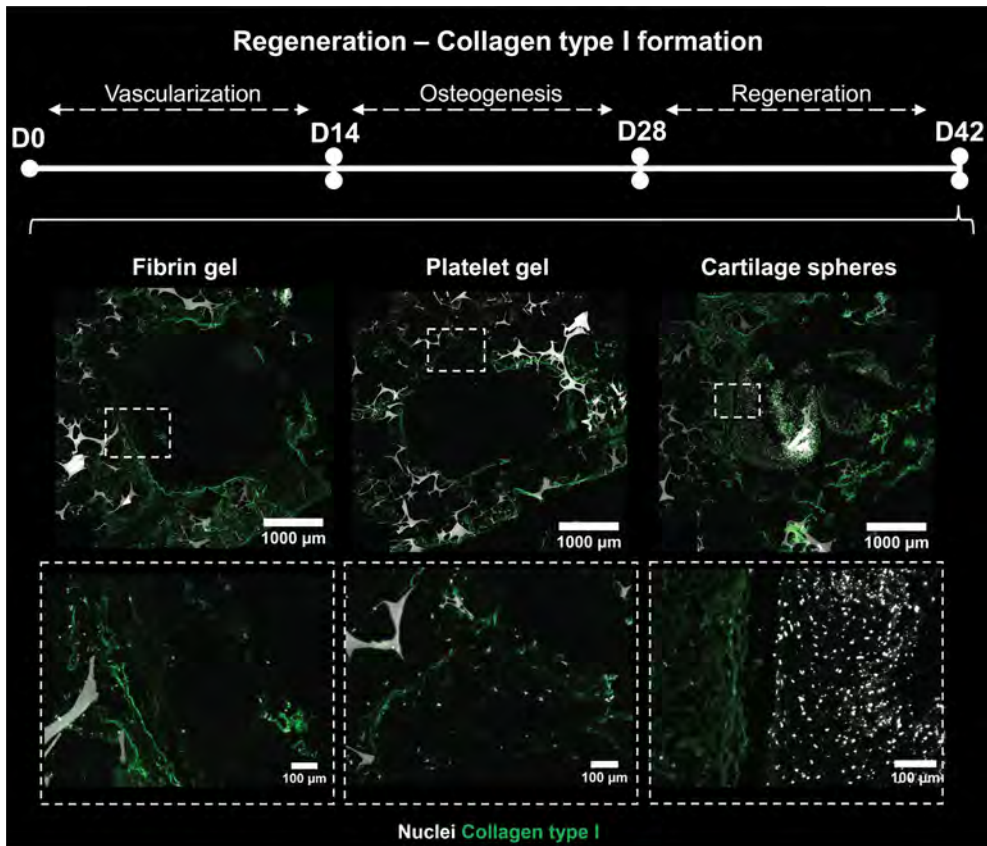


Figure S4.3. Collagen type I (green) immunohistochemical analysis. Top panel presents defect overview images, bottom panel present close-up images.

For model validation, *in vitro* cartilage sphere mineralization was compared to *in vivo* cartilage sphere mineralization 14 days after ectopic implantation in a rat model. *In vivo*, cartilage spheres were partly mineralized after 14 days, which is comparable to our *in vitro* model where parts of cartilage spheres were mineralized 14 days after artificial implantation.

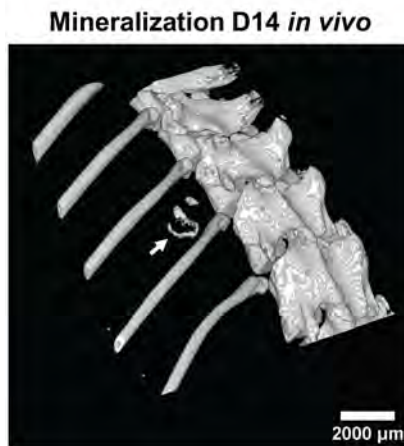


Figure S4.4. Cartilage sphere mineralization *in vivo*, 14 days after ectopic implantation in a rat model. Arrow points at implanted cartilage spheres, two spheres were implanted. Spheres were visualized with micro-computed tomography (μ CT).

Supporting media:

- **Video S4.1.** Three-dimensional visualization of vascular-like structures, collagen, hydroxyapatite and cell nuclei prior to implantation (day 28)
- **Video S4.2.** Three-dimensional visualization of cell migration in defect implanted with fibrin gel (day 42).
- **Video S4.3.** Three-dimensional visualization of cell migration in defect implanted with platelet gel (day 42).
- **Video S4.4.** Three-dimensional visualization of cell migration in defect implanted with cartilage spheres (day 42).



A fluorescence microscopy image showing a dense population of cells. The nuclei are stained blue, the cytoplasm and some extracellular matrix components are green, and there are prominent red structures, possibly representing specific organelles or protein expressions. The overall appearance is that of a complex, interconnected cellular network.

Part II

Advancing tissue engineering of *in vitro* human
bone remodeling models

5

In vitro models of bone remodeling: a systematic review and map of available literature

This chapter is an extract of:

Stefan J. A. Remmers¹, **Bregje W. M. de Wildt**^{1†}, Michelle A. M. Vis^{1†}, Eva S. R. Spaander¹, Rob B. M. de Vries², Keita Ito¹, Sandra Hofmann¹

¹ Orthopaedic Biomechanics, Department of Biomedical Engineering and the Institute of Complex Molecular Systems, Eindhoven University of Technology, Eindhoven, the Netherlands.

² SYRCLE, Department for Health Evidence, Radboud Institute for Health Sciences, Radboud University Medical Center, Nijmegen, the Netherlands.

†Authors contributed equally

Abstract

To enable the investigation of human healthy and pathological bone remodeling and to address the principal of reduction, refinement and replacement of animal experiments, *in vitro* bone remodeling models are increasingly being developed making use of an osteoclast-osteoblast co-culture. For these co-cultures many different culture parameters are used that could affect the cells' responses in the co-culture, limiting reproducibility and translation between experiments. Therefore, the aim of this study was to generate a systematic map from a database of existing osteoclast-osteoblast co-cultures representing an *in vitro* model for bone remodeling, published until January 6, 2020. Their methods and predetermined outcome measures (resorption, formation, and tartrate-resistant acid phosphatase and alkaline phosphatase quantification as their surrogate markers, respectively) were extracted. The systematic map derived from the database, underlines the variability between currently available *in vitro* remodeling models, which limits reproducibility and translation between them. Nevertheless, the systematic map and its evaluation could be used as a guide to design *in vitro* bone remodeling experiments, towards improved understanding of human bone remodeling.

5.1 Introduction

Bone is a highly dynamic tissue with mechanical and metabolic functions that are maintained by the process of bone remodeling by bone forming osteoblasts, bone resorbing osteoclasts, and regulating osteocytes. In healthy tissue, bone resorption and formation are in equilibrium. In diseases such as osteoporosis and osteopetrosis this equilibrium is disturbed, leading to pathological changes in bone mass that adversely affect the bone's mechanical functionality (207). Studies on bone physiology, bone disease and drugs for these diseases are routinely performed in animal models, which are considered a fundamental part of preclinical research. However, their use in pre-clinical studies often leads to poor translation of results to human clinical trials (208,209), and subsequent failure of promising discoveries to enter routine clinical use (23,25). These limitations and the desire to reduce, refine and replace animal experiments gave rise to the development of *in vitro* models (7,20). Over the last four decades, significant progress has been made in developing osteoclast-osteoblast co-cultures towards *in vitro* bone remodeling models.

The development of *in vitro* osteoclast-osteoblast co-cultures started with a publication of T.J. Chambers in 1982 (210), where the author induced quiescence of isolated tartrate-resistant acid phosphatase (TRAP)-positive rat osteoclasts with calcitonin and reversed their quiescence by co-culturing them with isolated rat osteoblasts in direct contact. At that time, studies involving osteoclasts resorted to the isolation of mature osteoclasts by disaggregation from fragmented animal bones. The first account of *in vitro* osteoclastogenesis in co-culture was realized in 1988 when Takahashi and co-authors (211) cultured mouse spleen cells and isolated mouse osteoblasts in the presence of 1,25-dihydroxyvitamin D₃ and found TRAP-positive dentine-resorbing cells. The herein described methods were used and adapted to generate osteoclasts for the following decade. Most of the studies published until this point in time used co-cultures as a tool for achieving osteoclastogenesis, as opposed to a model for bone remodeling. At that time, a co-culture of osteoblasts with spleen cells or monocytes was the only way of generating functional osteoclasts *in vitro*. In 1999, Suda and co-authors (212) discovered receptor activator of nuclear factor κ B ligand (RANKL) and macrophage colony stimulating factor (M-CSF) as the necessary and sufficient proteins required for differentiating cells from the monocyte/macrophage lineage into functional osteoclasts. This discovery marked the start of co-culture models developed for studying bone remodeling (**Figure 5.1**).

In recent years, many research groups have developed osteoclast-osteoblast co-cultures with the intent of studying both formation and resorption, but each group seems to be individually developing the protocols resulting in many functionally related experiments

that are methodologically different. In addition, the use of such methods is often not clearly stated within titles and abstracts. Simple title/abstract searches such as ‘osteoclast + osteoblast + co-culture’ show only a fraction of available studies using osteoclast-osteoblast co-cultures. Moreover, due to the use of co-cultures for osteoclastic differentiation, many osteoclast-osteoblast co-cultures have been performed that did not study any formation outcomes. These studies cannot be used as *in vitro* remodeling models, as this requires the evaluation of both resorption and formation. Finding and comparing different co-culture approaches and their results is thus complicated. Therefore, the aim of this study was to perform a systematic review, generate a database of extracted study methodological information, and map the experimental details to provide an overview of currently available *in vitro* models for bone remodeling employing osteoclast-osteoblast co-cultures.

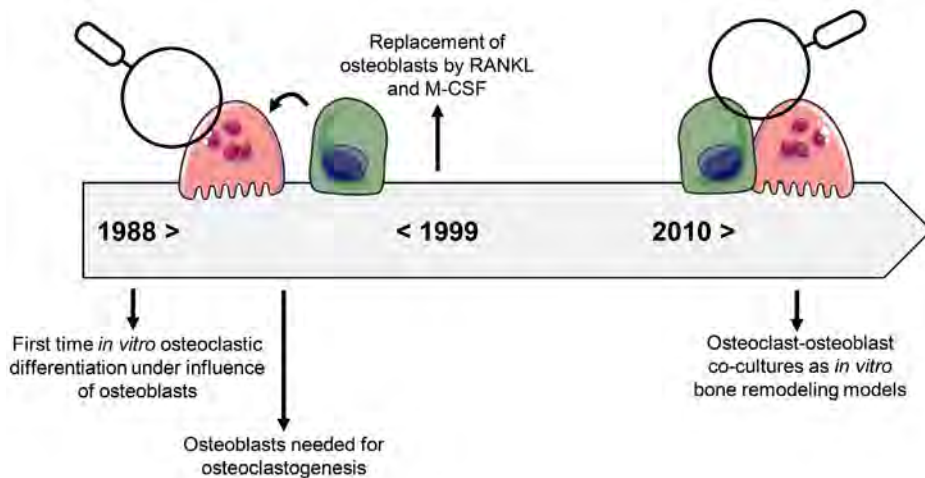


Figure 5.1. Timeline of the progression in osteoclast-osteoblast co-cultures. In 1988, osteoclasts were generated for the first time *in vitro* under influence of osteoblastic communication. From then, many co-cultures were performed in which osteoblastic formation was neglected. From 1999, RANKL and M-CSF were applied as differentiation factors in the culture medium, avoiding the need for osteoblasts. From 2010, osteoclast-osteoblast co-cultures are increasingly being employed to mimic bone remodeling *in vitro*. Abbreviations: receptor activator of nuclear factor κ B ligand (RANKL) and macrophage colony stimulating factor (M-CSF). The figure was created with Servier Medical Art, licensed under a Creative Commons Attribution 3.0 Generic License (<http://smart.servier.com>, accessed on 2 July 2021).

5.2 Methods

For this systematic map, a structured search protocol was developed using the SYRCLÉ protocol format (213). To ensure transparency of the publication, the protocol and search strings were made publicly available before completion of study selection via

Zenodo (214). In short, three online bibliographic literature sources were consulted with a comprehensive search query and the resulting publications were combined and screened using a three-step procedure: (i) identification of osteoclast-osteoblast co-cultures, (ii) identification of relevant outcome measures, (iii) search for additional articles in relevant reviews and the reference lists of studies included in the database.

5.2.1 Database Search

The online bibliographic literature sources Pubmed, Embase (via OvidSP) and Web of Science were searched on January 6, 2020, with a predefined search query consisting of the following components: ([osteoclasts] OR ([osteoclast precursors] AND [bone-related terms])) AND ([osteoblasts] OR ([osteoblast precursors] AND [bone-related terms])) AND [co-culture], where each component in square brackets represents a list of related thesaurus and free-text search terms. The full search strings can be found via Zenodo (214). The results of all three searches were combined. Conference abstracts and duplicates were removed using the duplicate removal tools of Endnote X7 and Rayyan web-based systematic review software (215). The entire screening and data collection process was performed independently by two researchers.

5.2.2 Screening step 1: Identification of osteoclast-osteoblast co-cultures

This step was performed to identify and extract osteoclast-osteoblast co-cultures from the complete list of studies identified from the three online bibliographic literature sources after automatic removal of conference abstracts and duplicates. Using Rayyan web-based systematic review software (215), the titles and abstracts were screened for the presence of primary studies using osteoclast-osteoblast co-cultures. Reviews, theses, chapters, and conference abstracts that were not automatically detected were excluded at this point. Relevant reviews were saved separately to serve as an additional source of studies that could have been missed by the systematic search (screening step 4).

In the selection process, co-culture was defined as the simultaneous (assumed) presence of osteoclasts and osteoblasts (or osteoclast-like and/or osteoblast-like cells) within the same culture system at any moment during the described experiment, such that the cells were able to communicate either via soluble factors in the medium and/or directly through cell contact (**Figure 5.2**). Both primary cells and cell lines of any origin were admitted including heterogeneous cell populations if these were clearly defined and expected to result in a biologically relevant number of the desired cell type. The presence of progenitor cells (such as monocytes or mesenchymal stem/stromal cells) was allowed only if these were either verified or expected to differentiate into osteoclasts and/or osteoblasts. Studies using a single animal or human donor for both cell types were allowed, but only if the two (progenitor) cell types were at one point separated, counted,

and reintroduced in a controlled manner. Trans-well systems (no direct cell contact but shared medium compartment with or without membrane), scaffolds (three-dimensional (3D) porous structure of any material including decellularized matrix), and bioreactor culture systems (culture exposed to physical stimuli such as strain, compression, fluid flow) were included. Conditioned media experiments were excluded because these do not allow real-time two-way exchange of cell signals. Explant-, organ- and other *ex vivo* cultures were excluded. When the study used any type of osteoclast-osteoblast co-culture as defined above, the study was included. When, based on the title and abstract, it was possible that there was a co-culture, but this was not described as such, the full-text publication was screened.

5.2.3 Screening step 2: Identification of relevant outcome measures

This step was used to identify co-cultures that specifically investigated relevant outcome measures related to bone remodeling: formation or resorption (primary outcome measures), or quantitative measurements of activity markers ALP or TRAP in a dedicated assay (secondary outcome measures) (**Figure 5.2**). The primary outcome measures of resorption and formation were chosen because these are the processes that are directly affected in bone diseases. Formation/resorption measurement was defined as any method that directly measures the area or volume of (tissue) mineralization by OBs or resorption by OCs or any method that measures by-products or biochemical markers that directly and exclusively correlate to formation/resorption respectively. The secondary outcome measures of ALP and TRAP were included because these are regarded as alternatives for the direct measurement of formation and resorption. The measurement of ALP and TRAP was defined as the detection of either the enzymatic activity or the direct quantification of these proteins present. Polymerase Chain Reaction (PCR) and Immuno-histological stainings (with or without image analysis) were not considered relevant outcome measures. The full texts of the studies identified in screening step 1 were screened for experimental techniques and outcome measures. Publications written in languages other than English with no translation available and publications where the full text could not be found were excluded at this point. When a relevant outcome measure was measured in both osteoclasts and osteoblasts in the co-culture, data was extracted. Studies in which both cell types were studied, but relevant outcome measures were only measured in either osteoclasts or osteoblasts, were excluded as well as studies in which only osteoclasts or osteoblasts were studied (*i.e.*, the other cell type was neglected for analysis).

5.2.4 Screening step 3: Review and reference list screening

To find additional studies that may have been missed during bibliographic searches, relevant review articles and studies labeled as category 1 were screened for additional unique relevant publications. Identified publications were screened as before.

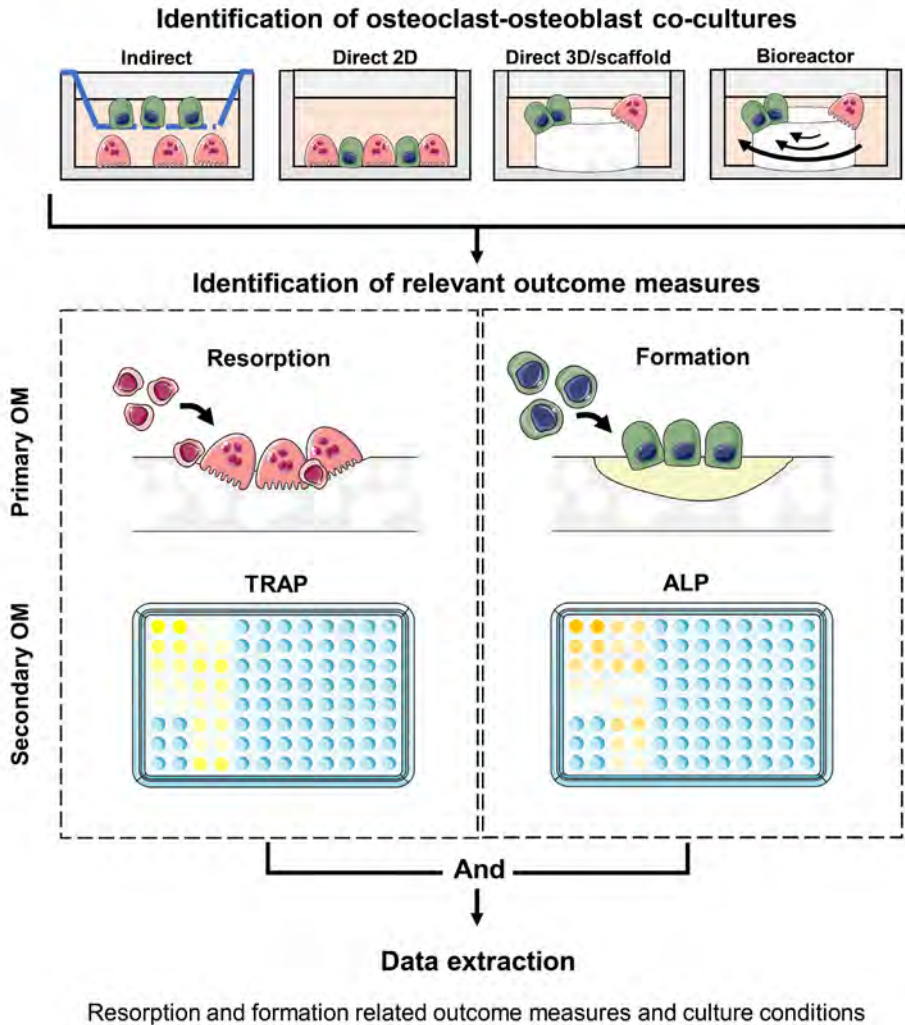


Figure 5.2. Schematic overview the used strategy. All identified studies were searched for osteoclast-osteoblast co-cultures, where co-culture was defined as osteoclasts and osteoblasts being present simultaneously and able to exchange biochemical signals. Osteoclast-osteoblast co-culture studies which used relevant outcome measures for both resorption and formation were included into the database. From these studies, methodological details on outcome measures and culture conditions were extracted. Abbreviations: two-dimensional (2D), three-dimensional (3D), outcome measures (OM), tartrate-resistant acid phosphatase (TRAP), alkaline phosphatase (ALP). The figure was modified from Servier Medical Art,

licensed under a Creative Common Attribution 3.0 Generic License (<http://smart.servier.com>, accessed on 2 July 2021).

5.2.5 Database generation and analysis

All information related to the culture conditions and relevant outcome measures was collected and organized into a database. Cell species (216), origin (cell line or primary) and type of both the osteoclasts and osteoblasts (7), seeding numbers, densities and ratios were collected or calculated (217,218). The culture surface material (219), sample size, culture duration, medium refreshing rate, environmental conditions and pre-culture duration were collected if available (220). The medium components and supplements were extracted (221), as well as medium components of any monoculture prior to the co-culture. For resorption outcomes, additional information on the resorbed substrate, the methodological procedure and quantification of results was collected. For formation outcomes, additional information on the type of analysis, the methodological procedure and quantification of results was collected. For both ALP and TRAP, additional information on the mechanism of the biochemical assay, whether it was conducted on lysed cells or supernatant, and information regarding the quantification was collected. In addition, the following information was collected, whether: the authors described their setup as a model specifically for remodeling, the experiment was conducted in 3D, the experiment applied bioreactors, more than 2 cell types were cultured simultaneously, the culture used a trans-well setup. Finally, the tested genes of all studies applying additional PCR and any proteins studied with ELISA or other supernatant analyses executed on the co-culture were noted.

5.2.6 Quality assessment and scripting

In the database, the culture conditions, cells and materials used are reported, and not the data obtained from them, or the results described in the publication. Quality assessment was thus limited to assessing the completeness of the necessary elements of the collected methodological details, to the extent that the description of used methods is complete enough to be properly represented in the database and related figures and tables. Publications in which information was missing are represented as ‘not reported’ (NR) if no information was provided, or ‘reference only’ if no information was provided but another study was referenced. If studies were missing critical information to allow for reproduction of the outcome measures (for example seeding ratio’s, culture surface material, medium or supplement information, critical steps in analyses), a red label was used to mark this missing information. If the missing information was not critical for the outcome measures but necessary for replication of the study (for example sample size, medium refresh rate, control conditions), an orange label was used.

Three scripts were written using Excel Visual Basics programming language to analyze and process the database. One script counts all instances of Excel cells labeled as ‘missing info’ and presents this number in two dedicated columns (missing critical or non-critical info). One script counts the frequency of occurrence of all years of publication. Finally, one script analyzes this database and extracts relevant descriptive statistical data on the collected information. On sheet 2 “Data” of the database Excel file, the statistical data and collected information are presented in the form of lists and tables together with the buttons to re-run the analyses based on the reader's requirements. The scripts are integrated within the excel file and can be used only when the file is saved as a ‘macro-enabled’ file (.xlsm) (**Supplementary file 5.1**).

5.3 Results

5.3.1 Search results

From three online bibliographic literature sources, 7687 studies were identified (Pubmed: 1964, Embase via OvidSP: 2709, Web of Science: 3014). 6874 studies remained after removing conference abstracts, and 3925 unique studies remained to be screened after duplicate removal (**Figure 5.3**).

5.3.2 Study inclusion

After screening step 1, 694 studies remained as osteoclast-osteoblast co-cultures. A list of these studies is available as a Supplementary file (**Supplementary file 5.2**). Screening step 2 further excluded one study because of a missing full text, 35 studies because they were in a language other than English, and 406 studies because no relevant outcome measure was used. From the 252 remaining studies, 77 studies investigated both osteoclasts and osteoblasts and in 39 of these studies, both osteoclasts and osteoblasts were studied using relevant outcome measures. These 39 studies were included in the database (**Figure 5.3**).

Screening step 4 identified 34 unique studies from the reference lists of the included 39 studies and identified another 25 unique studies from the 10 identified review publications. These additional 59 studies were screened as described previously and resulted in an additional three osteoclast-osteoblast co-cultures. However, these publications only studied either resorption or formation. As such, they were not included into the database. From the $N = 39$ included studies, $N = 45$ different experiments were identified. Experimental details from these studies have been extracted into the database (**Supplementary file 5.3**).

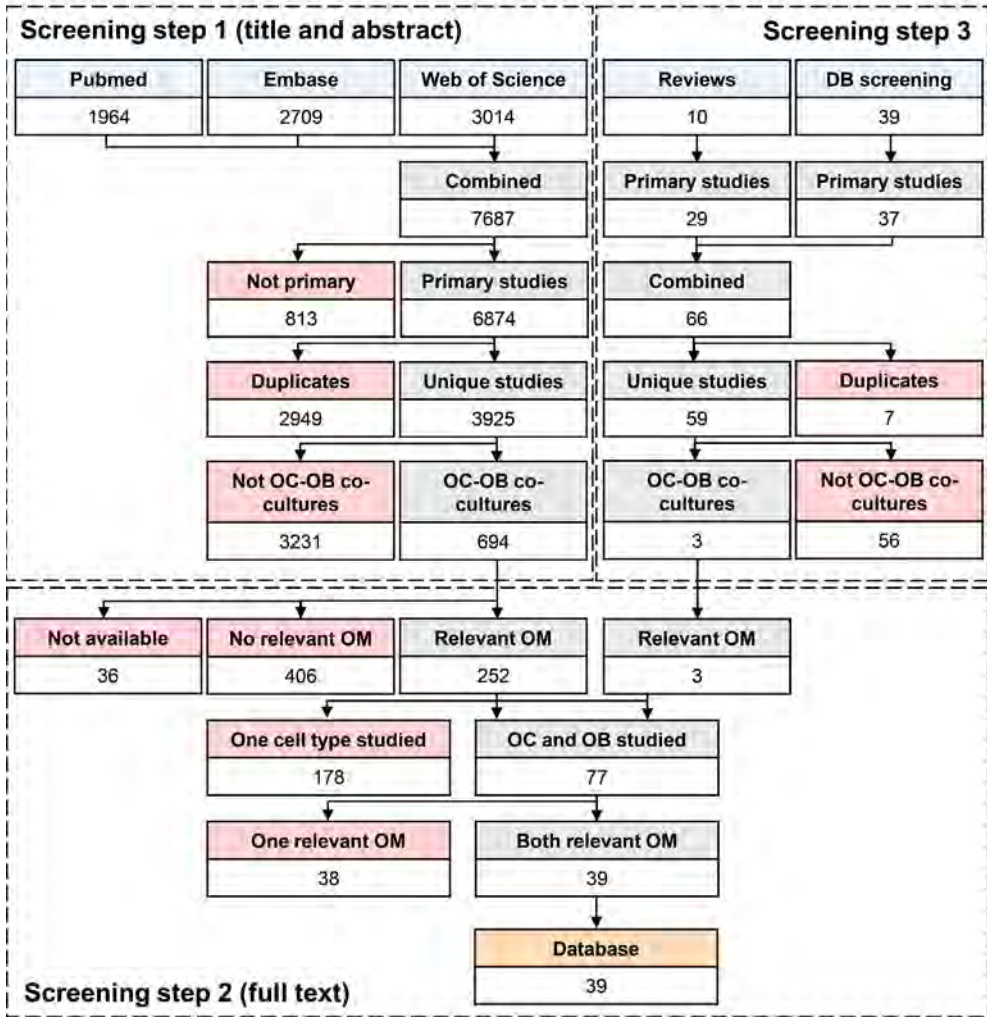


Figure 5.3. Flow diagram of systematic literature search and screening. Screening step 1: hits from 3 online bibliographic literature sources were combined, primary studies were selected, and duplicates were removed. Title and abstracts were screened for the presence of osteoclast-osteoblast co-cultures. Screening step 2: osteoclast-osteoblast co-cultures were screened in full text for relevant outcome measures. Papers in which both cell types were studied with relevant outcome measures were included in the database. Screening step 3: papers included into the database and reviews were screened for potentially missing relevant studies. Each selection step is marked with a colored header. Blue header: used as input for the review. Grey header: selection step. Red header: excluded studies. Orange header: database as presented in this systematic map. Abbreviations: outcome measures (OM), database (DB), osteoclast (OC), osteoblast (OB).

5.3.3 Publications per year

The publications included in the database span the time between 1997 and 2019, with only $N = 8$ publications before 2010 (**Figure 5.4**). This coincides with the progress in development of *in vitro* co-cultures of osteoclasts and osteoblasts, moving beyond co-cultures with osteoblasts to generate osteoclasts, and moving towards co-cultures of osteoclasts and osteoblasts to study for example cell-cell interactions (7).

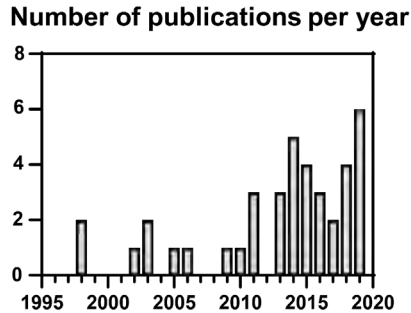


Figure 5.4. Relevant publications per year. The 39 selected publications of the database counted by year ranging from 1998 to 2019.

5.3.4 Osteoclasts

Cultures were all initiated with osteoclast progenitors: $N = 16$ studies introduced monocytes, $N = 11$ introduced mononuclear cells, the other studies used other precursors (**Table 5.1**).

The 6 oldest included studies used chicken and rat cells, all others used mouse or human cells. With only one exception combining a mouse ST-2 cell line with human monocytes (222), all studies used cells of exclusively a single species for the OB and OC source. Only one study claimed to introduce OCs directly into co-culture but failed to provide any information regarding the cell source and was therefore ignored from further investigation.

The OC seeding density ranged from 5×10^3 cells/cm² to 15×10^6 cells/cm² with a mean of 190×10^3 cells/cm² ($N = 25$) in two-dimensions (2D) (**Figure 5.5A**) and from 20×10^3 cells/cm³ to 70×10^6 cells/cm³ with a mean of 17×10^6 cells/cm³ ($N = 6$) in 3D (**Figure 5.5D**).

Table 5.1. Osteoclast origins and occurrences

	Monocytes	Mononuclear cells	Macrophages	Osteoclast precursors	Osteoclasts	Spleen cells	Per-row total
Human primary	10	6	1	3			20
Human cell line	4						4
Mouse primary	2		2	2			6
Mouse cell line			2				2
Rat primary		3				1	4
Chicken primary		2					2
Reference only					1		1
Per-column total	16	11	5	5	1	1	39

Each column represents a different cell type of osteoclast-like cell or a precursor. Each row represents a different source of cells, differentiating between both the origin species and whether the cells are primary cells or cell lines.

5.3.5 Osteoblasts

Most studies used human primary cells (**Table 5.2**). Almost half of the studies started the co-culture with osteoblasts, the others started with progenitor cells. As a result of ambiguous isolation methods and nomenclature which is subjective to changes over time (223), some cell descriptions in might refer to similar cell populations. This systematic map reflects the nomenclature used by the authors or extrapolated from the description and does not further interpret the provided information.

Except for the oldest 6 studies that used chicken and rat cells, all studies used human or mouse cells, most of which were primary cells. While the studies using rat and mouse cells mostly directly introduced osteoblasts (either isolated as such or differentiated before seeding), those that used human cells predominantly introduced progenitor cells. Those that used human primary osteoblasts purchased expandable human osteoblasts (224) or osteoblasts (225), undefined expanded bone cells (226), or differentiated mesenchymal stromal cells from bones obtained during a surgical procedure (227).

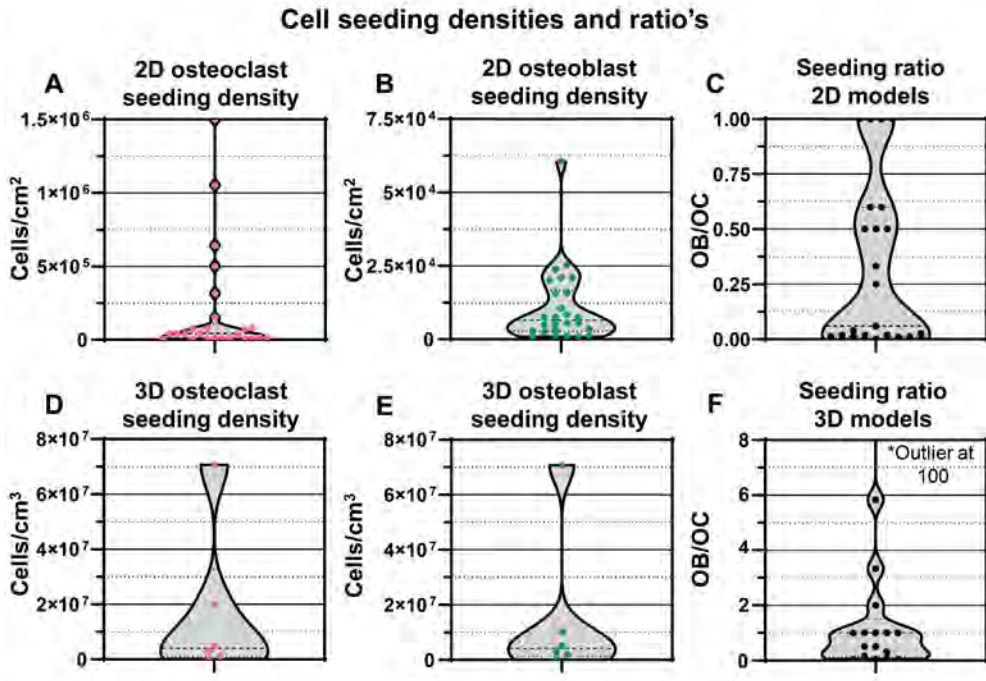


Figure 5.5. Seeding densities and seeding ratios. Violin plots of 2D and 3D seeding ratios of osteoclasts (A+D), osteoblasts (B+E) and respective seeding ratios in co-cultures (C+F). Values are calculated based on reported seeding numbers of the cells or precursors thereof per surface area or volume. Abbreviations: two-dimensional (2D), three-dimensional (3D), osteoblast (OB), osteoclast (OC).

Osteoblast densities ranged from 0.9×10^3 cells/cm² to 60×10^3 cells/cm² with a mean of 11×10^3 cells/cm² ($N = 26$) in 2D (**Figure 5.5B**) and from 0.3×10^3 cells/cm³ to 7×10^3 cells/cm³ with a mean of 15×10^6 cells/cm³ ($N = 6$) in 3D (**Figure 5.5E**). Osteoblast : osteoclast seeding ratios in 2D varied highly and ranged from 1:1500 to 1:1 (**Figure 5.5C**). Osteoblast : osteoclast seeding ratios in 3D ranged from 100:1 to 1:25 (**Figure 5.5F**).

Table 5.2. Osteoblast origins and occurrences.

	Osteoblasts	Mesenchymal stem cells	Mesenchymal stromal cells	Stromal cells	Stromal vascular Fraction	Osteoprogenitor cells	Per-row total
Human primary	4	9	2	6	1		22
Human cell line	1						1
Mouse primary	3	2					5
Mouse cell line	4						4
Rat primary	3					1	4
Chicken primary				2			2
Reference only	1						1
Per-column total	16	11	2	8	1	1	39

Each column represents a different cell type of osteoblast-like cells or their precursors. Each row represents a different source of cells, differentiating between both the origin species and whether the cells are primary cells or cell lines.

5.3.6 Medium composition

The behavior of cells is highly dependent on their environment, of which the biochemical part is predominantly determined by the culture medium composition. The main components of typical culture media are a base medium, fetal bovine serum (FBS) and specific supplements such as osteoblast and osteoclast differentiation factors. Eight different base (or complete) media were reported (**Figure 5.6A**), with α -MEM and DMEM accounting for approximately 70% of all experiments. FBS content ranged from 0% to 20%, with most studies using 10% (**Figure 5.6B**). Studies that did not use FBS supplementation used forms of complete media of which the composition was not described in the studies, but likely including a type of serum or equivalent serum-free supplements.

As osteoclast supplement, M-CSF concentration was reported in $N = 11$ studies and ranged from 10 ng/ml to 100 ng/ml with a mean of 39,82 ng/ml (Figure 5.6C). The other osteoclast supplement RANKL was reported in $N = 14$ studies and the concentration ranged from 10 ng/ml to 100 ng/ml with a mean of 49 ng/ml. Osteoblast supplements were recalculated to molarity if necessary (Figure 5.6C). Ascorbic acid (also referred to as ascorbic acid-2-phosphate, L-ascorbic acid or L-ascorbate-2-phosphate) concentration was reported in $N = 19$ studies and ranged from 0.05 mM to 0.57 mM, with a mean of 0.18 mM and one outlier at 200 mM that was disregarded for this calculation. Dexamethasone was used in $N = 13$ studies and was used in 2 different molarities: 6 times at 100 nM and 7 times at 10 nM. β -Glycerophosphate concentration was reported in $N = 17$ studies, and ranged from 1 mM to 46 mM, with a mean of 13 mM (Figure 5.6C). As additional often used medium supplement, 1,25-dihydroxyvitamin D3 was identified. The use of 1,25-dihydroxyvitamin D3 was reported in $N = 10$ studies at 2 different concentrations (*i.e.*, 10 nM and 100 nM), of which 10 nM was most frequently used (8 out of 10 times) (Figure 5.6C).

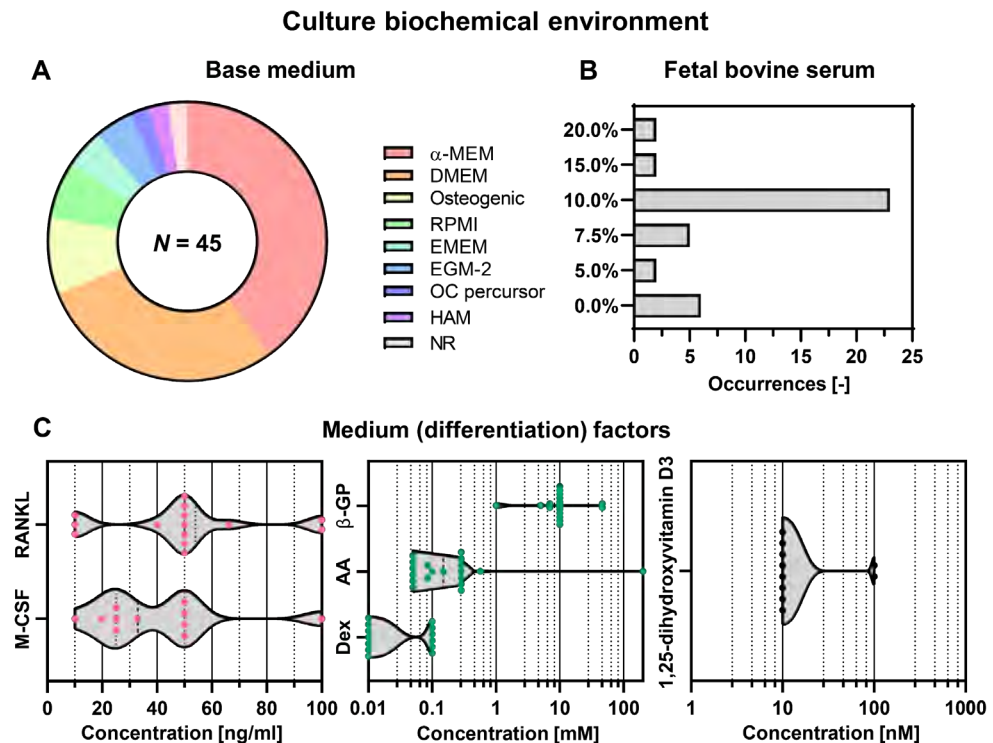


Figure 5.6. The differences in culture media used in the included studies. (A) The occurrence of all identified base and complete media used during the co-culture phase of each study. (B) Serum concentrations during the co-culture phase of each study. (C) Supplements administered during the co-

culture phase of each study. Abbreviations: not reported (NR), receptor activator of nuclear factor κ B ligand (RANKL), macrophage colony stimulating factor (M-CSF), β -glycerophosphate (β -GP), ascorbic acid (AA), dexamethasone (dex).

5.3.7 Culture substrate and biomechanical environment

From the 45 experiments extracted from the 39 studies, 29 studies were performed in 2D of which 20 allowing for direct osteoclast-osteoblast contact and 9 only allowing for indirect contact using well inserts (**Figure 5.7A**). In addition, 16 co-cultures were performed in 3D. From these 3D co-cultures, only 3 were performed under the influence of mechanical loading using fluid flow induced by either perfusion ($N = 2$) or culture vessel rotation ($N = 1$) (**Figure 5.7B**). Materials used for the 3D co-cultures included composite (*i.e.*, a combination of a natural organic protein/synthetic polymer and inorganic material) hydrogels ($N = 3$), organic scaffolds ($N = 2$), inorganic scaffolds ($N = 3$), and composite scaffolds ($N = 6$, with $N = 3$ for the combination natural organic protein/inorganic material and $N = 3$ for the combination synthetic polymer and inorganic material). One study created a 3D construct in the absence of a scaffold material (**Figure 5.7C**).

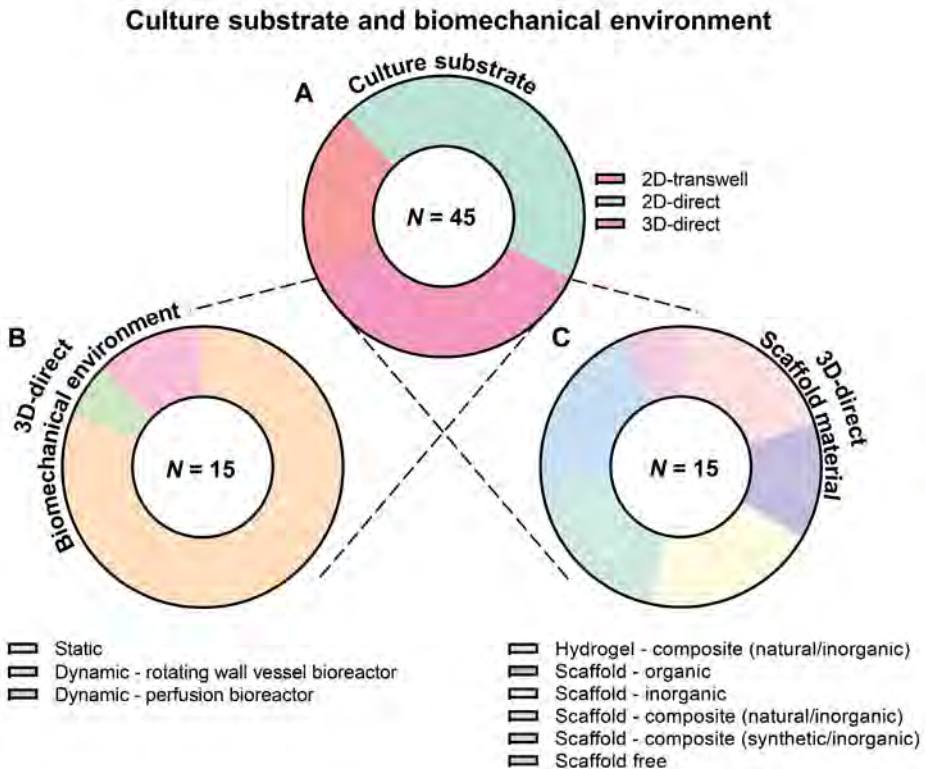


Figure 5.7. The differences in culture substrate and biomechanical environment used in the included

studies. (A) The occurrences of type of culture in terms of culture substrate (*i.e.*, 2D, 2D with trans-well or 3D). From the 3D studies, (B) the number of studies that used mechanical loading are highlighted, and (C) the different materials are presented. Abbreviations: two-dimensional (2D), three-dimensional (3D).

5.3.8 Outcome measures

Co-cultures from the 39 included studies were mostly analyzed with either direct resorption and formation outcome measures ($N = 11$) or with the surrogate markers for resorption and formation TRAP and ALP ($N = 13$), respectively (**Table 5.3**). Only one study analyzed resorption and formation directly and by the quantification of both TRAP and ALP (**Table 5.3**).

Table 5.3. The outcome measures that were used by the included studies to investigate resorption and formation.

		Primary outcome measures				
		No resorption or formation	Resorption only	Formation only	Resorption and formation	Per-row total
Secondary outcome measures	No ALP or TRAP	-	-	-	11	11
	ALP only	-	-	-	2	2
	TRAP only	-	-	4	3	7
	ALP + TRAP	13	3	2	1	19
	Per-column total	13	3	6	17	39

Each column presents which primary outcome measures were used. Each row presents which secondary outcome measures were used. Abbreviations: alkaline phosphatase (ALP), tartrate-resistant acid phosphatase (TRAP).

When identifying the methods to study resorption and formation, more than one method of analysis for resorption and/or formation was used in some studies. To study osteoclastic resorption, most studies used a resorbable surface (*e.g.*, calcium phosphate films, dentine discs, osteo assay surface) from which resorption pits could be visualized

directly using scanning electron microscopy (SEM) or with light microscopy (LM) in combination with contrast enhancing stainings (*e.g.*, Toluidine Blue or Von Kossa) (**Figure 5.8A**). Most often, resorption pits were quantified for their area and/or number. In some cases, the resorbed surface was characterized by SEM-based surface metrology (228,229). Resorption was also investigated using transmission electron microscopy (TEM) (222), non-destructive Second Harmonic Generation microscopy (SHIM) (230) or micro-computed tomography (μ CT) (228), supernatant calcium or phosphate levels to quantify mineral release, or with an ELISA for the collagen type I N-terminal telopeptide (NTx) release in the supernatant to quantify collagen degradation (**Figure 5.8A**).

The most common method to study osteoblastic formation was investigating mineralized nodule formation by staining techniques and/or imaging (**Figure 5.8B**). Alizarin Red staining could be quantified by releasing the dye from the minerals using acetic acid, followed by spectrophotometry (231). In addition, Alizarin Red or Von Kossa stainings were quantified based on LM images. Calcium was also directly quantified using Cresolphthalein complexone based assay on cultured cells. Non-destructive methods to measure formation included μ CT (228), SHIM (230), and supernatant analysis for calcium (*i.e.*, decreased supernatant calcium as a measure for matrix mineralization) (228,229), and for Collagen type I C-terminal pro-peptide (PICP), as a byproduct of collagen deposition (**Figure 5.8B**).

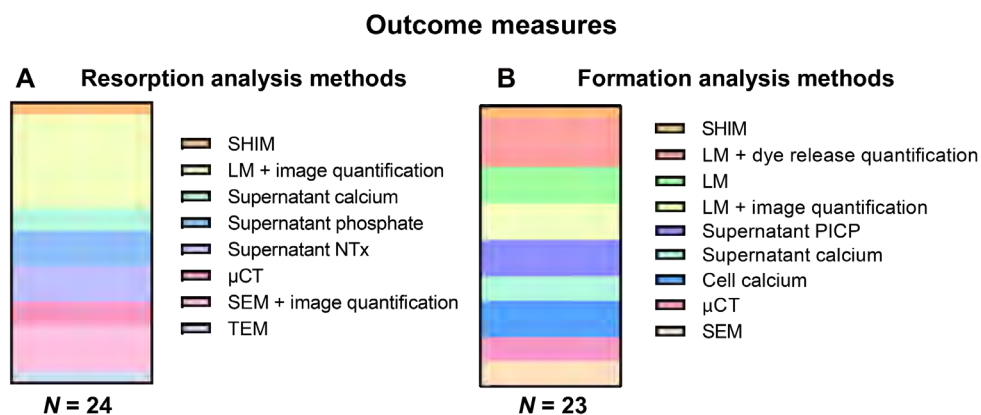


Figure 5.8. The differences in how primary outcome measures were studied in the included studies. (A) The different methods used to study resorption. (B) The different methods used to study formation. Abbreviations: Second Harmonic Generation microscopy (SHIM), light microscopy (LM), collagen type I N-terminal telopeptide (NTx), micro-computed tomography (μ CT), scanning electron microscopy (SEM), transmission electron microscopy (TEM), Collagen type I C-terminal pro-peptide (PICP).

5.4 Discussion

In recent years, many research groups have ventured into the realm of osteoclast-osteoblast co-cultures with the intent of studying both formation and resorption. Due to a lack of standardization within the field and the difficulty of finding publications based on methods instead of results, each group seems to have individually developed their own research tools, resulting in many functionally related experiments that are methodologically different. The aim of this study was to generate a systematic map of existing osteoclast-osteoblast co-culture studies that aimed at creating an *in vitro* model for bone remodeling published up to January 6, 2020, and to give an overview of their methods in a database which can be filtered, sorted, searched and expanded.

As an initial step in the bone remodeling cycle, osteoclasts get activated and resorb bone. To mimic this process *in vitro*, there is a clear preference for using human monocytes and mononuclear cells to generate osteoclasts. These have in the past two decades proven to be a reliable precursor population for osteoclasts (7), they can be obtained from human blood, and are thought to be better representatives for studying human physiology than cells of animal origin (208,209). The extraction of osteoclasts from bone is possible but cumbersome, it requires access to fresh bone material and generally does not yield relevant numbers of osteoclasts. Challenges in the pre-differentiation of osteoclasts from precursors before applied in experiments are the expected limited life span of 2 – 3 weeks (232,233), and the difficulty to handle them upon fusion of several precursors. Osteoclasts are probably therefore always differentiated from precursors within the actual experiments.

After osteoclasts have resorbed bone, osteoblasts deposit new bone matrix. To mimic this process *in vitro*, most studies have used human primary cells. The use of primary osteoblasts as well as osteoprogenitors including mesenchymal stromal/stem cells were both frequently observed, although when human cells were used, mesenchymal stromal/stem cells were more often used. The advantage of using osteoprogenitors such as mesenchymal stromal/stem cells is that these cells are capable of extensive proliferation before differentiation. Moreover, using progenitor cells allows for studying osteogenesis in addition to bone formation in co-culture, which is considered an important osteoclast-controlled event during coupling between resorption and formation *in vivo* (234). The advantage of using osteoblasts instead of osteoprogenitors, is that no differentiation is required during the experiment. As such, osteogenic differentiation factors might not be needed, and experimental conditions only affect mature osteoblasts rather than also osteogenesis. However, healthy human donor osteoblasts are scarce as there is often no need for bone surgery of which remnant materials could be used for cell isolation.

In terms of cell sources, animal cells may represent human physiology insufficiently (216), while human cells tend to cause large donor-induced variation (235). Moreover, the number of cells that can be isolated from one donor is limited and can also be donor-dependent (236). On the contrary, experiments using cell lines are often well reproducible and they allow for large-scale expansion. As such, the standardization and reproducibility of *in vitro* models could be facilitated by the use of cell lines (237). However, they sometimes only share partly the physiology of the primary cells (38). Therefore, it is recommended to use primary cells for *in vitro* bone remodeling models. If models are able to capture donor-induced variability, they could be useful for personalized medicine applications.

Both osteoclastic differentiation and resorption, and osteogenic differentiation and formation are dependent on culture conditions (238,239). For many cell-types, optimal culture conditions have been established. However, these culture conditions might not be optimal for co-cultures, where the culture conditions need to support both cell types (136). In terms of base medium, there is a clear preference for medium based on DMEM and α -MEM. Mineralization and osteogenic differentiation of osteoprogenitors have been shown to be dependent on the used base medium (240,241). In addition, osteoclastic differentiation has been shown to be dependent on the presence of ascorbic acid in α -MEM (242). Nevertheless, little attention is paid by researchers on the reasoning for their used base medium. Specific attention needs to be paid to the presence of phenol red in the base medium, which has affinity to estrogen receptors. Although the binding affinity is relatively low, the concentration in culture medium is considerably high which can lead to occupation of estrogen receptors (243,244). As estrogen deficiency is one of the major causes of osteoporosis in post-menopausal women, phenol red might influence the *in vitro* bone remodeling balance. Another variable in the medium composition is FBS (or FCS). Besides its ethical issues, it is known to have batch-to-batch and between-brand differences which can impact the results of an experiment tremendously (86,137,245,246). Alternatives like human serum (247), human platelet lysate (183), and defined serum free medium (184), are currently rapidly being explored for their use in *in vitro* models.

In terms of differentiation factors, many combinations of supplements have been registered in this map. Osteoclastic differentiation factors RANKL and M-CSF are both necessary and sufficient for osteoclastogenesis (212). However, mesenchymal stem/stromal cells and osteoblasts can produce RANKL and M-CSF themselves to trigger differentiation (211,248), and therefore the supplements are potentially not necessarily required in co-culture. They even might overrule the natural osteoblast/osteocyte-osteoclast communication that regulates bone mass *in vivo* (7).

While the presence of RANKL and M-CSF in the medium mainly affect osteoclastic differentiation, the presence of osteogenic differentiation factors seems to affect both osteoclasts and osteoblasts. Osteogenic differentiation factor β -glycerophosphate functions as a phosphate source for osteoblastic mineralization, but phosphate can also inhibit osteoclastic differentiation (249,250). Ascorbic acid is essential for collagen type I formation as the major organic protein of bone, but its effect on osteoclastic differentiation is controversially described with both positive and negative effects (242,251,252). Dexamethasone, as synthetic glucocorticoid, is required for osteogenic differentiation of mesenchymal stromal cells (253). The two used concentrations found in the systematic review represent the physiological glucocorticoid concentration of 10 nM, which is known to stimulate both osteogenesis and osteoclastogenesis (254,255). While the other found concentration (*i.e.*, 100 nM) is also known to stimulate osteogenesis, this concentration might inhibit osteoclastic differentiation (253,255). Moreover, sustained exogenous administration of glucocorticoids, for example to treat rheumatoid arthritis, can lead to glucocorticoid-induced osteoporosis *in vivo* (256). As such, when aiming at the development of a healthy bone remodeling model, the to be used dexamethasone concentration needs to be well considered. An additional factor that was often used was 1,25-dihydroxyvitamin D3. Initially, this factor was used to stimulate osteoclastic differentiation under influence of osteoblasts, which increased there RANKL secretion upon stimulation (211,212). The use of 1,25-dihydroxyvitamin D3 might therefore be of interest when the use of RANKL is not desired, like for *in vitro* bone remodeling models (7).

After selection of medium conditions, other environmental conditions need to be optimized including the culture substrate and the biomechanical environment. From all included studies, only three studies applied mechanical loading. *In vivo*, bone remodeling and adaptation is regulated by osteocytes under influence of interstitial fluid flow through the lacuno-canalicular network (114). Although its importance for remodeling *in vivo*, the influence of mechanical loading on bone remodeling *in vitro* is currently underexplored. While many co-cultures have been performed in 2D, *in vivo* bone cells reside in a 3D matrix. Besides the often different substrate stiffness, this also introduces differences in cell polarity, morphology, the cell's ability to migrate, receptor distribution, and diffusion of communication or differentiation factors (257). Besides, a biomimetic material allows for a two-way interaction (257). For example, *in vivo* resorption leads to the release of growth factors from bone which contributes to the attraction of osteoprogenitors to the resorption pit (234). However, studying remodeling in 3D requires different methods to study outcome measures. While TRAP and ALP can still be measured, studying resorption and formation, which is currently mostly done with 2D microscopy-based methods, becomes more complicated.

Registration with μ CT would allow for the detection of resorption and formation sites over time due to its non-destructive nature (258), but requires a radiopaque construct which can be created by preculture with mesenchymal stromal cells or osteoblasts to induce mineralization or an inorganic or composite scaffold (259). When using a precultured or composite collagen/mineral scaffold, supernatants can in addition be analyzed for the presence of NTx and CTx as collagen degradation markers over time (260,261). As main organic protein of the bone matrix, the formation of collagen is as important as mineralization (110). To facilitate the measurement of collagen formation over time, PICP can be measured from the supernatant (262). The use of these non-destructive analyses techniques would allow for the evaluation of temporal (263), and (when μ CT is included) spatial characteristics of *in vitro* remodeling (259), something that has previously been done separately but not within one model system.

In our effort to create a database of all *in vitro* bone remodeling models, we faced some limitations. The quality of reporting in included studies is often lacking. Missing information for reproducing the methods of the studies was identified, and only 13 out of 39 studies included in the database did not miss at least a high-level description of all indexed characteristics. While many culture variables were identified, we were not able to identify an ideal protocol. Different protocols likely work for different labs and/or research questions. Instead, the systematic map allows for searching through culture characteristics and outcome measures of all relevant osteoclast-osteoblast co-cultures. To facilitate this, the database contains the possibility to search, sort and filter through the characteristics (**Supplementary file 5.1** for instructions). This also allows researchers to use the database as a guide to design experiments.

5.5 Conclusion

With this systematic map, we have generated an overview of existing osteoclast-osteoblast co-cultures that represent *in vitro* bone remodeling models published until January 6, 2020. Their methods and predetermined outcome measures (resorption, formation, TRAP, and ALP quantification) were extracted. The constructed database allows researchers to quickly identify publications relevant to their specific question, based on the provided instructions to expand and manipulate the database. The systematic map derived from the database, underlines the variability between currently available *in vitro* remodeling models, which hampers translation between them. Nevertheless, the systematic map and its evaluation could be used as a guide to design *in vitro* bone remodeling experiments, towards improved understanding of human bone remodeling addressing the principle of reduction, refinement and replacement of animal experiments.

Author contributions

S.R., R.d.V., and S.H. contributed to the conceptualization and methodology. S.R., B.d.W., M.V. and E.S. contributed to data curation and analysis. S.R. wrote the software. S.R. and B.d.W. contributed to the preparation of the figures. S.R., B.d.W., and S.H. contributed in supervision. S.R. wrote the original manuscript. All authors contributed to manuscript revision and approved the submitted version. S.R. and S.H. acquired funding for this research.

Acknowledgement

S.R. was supported by ZonMw More Knowledge with Fewer Animals Program (MKMD), project number 114024141. S.R. and S.H. were financially supported by the European Union's Seventh Framework Program (FP/2007-2013), Grant Agreement No. 336043 (project REMOTE). B.d.W., M.V. and S.H. are financially supported by the research program TTW with project number TTW 016.Vidi.188.021, which is (partly) financed by the Netherlands Organization for Scientific Research (NWO).

Supplementary information

Supplementary file 5.1. This document provides instructions on how to operate the databases, how to add publications and expand the analyses with more elements.

Supplementary file 5.2. List of all osteoclast-osteoblast co-cultures. This list contains the initial list of 694 osteoclast-osteoblast cocultures obtained after screening, before full-text investigation and exclusion based on outcome measures.

Supplementary file 5.3. This database contains all studies in which at least one relevant outcome measure was investigated for both osteoclasts and osteoblasts. Characteristics of cells, methods and culture conditions, and descriptive statistics are listed in this database.



6

Human platelet lysate as alternative of fetal bovine serum for enhanced human *in vitro* bone resorption and remodeling

This chapter is based on:

Bregje W.M. de Wildt, Keita Ito, Sandra Hofmann

Orthopaedic Biomechanics, Department of Biomedical Engineering and Institute for Complex Molecular Systems (ICMS), Eindhoven University of Technology, Eindhoven, The Netherlands

Frontiers in Immunology, 13 (2022) 915277

Abstract

To study human physiological and pathological bone remodeling while addressing the principle of replacement, reduction and refinement of animal experiments (3Rs), human *in vitro* bone remodeling models are being developed. Despite increasing safety-, scientific-, and ethical concerns, fetal bovine serum (FBS), a nutritional medium supplement, is still routinely used in these models. To comply with the 3Rs and to improve the reproducibility of such *in vitro* models, xenogenic-free medium supplements should be investigated. Human platelet lysate (hPL) might be a good alternative as it has been shown to accelerate osteogenic differentiation of mesenchymal stromal cells (MSCs) and improve subsequent mineralization. However, for a human *in vitro* bone model, hPL should also be able to adequately support osteoclastic differentiation and subsequent bone resorption. In addition, optimizing co-culture medium conditions in mono-cultures might lead to unequal stimulation of co-cultured cells. Here, we compared supplementation with 10% FBS vs. 10%, 5%, and 2.5% hPL for osteoclast formation and resorption by human monocytes (MCs) in mono-culture and in co-culture with (osteogenically stimulated) human MSCs. Our results indicate that the supplementation of hPL can lead to a less donor-dependent and more homogeneous osteoclastic differentiation of MCs when compared to supplementation with 10% FBS. In co-cultures, osteoclastic differentiation and resorption in the 10% FBS group was almost completely inhibited by MSCs, while the supplementation with hPL still allowed for resorption, mostly at low concentrations. The addition of hPL to osteogenically stimulated MSC mono- and MC-MSC co-cultures resulted in osteogenic differentiation and bone-like matrix formation, mostly at high concentrations. Therefore, we conclude that hPL could support both osteoclastic differentiation of human MCs and osteogenic differentiation of human MSCs in mono- and in co-culture, and that this can be balanced by the hPL concentration. Thus, the use of hPL could limit the need for FBS, which is currently commonly accepted for *in vitro* bone remodeling models.

6.1 Introduction

Bone has multiple mechanical and metabolic functions that are maintained through lifelong remodeling by bone resorbing osteoclasts, bone forming osteoblasts, and regulating osteocytes. In the healthy situation, bone resorption and formation are mostly in balance, resulting in no net bone loss or gain. A shift in this balance, towards more formation or resorption, is a hallmark for pathologies like osteopetrosis or osteoporosis, respectively. Studies on these bone pathologies and development of drugs for their treatment are routinely performed in animal models. However, animal models represent human physiology insufficiently which is likely one of the reasons that only 9.6% of preclinically developed drugs are approved for regular clinical use (23,25). Human *in vitro* models could enable the investigation of human healthy and pathological bone remodeling while addressing the principle of reduction, refinement, and replacement of animal experiments (3Rs) (7,111). In this regard, osteoclast-osteoblast co-cultures have recently gained significant interest (43,259,264,265). In these co-cultures, human monocytes (MCs) and mesenchymal stromal cells (MSCs) are most frequently used as progenitor cells which are in culture differentiated into osteoclasts and osteoblasts (and eventually osteocytes), respectively (43). An advantage of using these progenitor cells is the possibility to personalize *in vitro* models (121).

Fetal bovine serum (FBS) is a culture medium supplement sourced from unborn calves at the slaughterhouse (245). FBS is currently easily available, relatively inexpensive, and it contains an excess of nutrients and proteins that support cell adhesion, growth, and proliferation. As a result, FBS is historically the most commonly used medium supplement for *in vitro* cultures, including for osteoclast-osteoblast co-cultures (43,245). However, several safety, scientific, and ethical concerns against the use of FBS have been raised (245,246). Batch to batch variation, zoonotic pathogens, and xenogeneic proteins that are incompatible with human physiology may cause undesired and irreproducible experimental results (86,245,266). In addition, with the aim to comply to the 3Rs, the use of animal components for *in vitro* alternatives to animal experiments is controversial (246). To overcome these concerns, human platelet lysate (hPL) has been suggested as a physiologically relevant alternative for FBS (246). Platelets contain a variety of proteins and nutrients that are vital for tissue regeneration (267–269), and may have an influence on healthy and pathological bone remodeling (270,271). Their cargo can be released by lysis through *e.g.*, freeze thaw cycles, sonification or platelet activation, resulting in platelet lysate.

While the use of hPL to replace FBS has been widely studied for human MSC cultures and osteogenic differentiation of these cells (272–279), the influence of hPL on osteoclastic differentiation of MCs is relatively unknown. Platelet-released supernatants

could stimulate osteoclast differentiation and activity of human peripheral blood mononuclear cells (PBMCs) (280). This stimulatory effect was reduced by the presence of serum in the platelet-released supernatant (280). Recently, one study was published on the use of human serum and hPL as alternative of FBS for bone and cancer tissue models (247). They found an increase in Cathepsin K expression in human MC mono-cultures supplemented with 5% hPL. In contrast to cultures supplemented with 10% FBS and 10% human serum, they could not detect resorptive activity when measuring calcium concentration in the supernatant (247). This indicates that platelet-released factors and hPL could support osteoclastic differentiation of human PBMC and MC mono-cultures, but contradictory results are reported. Physiological bone remodeling is controlled by the direct and indirect interactions between osteoclasts and osteoblasts, with the receptor activator of nuclear factor κ B ligand (RANKL)/osteoprotegerin (OPG) ratio as most important driver (281,282). These interactions cannot be mimicked in mono-cultures. Thereby, co-culture medium should equally support both cell types to enable this interaction and to avoid unequal cell stimulation (7,283). As such, studying the effect of hPL on MCs and MSCs and their differentiation in mono-cultures might be insufficient for the translation to *in vitro* bone remodeling models. Therefore, we investigated the use of three concentrations of hPL as a xenogeneic-free and physiologically relevant alternative for FBS on osteoclastic differentiation by MCs in mono-cultures. In addition, we explored the use of hPL for *in vitro* bone remodeling models by studying its influence on osteoclastic differentiation in MC-MSC co-cultures and osteogenically stimulated MC-MSC co-cultures (**Figure 6.1**).

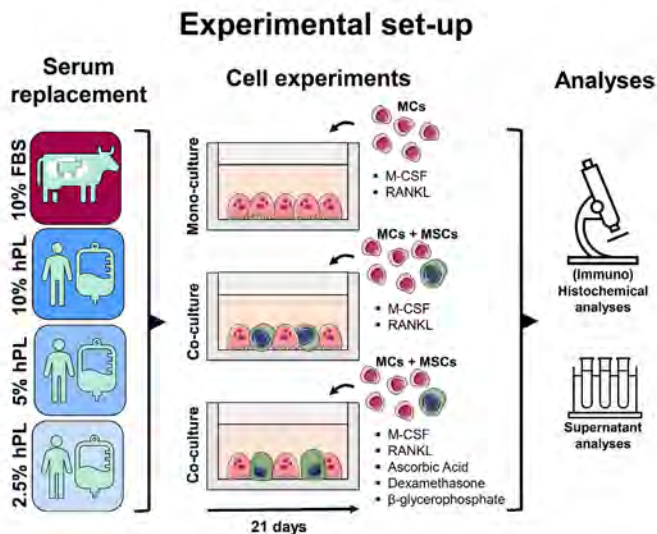


Figure 6.1. Medium supplementation with 10%, 5%, and 2.5% hPL were compared with 10% FBS for MC mono-cultures and (osteogenically stimulated) MC-MSC co-cultures. Cell cultures were analyzed using

(immuno)histochemical and (immuno)cytochemical analyses to assess resorption, cell markers and cell morphology, and supernatant analyses to measure osteoclast activity and secreted RANKL and OPG. The figure was modified from Servier Medical Art, licensed under a Creative Common Attribution 3.0 Generic License (<http://smart.servier.com/>, accessed on 8 July 2021). Abbreviations: fetal bovine serum (FBS), human platelet lysate (hPL), monocytes (MCs), mesenchymal stromal cells (MSCs), macrophage colony-stimulating factor (M-CSF), receptor activator of nuclear factor κ B ligand (RANKL), osteoprotegerin (OPG).

6.2 Materials and Methods

In this study, medium supplementation with 10%, 5%, and 2.5% hPL were compared with 10% FBS for MC mono-cultures and (osteogenically stimulated) MC-MSC co-cultures. The tested concentrations were based on previous research. FBS is most frequently used in a concentration of 10% for MC-MSC co-cultures (43). For MSC expansion and osteogenic differentiation, 10% and 5% hPL are the most frequently used concentration (276,277,279). The 2.5% hPL concentration was added based on the hPL manufacturer's advice for MC cultures. Cell cultures were analyzed using (immuno)histochemical and (immuno)cytochemical analyses to assess resorption, cell markers and cell morphology, and supernatant analyses to measure osteoclast activity and secreted RANKL and OPG.

6.2.1 Cell culture experiments

MC isolation

PBMCs were isolated from human peripheral blood buffy coats of three healthy donors (Sanquin, Eindhoven, The Netherlands; collected under their institutional guidelines and with informed consent per the Declaration of Helsinki). Buffy coats (~50 ml) were diluted with 0.6% w/v sodium citrate in phosphate buffered saline (citrate-PBS) until a final volume of 200 ml and layered per 25 ml on top of 10 ml Lymphoprep™ (07851, StemCell technologies, Köln, Germany) in 50 ml centrifugal tubes. After density gradient centrifugation (20 min at 800x *g*, lowest break), PBMCs were collected, resuspended in citrate-PBS, and washed four times in citrate-PBS supplemented with 0.01% bovine serum albumin (BSA, 10735086001, Sigma-Aldrich, Zwijndrecht, The Netherlands). PBMCs were frozen at 10⁵ cells/ml in freezing medium containing RPMI-1640 (RPMI, A10491, Thermo Fisher Scientific, Breda, The Netherlands), 20% FBS (BCBV7611, Sigma-Aldrich) and 10% dimethyl sulfoxide (DMSO, 1.02952.1000, VWR, Radnor, PA, USA) and stored in liquid nitrogen until further use. Before MC isolation, PBMCs were thawed, collected in medium containing RPMI, 10% FBS (BCBV7611, Sigma-Aldrich) and 1% penicillin-streptomycin (p/s, 15070063, Thermo Fisher Scientific), and after centrifugation resuspended in isolation buffer (0.5% w/v BSA in 2mM EDTA-PBS). MCs were enriched from PBMCs with manual magnetic

activated cell separation (MACS) using the Pan Monocyte Isolation Kit (130-096-537, Miltenyi Biotec, Leiden, The Netherlands) and LS columns (130-042-401, Miltenyi Biotec) according to the manufacturer's protocol, and directly used for experiments.

MSC isolation and expansion

MSCs were isolated from human bone marrow (1M-125, Lonza, Walkersville, MD, USA; collected under their institutional guidelines and with informed consent) and characterized for surface markers and multilineage differentiation, as previously described (124). MSCs were frozen at passage 3 with 1.25×10^6 cells/ml in freezing medium containing FBS (BCBV7611, Sigma-Aldrich) with 10% DMSO and stored in liquid nitrogen until further use. Before experiments, MSCs were thawed, collected in high glucose DMEM (hg-DMEM, 41966, Thermo Fisher Scientific), seeded at a density of 2.5×10^3 cells/cm² and expanded in medium containing hg-DMEM, 10% FBS (BCBV7611, Sigma-Aldrich), 1% Antibiotic Antimycotic (anti-anti, 15240, Thermo Fisher Scientific), 1% Non-Essential Amino Acids (11140, Thermo Fisher Scientific), and 1 ng/mL basic fibroblastic growth factor (bFGF, 100-18B, PeproTech, London, UK) at 37 °C and 5% CO₂. After 9 days, cells were detached using 0.25% trypsin-EDTA (25200, Thermo Fisher Scientific) and directly used for experiments at passage 4.

MC mono-culture

For each donor, MCs were seeded in a culture plastic 96-wells plate and an osteo assay surface 96 wells plate (CLS3988, Corning, Amsterdam, The Netherlands) at a density of 9×10^4 cells/well (3-4 repeats per donor, $N = 9-12$). MCs were cultured in priming medium containing α -MEM (41061, Thermo Fisher Scientific), 10% FBS (SFBS, Bovogen, East Keilor, Australia) or 10%, 5%, or 2.5% hPL (PE20612, PL BioScience, Aachen, Germany), 1% anti-anti, and 50 ng/ml macrophage colony-stimulating factor (M-CSF, 300-25, PeproTech). After 48 hours, priming medium was replaced by osteoclast medium (priming medium + 50 ng/ml RANKL (310-01, PeproTech) to induce osteoclastic differentiation. Cells were kept in culture for 21 days at 37 °C and 5% CO₂, medium was replaced 3x per week. Medium samples were collected and stored at -80 °C on day 2, 7, 14 and 21 and culture photographs were taken (Invitrogen EVOS XL Digital Inverted Microscope).

MC-MSC co-cultures

MCs of three donors were mixed with MSCs such that $\frac{1}{5}$ of the well area was covered by MSCs and $\frac{4}{5}$ by MCs. To accomplish this, MSCs and MCs were first mixed in the correct cell-ratio and then seeded together at a density of 2.5×10^3 MSCs and 7.2×10^4 MCs per well of a culture plastic 96-wells plate and an osteo assay surface 96 wells plate (3-4 repeats per donor, $N = 9-12$). By plating both cells in the same well, both direct

and indirect cell-communication could be studied, which cannot be mimicked with trans-well systems. For MC-MSC co-cultures, cells were initially cultured in priming medium and after 48 hours, priming medium was replaced by osteoclast medium for the remaining culture period. For osteogenic MC-MSC co-cultures, cells were initially cultured in priming medium with osteogenic supplements (10 mM β -glycerophosphate (G9422, Sigma-Aldrich), 50 μ g/ml ascorbic acid-2-phosphate (A8960, Sigma-Aldrich), and 100 nM Dexamethasone (D4902, Sigma-Aldrich)). After 48 hours, priming medium was replaced by osteoclast medium with osteogenic supplements for the remaining culture period. Cells of both co-cultures were kept in culture for 21 days at 37 °C and 5% CO₂, medium was replaced 3x per week. Medium samples were collected and stored at -80 °C on day 2, 7, 14 and 21.

Osteogenic MSC mono-culture

Osteogenic MSC mono-cultures ($N = 4$) were performed to compare the effect of FBS with hPL on osteogenic differentiation by MSCs and subsequent bone-like matrix production. The FBS and different concentrations of hPL were tested in an *in vitro* model for woven bone formation, as previously described (116). As the influence of hPL on osteogenic differentiation by MSCs has been frequently studied, we mainly focused on osteoclastic differentiation of MCs. Therefore, the details of this culture and its analyses can be found in the supplementary information.

6.2.2 Resorption assay

To measure osteoclastic resorption after 21 days of culture, cells on Osteo Assay wells plates were removed by 5 min incubation with 5% bleach in ultra-pure water (UPW) and washed twice with UPW. As co-cultured cells were difficult to remove with the described treatment, cell remnants of co-cultures were mechanically removed by carefully scraping the wells with a pipet tip. To visualize the non-resorbed surface, osteo assay wells were stained with a modified Von Kossa. Briefly, wells were incubated with 5% w/v silver nitrate (209139, Sigma-Aldrich) in UPW for 30 min in the dark, washed with UPW, and incubated for 4 min with 5% w/v sodium carbonate (S7795, Sigma-Aldrich) in 3.7% neutral buffered formaldehyde. The staining solution was completely aspirated, and plates were dried for 1 h at 50 °C. To capture the entire well, tile scans were made with a bright field microscope (Zeiss Axio Observer Z1, 5x/0.13 EC Epiplan-Neofluar objective). Tile scans were stitched with Zen Blue software (version 3.1, Zeiss, Breda, The Netherlands). To enable segmentation and resorption quantification, scratches that were introduced by mechanical cell removal in co-cultures were manually masked whereafter image contrast was increased using Fiji (125). A clipping mask was created in Illustrator (Adobe Inc., San Jose, CA, USA) to remove the edges of the wells (**Figure S6.1**). Segmentation was performed in MATLAB (version

2019b, The MathWorks Inc., Natick, MA, USA), using Otsu's method for binarization with global thresholding, where the threshold was kept constant throughout the entire image (284). The total number of pixels within the well and the number of resorbed pixels were determined, such that the percentage resorbed area per well could be quantified.

6.2.3 Fluorescent stainings

MC mono-cultures were stained with DAPI and Phalloidin to visualize cell nuclei and the actin cytoskeleton, respectively. In short, cells were fixed in 3.7% neutral buffered formaldehyde for 15 min, permeabilized in 0.5% triton X-100 in PBS for 10 min and blocked in 10% normal goat serum in PBS for 30 min. Cells were incubated with 0.1 $\mu\text{g}/\text{ml}$ DAPI (D9542, Sigma-Aldrich) and 50 pmol Atto 647-conjugated Phalloidin (65906, Sigma-Aldrich) in PBS for 1 h. Images were taken with a confocal laser scanning microscope (Leica TCS SP8X, 20x/0.4 HC PL Fluotar L objective) at 2 different locations per well with 3 – 4 wells per donor. Images were subsequently deconvolved using the CLME deconvolution algorithm with the Batch Express function of Huygens Professional (version 20.04, Scientific Volume Imaging, The Netherlands). Cell morphology and cell area were extracted from the images using a custom-made pipeline in CellProfiler (version 4.04) (285). By using the actin cytoskeleton images, cells were segmented with the Minimum Cross-Entropy method with adaptive threshold. Cell eccentricity (as measure for morphology) and cell area were subsequently determined by CellProfiler (285).

To study the influence of MSCs on osteoclastic differentiation, MC-MSC co-cultures were stained with DAPI, Phalloidin, RANKL and OPG. Cell differentiation in MC-MSC co-cultures and osteogenic MC-MSC co-cultures was visualized with a staining for DAPI, Phalloidin, integrin- $\beta 3$ as osteoclastic differentiation marker and runt-related transcription factor 2 (RUNX2) as osteoblastic differentiation marker. Briefly, one well per donor was fixed in 3.7% neutral buffered formaldehyde for 15 min, permeabilized in 0.5% triton X-100 in PBS for 10 min and blocked in 10% normal goat serum in PBS for 30 min. Primary antibodies were incubated overnight at 4 °C, secondary antibodies were incubated with 0.1 $\mu\text{g}/\text{ml}$ DAPI and 50 pmol Atto 647-conjugated Phalloidin for 1 h at room temperature. Antibodies are listed in **Table S6.1**. Images were acquired with a confocal laser scanning microscope (Leica TCS SP8X, 20x/0.65 HC PL Apo CS2 objective). All images were prepared for presentation in Fiji (127).

6.2.4 Tartrate resistant acid phosphatase activity

Tartrate resistant acid phosphatase (TRAP) as a measure for osteoclastic differentiation was measured in culture medium supernatants. 10 μl supernatant or p-nitrophenol

standard was incubated with 90 μ l p-nitrophenyl phosphate buffer (1 mg/ml p-nitrophenyl phosphate disodium hexahydrate (71768, Sigma-Aldrich), 0.1 M sodium acetate, 0.1% triton X-100 and 30 μ l/ml tartrate solution (3873, Sigma-Aldrich) in PBS) in 96-wells assay plates for 90 min at 37 °C. To stop the reaction, 100 μ l 0.3 M NaOH was added. Absorbance was read at 405 nm using a plate reader (Synergy™ HTX, Biotek) and absorbance values were converted to TRAP activity (converted p-nitrophenyl phosphate in nmol/ml/min) using standard curve absorbance values.

6.2.5 RANKL and OPG quantification

Secreted RANKL and OPG were quantified in culture medium supernatants from day 7 of MC-MSC co-cultures with RANKL (ab213841, Abcam, Cambridge, UK) and OPG (EHTNFRSF11B, Thermo Fisher Scientific) enzyme-linked immunosorbent assays (ELISAs) according to the manufacturer's protocols. To account for OPG and RANKL already present in FBS or hPL, FBS and hPL samples were included in the assays. To measure RANKL, samples were added to anti-human RANKL coated microwells. After 90 min incubation at 37 °C, samples were replaced by biotinylated antibody solution followed by 60 min incubation at 37 °C. After thorough washing, avidin-biotin-peroxidase complex (ABC) solution was added, and plates were incubated for 30 min at 37 °C. Wells were again washed and color developing agent was added followed by 15 min incubation in the dark at 37 °C. To stop the reaction, stop solution was added and absorbance was measured at 450 nm in a plate reader. To measure OPG, samples were added to anti-human OPG coated microwells and incubated for 2.5 h at room temperature with gentle shaking. Wells were subsequently washed; biotinylated antibody solution was added followed by 60 min incubation at room temperature with gentle shaking. After washing, streptavidin-HRP solution was added and incubated in the wells for 45 min with gentle shaking. Wells were subsequently washed and incubated with substrate solution for 30 min in the dark with gentle shaking. The enzymatic reaction was stopped with stop solution and absorbance was measured at 450 nm in a plate reader. All absorbance values were converted to RANKL and OPG concentrations using standard curve absorbance values.

6.2.6 Supplement characterization

Total protein measurement

To quantify total protein content in FBS and hPL, a bicinchoninic acid (BCA) assay (23225, Thermo Fisher Scientific) was performed according to the manufacturer's instructions. In short, 200 μ l BCA working reagent was added to 25 μ l sample in 96-wells assay plates, followed by 30 sec mixing on a plate shaker and 30 min incubation at 37 °C. The assay plate was then cooled to room temperature and absorbance was

measured at 562 nm on a plate reader. Absorbance values were converted to protein concentrations using standard curve absorbance values.

Alkaline phosphatase and tartrate resistant phosphatase activity

As mineralization can be directly influenced by serum alkaline phosphatase (ALP) activity (137), ALP and TRAP activity were measured in FBS and hPL. TRAP activity was measured as described in **Section 6.2.4**. ALP activity was determined by adding 20 μl of 0.75 M 2-amino-2-methyl-1-propanol (A65182, Sigma-Aldrich) to 80 μl sample in 96-wells assay plates. Subsequently, 100 μl substrate solution (10 mM p-nitrophenyl-phosphate (71768, Sigma-Aldrich) in 0.75 M 2-amino-2-methyl-1-propanol) was added and wells were incubated at room temperature for 15 minutes. To stop the reaction, 100 μl 0.2 M NaOH was added. Absorbance was measured with a plate reader at 450 nm and these values were converted to ALP activity (converted p-nitrophenyl phosphate in $\mu\text{mol/ml/min}$) using standard curve absorbance values.

Calcium measurement

Since extracellular calcium could influence osteoclast attachment and osteoclastic resorption (286), a calcium assay (Stanbio, 0150-250, Block Scientific, Bellport, NY, USA) was performed to measure calcium concentration in FBS and hPL, according to the manufacturer's instructions. Briefly, 95 μl Cresolphthalein complexone reaction mixture was added to 5 μl sample and incubated at room temperature for 1 min. Absorbance was measured at 550 nm with a plate reader and absorbance values were converted to calcium concentrations using standard curve absorbance values.

Phosphate measurement

As high extracellular phosphate levels could inhibit osteoclast differentiation (250,287), phosphate concentration in FBS and hPL was measured using a Malachite Green phosphate assay (MAK307, Sigma-Aldrich). According to the manufacturer's instructions, 80 μl of sample was mixed with 20 μl of working reagent in 96-wells assay plates. Wells were incubated for 30 min at room temperature and absorbance was subsequently measured at 620 nm using a plate reader. Absorbance values were converted to phosphate concentrations using standard curve absorbance values.

Multiplex immunoassays

To explore the protein content of hPL, a total of 21 proteins that have been reported to influence bone resorption, formation or remodeling were quantified using multiplex immunoassays at the Multiplex Core Facility (MCF) of the Laboratory for Translational Immunology of the University Medical Center Utrecht, the Netherlands. Immunoassays were developed and validated by the MCF and based on Luminex xMap technology (Luminex, Austin, TX, USA) (158). In short, hPL was incubated with MagPlex

microspheres (Luminex) for 1 h at room temperature with continuous shaking, followed by 1 h incubation with biotinylated antibodies and 10 min incubation with phycoerythrin-conjugated streptavidin in high performance ELISA buffer (HPE, Sanquin, Hamburg, Germany). Data acquisition was performed with FLEXMAP 3D equipment in combination with xPONENT software (version 4.3, Luminex), and analyzed by 5-parametric curve fitting using Bio-Plex Manager software.

6.2.7 Statistical analyses

Statistical analyses were performed, and graphs were prepared in GraphPad Prism (version 9.3.0, GraphPad, La Jolla, CA, USA) and R (version 4.1.2) (131). Data were tested for normality in distributions and equal variances using Shapiro-Wilk tests and Levene's tests, respectively. When these assumptions were met, mean \pm standard deviation are presented, and to test for differences, an independent t-test (for the comparison in phosphatase activity and protein, phosphate, and calcium concentration between FBS and hPL), one-way ANOVA (for RANKL and OPG data), or two-way ANOVA (for TRAP data) were performed followed by Tukey's post hoc tests with adjusted p-value for multiple comparisons. Other data are presented as median \pm interquartile range and were tested for differences with the non-parametric Kruskal-Wallis test with Dunn's post hoc tests with adjusted p-value for multiple comparisons. With a p-value of <0.05 differences were considered statistically significant.

6.3 Results

6.3.1 HPL outperforms FBS for osteoclast differentiation and resorption in MC mono-cultures

After 21 days culture with different concentrations of hPL and 10% FBS, decellularized and Von Kossa stained osteo-assay plates of MC mono-cultures cultured with hPL showed more resorption than MCs cultured with FBS (**Figure 6.2A-D**). Resorption under influence of hPL seemed to have a dose dependent response, with most resorption in MCs cultured with 10% hPL and least resorption when cultured with 2.5% hPL. Quantification after segmentation of these osteo-assay plates revealed a significantly different resorbed area under influence of different serum supplements and a high variation in MCs cultured with FBS ($67.7\% \pm 86.5\%$) when compared to MCs cultured with 10% and 5% hPL ($84.4\% \pm 9.50\%$ and $77.4\% \pm 16.12\%$, respectively) (**Figure 6.2E**). This high variation might indicate a donor-dependent response of osteoclastic differentiated MCs to 10% FBS. TRAP activity measurements supported the resorption results, with highest TRAP activity for cells cultured with 10% hPL which differed significantly with TRAP activity for cells cultured with 10% FBS at all time points (**Figure 6.2F**).

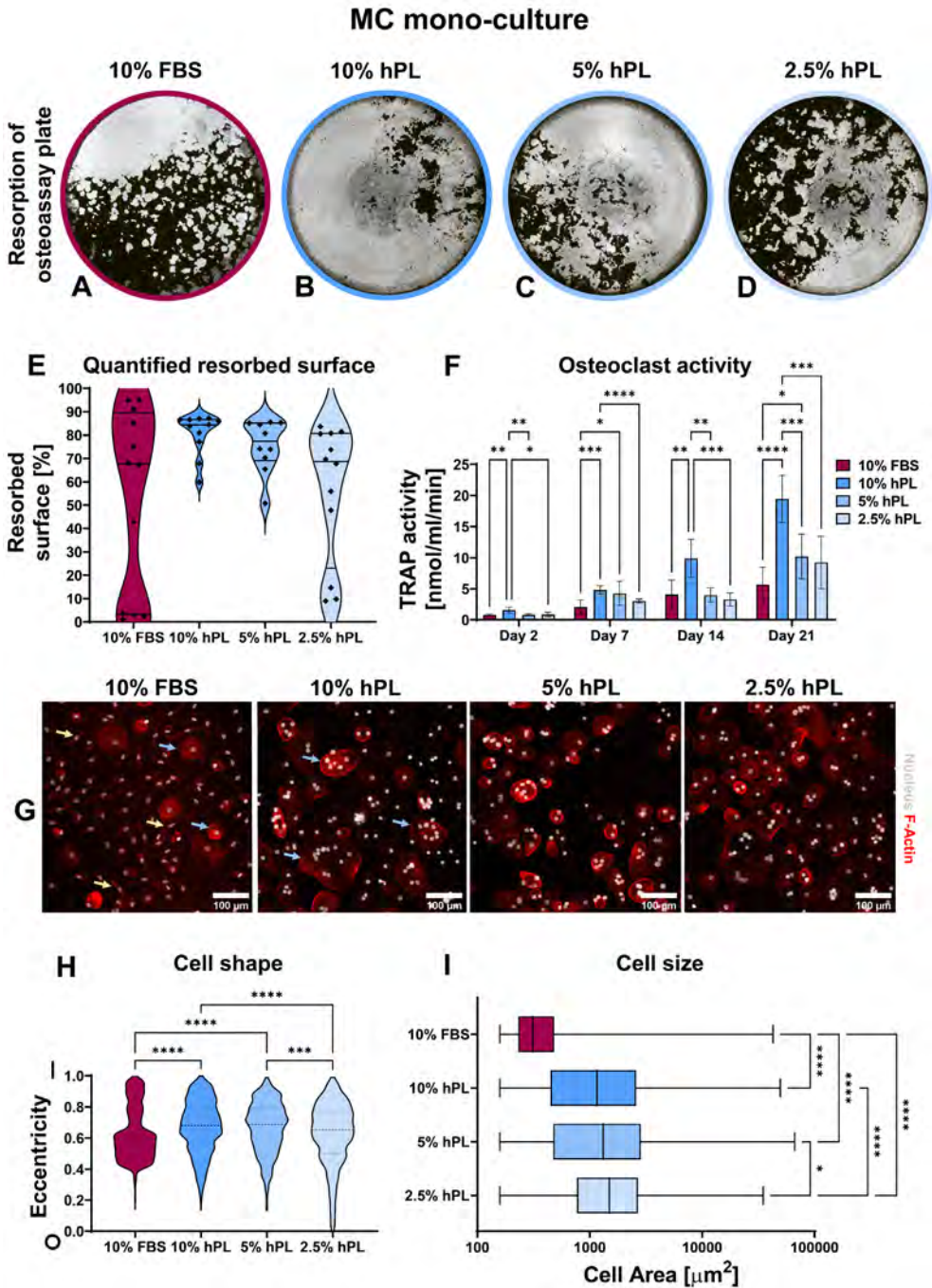


Figure 6.2. (A-D) Von Kossa stained decellularized resorption plates of MC mono-cultures. (E) Quantification of resorbed area, $p < 0.05$ (Kruskal-Wallis). (F) TRAP activity quantification, $p < 0.05$ for

culture time, culture condition and their interaction (two-way ANOVA and Tukey's post hoc tests within each time point). **(G)** Micrographs of MCs stimulated to undergo osteoclastic differentiation, stained for F-Actin (red) and the nucleus (gray). **(H)** Quantification of cell shape, 0 indicates a perfect circle while 1 indicates a line, $p < 0.05$ (Kruskal-Wallis and Dunn's post hoc tests). **(I)** Quantification of cell size, $p < 0.05$ (Kruskal-Wallis and Dunn's post hoc tests). Asterisks in figures represent results of post hoc analyses ($*p < 0.05$, $**p < 0.01$, $***p < 0.001$, $****p < 0.0001$). Abbreviations: fetal bovine serum (FBS), human platelet lysate (hPL), monocytes (MCs), tartrate resistant acid phosphatase (TRAP).

TRAP activity increased over the entire culture duration over all conditions but seemed to increase more for MCs cultured with hPL towards day 21. At day 21, TRAP activity of both 10% and 5% hPL groups was significantly higher than TRAP activity in the 10% FBS group. When looking at cell morphology, cells cultured under influence of hPL showed typical osteoclast characteristics like an actin ring and multiple nuclei (**Figure 6.2G**). In wells cultured with FBS, a more heterogeneous cell population was found, including both osteoclastic cells and spindle shaped cells (**Figure 6.2G**, blue arrows and yellow arrows, respectively). Quantification of cell shapes, expressed as eccentricity, found in all processed images revealed indeed two different cell morphologies for cells cultured with FBS: cells with an eccentricity value close to 1, having a longitudinal possibly macrophage-like morphology, and cells with an eccentricity value around 0.5, which are more rounded and possibly indicative for the osteoclast-like cells (**Figure 6.2H**). This morphology significantly differed from the cell morphology in wells that were cultured with 10% and 5% hPL, which showed a more normal distribution of cell eccentricity. Besides the difference in cell shape, cell size, which is associated with osteoclast functionality (288), was also significantly lower in cells cultured with FBS compared to cells cultured with hPL (**Figure 6.2I**). Interestingly, cells cultured with 2.5% hPL showed a significantly rounder morphology and were significantly bigger than cells cultured with 10% and 5% hPL. As osteoclasts have a lifespan of approximately 2-3 weeks (232,289), MCs that have undergone quick osteoclastic differentiation, which is potentially the case in the 10% hPL group, could have released the well surface already before fixation at day 21, possibly affecting some results. This seems likely the case judging from culture photographs of day 18 (**Figure S6.2**).

6.3.2 MSCs reverse the hPL dose-dependent resorptive activity of osteoclasts

After 21 days of MC co-culture with MSCs, again most resorption was present in groups cultured with hPL when compared to cells cultured with 10% FBS (**Figure 6.3A-D**). However, opposite to the MC mono-culture, a reversed dose-dependent relationship was found between hPL concentration and resorbed area (**Figure 6.3B-E**). While in mono-culture resorption was highest in 10% hPL, in co-culture with MSCs resorption was highest in 2.5% hPL. Quantification after segmentation of the resorbed area confirmed significantly more resorption in wells cultured with 5% and 2.5% hPL when compared to 10% FBS (**Figure 6.3E**).

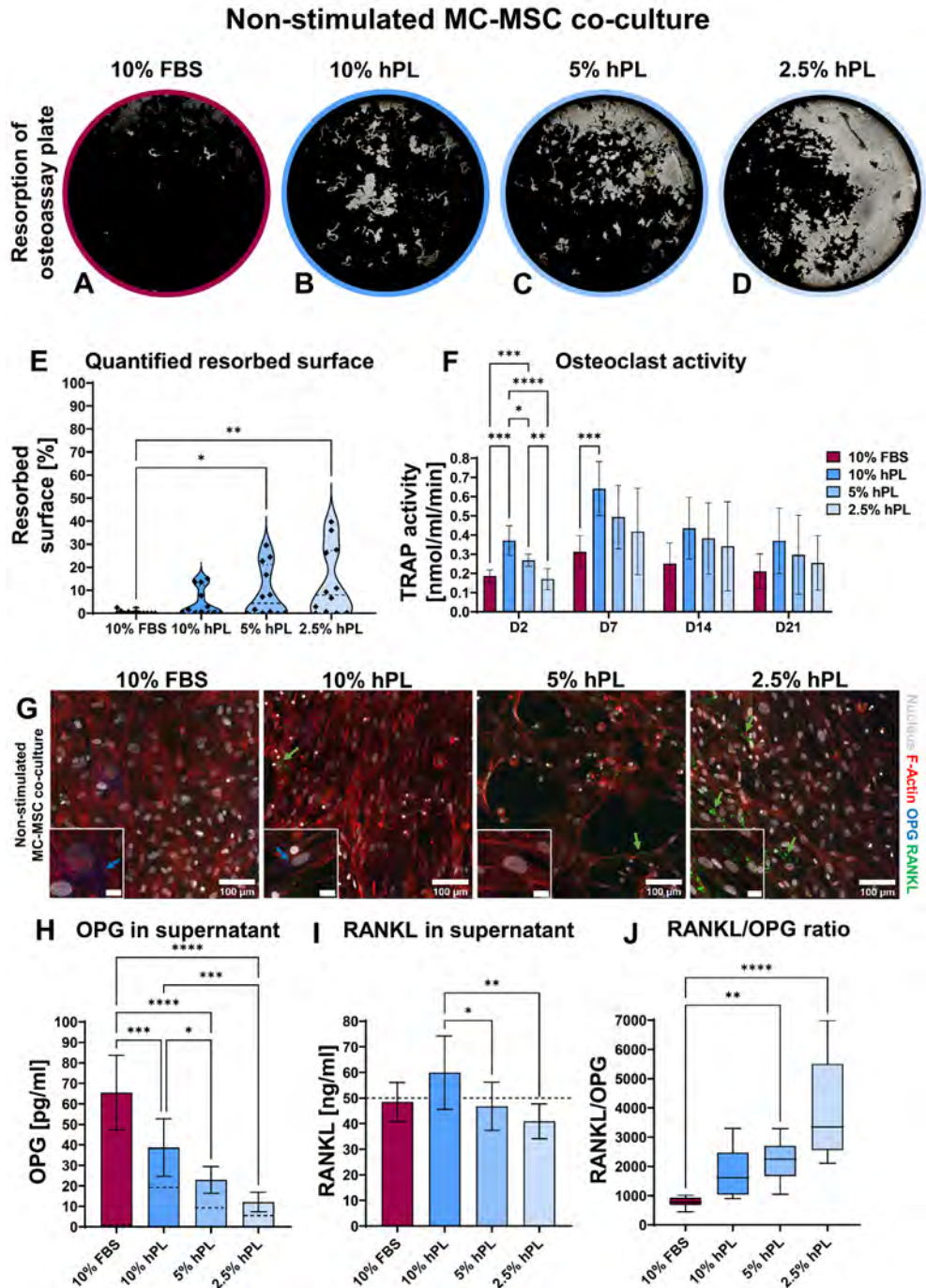


Figure 6.3. (A-D) Von Kossa stained decellularized resorption plates of MC-MSC co-cultures. (E) Quantification of resorbed area, $p < 0.05$ (Kruskal-Wallis and Dunn's post hoc tests). (F) TRAP activity

quantification, $p < 0.05$ for culture time, culture condition, no interaction effect (two-way ANOVA and Tukey's post hoc tests within each time point). **(G)** Micrographs of MC-MSC co-cultures stimulated to undergo osteoclastic differentiation, stained for F-Actin (red), the nucleus (gray), OPG (blue) and RANKL (green). Images were taken at locations rich of MSCs to detect their influence on OPG and RANKL production. Scale bar in insert is $20 \mu\text{m}$. **(H)** Quantification of OPG in supernatant, dashed lines represent concentration in the medium control, $p < 0.05$ (one-way ANOVA and Tukey's post hoc tests). **(I)** Quantification of RANKL in supernatant, dashed line represents concentration exogenous RANKL added to the medium, $p < 0.05$ (one-way ANOVA and Tukey's post hoc tests). **(J)** RANKL/OPG ratio in supernatant, $p < 0.05$ (Kruskal-Wallis and Dunn's post hoc tests). Asterisks in figures represent results of post hoc analyses (* $p < 0.05$, ** $p < 0.01$, *** $p < 0.001$, **** $p < 0.0001$). Abbreviations: fetal bovine serum (FBS), human platelet lysate (hPL), monocytes (MCs), mesenchymal stromal cells (MSCs), tartrate resistant acid phosphatase (TRAP), osteoprotegerin (OPG), receptor activator of nuclear factor κB ligand (RANKL).

In addition, while MC mono-cultures showed an increase in TRAP activity over time, in co-culture with MSCs TRAP activity initially increased but decreased again after day 7 (**Figure 6.3F**). No different TRAP activity between groups could be found on day 14 and day 21 of culture. This indicates an inhibitory effect of MSCs on osteoclastic differentiation of MCs. As MSCs could influence osteoclastic differentiation by the RANKL/OPG ratio (281), these factors were visualized in the cell cultures and quantified in culture supernatants. Immunocytochemical staining revealed some MSCs expressing OPG in wells cultured with FBS and 10% hPL (**Figure 6.3G**). In contrast, RANKL was mostly present on the cell surface of MSCs cultured with 2.5% hPL (**Figure 6.3G**). Quantification of OPG in the medium on day 7 showed the same trend, with significantly more OPG production in wells cultured with FBS than in wells cultured with hPL at any of the concentrations (**Figure 6.3H**). Of importance, as OPG could not be measured in FBS, all OPG measured in the culture medium supernatant is a result of OPG production by the cells, while for hPL, some OPG measured could already be explained by the OPG concentration measured in hPL (**Figure 6.3H**, dashed lines in bars). The RANKL concentration that was measured in the culture medium supernatant could mainly be explained by the used concentration in the cell culture medium (50 ng/ml) (**Figure 6.3I**). Only in wells cultured with 10% hPL additional RANKL seemed to be produced by the cells, which resulted in a significantly higher RANKL concentration than in wells cultured with 5% or 2.5% hPL. Overall, the RANKL/OPG ratio measured in culture medium supernatants was highest in wells cultured with 2.5% hPL (**Figure 6.3J**), which makes this concentration probably the most potent inducer of osteoclastic differentiation in co-culture with MSCs.

6.3.3 Osteogenic stimulation of MSCs impedes osteoclast motility independent from hPL dose

When stimulating MC-MSC co-cultures with osteogenic factors added to the medium, 10% FBS again seemed to induce the least resorption (**Figure 6.4A-D**). Quantification after segmentation of the resorbed area revealed indeed least resorption in wells cultured with FBS, although not statistically significant (**Figure 6.4E**). Resorption in groups cultured with hPL also seemed limited and the resorbed area featured a different shape from wells cultured without osteogenic supplements (**Figure 6.4G**). Osteoclasts in non-stimulated MC-MSC co-cultures formed resorption trenches in the osteo assay surface, whereas osteoclasts in osteogenically stimulated MC-MSC co-cultures formed resorption pits (290). Similar to the MC-MSC co-cultures, osteogenically stimulated MC-MSC co-cultures showed an initial increase in TRAP activity, followed by a decrease after day 7 (**Figure 6.4F**). After 21 days of culture, no differences in TRAP activity were found between the different concentrations of hPL. It is expected that OPG and RANKL also played a role in the inhibition of osteoclastic differentiation in osteogenically stimulated MC-MSC co-cultures, although no clear differences between groups were found after immunocytochemical staining of OPG and RANKL (**Figure S6.3**). Osteogenically stimulated MSC mono-cultures indeed showed a similar trend as in MC-MSC co-cultures, with highest OPG concentration in cells cultured with 10% FBS (69.9 ± 4.07 pg/ml) and lowest in cells cultured with 2.5% hPL (23.5 ± 3.81 pg/ml) (**Figure S6.4**). Secreted RANKL could only be detected in osteogenically stimulated MSCs cultured with 10% hPL (**Figure S6.4**). To investigate the influence of osteogenic stimulation on MC and MSC differentiation, cells were stained for differentiation markers RUNX2 (osteogenic transcription factor (128)) and Integrin- $\beta 3$ (mature osteoclast marker (291)). Osteogenic differentiation was confirmed by the presence of nuclear RUNX2 in all groups cultured with osteogenic supplements (**Figure 6.4I**). MSCs cultured with 10% FBS and osteogenic supplements showed most clear nuclear RUNX2 expression (**Figure 6.4I**). FBS seems to be superior to hPL for osteogenic differentiation, as confirmed by the abundant presence of collagen, nuclear RUNX2, osteopontin, ALP and mineralization in osteogenically stimulated MSC mono-cultures (**Figure S6.4**). Surprisingly, also non-stimulated MSCs in MC-MSC co-cultures expressed nuclear RUNX2, with most clear presence in nuclei of cells cultured with hPL (**Figure 6.4H**). RUNX2 was also observed in the cytoplasm of MCs and osteoclasts, which has recently been discovered and suggested to promote osteoclastic differentiation (292). A clear difference between osteogenically stimulated and non-stimulated co-cultures was found for the Integrin- $\beta 3$ staining. Integrin- $\beta 3$ was mainly present in osteoclasts cultured with osteogenically stimulated MSCs (**Figure 6.4I**).

Non-stimulated and osteogenically stimulated MC-MSC co-culture

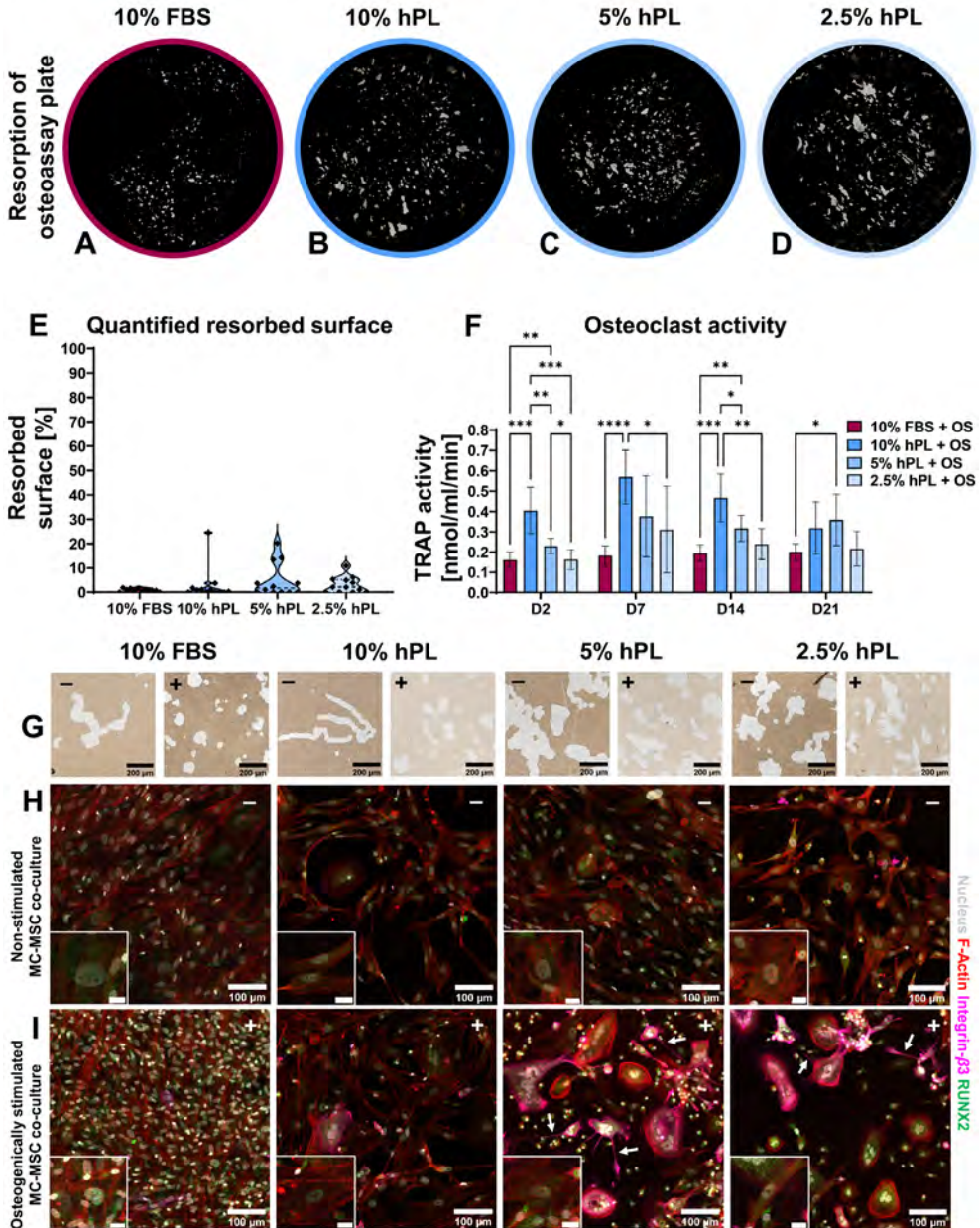


Figure 6.4. (A-D) Von Kossa stained decellularized resorption plates of osteogenically stimulated MC-MSC co-cultures. (E) Quantification of resorbed area, $p=ns$ (Kruskal-Wallis test). (F) TRAP activity quantification, $p<0.05$ for culture time, culture condition and their interaction (two-way ANOVA and

Tukey's post hoc tests within each time point). **(G)** Micrographs of osteo assay plates indicating resorption trenches and resorption pits of non-stimulated co-cultures (-) and osteogenically stimulated co-cultures (+). **(H)** Micrographs of non-stimulated MC-MSC co-cultures, and **(I)** osteogenically stimulated MC-MSC co-cultures, stained for F-Actin (red) the nucleus (gray), Integrin- β 3 (pink) and RUNX2 (green). Scale bar in insert is 20 μ m. Asterisks in figures represent results of post hoc analyses (* p <0.05, ** p <0.01, *** p <0.001, **** p <0.0001). Abbreviations: fetal bovine serum (FBS), human platelet lysate (hPL), monocytes (MCs), mesenchymal stromal cells (MSCs), tartrate resistant acid phosphatase (TRAP), osteogenic supplements (OS), runt-related transcription factor 2 (RUNX2).

These integrin- β 3 positive cells also showed cell processes that were not observed in MC mono-cultures or non-stimulated MC-MSC co-cultures (**Figure 6.4I**, white arrows).

6.3.4 Supplement characterization

To explore the differences between cells cultured with FBS or hPL found in this study, we attempted to characterize some components of the hPL used. For hPL, a higher protein concentration (45.4 mg/ml) was measured compared to FBS (36.7 mg/ml) (**Figure 6.5A**). Interestingly, quantification of ALP as mineralization related phosphatase, and TRAP as resorption related phosphatase, revealed a clear difference between FBS and hPL (**Figure 6.5B**). Whereas a significantly higher ALP activity was measured in FBS than in hPL, TRAP activity was significantly higher in hPL. With Luminex, the concentration of 21 proteins that have been reported to influence bone remodeling, were quantified (**Figure 6.5E**) and compared to effective concentrations used for *in vitro* studies related to bone remodeling (**Table S6.2**). As a result, relative high concentrations of pro-inflammatory cytokines were measured (interleukin (IL) 1- α : 284 pg/ml, IL1- β : 208 pg/ml, IL6: 624 pg/ml, IL17: 370 pg/ml and tumor necrosis factor- α (TNF- α): 237 pg/ml), when compared to the concentration of anti-inflammatory cytokines (IL4: 32.7 pg/ml and IL10: 197 pg/ml) (**Figure 6.5E**). Based on *in vitro* studies from literature, most of these factors could only have had an effect on osteoclast differentiation and resorption at higher concentrations (**Table S6.2**). Only the IL17 concentration measured in hPL was within the range of reported effective *in vitro* concentrations on osteoclast for the 10% and 5% hPL groups. In addition, the important proteins for osteoclast adhesion, osteopontin and fibronectin, were detected in hPL (2.15 ng/ml and 3.21 μ g/ml, respectively). As expected, hPL also contained growth factors typical for platelets which might have affected osteoclastic differentiation and resorption (epidermal growth factor (EGF): 1.62 ng/ml, basic fibroblastic growth factor (bFGF): 812 pg/ml, vascular endothelial growth factor (VEGF): 869 pg/ml and platelet derived growth factor-BB (PDGF-BB): 8.16 ng/ml). One discrepancy was found in our data. The OPG concentration in hPL was measured with Luminex and ELISA, but Luminex gave a much higher concentration (193 pg/ml

for ELISA compared to 1.69 ng/ml for Luminex). Quantification of calcium concentrations revealed a higher calcium concentration for hPL (15.5 $\mu\text{mol/ml}$) than for FBS (2.11 $\mu\text{mol/ml}$), which is for 10% hPL comparable to the for osteoclastogenesis most optimal calcium concentration found in literature (10% hPL: $\sim 1.55 \mu\text{mol/ml}$, most effective concentration in literature: 1.2 $\mu\text{mol/ml}$ (290)) (Figure 6.5C). For phosphate, a higher concentration was found in FBS (3.34 $\mu\text{mol/ml}$) when compared to hPL (1.95 $\mu\text{mol/ml}$) (Figure 6.5D). However, for both medium supplements this was below the range of effective concentrations found in literature (Table S6.2).

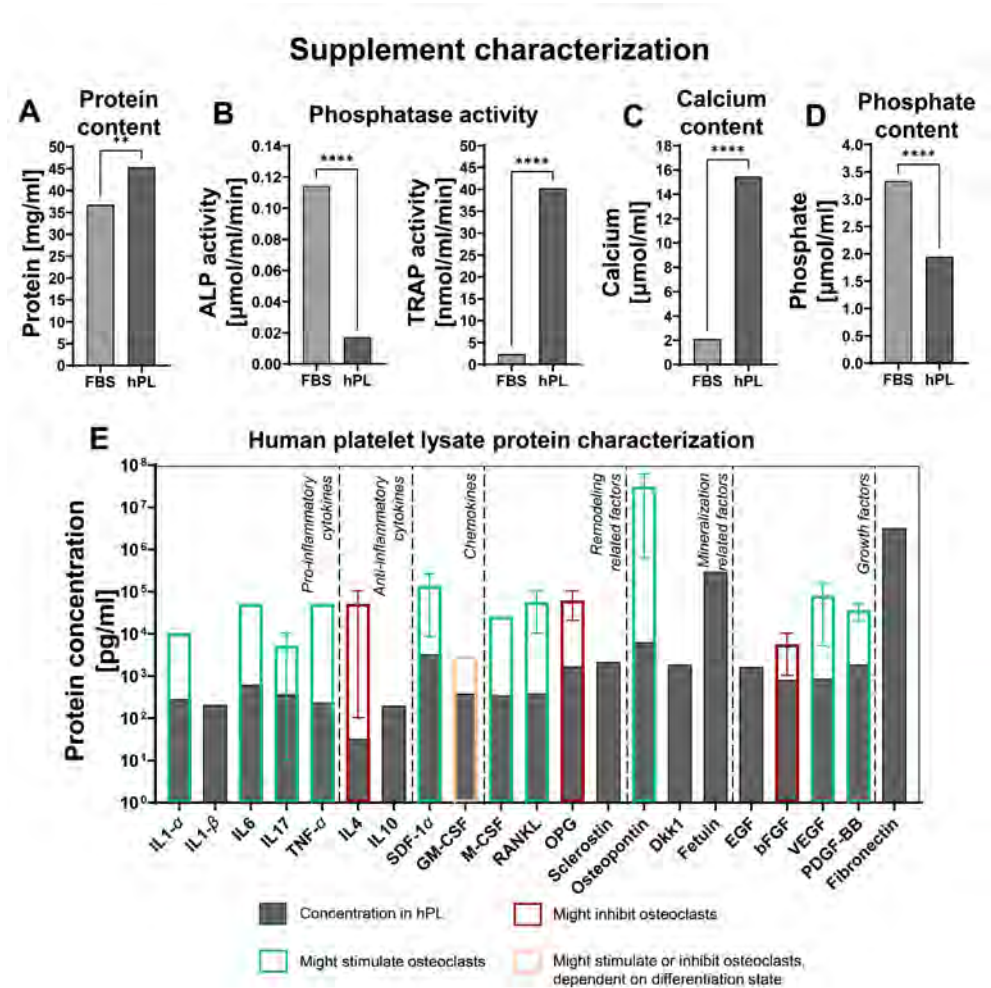


Figure 6.5. (A) Protein concentration in FBS and hPL, $p < 0.05$ (independent t-test). (B) Phosphatase activity (ALP and TRAP) in FBS and hPL, $p < 0.05$ (independent t-test). (C) Calcium concentration in FBS and hPL, $p < 0.05$ (independent t-test). (D) Phosphate concentration in FBS and hPL, $p < 0.05$ (independent t-test). Asterisks indicate significant differences (** $p < 0.01$, **** $p < 0.0001$). (E) Quantification of bone and

bone-remodeling related factors in hPL. Transparent bars indicate the mean effective concentration found by *in vitro* experiments from literature, error bars represent minimal and maximal reported effective concentration, border color represents the direction of the found effect. Abbreviations: fetal bovine serum (FBS), human platelet lysate (hPL), alkaline phosphate (ALP), tartrate resistant acid phosphatase (TRAP), interleukin (IL), tumor necrosis factor (TNF), stromal derived factor (SDF), granulocyte-macrophage colony-stimulating factor (GM-CSF), macrophage colony-stimulating factor (M-CSF), receptor activator of nuclear factor κ B ligand (RANKL), osteoprotegerin (OPG), Dickkopf WNT Signaling Pathway Inhibitor 1 (Dkk-1), epidermal growth factor (EGF), basic fibroblastic growth factor (bFGF), vascular endothelial growth factor (VEGF), platelet derived growth factor-BB (PDGF-BB).

6.4 Discussion

Although alternatives are available, FBS is still the most commonly used culture medium supplement. However, its use is increasingly considered controversial due to several safety, scientific and ethical concerns (245,246). Also, for osteoclast-osteoblast co-cultures with human MCs and MSCs as progenitors, aiming at mimicking human bone remodeling and related pathologies *in vitro*, FBS is still the common standard (43). hPL has been suggested as alternative for FBS and is already frequently studied for MSC propagation and osteogenic differentiation of these cells (272–279). In contrast, the effect of hPL on osteoclastic differentiation of MCs is relatively unknown. Therefore, the aim of this study was to investigate the influence of hPL as culture medium supplement at concentrations of 10%, 5% and 2.5% on osteoclastic differentiation and resorption of human MCs, using 10% FBS as a control. In addition, as physiological bone resorption is partly regulated by cells of the MSC-osteoblast-osteocyte lineage with the RANKL/OPG ratio, the influence of hPL at different concentrations on osteoclastic differentiation and resorption was also investigated under influence of (osteogenically stimulated) MSCs.

We initially studied the potential of hPL to support osteoclastic differentiation in MC mono-cultures. As a result, osteoclastic differentiation and formation could be enhanced when using hPL instead of FBS. Whereas hPL induced MCs to undergo homogeneous osteoclastic differentiation followed by resorption consistent for all donors and hPL concentrations, MCs' response to FBS seemed less reproducible. More specifically, FBS induced a heterogeneous cell population and differences in resorptive activity between different donors. The differences in resorptive activity between different donors was not reflected in the variation in TRAP activity measured in the culture medium supernatant, as observed before (293). The spindle shaped cells in MC mono-cultures supplemented with 10% FBS could indicate differentiation towards macrophages, a phenomenon that has been reported previously for MCs cultured in FBS and stimulated to undergo osteoclastic differentiation (247). Human MCs can polarize into macrophage phenotypes including the more pro-inflammatory M1 and the

more anabolic M2 macrophages with both different roles in tissue regeneration and remodeling (294). Villasante et al. (2021) found more elongated cells in MCs treated with FBS when compared to MCs treated with human serum and hPL (247). These elongated cells were characterized as M2 macrophages based on their shape and gene expression profile (247,295). Human serum induced M1 polarization which could have enabled further differentiation towards osteoclasts (247,296). As platelets are activated upon tissue damage likely stimulating M1 polarization, hPL might have positively influenced osteoclast formation by precursor differentiation (296). In co-culture with MSCs, hPL indeed induced M1 polarization in MC derived macrophages (283). This hypothesis would need further characterization of cell markers and secretory profiles at multiple time points during culture. Although this is a limitation of the current study, future studies would benefit from including analyses on macrophage polarization in addition to analyses on osteoclast differentiation. Furthermore, it is recommended that future studies aim to elucidate the molecular mechanisms involved in the osteoclastic differentiation process under influence of hPL, using for example gene expression analyses.

Next, the influence of 10%, 5%, and 2.5% hPL and 10% FBS on osteoclastic differentiation and resorption in co-culture with MSCs and osteogenically stimulated MSCs was investigated. MCs/osteoclasts and MSCs/osteoblasts both have their preferred medium that supports their growth and function but that could inhibit the co-cultured cells in osteoclast-osteoblast co-cultures (7,43). As such, supporting only osteoclasts could lead to imbalanced or pathological remodeling as for example in osteoporosis (259). Therefore, culture medium for “physiological” or “healthy” *in vitro* bone remodeling models should be carefully developed and tested such that it supports the balanced function of both osteoclasts and osteoblasts (43). The reversed dose-dependent effect that was found in MCs co-cultured with non-stimulated MSCs, when compared to MC mono-cultures, underlines the importance of developing co-culture medium using co-cultures. While hPL again outperformed 10% FBS for osteoclast differentiation and resorption, 2.5% hPL induced most resorption in MC-MSC co-cultures. The secreted RANKL/OPG ratio, as a major predictor for osteoclastogenesis, was indeed highest in cells cultured with 2.5% hPL and lowest in cells cultured with 10% FBS. FBS seemed to inhibit osteoclastic differentiation and resorption almost completely in MC-MSC co-cultures. Recently Tylek et al. (2019) found a shift towards MSCs being the most prominent cell type in macrophage-MSC co-cultures under influence of FBS supplementation, while hPL equally supported both cell-types in terms of attachment and proliferation (283). As mainly MSCs were observed in (osteogenically stimulated) MC-MSC co-cultures, FBS might have supported mainly MSCs. In line with this observation, FBS also seemed to induce best the osteogenic differentiation of MSCs

as detected by most prominent nuclear RUNX2 in osteogenically stimulated MC-MSC co-cultures. MSC mono-cultures supported this finding with highest ALP activity, most mineralization, and most prominent collagen formation when constructs were cultured with 10% FBS. In these mono-cultures, OPG measurements followed the same trend as ALP activity, mineralization and collagen formation observations. This is in line with the hypothesis that during the bone formation phase of the remodeling cycle, osteoclastic resorption is inhibited by osteoblasts through the RANKL/OPG ratio as resorption is not desired anymore (7). Taken together, 10% FBS seemed to unequally support MCs and MSCs when co-cultured. More specifically, FBS induced the most prominent effect on MSCs and their osteogenic differentiation while hPL supported both osteogenic and osteoclastic differentiation. As we only studied osteogenic differentiation in MC-MSC co-cultures by localizing RUNX2 expression, future studies could further elucidate the influence of FBS and hPL on osteogenic differentiation in MC-MSC co-cultures as *in vitro* remodeling models.

Interestingly, osteogenic stimulation of MC-MSC co-cultures induced differences in resorption patterns on osteo assay surfaces when compared to non-stimulated MC-MSC co-cultures. Instead of resorption trenches, osteogenic stimulation led to the formation of resorption pits. This phenomenon was observed in both FBS and hPL treated groups, indicating an effect of the osteogenic supplements. The difference in resorption trenches and pits has been described as a result of insufficient collagen degradation by cathepsin K, impeding osteoclasts' motility which results in a pit instead of a trench (290). The formation of these trenches has been described for remodeling pathologies like osteoporosis and might thus be undesirable for "healthy" *in vitro* bone remodeling models (290). It is unclear whether the pits found in this study are a result of collagen production by osteogenically differentiated MSCs, or a difference in cathepsin K production by osteoclasts in the different co-cultures. While this is a limitation of the current study, it would be interesting for future research to evaluate cathepsin K production and collagen formation and degradation markers like c-propeptide of type I procollagen (PICP) and c-terminal telopeptide of type-I collagen (CTX), respectively (43). In these osteogenically stimulated co-cultures, integrin- β 3 and extended cell processes were also observed which could not be detected in non-stimulated co-cultures. Inhibition of the mature osteoclast marker integrin- β 3 has been observed to limit osteoclast migration (297). The observed cell extensions were previously described as a result of osteoclast fission or incomplete cytokinesis, processes that are believed to regulate osteoclastic resorption (298–300). Osteoclast fission has also been described *in vivo* and is suggested to improve osteoclast migration (300). Therefore, we suggest that based on pit shape, integrin- β 3 expression and the presence of cell extensions, osteoclasts in osteogenically stimulated MC-MSC co-cultures

featured a different but more “physiologically relevant” osteoclast phenotype than in non-stimulated co-cultures.

Major issues in the development of *in vitro* models are the difficulty to reproduce these models and to translate results from *in vitro* to *in vivo*. The use of different bovine-derived sera contributes to these issues, because of its xenogeneic origin and its variability between different batches and sources (86,245,301). While the replacement of FBS by hPL could improve the biomimicry with physiological bone remodeling, reproducibility issues might still remain unsolved. Characterization and standardization in the preparation of hPL could improve these reproducibility issues (246). Efforts for this standardization and characterization have already been initiated (273,302,303). In this study, we therefore used a commercial hPL obtained from >300 donor units whereas a hPL preparation from 200 donor units seems already sufficient for standardization (273). However, like for FBS, batch to batch variability may still exist and this limitation should be taken into consideration when interpreting the results of this study. To support the characterization of bioactive factors in hPL, we aimed at quantifying a panel of bone- and bone remodeling-related factors in hPL. Of importance, these factors were measured in the pure supplements, their concentration on the cells is dependent on the used concentration of the supplement in the culture medium. We compared the concentrations of the measured factors with the effective concentrations in *in vitro* studies, taking the dilution in the culture medium into account. Although it is expected that the combination of the different hPL components exert the found effects, some factor concentrations stood out. For example, our hPL contained relatively high levels of growth factors like PDGF-BB, bFGF, EGF and VEGF, which likely exceed the growth factor concentrations in FBS (275). However, these growth factors were all below the effective levels derived from *in vitro* studies. Only calcium and IL17 were in the effective range for 10% hPL and 5% hPL, respectively. The relatively high calcium concentration in 10% hPL could improve proteolytic activity in osteoclasts, while a low concentration improves attachment and migration (286). In addition, the IL17 concentrations in 10% and 5% hPL have previously directly induced osteoclastic differentiation of human buffy coat derived monocytes in the absence of osteoblasts (304). To proof whether such factors have had significant effects in this study, inhibition or removal of these factor would need to be performed which was outside the scope of this research. Besides, synergistic effects of factors might also be possible (305). Of note, due to the presence of fibrinogen in hPL, coagulation is often prevented by the addition of heparin. However, heparin supplementation could induce the secretion of inflammatory cytokines in macrophages (283). In addition, heparin has a high affinity to OPG, meaning that it could influence the physiological MSC-osteoblast-osteocyte regulated inhibition of osteoclasts (306). For these reasons, using heparin as anti-

coagulant for hPL should always be limited or avoided for MC-MSC co-cultures. Other methods to prevent coagulation, such as mechanical fibrinogen-depletion, could prevent the need for heparin supplementation (307). Although for this study fibrinogen-depleted hPL was used, potential remnants of heparin also might have caused the discrepancy between the OPG concentrations measured with Luminex and ELISA, as heparin could induce coagulation of OPG microspheres in Luminex (158).

6.5 Conclusion

With this study, we demonstrated that FBS can be replaced by hPL for osteoclastic differentiation of human MCs. A hPL concentration of 2.5% is already sufficient for homogeneous osteoclastic differentiation, but resorption can be enhanced by increasing the concentration to 5% or 10%. In contrast to FBS, hPL could support both osteoclastic and osteogenic differentiation. The addition of 10% hPL to co-cultures will likely lead to a balance towards formation, while 2.5% will shift the balance towards resorption. Thus, a concentration of 5% hPL is recommended. These findings indicate hPL's potential for *in vitro* bone remodeling models. The use of hPL could therefore limit the need for FBS, which is currently the common standard for these models. Accordingly, this study directly contributes to the reduction, refinement and replacement of animal experiments.

Author contributions

B.d.W., K.I. and S.H. contributed to conception, methodology and design of the study. B.d.W. performed and analyzed the experiments. B.d.W. wrote the original draft of the manuscript and prepared the figures. All authors contributed to manuscript revision and approved the submitted version. K.I. and S.H. contributed in the supervision. S.H. acquired funding for this research.

Acknowledgement

We thank Stefan Remmers and Freek van der Heijden for their assistance in the resorption assay analysis. We thank the Multiplex Core Facility of the Laboratory for Translational Immunology of the University Medical Center Utrecht, the Netherlands, for the hPL characterization with Luminex. This work is part of the research program TTW with project number TTW 016.Vidi.188.021, which is (partly) financed by the Netherlands Organization for Scientific Research (NWO).

Supplementary information

Supplementary materials and methods

We investigated the influence of FBS and hPL on osteogenic differentiation and bone-like matrix production in a three-dimensional (3D) MSC mono-culture. The materials and methods used for this part of the study are described below. The results on this part of the study can be found in **Figure S6.4**.

Scaffold fabrication

Bombyx mori L. silkworm cocoons were degummed by boiling them in 0.2 M Na₂CO₃ for 1 h. After drying, silk was dissolved in 9 M LiBr, filtered, and dialyzed against ultra-pure water (UPW) for 36 h using SnakeSkin Dialysis Tubing (11532541, Thermo Fisher Scientific, Breda, The Netherlands). The dialyzed silk fibroin solution was frozen at -80° C and lyophilized for 7 days. Lyophilized silk fibroin was dissolved in hexafluoro-2-propanol at a concentration of 17% (w/v) and casted in scaffold molds containing NaCl granules with a size of 250-300 μm as template for the pores. Molds were covered to improve the silk fibroin blending with the granules. After 3 h, covers were removed from molds, and hexafluoro-2-propanol was allowed to evaporate for 7 days whereafter β-sheets were induced by submerging silk fibroin-salt blocks in 90% MeOH for 30 min. NaCl was dissolved from the scaffolds in ultra-pure water, resulting in porous sponges. These sponges were cut into scaffolds of 3 mm in height and 5 mm in diameter. Scaffolds were sterilized by autoclavation in PBS at 121° C for 20 min.

Cell culture experiments

MSCs were isolated from human bone marrow (Lonza, Walkersville, MD, USA), characterized, stored, and expanded until passage 4 as described in **Section 6.2.1**. Cells were seeded at a density of 10⁶ cells per scaffold (*N* = 4 scaffolds per condition) and seeding was performed dynamically for 6 hours in 50 ml tubes on an orbital shaker at 150 RPM in expansion medium (125). The cell-loaded scaffolds were cultured for 4 weeks at 37 °C and 5% CO₂ in custom-made spinner flask bioreactors and a rotational speed of 300 RPM. MSCs were stimulated to undergo osteogenic differentiation with osteogenic medium containing lg-DMEM (22320, Thermo Fisher Scientific), 10% FBS (SFBS, Bovogen, East Keilor, Australia) or 10%, 5%, or 2.5% human platelet lysate (hPL, PE20612, PL BioScience, Aachen, Germany), 1% anti-anti, 10 mM β-glycerophosphate (G9422, Sigma-Aldrich), 50 μg/ml ascorbic acid-2-phosphate (A8960, Sigma Aldrich), and 100 nM Dexamethasone (D4902, Sigma-Aldrich)). Medium was refreshed 3 times per week and samples were collected and stored at -80 °C on day 7.

Micro-computed tomography (μ CT)

Bioreactors were scanned and analyzed with a μ CT100 imaging system (Scanco Medical, Brüttisellen, Switzerland) after 4 weeks of culture. Scanning was performed at an isotropic nominal resolution of 17.2 μ m, energy level of 45 kVp, intensity of 200 μ A, integration time of 300 ms and with twofold frame averaging. To reduce part of the noise, a constrained Gaussian filter was applied with filter support 1 and filter width sigma 0.8 voxel. Filtered images were segmented to detect mineralization at a global threshold of 24% of the maximum grayscale value. Unconnected objects smaller than 30 voxels were removed through component labeling.

(Immuno)histochemistry

Scaffolds ($N = 2$) were soaked for 15 minutes in each 5% (w/v) sucrose and 35% (w/v) sucrose in phosphate buffered saline (PBS). Samples were embedded in Tissue Tek® (Sakura, Alphen aan den Rijn, The Netherlands) and quickly frozen with liquid N₂. Cryosections were sliced with a thickness of 5 μ m. Upon staining, sections were fixed for 10 minutes in 3.7% neutral buffered formaldehyde and washed twice with PBS.

To visualize collagen deposition, sections were stained with Picrosirius Red. Sections were soaked in Weigert's Iron Hematoxylin (HT1079, Sigma-Aldrich) solution for 10 minutes, washed in running tap water for 10 minutes, and stained in 1% w/v Sirius Red (36,554-8, Sigma-Aldrich) in picric acid solution (36011, Sigma-Aldrich) for one hour. Subsequently, sections were washed in two changes of 0.5% acetic acid and dehydrated in one change of 70% and 96% EtOH, three changes of 100% EtOH, and two changes of xylene. Sections were mounted with Entellan (107961 Sigma-Aldrich) and imaged with a bright field microscope (Zeiss Axio Observer Z1, 20x/0.8 Plan-Apochromat objective).

To study osteogenic differentiation, sections were stained with DAPI, CNA35, osteopontin and RUNX2. Briefly, sections were permeabilized in 0.5% triton X-100 in PBS for 5 min and blocked in 10% normal goat serum in PBS for 30 min. Primary antibodies were incubated overnight at 4 °C, secondary antibodies were incubated with 0.1 μ g/ml DAPI and 1 μ mol/mL CNA35-mCherry (132) for 1 h at room temperature. Antibodies are listed in **Table S6.1**. Images were acquired with a laser scanning microscope (Leica TCS SP5X, 63x/1.2 HCX PL Apo CS objective). All images were prepared for presentation in Fiji (127).

DNA quantification

Lyophilized samples ($N = 3$) were weighted and digested overnight in papain digestion buffer (containing 100 mmol phosphate buffer, 5 mmol L-cysteine, 5 mmol EDTA and 140 μ g/ml papain (P4762, Sigma-Aldrich)). DNA was quantified using the Qubit

Quantification Platform (Q32851, Thermo Fisher Scientific), according to the manufacturer's instructions.

Alkaline phosphatase activity

Scaffolds ($N = 3$) were washed in PBS and disintegrated using steel balls and a mini-beadbeater™ (Biospec, Bartlesville, OK, USA) in cell lysis buffer containing 0.2% (v/v) Triton X-100 and 5 mM MgCl₂. Alkaline phosphatase (ALP) activity in cell lysates was determined by adding 20 μ l of 0.75 M 2-amino-2-methyl-1-propanol (A65182, Sigma-Aldrich) to 80 μ l sample in 96-wells assay plates. Subsequently, 100 μ l substrate solution (10 mM p-nitrophenyl-phosphate (71768, Sigma-Aldrich) in 0.75 M 2-amino-2-methyl-1-propanol) was added and wells were incubated at room temperature for 15 minutes. To stop the reaction, 100 μ l 0.2 M NaOH was added. Absorbance was measured with a plate reader at 450 nm and these values were converted to ALP activity (converted p-nitrophenyl phosphate in μ mol/ml/min) using standard curve absorbance values.

Receptor activator of nuclear factor κ B ligand (RANKL) and osteoprotegerin (OPG) quantification

Secreted RANKL and OPG were quantified in culture medium supernatants from day 7 of 2 different bioreactors containing 4 scaffolds each ($N = 2$) with RANKL (ab213841, Abcam, Cambridge, UK) and OPG (EHTNFRSF11B, Thermo Fisher Scientific) enzyme-linked immunosorbent assays (ELISAs) according to the manufacturer's protocols and as described in **Section 6.2.5**.

Supplementary tables

The antibodies that were used for immunofluorescent stainings of MC-MSC co-cultures (non-stimulated and osteogenically stimulated) and three-dimensional osteogenically stimulated MSC mono-cultures are listed in **Table S6.1**.

Table S6.1. List of antibodies that were used in this study.

Antigen	Supplier	Catalogue No.	Conjugate	Species	Dilution
RANKL	Abcam	ab45039		Mouse	1:200
OPG	Abcam	ab9986		Rabbit	1:500
Integrin- β 3	Biorbyt	orb248939		Mouse	1:200
RUNX2	Abcam	ab23981		Rabbit	1:500
Osteopontin	Thermo Fisher	14-9096-82		Mouse	1:200
Anti-mouse IgG1	Molecular Probes	A21121	Alexa 488	Goat	1:200
Anti-Rabbit IgG	Molecular Probes	A21428	Alexa 555	Goat	1:200
Anti-Rabbit IgG	Molecular Probes	A21244	Alexa 647	Goat	1:200

Abbreviations: runt-related transcription factor 2 (RUNX2), receptor activator of nuclear factor κ B ligand (RANKL), osteoprotegerin (OPG).

To explore the protein content of hPL, a total of 21 proteins that have been reported to influence bone resorption, formation or remodeling were quantified using multiplex immunoassays. In addition, calcium and phosphate concentration were quantified as well. The concentrations from these analyses were compared to effective concentrations from *in vitro* experiments reported in literature. The results from these quantifications and the literature research are reported in **Table S6.2**.

Table S6.2 Measured concentrations from hPL characterization experiments and effective concentrations reported in literature.

Analyte	Effect on bone remodeling	Effective conc. from <i>in vitro</i> experiments	Conc. in hPL	Unit
IL1- α	Could enhance osteoclastic differentiation in the presence of RANKL (308,309). Suggested to enhance osteoclast survival (310). Can induce osteoblast apoptosis and inhibit osteogenesis (311).	10,000 NR 500 – 10,000	283.94	pg/ml
IL1- β	Could enhance osteoclastic differentiation in the presence of RANKL (308,309). Could inhibit osteogenesis by decreasing RUNX2 expression, can stimulate ALP production and mineralization (312).	NR 100 – 1,000	207.67	pg/ml
IL4	Can inhibit osteoclastic resorption in a dose dependent manner (313). Can inhibit osteoclast formation (314). Can inhibit osteogenesis in adipose tissue derived MSCs, which can be counteracted by IL6 (305,315).	10,000 – 100,000 100 – 10,000 10,000	32.72	pg/ml
IL6	Could enhance osteoclastic differentiation in co-culture by stimulating RANKL production by co-cultured cells (316). In co- presence of TNF- α , can induce osteoclastic differentiation in absence of RANKL (317). Stimulatory and inhibitory effects on osteogenesis/osteoblasts reported, dependent on cell differentiation state (316,318).	NR 50,000 10,000	623.59	pg/ml
IL10	Could suppress osteoclastic differentiation (319). Can promote osteogenic differentiation of bone marrow derived MSCs at low physiological concentrations (320). Can inhibit osteogenic differentiation of bone marrow derived MSCs at high pathological concentration (320).	NR 10 – 1,000 10,000 - 100,000	196.80	pg/ml
IL17	Different outcomes on osteoclasts reported (321). Could directly induce osteoclastic differentiation (304). Enhanced proliferation and stimulated osteogenesis. Can induce RANKL and M-CSF expression and osteoclastic differentiation in co-culture with PBMCs (322).	NA 10 – 1,000 20,000 – 50,000	369.86	pg/ml

TNF- <i>a</i>	Could enhance osteoclastic differentiation in the presence of RANKL (309). In co- presence of IL-6, can induce osteoclastic differentiation in absence of RANKL (317). Could inhibit osteogenesis by decreasing RUNX2 expression, can stimulate ALP production and mineralization (312).	NR 50,000 100 – 10,000	236.61	pg/ml
SDF-1 <i>a</i>	Hypothesized to recruit osteoclast precursors (188). Important role in migration of MSCs, especially in inflammation (185). Could support early osteogenic differentiation (186).	~8.526 – 255.8* 150 NR	3.292	ng/ml
RANKL	Expressed by a multiple cell types, but typically by osteoblastic cells, required for osteoclast differentiation (198). Multiple concentrations are used to induce osteoclastogenesis <i>in vitro</i> (43).	10,000 – 100,000	394.34	pg/ml
OPG	Can prevent RANKL from binding to the RANK receptor on preosteoclasts, inhibits osteoclastogenesis (198,199).	20 – 100	1.6876	ng/ml
Sclerostin	Inhibits bone formation and osteogenesis and could stimulate RANKL secretion by osteocytes, thereby promoting osteoclastogenesis (160).	NR	6.4137	ng/ml
Osteopontin	Instrumental for intrafibrillar mineralization and promotes osteoclast activation (200). Stimulates osteoclastogenesis and plays a major role in the formation of sealing zones (323). Promotes osteoclast precursor migration (201).	100,000** NA ~600 – 60,000*	2.1524	ng/ml
Dkk-1	Inhibitor for osteogenic differentiation and bone formation. Can inhibit osteoclast induced mineralization by osteoblasts (324).	200	1.86	ng/ml
M-CSF	Can regulate multiple steps of human <i>in vitro</i> osteoclastogenesis, including osteoclast precursor proliferation, differentiation, and fusion, and osteoclast resorption (325).	25,000	346.29	pg/ml
GM-CSF	Can suppress osteoclastogenesis in early differentiation stages, but promotes fusion of mature osteoclasts (326).	3,000	381.78	pg/ml

EGF	Stimulatory effect on osteogenic differentiation of dental pulp stem cells, could enhance mineralization (327). Could promote osteoblast proliferation and protein expression, but not mineralization (328). Might improve osteoclast survival and differentiation through binding to the EFG receptor (329). Could promote ALP production and mineralization by MSCs (330).	10 10 NA 50	1.6238	ng/ml
Basic FGF	Inhibitory effect on osteogenic differentiation of dental pulp stem cells (327). Might promote osteoblast-like cell differentiation towards osteocyte (331). Contradictory results reported. Likely, proliferative and stemness maintaining effect at lower concentrations (332). Could inhibit osteoclast formation when co-cultured with MSC-like cells (333).	10,000 10,000 ≤ 10,000 1,000 – 10,000	811.81	pg/ml
VEGF	Could enhance osteoclast survival and resorption (192,193). Intracellular but not exogenous inhibits adipogenic differentiation and promotes osteogenic differentiation of bone marrow derived MSCs (193).	5,000 – 150,000 NA	868.60	pg/ml
Fetuin	Could inhibit osteogenic differentiation and mineralization, could induce adipogenic differentiation in bone marrow cultures (334). Might inhibit extracellular collagen mineralization (335).	4,840,000,000* NR	297.13	ng/ml
Fibronectin	Could inhibit osteoclastogenesis (204,205). Could enhance mature osteoclast activity and resorption (204). Could enhance osteogenic differentiation and bone-like matrix formation of bone marrow derived MSCs at low coating densities, and inhibit differentiation but promote proliferation at higher coating densities (206).	0.1 – 20** 20** NA	3.2096	μg/ml
PDGF-BB	Can enhance osteoclastogenesis of macrophage-like cells (189). Could promote osteogenic differentiation of adipose derived but not bone marrow derived MSCs (336). No effect on ALP formation and mineralization by MSCs (330).	20 - 50 20 10	8.159	ng/ml

Calcium	Higher proteolytic activity in osteoclasts cultured with high calcium concentration than when cultured with a low concentration. Could improve attachment and migration with low calcium concentrations (286). Too high calcium concentrations can inhibit osteoclast activity and from 20 $\mu\text{mol/ml}$ induce osteoclast apoptosis (286,337). Could promote proliferation and osteogenic differentiation of MSCs (338).	1.2 (high) 0.5 (low) 5 - 20 7.8	15.49	$\mu\text{mol/ml}$
Phosphate	Inhibited osteoclastogenesis from bone marrow cultures in co-culture with osteoblast-like cells (249). Inhibited osteoclastogenesis of human PBMCs and macrophage-like cells in a dose-dependent response (250). Can promote proliferation of human bone marrow derived MSCs (339). Can promote migration, osteogenic differentiation and mineralization of human bone marrow derived MSCs (339).	1 – 10 1.5 – 4 2 – 10 4 – 10	1.948	$\mu\text{mol/ml}$

* Calculated from the molecular weight found in literature. ** Concentration used for coating of culture substrate. Abbreviations: human platelet lysate (hPL), concentration (conc.), not reported (NR), not applicable (NA), monocyte (MC), mesenchymal stromal cell (MSC), peripheral blood mononuclear cell (PBMC), runt-related transcription factor 2 (RUNX2), alkaline phosphatase (ALP), interleukin (IL), tumor necrosis factor (TNF), stromal derived factor (SDF), granulocyte-macrophage colony-stimulating factor (GM-CSF), macrophage colony-stimulating factor (M-CSF), receptor activator of nuclear factor κB ligand (RANKL), osteoprotegerin (OPG), Dickkopf WNT Signaling Pathway Inhibitor 1 (Dkk-1), epidermal growth factor (EGF), basic fibroblastic growth factor (bFGF), vascular endothelial growth factor (VEGF), platelet derived growth factor-BB (PDGF-BB).

Supplementary figures

To visualize the non-resorbed surface, osteo assay wells were stained with a modified Von Kossa. To capture the entire well, tile scans were made with a bright field microscope. Tile scans were stitched with Zen Blue software (version 3.1, Zeiss, Breda, The Netherlands). To enable segmentation and resorption quantification, scratches that were introduced by mechanical cell removal in co-cultures were manually masked whereafter image contrast was increased using Fiji (127). A clipping mask was created in Illustrator (Adobe Inc., San Jose, CA, USA) to remove the edges of the wells. Segmentation was performed in MATLAB (version 2019b, The MathWorks Inc., Natick, MA, USA), using Otsu's method for binarization with global thresholding, where the threshold was kept constant throughout the entire image (**Figure S6.1**) (284).

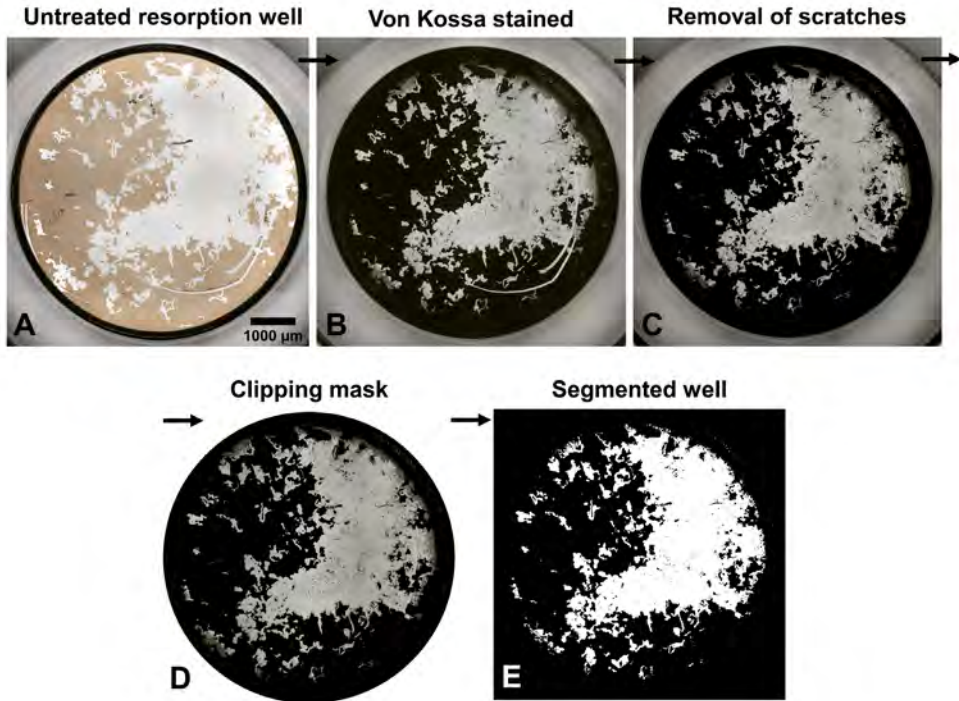


Figure S6.1. Workflow osteo assay wells from raw data to image segmentation. Decellularized resorption wells (A) were stained with Von Kossa (B). Scratches were manually masked (C) and a clipping mask was used to remove the edges of the well (D). Lastly, images were segmented such that the resorbed surface could be quantified (E).

As osteoclasts have a life-span of approximately 2-3 weeks (232,289), culture photographs were taken on day 18/21 of MC mono-cultures (Figure S6.2). By day 18, MCs have likely differentiated into mature osteoclasts and apoptosis might not yet have taken place.

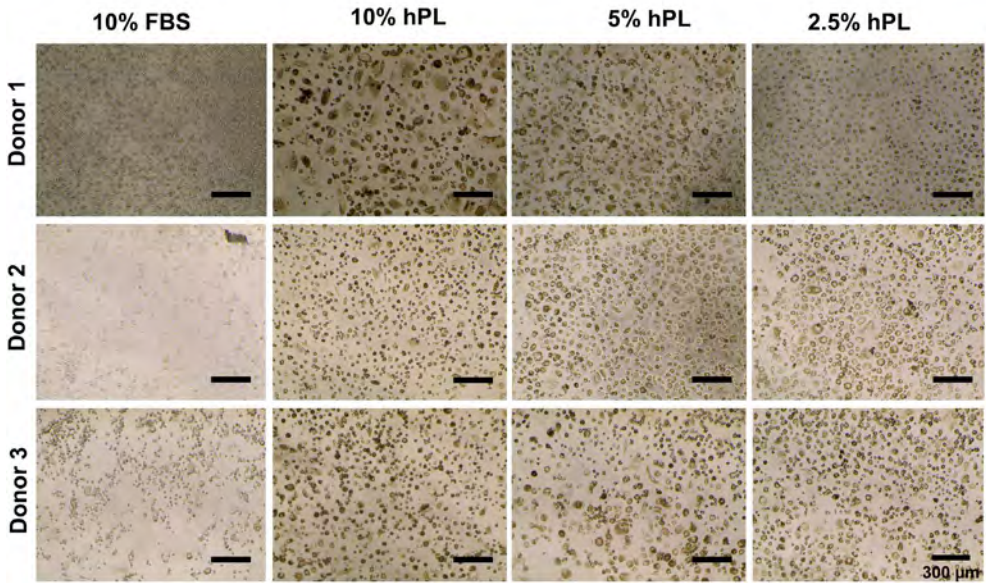


Figure S6.2. Micrographs of all MC donors on day 18 in mono-cultures. Clear differences can be observed between MCs cultured with FBS and hPL, indicating a heterogeneous cell population in MCs cultured with FBS. No clear differences were observed between donors, with only in donor 1 a concentration dependent size difference in MCs cultured with hPL. Abbreviations: fetal bovine serum (FBS), human platelet lysate (hPL), monocyte (MC).

To check whether osteogenically stimulated MC-MSC co-cultures showed differences in RANKL and OPG expression, cells were stained for these proteins (**Figure S6.3**).

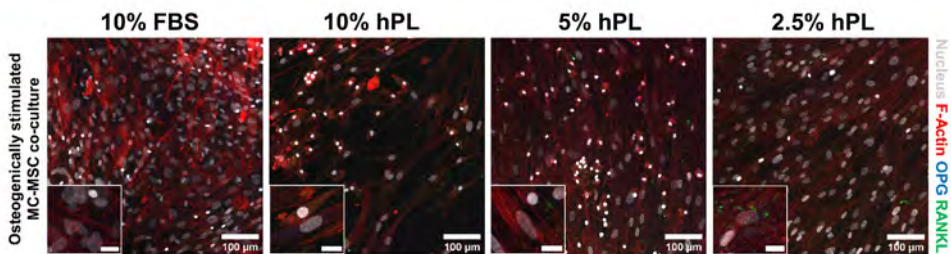


Figure S6.3. Micrographs of osteogenically stimulated MC-MSC co-cultures, stained for F-Actin (red), the nucleus (gray), OPG (blue) and RANKL (green). It is expected that OPG and RANKL also played a role in the inhibition of osteoclastic differentiation in osteogenically stimulated MC-MSC co-cultures, although no clear differences between groups were found after immunocytochemical staining of OPG and RANKL. Scale bar in insert is 20 μ m. Abbreviations: fetal bovine serum (FBS), human platelet lysate (hPL), monocyte (MC), mesenchymal stromal cell (MSC), receptor activator of nuclear factor κ B ligand (RANKL), osteoprotegerin (OPG).

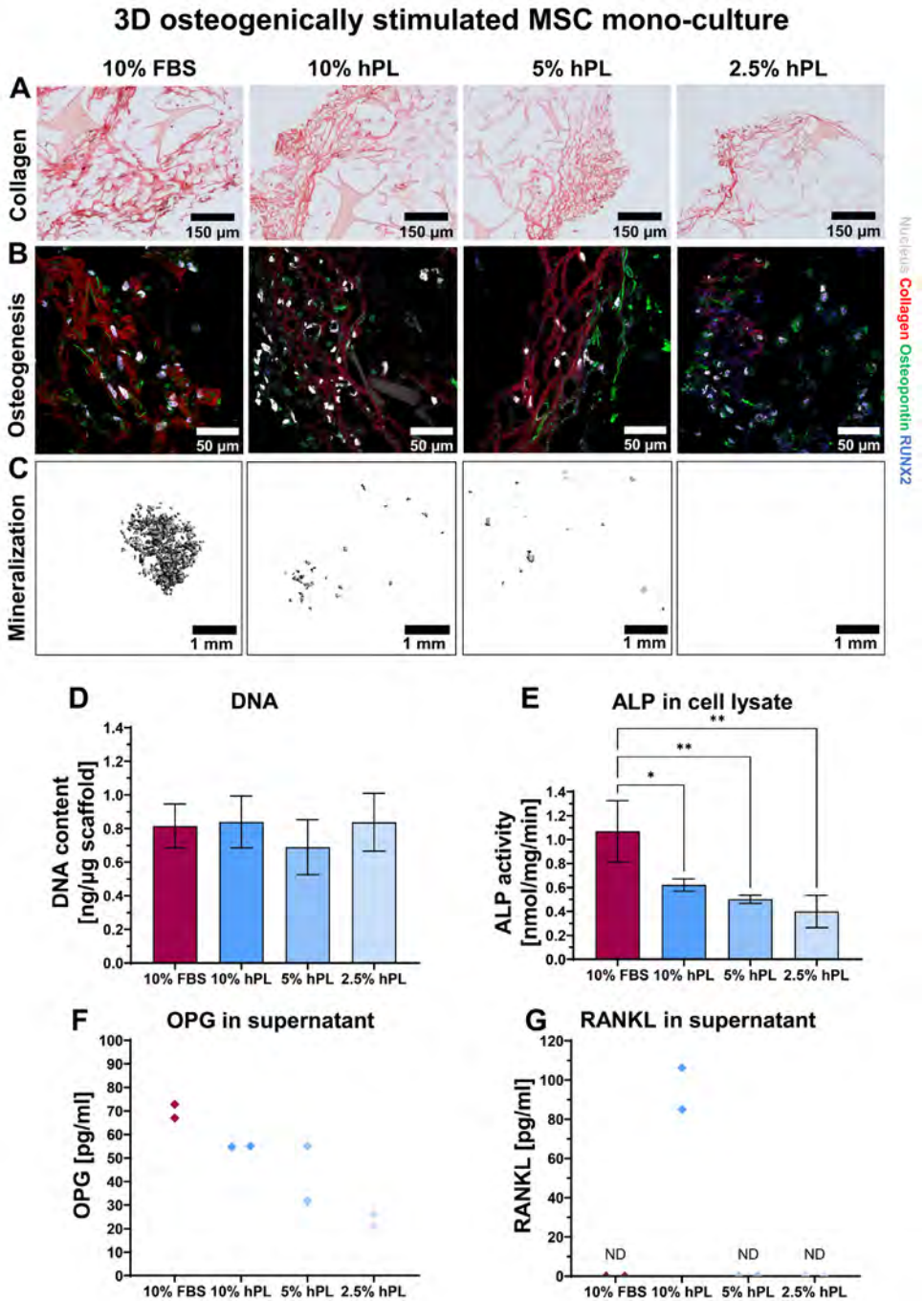


Figure S6.4. Results from 3D osteogenically stimulated MSC mono-cultures indicating most osteogenic differentiation and bone-like matrix formation in MSCs cultured with FBS. (A) Picosirius red staining

indicating collagen formation in osteogenically stimulated 3D MSC monocultures after 4 weeks culture, most collagen seemed present in constructs cultured with 10% FBS and 10% hPL. **(B)** Staining for osteogenic markers indicating osteogenic differentiation of 3D MSC monocultures after 4 weeks culture in all conditions. Sections were stained for cell nuclei (gray), collagen (red), osteopontin (green) and RUNX2 (blue). **(C)** Micro-computed tomography scans of constructs, indicating most mineralization in constructs cultured with FBS. No mineralization was found in constructs cultured with 2.5% hPL. **(D)** DNA quantification in cultured constructs, no clear differences were found between different conditions. **(E)** ALP activity quantification revealed most ALP in lysates of constructs cultured with 10% FBS, $p < 0.05$ (one-way ANOVA and Tukey's post hoc tests) **(F)** OPG quantification in culture medium supernatants of 2 bioreactors (containing 4 tissue constructs each) revealed most OPG in constructs cultured with 10% FBS. **(G)** RANKL was only detected in constructs cultured with 10% hPL. ($*p < 0.05$, $**p < 0.01$) Abbreviations: fetal bovine serum (FBS), human platelet lysate (hPL), monocytes (MCs), mesenchymal stromal cells (MSCs), runt-related transcription factor 2 (RUNX2), alkaline phosphatase (ALP), osteoprotegerin (OPG), receptor activator of nuclear factor κ B ligand (RANKL), not detected (ND).

7

Bioinspired silk fibroin mineralization for advanced *in vitro* bone remodeling models

This chapter is based on:

Bregje W.M de Wildt^{1,2}, Robin van der Meijden³, Paul A.A. Bartels^{2,4}, Nico A.J.M. Sommerdijk³, Anat Akiva³, Keita Ito^{1,2} and Sandra Hofmann^{1,2}

1. Orthopaedic Biomechanics, Department of Biomedical Engineering, Eindhoven University of Technology, Eindhoven, The Netherlands.

2. Institute for Complex Molecular Systems (ICMS), Department of Biomedical Engineering, Eindhoven University of Technology, Eindhoven, The Netherlands.

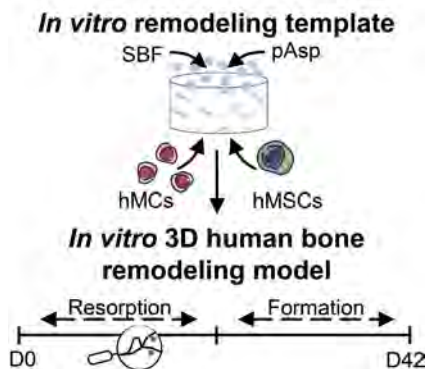
3. Department of Biochemistry, Radboud Institute for Molecular Life Sciences, Radboud University Medical Center, Nijmegen, The Netherlands.

4. Biomedical Materials and Chemistry, Department of Biomedical Engineering, Eindhoven University of Technology, Eindhoven, The Netherlands.

Abstract

Human *in vitro* bone models can create the possibility for investigation of physiological bone remodeling while addressing the principle of replacement, reduction and refinement of animal experiments (3R). Current *in vitro* models lack cell-matrix interactions and their spatiotemporal complexity. To facilitate these analyses, a bone-mimetic template was developed in this study, inspired by bone's extracellular matrix composition and organization. Silk fibroin (SF) was used as an organic matrix, poly-aspartic acid (pAsp) was used to mimic the functionality of non-collagenous proteins, and 10x simulated body fluid served as mineralization solution. By using pAsp in the mineralization solution, minerals were guided towards the SF material resulting in mineralization inside and as a coating on top of the SF. After cytocompatibility testing, remodeling experiments were performed in which mineralized scaffold remodeling by osteoclasts and osteoblasts was tracked with non-destructive micro-computed tomography and medium analyses over a period of 42 days. The mineralized scaffolds supported osteoclastic resorption and osteoblastic mineralization, in the physiological bone remodeling specific sequence. This model could therefore facilitate the investigation of cell-matrix interactions and may thus reduce animal experiments and advance *in vitro* drug testing for bone remodeling pathologies like osteoporosis, where cell-matrix interactions need to be targeted.

Graphical abstract



7.1 Introduction

Bone is a highly dynamic tissue with multiple mechanical and metabolic functions that are maintained by the process of bone remodeling. Physiological bone remodeling follows a specific sequence of events: activation, bone resorption by osteoclasts, reversal, and bone formation by osteoblasts (91). Unbalanced bone remodeling can result in pathologies such as osteoporosis and osteopetrosis. Studies of these bone pathologies and their drug development are routinely performed in animal models. However, animal models represent human physiology insufficiently which is likely one of the reasons that only 9.6% of preclinically developed drugs are approved for regular clinical use (23,25). Human *in vitro* bone models can potentially facilitate the investigation of physiological human bone remodeling while addressing the principle of replacement, reduction, and refinement of animal experiments. Current studies aiming at mimicking bone remodeling mostly use osteoblast-osteoclast (progenitor) co-cultures to study indirect or direct cell-cell interactions in two dimensions (2D) (340–345). Although these studies have improved the understanding in factors involved in bone remodeling, they do not allow for studying the interactions with a three-dimensional (3D) complex bone-like matrix (7). Researchers that have attempted to mimic bone remodeling in 3D often (i) neglect the specific sequence of events (*i.e.*, resorption, transition, formation (**Figure 7.1A**)) by starting their culture with osteoblast (progenitors) (259,260), or (ii) only look at osteoclast and osteoblast markers with *e.g.*, gene expression or enzymatic activity assays rather than at their function to resorb and form a bone-like matrix (43,346). As such, functional cell-matrix interactions and their temporal dynamics are often neglected (91) (**Figure 7.1B**). To enable the investigation of functional cell-matrix interactions and to mimic the sequence of these interactions *in vitro*, a bone-mimetic template is required (91,110,347–349).

Bone tissue consists mainly of organic collagen type I and the inorganic mineral carbonated hydroxyapatite, which are highly organized at multiple hierarchical levels (5). Collagen mineralization starts when mineral precursors enter the collagen gap regions where carbonated hydroxyapatite crystals nucleate and grow outside the dimensions of the collagen fibril, resulting in mineralization inside (intrafibrillar) and outside (extrafibrillar) the collagen fibrils (78). A bone-mimetic template should include these characteristics. While the use of collagen type I as organic matrix seems obvious, drawbacks are the high biodegradability, low mechanical strength, and the difficulty of *in vitro* collagen self-assembly resulting in poorly organized low-density networks (350,351). The fibrous protein silk fibroin (SF) is a suitable organic alternative, thanks to its excellent mechanical properties, ease to process, and biocompatibility (352). SF features a unique structure which consists of hydrophobic β -sheets and hydrophilic amorphous acidic spacers, of which the latter could act as nucleation sites for mineral

crystals similar to the collagen gap regions in bone (353). To mineralize SF, simulated body fluid (SBF) has been widely used (354). Immersing materials in this solution containing physiological ion concentrations results in the formation of calcium phosphate crystalline structures like apatite found in real bone (355). However, material mineralization with SBF could take up to 4 weeks and requires frequent replenishment of the solution (355,356). This mineralization period often only results in a non-uniform mineral coating, rather than infiltration of minerals into the material's structure (354). *In vivo*, non-collagenous proteins are believed to play an instrumental role in the infiltration of mineral precursors into collagen fibrils (57). In bone tissue, extracellular levels of calcium and phosphate ions are supersaturated and their precipitation is therefore controlled by these acidic proteins (57). *In vitro*, poly-aspartic acid (pAsp) can be used to mimic the functionality of these acidic non-collagenous proteins as its addition to a mineralization solution has been shown to induce intrafibrillar collagen mineralization (357). As such, pAsp might improve mineral distribution and infiltration for SF as well. Therefore, in this study a bone-mimetic template was developed using SF as organic material mineralized with SBF under influence of pAsp (**Figure 7.1C**). While such material might not be sufficient to induce bone regeneration on its own due to insufficient bioactivity, its biomimicry, biocompatibility and biodegradability would have the potential to support *in vitro* remodeling (358).

To develop this bone-mimetic template, we evaluated the use of pAsp as a substitute to the mineralization solution and/or integrated into the SF material to improve SF mineralization. The integration of pAsp into the SF materials has been studied before and resulted dependent on the used concentration in pAsp associated mineral crystal growth along an SF electrospun fiber (359), or chunks of mineral on the surface of SF films and scaffolds (360,361), which negatively affected cell behavior (361). The use of pAsp as a substitute to SBF solution to mineralize SF with a polymer-induced liquid precursor phase (PILP) mechanism has (to our knowledge) not been explored. The effects of the material preparation methods on material cytocompatibility were tested in two-dimensional (2D) films for human monocytes (MCs) and mesenchymal stromal cells (MSCs) as the osteoclast and osteoblast progenitors, respectively. Improved mineralization methods were also applied to and evaluated in three-dimensional (3D) porous SF scaffolds. *In vitro* remodeling of these scaffolds by human osteoclastogenically stimulated MCs and osteogenically stimulated MSCs was tracked longitudinally which enabled the investigation of cell-matrix interactions and their temporal dynamics. As a result, pAsp was instrumental for SF mineralization in a similar manner as for collagen mineralization. Mineralized SF scaffolds supported osteoclastic resorption and enhanced osteoblastic mineralization. As such, our model allowed for investigating functional cell-matrix interactions and their dynamics and may therefore

advance *in vitro* drug testing for bone remodeling pathologies like osteoporosis, where cell-matrix interactions need to be targeted.

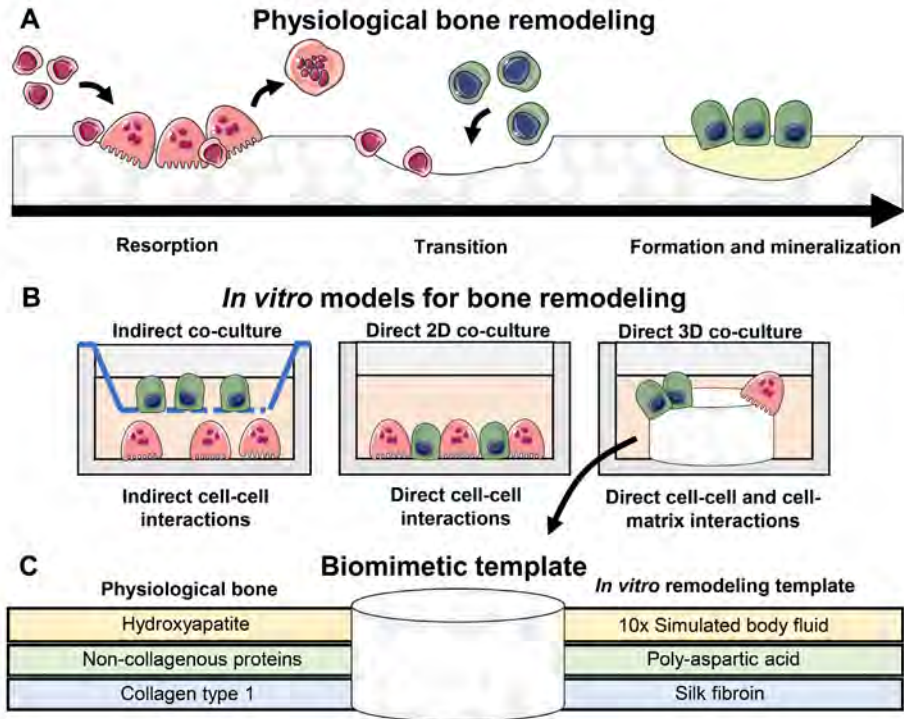


Figure 7.1. Reasoning towards the work presented in this study. (A) The physiological bone remodeling cycle starting with resorption after activation, then there is a transition phase followed by formation, mineralization and subsequent termination. (B) Current *in vitro* models for bone remodeling lack the investigation of cell-matrix interactions. (C) The proposed biomimetic template including the components present in physiological bone. Abbreviations: two-dimensional (2D), three-dimensional (3D). The figure was created with Servier Medical Art, licensed under a Creative Common Attribution 3.0 Generic License (<http://smart.servier.com/>, accessed on 8 July 2021).

7.2 Results

7.2.1 Mineralization optimization and characterization of silk fibroin films

While intrafibrillar mineralization of small amounts of collagen using pAsp as a nucleation inhibitor in the mineralization solution has been established, large scale intrafibrillar mineralization of collagen scaffolds is still challenging (351,362). The use of nucleation inhibitors only in solution does not fully represent the physiological

situation in which non-collagen proteins are bound to the matrix and might thus not provide the optimal conditions for homogeneous scaffold mineralization (363). Therefore, we choose to not only study the effect of pAsp in the mineralization solution on SF mineralization, but we also mixed it into the SF (**Figure 7.2A**). To enable the screening of multiple parameters and to facilitate the analyses, mineralization optimization and characterization was performed in 2D. Pure SF (SF w/o pAsp) and SF containing 5 wt% pAsp (SF w/5% pAsp) solutions were casted to form films with a diameter of 10 mm and a thickness of ~ 300 μm . To check for the presence of pAsp in SF w/5% pAsp films, films were stained with the cationic dye alcian blue to allow for visualization of the negatively charged pAsp. The addition of pAsp indeed led to a more intense blue stain in SF films with 5% pAsp when compared to plain SF films (**Figure S7.1**). The presence of a small amount of pAsp in the SF material was also confirmed by chemical analyses. Raman spectroscopy measurements revealed a small peak at 1783 cm^{-1} , suggesting the presence of pAsp (**Figure S7.2**). X-ray photoelectron spectroscopy (XPS) measurements revealed a carbon peak with wider shape, which is likely attributed to the carboxyl group in pAsp (**Figure S7.3**). By measuring the water contact angle an increase in hydrophilicity of SF w/5% pAsp was observed by a decrease in water contact angle (**Figure 7.2B**). Both types of films were subsequently mineralized using 10x SBF (356) (SBF) or 10x SBF with $100\text{ }\mu\text{g/ml}$ pAsp (SBF-pAsp). Films were mineralized in this solution for either one week (W1, no replenishment of mineralization solution) or two weeks (W2, one mid-way replenishment of mineralization solution). Baseline films were used as non-mineralized controls (NM-control) (**Figure 7.2A**). After mineralization, the property of pAsp to prevent mineral precipitation in solution was verified by measuring the optical density of the mineralization media. The addition of pAsp to the mineralization solution indeed led to a statistically significant decrease in mineralization solution optical density (**Figure 7.2C**). Mineralization solution optical density was also significantly decreased after one mineralization solution replenishment (W2). In the films where pAsp was added to the mineralization solution the optical density after W2 reduced towards almost the optical density of ultra-pure water (UPW). Most likely, optical density was reduced after W2 because some calcium phosphate crystals were already nucleated on the film to which calcium and phosphate ions could precipitate more easily (364). A reverse effect was found for the calcium content (**Figure 7.2D**). Both the addition of pAsp to the mineralization solution as well as the replenishment of the solution resulted in a statistically significant increase in calcium content of the film, whereas the addition of pAsp to the SF material did not affect its mineralization.

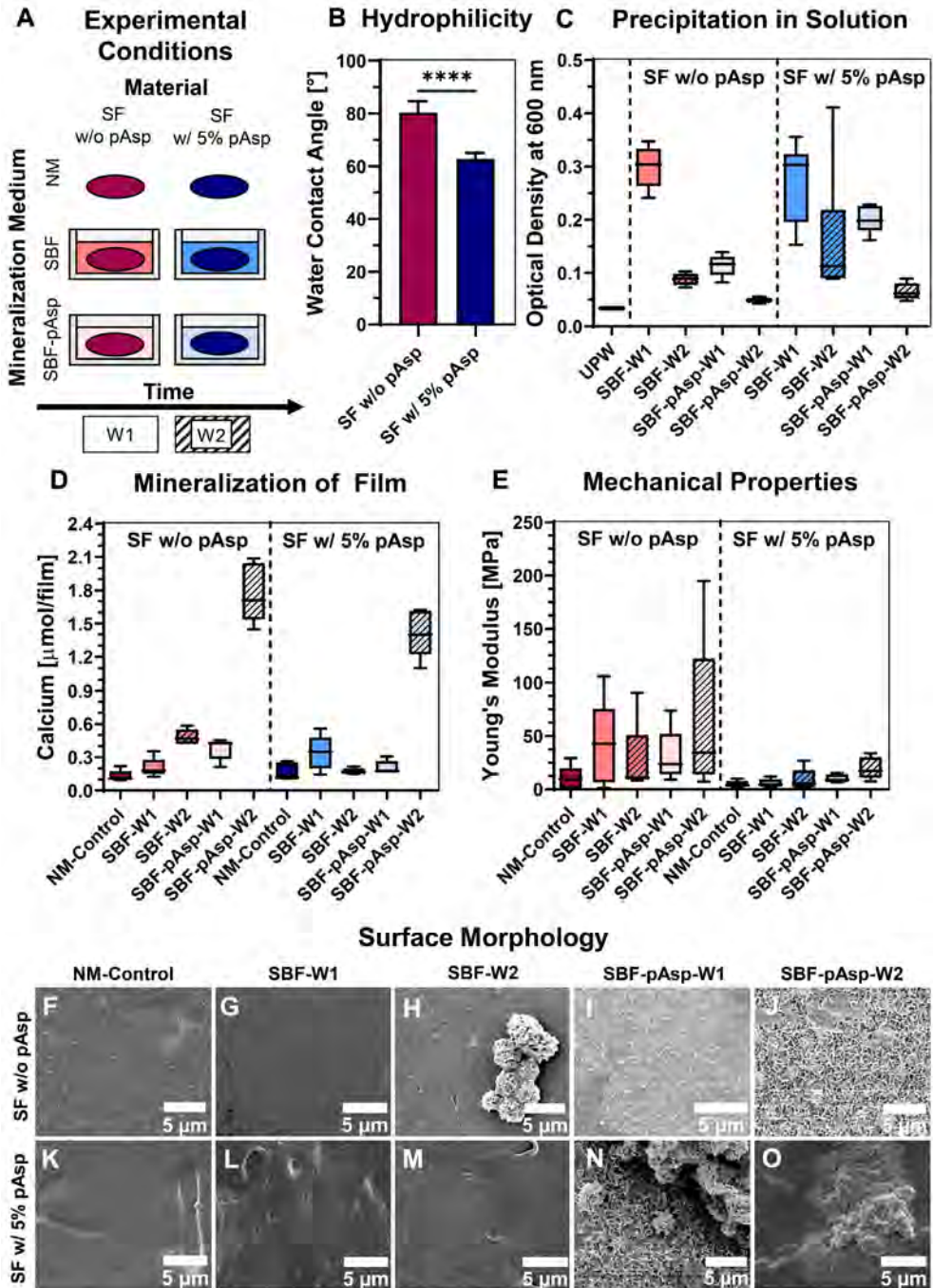


Figure 7.2. Mineralization optimization and characterization of SF films. (A) Experimental variables included in the mineralization optimization. (B) Water contact angle quantification, $N = 5$, $p < 0.0001$

(Independent t-test). **(C)** Solution optical density measurement to detect mineral precipitation, $N = 8$, $p < 0.0001$ for mineralization time and mineralization solution (Kruskal-Wallis test for main effects with Bonferroni correction for multiple comparisons). **(D)** Mineral quantification in film, measured by calcium content, $N = 5$, $p < 0.01$ for mineralization time and $p < 0.05$ for mineralization solution (Kruskal-Wallis test for main effects with Bonferroni correction for multiple comparisons). **(E)** Stiffness measured with nanoindentation, $N = 5$, $p < 0.01$ for the material (Kruskal-Wallis test for main effects with Bonferroni correction for multiple comparisons) **(F-O)** Surface and mineral morphology visualized with scanning electron microscopy. Abbreviations: silk fibroin (SF), simulated body fluid (SBF), poly-aspartic acid (pAsp), non-mineralized (NM), week (W), ultra-pure water (UPW)

Calcium content results were confirmed by alizarin red staining of film cross-sections with a clear red staining on top of films mineralized with pAsp in the mineralization solution after W2 (**Figure S7.4E+J**, cross-sections). In these groups, only mineralized SF w/o pAsp films showed red staining inside the film indicating mineral infiltration into the films (**Figure S7.4E**, cross-section). While the addition of pAsp to the material did not affect its mineralization, it caused a statistically significant decrease in Young's modulus (stiffness) compared to plain SF films, as measured with nanoindentation (**Figure 7.2E**).

When visualizing the film surfaces with scanning electron microscopy (SEM), non-mineralized SF w/5% pAsp films had a rougher surface than SF w/o pAsp films (**Figure 7.2F+K**). Mineral crystals on the surface were observed in SF w/o pAsp films mineralized with only SBF after W2, and in all films mineralized with pAsp in the solution after W1 and W2 (**Figure 7.2H-J** and **Figure 7.2N-O**). As mineralization duration (W2) and the addition of pAsp to the solution positively influenced mineralization of the films, these mineralization conditions were used for 3D scaffold mineralization and cytocompatibility testing of the 2D films. Although the addition of pAsp to the material did not improve mineralization, this condition was still included to investigate the influence of bound pAsp on mineral distribution throughout the scaffold. In addition, the increased hydrophilicity and roughness of the SF w/5% pAsp films might still be beneficial for cell proliferation, osteoprogenitor differentiation, and osteoclastic resorption (365–368).

7.2.2 Characterization of mineralized silk fibroin scaffolds

SF scaffolds w/o pAsp and SF w/5% pAsp were mineralized using a mineralization solution of SBF with 100 $\mu\text{g}/\text{ml}$ pAsp for 2 weeks with one solution replenishment after one week. Like in the films, calcium was detected in the mineralized scaffolds with no differences between the SF w/o pAsp and SF w/5% pAsp (**Figure 7.3A**). Mineralization led to an increased scaffold stiffness measured with an unconfined compression test (**Figure 7.3B**). Although not statistically significant, the addition of pAsp to the material seemed to negatively influence the average stiffness, something that was also observed in the films. Next, the scaffolds were analyzed for mineral distribution. Because of the radiolucent nature of SF when immersed in water, mineralization could be localized with micro-computed tomography (μCT) scanning of the scaffolds. It was hypothesized that the addition of pAsp to the material could lead to improved mineral distribution throughout the scaffold. However, a positive influence of the addition of pAsp to the scaffold on mineral distribution could not be detected (**Figure 7.3C** and **Figure S7.5**). In both the radiographs and the quantification of the percentage minerals present in the central $\sim 8\%$ scaffold volume, no clear differences were found between the two material types.

By drying the mineralized scaffolds, their 3D morphology could be characterized after μCT scanning (**Figure 7.3D** and **Figure S7.5**). These analyses revealed a smaller average pore size per scaffold, measured as trabecular separation. By fitting largest possible spheres in the reconstructed μCT scans and deriving their diameter, the distribution of individual pore diameters was obtained (131). In the pore size distribution, small differences were observed with a peak at a smaller pore size for SF w/5% pAsp scaffolds and a wider curve for plain SF scaffolds, which underline the found differences in average pore size (**Figure 7.3D+E**). Although not significant, the decrease in average trabecular separation by the addition of pAsp to the material seemed reflected by an increase in trabecular thickness, trabecular number and trabecular connectivity density, and a decrease in porosity (**Figure 7.3D** and **Figure S7.5**). We then studied the mineral morphology with SEM. Minerals in the plain SF scaffolds (**Figure 7.3H**) appeared more homogeneously distributed in a layer on the surface when compared to minerals in SF w/5% pAsp scaffolds (**Figure 7.3I**). On SF w/5% pAsp scaffolds, minerals appeared more often as chunks, which likely caused the differences in scaffold morphology parameters. Mineral infiltration seemed present in both scaffolds w/o pAsp and w/5% pAsp detected by alizarin red stained scaffold sections and a change in cross-section structure after mineralization (**Figure 7.3L+M**).

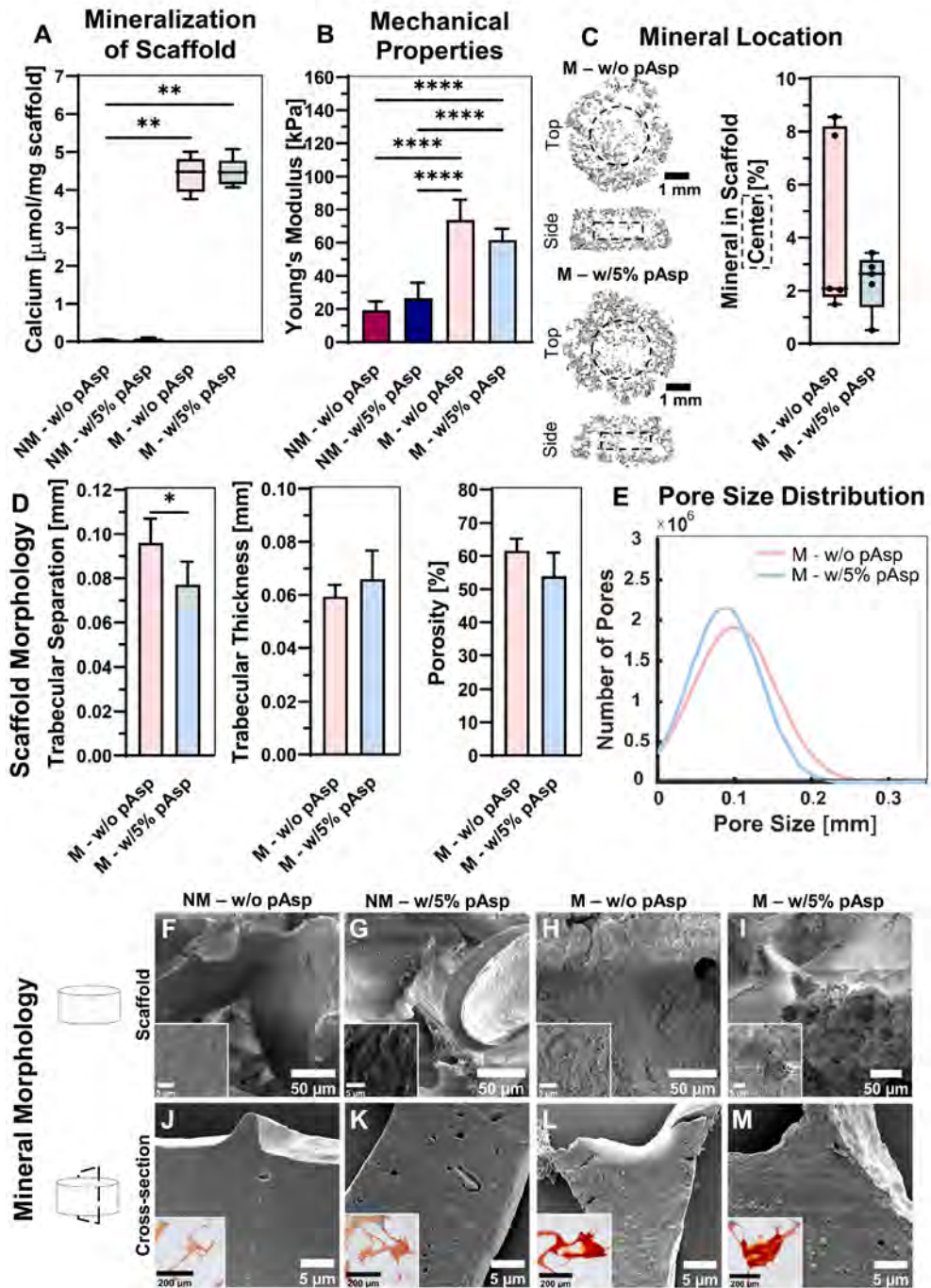


Figure 7.3. Characterization of mineralized SF scaffolds. (A) Mineral quantification in scaffold, measured by calcium content, $N = 5$, $p < 0.05$ (Kruskal-Wallis and Dunn's post hoc tests). (B) Stiffness measured

with a full unconfined compression test, $N = 5$, $p < 0.05$ (One-way ANOVA and Holm-Šidák's post hoc tests). (C) Mineral location visualized with μ CT and quantified in the central $\sim 8\%$ scaffold volume to indicate mineral distribution. Dashed boxes represent the segmented part for mineral quantification in the center, $N = 5$, *ns* (Mann-Whitney U). (D) Quantified scaffold morphology obtained with μ CT, including the trabecular separation (average pore size), $N = 5$, $p < 0.05$ (Independent t-test), trabecular thickness, $N = 5$, *ns* (Independent t-test), porosity, $N = 5$, *ns* (Independent t-test), and (E) the pore size distribution derived from $N = 5$ scaffolds (gaussian fit). (F-I) Mineral morphology on scaffold surface visualized with SEM. (J-M) Morphology visualized with SEM and micrographs of calcium localization (insert, alizarin red staining) of cross-sections from scaffolds. (* $p < 0.05$, ** $p < 0.01$, *** $p < 0.001$, **** $p < 0.0001$). Abbreviations: poly-aspartic acid (pAsp), non-mineralized (NM), mineralized (M), silk fibroin (SF), micro-computed tomography (μ CT), scanning electron microscopy (SEM).

To further investigate mineral infiltration into the SF material, Raman microscopy and spectroscopy were performed on scaffold cross-sections. The infiltration of mineral was observed in both SF w/o pAsp and SF w/5% pAsp scaffolds (**Figure 7.4**). Hydroxyapatite was observed throughout the whole scaffold trabecula, with a higher degree of mineralization at the surface of the trabecula indicated by the differences in the 960, 420 and 590 cm^{-1} areas representing the ν_1 , ν_2 and ν_4 vibrations of hydroxyapatite respectively (**Figure 7.4C+D**). The co-localization of hydroxyapatite with SF was observed by the presence of the 1250, 1450, 1615 and 1660 cm^{-1} areas representing the Amine III, CH_2 bend, Aromatic amino acid C=C bonds, and Amide I vibrations of SF, respectively (**Figure 7.4C+D**). In SF w/5% pAsp scaffolds, more mineral precipitation was observed at the trabecula surface. These minerals precipitated in the presence of pAsp, identified through the presence of the 1783 cm^{-1} peak (**Figure 7.4D**). XPS measurements revealed the presence of calcium, phosphate and pAsp in both mineralized SF w/o pAsp and SF w/5% pAsp scaffolds (**Figure S7.3**). The presence of pAsp was observed by the carbon peak with wider shape relative to non-mineralized SF w/o pAsp scaffolds indicative for the presence of the carboxyl group of pAsp. As such, pAsp was likely instrumental for the mineralization of both SF w/o pAsp and SF w/5% pAsp scaffolds.

7.2.3 Cytocompatibility testing of mineralized silk fibroin films

Before the mineralized scaffolds were used for a co-culture experiment to study their remodeling *in vitro*, we first tested the materials' cytocompatibility by running monocultures of human MCs and MSCs as the osteoclast and osteoblast progenitors, respectively. SF w/o pAsp and SF w/5% pAsp films, mineralized and non-mineralized, were evaluated for their cytocompatibility. For MSCs, the presence of w/5% pAsp in SF films seemed to negatively influence cell content which could be observed from DNA content measurements after 7 days culture (**Figure 7.5C**). These results were confirmed by micrographs of nuclei and F-actin staining from day 7, with clearly most cells present on mineralized SF w/o pAsp films (**Figure 7.5D-G**).

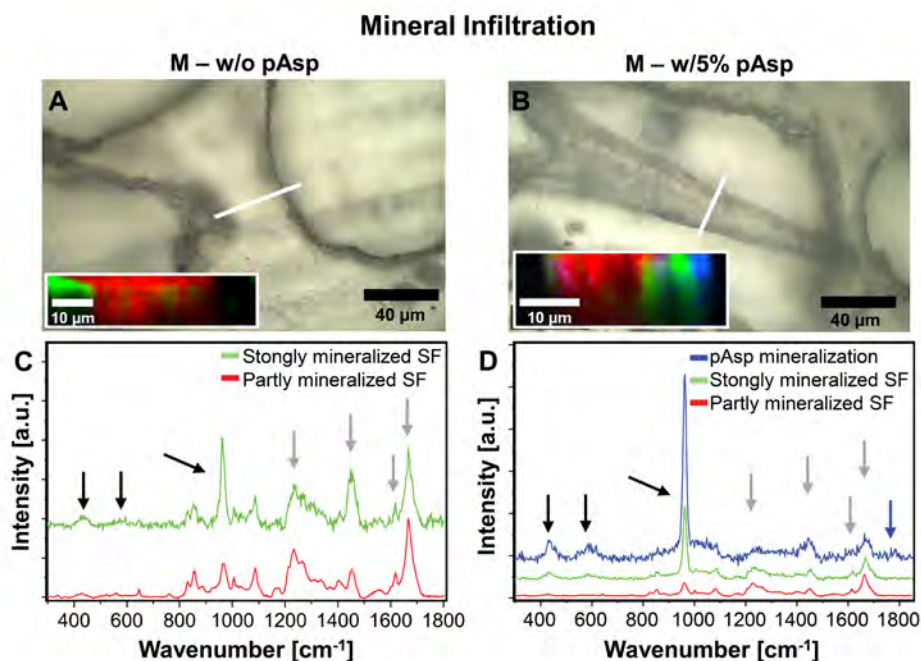


Figure 7.4. Raman microscopic analysis of mineralized SF scaffold sections to detect mineral infiltration. (A) Optical image of section of mineralized plain SF scaffold, scanned area highlighted in white. Insert in optical image presents the distribution of the strongly mineralized SF (green) and partly mineralized SF (red) in the analyzed ($50 \times 12 \mu\text{m}$) area. (B) Section of mineralized SF scaffold with 5% pAsp in the SF material. Insert in optical image presents the distribution of mineralized pAsp (blue), strongly mineralized SF (green) and partly mineralized SF (red). (C) Raman spectra of the mineralized plain SF scaffold. (D) Raman spectra of the mineralized SF scaffold with 5% pAsp added to the SF material. Mineralization with pAsp was identified through the presence of the 1783 cm^{-1} peak (blue arrow). (C–D) Black arrows indicate the 960 , 420 and 590 cm^{-1} areas representing the ν_1 , ν_2 , ν_4 , vibrations of hydroxyapatite. The co-localization with SF was observed by the presence of the 1250 , 1450 , 1615 and 1660 cm^{-1} areas representing the Amine III, CH_2 bend, Aromatic amino acid $\text{C}=\text{C}$ bonds, and Amide I vibrations of SF, respectively (gray arrows). Abbreviations: poly-aspartic acid (pAsp), mineralized (M), silk fibroin (SF).

To check whether these observations are a result of proliferation, cell death, or cell attachment, metabolic activity and cytotoxicity (*i.e.*, cell death) were tracked over time. For the metabolic activity, the conversion of resazurin to fluorescent resorufin by viable cells was measured. These results reflected the DNA measurements, with highest metabolic activity in SF w/o pAsp films over the entire culture period (**Figure 7.5A**). Supernatant lactate dehydrogenase (LDH) activity, which is an intracellular enzyme released into the medium upon cell death, did not reveal clear cytotoxic effects of the different films (**Figure 7.5B**). Differences in cytotoxicity could be explained by the number of cells present on these films as indicated above. This indicates that the higher number of cells on SF w/o pAsp films is the result of cell attachment rather than more

proliferation on these films or more cell death in SF w/5% pAsp films. This is in contrast with literature reporting often a positive influence of hydrophilicity on cell attachment (369,370). Interestingly, on mineralized SF w/o pAsp films, small particles in the proximity of cells were observed with SEM, which might indicate the presence of mineral nodules or matrix vesicles (371) (**Figure 7.5J**, white arrows). For MCs, no clear effects of the addition of pAsp to the material nor of mineralization were found in terms of DNA content on day 7 (**Figure 7.5N**). These results were in line with the metabolic activity measurements and with micrographs of a nuclei and F-actin staining from day 7 (**Figure 7.5L** and **Figure 7.5O-R**). Only cytotoxicity in MCs cultured on mineralized SF w/5% pAsp films seemed higher than in MCs cultured on a film where pAsp was not added to the material (**Figure 7.5M**). This effect was however only observed on day 2 and day 7. After a period of 7 days, multinucleated osteoclast-like cells were observed in all conditions (**Figure 7.5O-R**, white arrows). To check whether these osteoclast-like cells also had the capability to resorb the material, films were visualized with SEM. In mineralized films, resorption pits were indeed observed indicating osteoclastic resorption (**Figure 7.5U+V**, white arrows). Resorption pits seemed largest in SF w/5% pAsp films (**Figure 7.5V**), indicating that resorption might be enhanced by the increased hydrophilicity as earlier observed (367). Based on these cytocompatibility evaluations, both SF w/o pAsp and SF w/5% pAsp can be considered suitable for cell culture with human MCs and MSCs. Because the addition of pAsp to the material led to reduced MSC attachment, a decreased pore size, and a heterogeneous mineral morphology, pAsp was left out the material for the 3D *in vitro* remodeling model.

7.2.4 *In vitro* remodeling of mineralized silk fibroin scaffolds

To investigate whether our bioinspired mineralized SF scaffold could enable the *in vitro* investigation of cell-matrix interactions and their temporal dynamics as described for physiological bone remodeling, we performed a MC-MSc co-culture for 42 days (**Figure 7.6A**). On day 21, medium was switched from osteoclastogenic to osteogenic. To track the remodeling dynamics, constructs were weekly scanned with μ CT, culture medium supernatants were collected, and constructs were sacrificed for analyses at day 21 and 42. Cell supernatants or cell lysates were analyzed for resorption (tartrate resistant acid phosphatase (TRAP) (43,293)), transition (LDH to indicate potential osteoclast apoptosis), and formation (alkaline phosphatase (ALP) and pro-collagen 1 c-terminal propeptide (PICP) (43)) markers. First, the influence of μ CT scanning on cell death was evaluated over 21 days. No differences between scanned and unscanned constructs were found, μ CT scanning was therefore considered as a harmless method to track *in vitro* remodeling (**Figure S7.6**). From day 7 to day 28, elevated TRAP activity was measured whereafter TRAP activity reduced to baseline levels (**Figure 7.6B**).

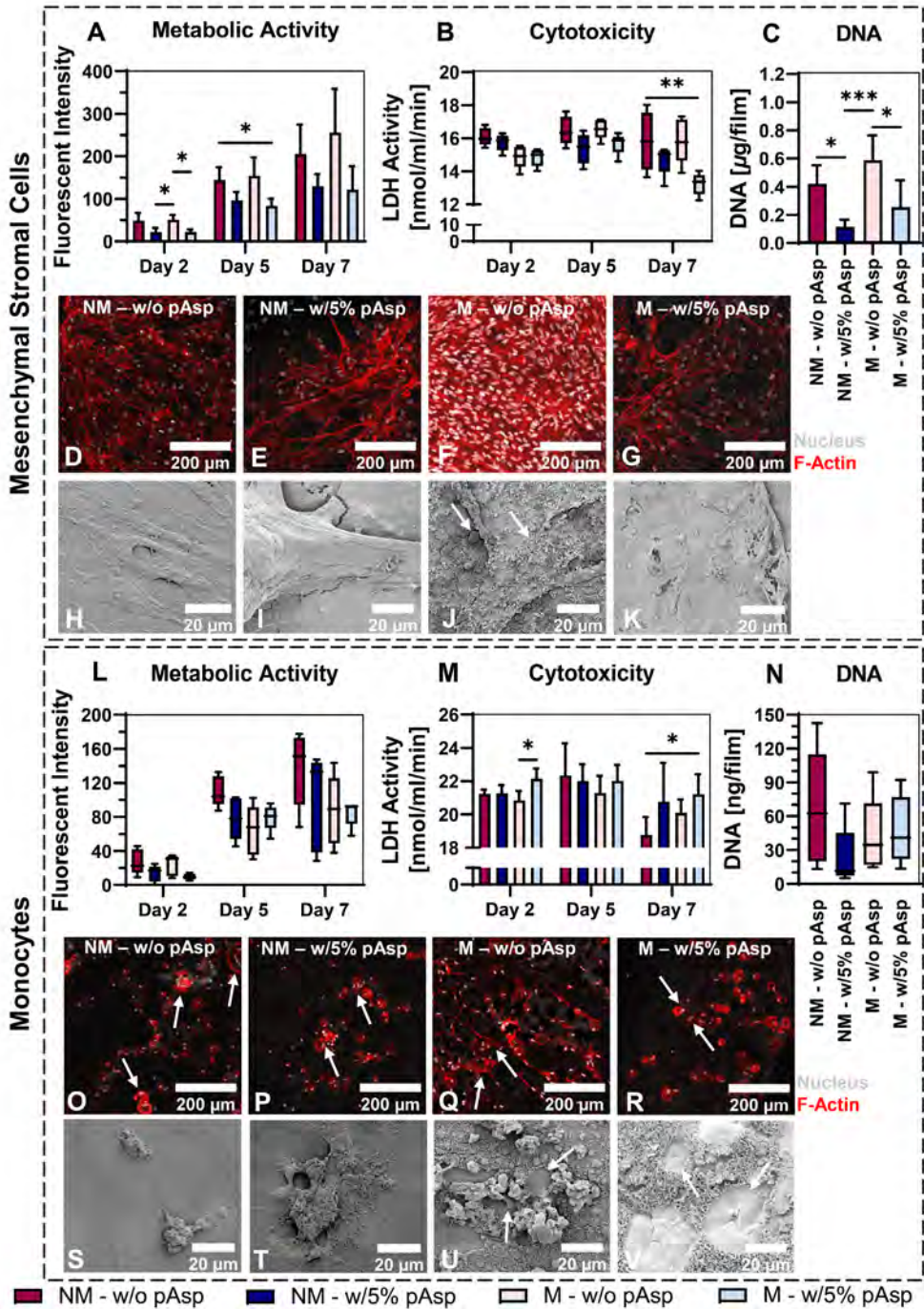


Figure 7.5. Cytocompatibility testing of mineralized SF films. (A) Metabolic activity measurements of MSCs using PrestoBlue™, $N = 5$, $p < 0.05$ (Two-way ANOVA and Tukey's post hoc tests within each time

point). **(B)** Cytotoxicity (cell death) for MSCs measured by LDH release in the medium, $N = 5$, $p < 0.05$ (Kruskal-Wallis and Dunn's post hoc tests). **(C)** DNA content per film for MSCs, $N = 5$, $p < 0.05$ (One-way ANOVA and Holm-Šidák's post hoc tests). **(D-G)** Micrographs of MSCs stimulated to undergo osteogenic differentiation, stained for F-Actin (red) and the nucleus (gray). **(H-K)** Visualization of MSC layer on films with SEM. **(L)** Metabolic activity measurements of MCs, $N = 5$, *ns* (Kruskal-Wallis test). **(M)** Cytotoxicity for MCs, $N = 5$, $p < 0.05$ (Two-way ANOVA and Tukey's post hoc tests within each time point). **(N)** DNA content per film for MCs, $N = 5$, *ns* (Kruskal-Wallis test). **(O-R)** Micrographs of MCs stimulated to undergo osteoclastic differentiation, stained for F-Actin (red) and the nucleus (gray). **(S-V)** Visualization of cells and resorption on films with SEM. ($*p < 0.05$, $**p < 0.01$, $***p < 0.001$, $****p < 0.0001$). Abbreviations: poly-aspartic acid (pAsp), non-mineralized (NM), mineralized (M), mesenchymal stromal cells (MSCs), monocytes (MCs), lactate dehydrogenase (LDH), scanning electron microscopy (SEM).

During this resorption phase, TRAP activity in mineralized co-cultured constructs was significantly higher from day 14 on. This indicates that the 3D mineralized surface promotes osteoclast activity, which was observed earlier (259). In addition to the TRAP measurements, mineral resorption, which could only be studied in radiopaque mineralized constructs, seemed increased during the same period and resorption sites were identified (**Figure 7.6E+H**, yellow arrows, and **Figure S7.6**).

As osteoclasts finished resorption around day 28, LDH activity as a measure for cell death, increased from day 21 to day 35 (**Figure 7.6C**). It is well accepted that differentiated osteoclasts have a relative short lifespan of about 2-3 weeks (232,289). Cell death after 21 days was therefore in line with our expectations. The increased osteoclastic activity in mineralized co-cultured constructs was however not associated with prolonged osteoclast survival (**Figure 7.6C**). On day 21 and 28, a higher LDH activity was even measured in cell supernatants of mineralized co-cultured constructs, indicating more cell death in these constructs. This was confirmed by DNA quantification at day 21 and 42, although not statistically significant (**Figure 7.7Q**). From day 21 on, osteogenic medium was provided which resulted in a further increase in mineralized volume in both scaffolds (**Figure 7.6D+G-H**). This increase was higher at all time points for mineralized scaffolds. In addition, formation sites in mineralized co-cultured constructs were localized over the entire scaffold and included spots which were previously resorbed, which might be attributed to osteoclast-osteoblast coupling (**Figure 7.6H**, yellow arrows and **Figure S7.6**). This could also explain the decrease in the cumulative percentage resorbed scaffold from day 21; resorption sites might have been filled with newly formed mineral (**Figure 7.6E**). Taken together, we were able to track the remodeling dynamics in our *in vitro* human bone model and these dynamics seemed to recapitulate the physiological bone remodeling cycle (**Figure 7.6F**).

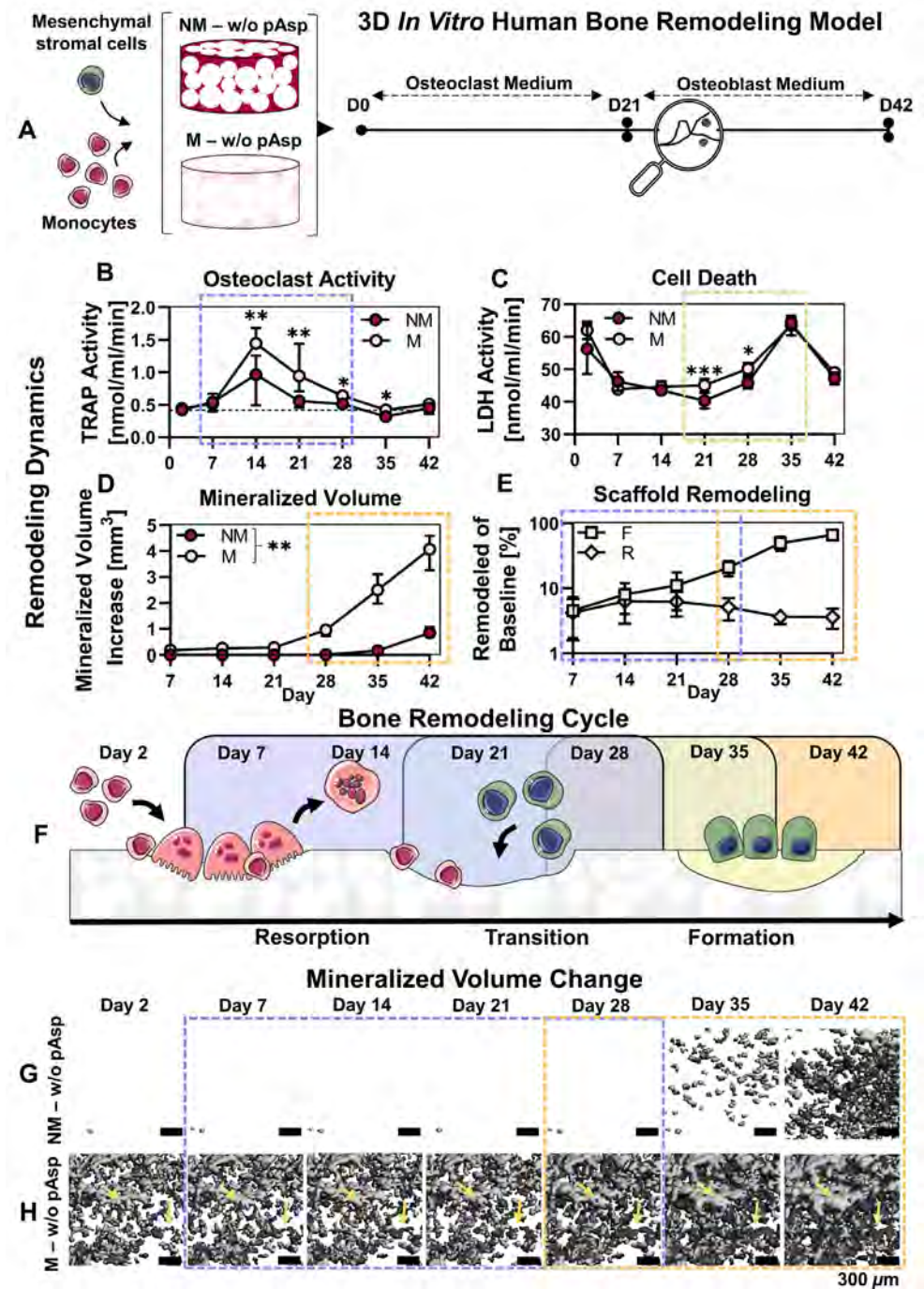


Figure 7.6. *In vitro* remodeling of mineralized silk fibroin scaffolds. (A) Experimental set-up. (B) TRAP activity quantification as a measure for osteoclast activity, dashed line represents the median value at

baseline (day 2), $N \geq 6$, $p < 0.05$ (Mann-Whitney U tests per time point with Bonferroni correction for multiple comparisons). (C) Cell death measured by LDH release in the medium, $N \geq 6$, $p < 0.05$ (Two-way ANOVA and Tukey's post hoc tests within each time point). (D) Mineralized volume measured with μ CT, $N = 8$, $p < 0.01$ for each time point (Mann-Whitney U tests per time point with Bonferroni correction for multiple comparisons). (E) Cumulative mineral formation (F) and resorption (R) as a percentage of the baseline scaffold, obtained after registration of μ CT scans, $N \geq 6$. (F) The physiological bone remodeling cycle described in literature and the similarities to the remodeling dynamics found in the presented model. (G) Mineralization over time visualized with μ CT for non-mineralized scaffolds. (H) Resorption and mineralization over time visualized with μ CT for mineralized scaffolds. Yellow arrows represent remodeling/coupling sites. Dashed boxes in figure represent the respective remodeling phases (purple = resorption, green = translation, orange = formation). (* $p < 0.05$, ** $p < 0.01$, *** $p < 0.001$, **** $p < 0.0001$). Abbreviations: poly-aspartic acid (pAsp), non-mineralized (NM), mineralized (M), tartrate resistant acid phosphatase (TRAP), lactate dehydrogenase (LDH), micro-computed tomography (μ CT), day (D). The bone remodeling cycle illustration was modified from Servier Medical Art, licensed under a Creative Commons Attribution 3.0 Generic License (<http://smart.servier.com/>, accessed on 8 July 2021).

Next, we characterized cell differentiation and organic matrix formation by the cells in the model. The presence of multinucleated cells was confirmed at day 21 and day 42 for both conditions by staining of the nucleus and the cytoskeleton (**Figure 7.7A-D**, white arrows). Osteoclast-like cells were also observed on the scaffold surface after 21 days of culture with SEM (**Figure 7.7E+F**, white arrows). These cells seem to resorb the mineral surface on mineralized scaffolds (**Figure 7.7F**). The osteoclast resorption marker cathepsin K was also highly expressed by cells on mineralized scaffolds in the resorption phase, indicating more functional osteoclasts on these scaffolds (day 21, **Figure 7.7J**). Interestingly, an excess of osteopontin, which can be produced by both osteoclasts and osteoblasts, was found in mineralized constructs after 21 days of culture. *In vivo*, osteopontin is also found on mineralized surfaces and is a major component of the cell-matrix interface (cement line) (372). Osteoclastic osteopontin is important for sealing zone formation and osteoclast migration (97,323,373). On mineralized scaffolds, osteoclasts have likely secreted osteopontin to allow for attachment and subsequent resorption (97). Osteopontin is also known as mineralization inhibitor in its phosphorylated state (381). However, excessive mineralization in mineralized scaffolds was still observed, meaning that the amount of osteopontin was not sufficient or that osteopontin was de-phosphorylated by osteoclasts through TRAP (374). After 42 days, osteopontin was present in both conditions and osteogenic differentiation was confirmed by the presence of nuclear runt-related transcription factor 2 (RUNX2). In addition, little collagen formation was observed at both time-points and in both conditions (**Figure 7.7A-D**), but mostly in the mineralized co-cultured constructs after 42 days of culture (**Figure 7.7D**). By measuring PICP in the medium, collagen formation at day 21 and 42 was quantified. Collagen type I formation was comparable for non-mineralized and mineralized co-cultured constructs (**Figure 7.7R**). While

osteogenic differentiation medium was supplied from day 21, no further increase in collagen synthesis was observed. Collagen synthesis even tended to decrease in mineralized co-cultured constructs on day 42. This might be explained by a lack of mechanical loading in the system, which is crucial for *in vivo* bone adaptation and *in vitro* woven bone formation including collagen synthesis (116,375). Another explanation might be the excessive mineralization upon osteogenic stimulation in mineralized co-cultured constructs (**Figure 7.6D**). Mineralization occurred over the entire scaffold surface (**Figure S7.6**). As such, remodeling might have been terminated and cells therefore have undergone apoptosis, have been terminally differentiated into quiescent bone lining cells, or have been embedded into mineralized matrix and differentiated into osteocytes (376). This could also explain the differences found in ALP activity from the construct lysates (**Figure 7.7S**). Cells in non-mineralized constructs have clearly undergone differentiation towards ALP producing and thus mineralizing osteoblasts. As *in vitro* mineralization with osteogenic differentiation medium occurs after dephosphorylation of β -glycerophosphate by ALP, it is expected that the increase in mineralization for mineralized constructs was the result of ALP synthesis by the cells in these constructs. This could however not be detected on day 42, underlining the hypothesis that remodeling has been terminated on the mineralized SF scaffolds (137). Interestingly, a statistically significant higher sulphated GAG content was found on day 21 (**Figure 7.7T**). These GAGs were visualized between the trabecular-like structures (**Figure S7.7**). Although the origin of these GAGs is unclear, they have been shown to inhibit collagen degradation by osteoclastic cathepsin K, promote osteogenic differentiation and bone-like matrix formation, and promote mineralization (377–380).

7.3 Discussion

Current *in vitro* 3D bone remodeling models often lack the spatiotemporal investigation of the remodeling events (*i.e.*, resorption, transition, formation) by starting their culture with osteoblast (progenitors) (259,260), or by only looking at osteoclast and osteoblast markers with *e.g.*, gene expression or enzymatic activity assays rather than at their functionality to resorb and form a bone-like matrix (43,293). To enable the investigation of functional cell-matrix interactions and their spatiotemporal dynamics, materials should be developed that support osteoclast and osteoblast functionality. Therefore, we developed a bioinspired scaffold using SF as fibrous organic protein, that was mineralized with hydroxyapatite under influence of the non-collagenous protein mimic pAsp.

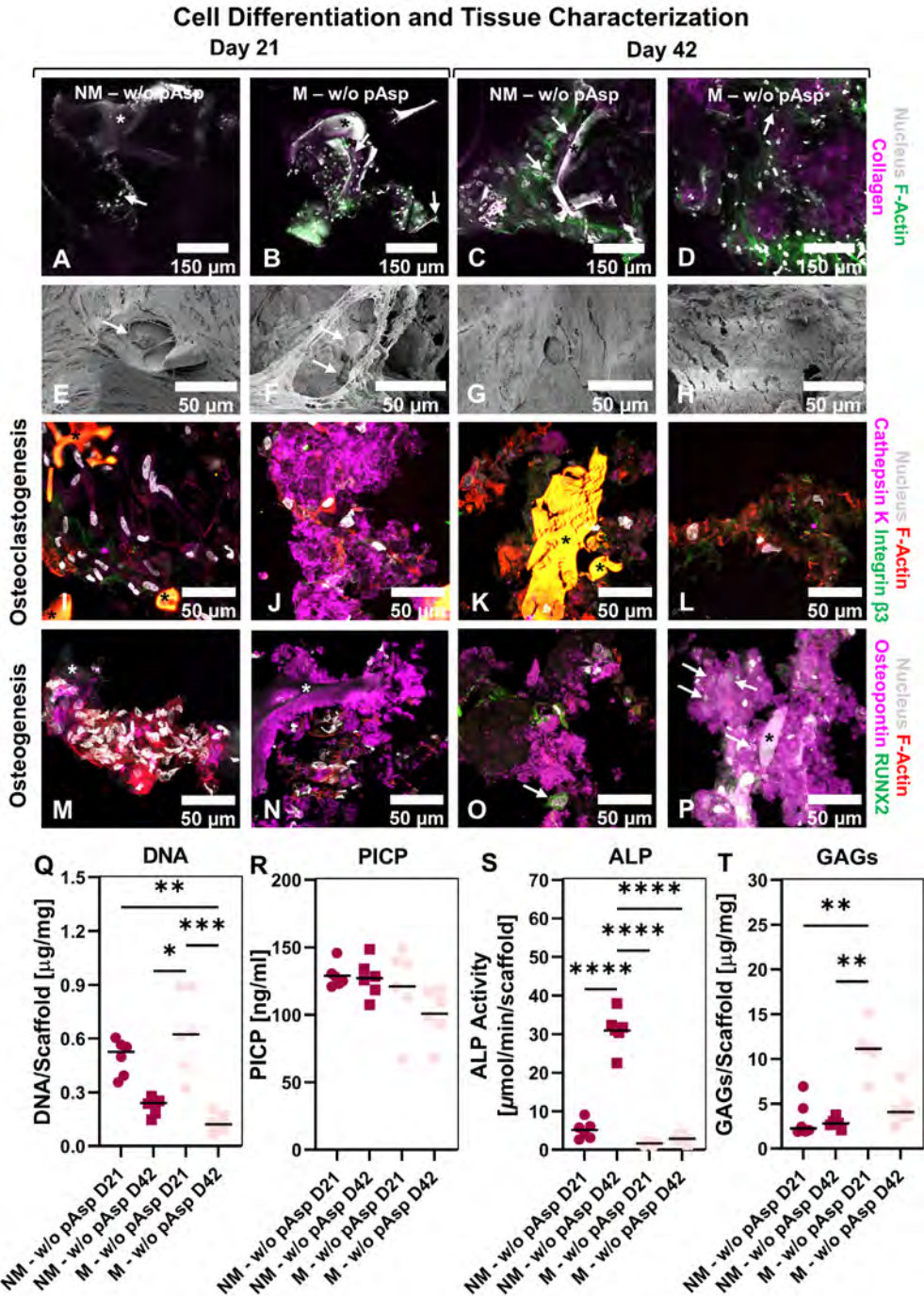


Figure 7.7. Cell differentiation and tissue formation in *in vitro* bone remodeling model. (A–D) Micrographs of 3D remodeling constructs, stained for collagen (magenta), F-Actin (green), and the nucleus (gray). White

arrows indicate osteoclasts. **(E-H)** Morphology of and resorption sites on co-cultured constructs visualized with SEM. White arrows indicate osteoclasts. **(I-L)** Immunohistochemical analysis of sections for F-Actin (red), the nucleus (gray), and osteoclast markers cathepsin K (magenta) and integrin- β 3 (green). **(M-P)** Immunohistochemical analysis of sections for F-Actin (red), the nucleus (gray), and osteogenic markers osteopontin (also produced by osteoclasts, magenta) and RUNX2 (green). Asterisks indicate the scaffold trabeculae. **(Q)** DNA quantification in co-cultured constructs, $N = 6$, $p < 0.05$ (Kruskal-Wallis and Dunn's post hoc tests). **(R)** PICP quantification as a measure for collagen formation in co-cultured constructs, $N = 6$, *ns* (One-way ANOVA). **(S)** ALP activity quantification as a measure for osteoblast activity, $N = 6$, $p < 0.05$ (One-way ANOVA and Holm-Šidák's post hoc tests). **(T)** GAG content quantification, $N = 6$, $p < 0.05$ (Kruskal-Wallis and Dunn's post hoc tests). (* $p < 0.05$, ** $p < 0.01$, *** $p < 0.001$, **** $p < 0.0001$). Abbreviations: poly-aspartic acid (pAsp), non-mineralized (NM), mineralized (M), day (D), runt-related transcription factor 2 (RUNX2), pro-collagen 1 c-terminal propeptide (PICP), alkaline phosphatase (ALP), glycosaminoglycan (GAG).

Like as in collagen, pAsp in the mineralization solution was instrumental for mineral infiltration into the SF. As a result, minerals appeared inside and on the surface of the SF films and trabecular-like structures within the scaffolds. This is comparable to bone, where minerals appear inside (intrafibrillar) and outside (extrafibrillar) to the collagen fibrils (78). In collagen, pAsp functions as a mineralization inhibitor in solution; guiding minerals to the collagen gap-region where the confinement induces mineral nucleation (54). Here, we have shown that pAsp functions similarly for the mineralization of SF. One hypothesis for this biomimetic mineralization is that the hydrophilic regions in SF allow for PILP or amorphous calcium phosphate infiltration, resulting in mineral nucleation within the SF structure (353). In an attempt to unravel the mechanism by which SF mineralizes, researchers have decomposed SF into its hydrophobic and hydrophilic regions and mixed them separately into dense collagen gels (353). Only the hydrophilic SF component induced mineralization of the collagen gel upon exposure to SBF (353). An attempt to biomimetically mineralize SF was done by Jin et al., (2015) (381). They found that in the presence of a SF template in the form of a hydrogel, mineral crystals were uniformly shaped and oriented, suggesting that mineral crystal growth was confined by SF (381). As such, hydrophilic SF regions could provide the necessary nucleation sites while hydrophobic regions may provide confinement for crystal growth, a mechanism which has recently been described for collagen mineral growth (382). As these hydrophilic SF regions have shown to promote mineralization when mixed with dense collagen gels, mineral nucleation in SF is likely not (solely) induced by confinement (353).

When pAsp was merged into the SF, pAsp could not improve mineral distribution through the scaffold. The addition of pAsp to the material even seemed to induce more heterogeneous mineralization (chunks instead of a layer). Three times before (to our knowledge), the influence of SF – pAsp materials on mineralization has been studied (360,361). Comparable to our results, Kim et al. (2008) (361) found chunks of mineral

on the surface of their scaffold when ~ 9 wt% pAsp was mixed with the SF. Ma et al., (2010) (360) also found a comparable result for SF with 5% pAsp added. The minerals became more homogeneous when higher concentrations were added (*i.e.*, 15 wt%) (360), something that was also observed by Li et al., (2005) (*i.e.*, 20 wt% compared to 1 wt%) (359). As there was no clear cytotoxic effect of the addition of pAsp to the SF in our study, the addition of higher concentrations of pAsp needs to be investigated. This might further increase the hydrophilicity and therefore also improve cell proliferation, osteoprogenitor differentiation, and osteoclastic resorption as reported in literature (365–368). These effects were not observed with the addition of 5% pAsp. However, the stiffness is expected to decrease further with higher concentrations of pAsp which could affect cell behavior (383). To further improve the mineral distribution through large scaffolds, perfusion of the mineralization solution needs to be explored (384).

Other *in vitro* remodeling models have used synthetic (mineralized) polymers, organic matrices or inorganic materials in the form of hydrogels or woven scaffolds (43). When composite materials are used for *in vitro* remodeling studies, organic materials are often mineralized by blending it with inorganic salts during fabrication or by coating it with supersaturated solutions (222,385). As such, most 3D materials used for current *in vitro* remodeling models lack mimicry with physiological bone. While biom mineralized collagen type I scaffolds, featuring all components of physiological bone, are a promising material for *in vitro* bone remodeling models, they are often difficult to fabricate at the high density found in physiological bone. Recently, researchers looked at osteoclastic differentiation and resorption on such scaffolds. They found that despite its biomimicry, osteoclasts were unable to resorb the scaffold, probably as a result of the low fiber density (386). Here, we found that mineralized SF could support osteoclastic resorption. Mineralized SF scaffolds also seemed to stimulate a more physiologically relevant cell phenotype, indicated from their cathepsin K, osteopontin and glycosaminoglycan synthesis. In addition, using SF rather than collagen type I allows for a differential analysis of supplied and formed material (116). As altered collagen type I formation is a hallmark for bone pathologies like osteogenesis imperfecta and osteoporosis (40,41), the ability to study its formation should be considered for *in vitro* bone models (110). One limitation of the use of solely composite materials is likely the reduced osteoclast-osteoblast coupling. *In vivo*, coupling includes besides secreted, cell-bound, and topographical cues, also the release of growth factors from the bone matrix (95). Factors like transforming growth factor β (TGF- β), bone morphogenetic protein 2 (BMP-2), platelet derived growth factor (PDGF), and insulin-like growth factor (IGF) that are deposited by osteoblasts, stored in the matrix and released upon resorption, potentially stimulate MSC migration and osteogenic differentiation (95). While the use of native bone matrix could facilitate full investigation of cell-matrix and cell-cell

interactions, proper decellularization needs to be performed as osteocyte (90% of bone cell population) apoptosis could induce pathological osteoclastic resorption (387). Introducing a pre-model phase where bone-like matrix is built by osteoblasts before remodeling is initiated might overcome these limitations (230,259). However, these models are time consuming, laborious, and might face reproducibility issues as the to be remodeled matrix is already susceptible for variation. Such complex models might improve the mimicry to bone remodeling *in vivo* but might in parallel complicate drug screening *in vitro*.

In the *in vitro* model presented in this study, coupling was observed by re-mineralization of resorption sites after osteogenic medium was provided. Mineralization was however not limited to resorption sites and the total mineralized volume was therefore increased over time. As healthy bone remodeling is characterized by balanced resorption and formation, our model does probably not yet fully represent the homeostatic physiological bone remodeling environment. While mineral resorption and formation was unbalanced in mineralized scaffolds, collagen synthesis as part of the osteoblastic formation seemed to stay behind with mineralization. Only little collagen formation could be detected in our model, despite the presence on osteogenic differentiation factors after 42 days. *In vivo*, the bone formation phase takes about 4 – 5 months and starts with osteoid (*i.e.*, collagen and non-collagenous proteins) formation followed by mineralization (388). Most likely, the addition of exogenous phosphate with the β -glycerophosphate supplement in osteogenic medium steers this balance towards mineralization with limited osteoid formation and thus osteoblastic control (110). As in our model osteoclasts dissolved mineral from the scaffold, phosphate might have been released into the medium and the additional supplementation with β -glycerophosphate might have been redundant. The influence and the optimization of environmental factors (*e.g.*, supplied medium or mechanical loading) should therefore be considered for future studies. For example, applying fluid shear stress to the cells to stimulate the osteoid formation and thereby potentially improving osteoblastic control over mineralization (90,110,116,117).

7.4 Conclusion

Taken together, we have successfully exploited collagen mineralization techniques to mineralize SF films and scaffolds. In this regard, pAsp was instrumental to guide minerals into the SF structure. Mineralized SF scaffolds have subsequently demonstrated to support osteoclastic differentiation and resorption and to enhance mineralization. Functional cell-matrix interactions and their dynamics were successfully tracked with mainly non-destructive methods (μ CT and medium analyses). The

observed remodeling dynamics recapitulated the physiological bone remodeling cycle. Therefore, our *in vitro* bone remodeling model may reduce animal experiments and advance *in vitro* drug development for bone remodeling pathologies like osteoporosis where cell-matrix interactions need to be targeted.

7.5 Experimental Section

7.5.1 Preparation of silk fibroin films and scaffolds

Bombyx mori L. silkworm cocoons were degummed by boiling them in 0.2 M Na₂CO₃ for 1 h. After drying, silk was dissolved in 9 M LiBr, filtered, and dialyzed against UPW for 36 h using SnakeSkin Dialysis Tubing (11532541, Thermo Fisher Scientific, Breda, The Netherlands). After dialysis, the mass fraction of SF in solution was determined by measuring the dry weight per ml SF solution after lyophilization. For SF w/5% pAsp films and scaffolds, 5 wt% poly-aspartic acid sodium salt (P3418, Sigma-Aldrich, Zwijndrecht, The Netherlands) was mixed into the dialyzed SF solution. SF solution was then frozen at -80° C and lyophilized for 7 days. Lyophilized SF and SF with 5 wt% pAsp were dissolved in hexafluoro-2-propanol (003409, Fluorochem, Hadfield, UK) at a concentration of 17% (w/v) and casted onto 10 mm diameter cover slips (for SF films), or in scaffold molds containing NaCl granules with a size of 250-300 μm as template for the pores (for SF scaffolds). Hexafluoro-2-propanol in SF films was directly allowed to evaporate for 3 days. Scaffold molds were first covered to improve the SF blending with the granules. After 3 h, covers were removed, and hexafluoro-2-propanol was allowed to evaporate for 7 days. After complete evaporation, β-sheets were induced by submerging SF films and SF-salt blocks in 90% MeOH for 30 min. NaCl was dissolved from the scaffolds in UPW, resulting in porous sponges. These sponges were cut into scaffolds of 3 mm in height and 5 mm in diameter.

7.5.2 Mineralization treatment

For mineralization of scaffolds and films, a 10x SBF stock was prepared as described by A.C. Tas and S.B. Bhaduri (2004) (356). Just prior to mineralization, mineralization solution was prepared by adding 100 μg/ml pAsp to 10x SBF, followed by the addition of NaHCO₃ until a final concentration of 10 mM, both under vigorous steering. This resulted in a mineralization solution with a pH of ~6.3. For 10X SBF controls, pAsp was not added to the mineralization solution. Films and scaffolds were incubated for 2 weeks at 37 °C on an orbital shaker at 150 RPM in mineralization solution with a solution replenishment after 1 week. Mineralization solution volume was calculated from the apparent surface area of the sample as described by T. Kokubo and H. Takadama (2006) (355), where r is the radius of the sample and h the height (**Equation 7.1**). SF films were considered 2D.

$$\text{Mineralization medium volume} = \frac{2\pi r(r+h)}{10} \quad (7.1)$$

After mineralization, scaffolds and films were washed 3 x 15 min in an excess of UPW. Films and scaffolds for cell experiments were sterilized by autoclaving in phosphate buffered saline (PBS) at 121° C for 20 min.

7.5.3 Cell culture experiments

Monocyte isolation

Peripheral blood mononuclear cells (PBMCs) were isolated from a human peripheral blood buffy coat of one healthy donor (Sanquin, Eindhoven, The Netherlands; collected under their institutional guidelines and with informed consent per declaration of Helsinki). The buffy coat (~50 ml) was diluted with 0.6% w/v sodium citrate in PBS (citrate-PBS) until a final volume of 200 ml and layered per 25 ml on top of 10 ml Lymphoprep™ (07851, StemCell technologies, Köln, Germany) in 50 ml centrifugal tubes. After density gradient centrifugation (20 min at 800x g, lowest break), PBMCs were collected, resuspended in citrate-PBS, and washed four times in citrate-PBS supplemented with 0.01% bovine serum albumin (BSA, 10735086001, Sigma-Aldrich). PBMCs were frozen at 10⁵ cells/ml in freezing medium containing RPMI-1640 (RPMI, A10491, Thermo Fisher Scientific), 20% fetal bovine serum (FBS, BCBV7611, Sigma-Aldrich) and 10% dimethyl sulfoxide (DMSO, 1.02952.1000, VWR, Radnor, PA, USA) and stored in liquid nitrogen until further use. Before MC isolation, PBMCs were thawed, collected in medium containing RPMI, 10% FBS (BCBV7611, Sigma-Aldrich) and 1% penicillin-streptomycin (p/s, 15070063, Thermo Fisher Scientific), and after centrifugation resuspended in isolation buffer (0.5% w/v BSA in 2mM EDTA-PBS). MCs were enriched from PBMCs with manual magnetic activated cell separation (MACS) using the Pan Monocyte Isolation Kit (130-096-537, Miltenyi Biotec, Leiden, Netherlands) and LS columns (130-042-401, Miltenyi Biotec) according to the manufacturer's protocol, and directly used for experiments.

Mesenchymal stromal cell isolation and expansion

MSCs were isolated from human bone marrow (1M-125, Lonza, Walkersville, MD, USA; collected under their institutional guidelines and with informed consent) and characterized for surface markers and multilineage differentiation, as previously described (124). MSCs were frozen at passage 4 with 1.25*10⁶ cells/ml in freezing medium containing FBS (BCBV7611, Sigma-Aldrich) with 10% DMSO and stored in liquid nitrogen until further use. Before experiments, MSCs were thawed, collected in high glucose DMEM (hg-DMEM, 41966, Thermo Fisher Scientific), seeded at a density of 2.5*10³ cells/cm² and expanded in medium containing hg-DMEM, 10% FBS (BCBV7611, Sigma-Aldrich), 1% Antibiotic Antimycotic (anti-anti, 15240, Thermo

Fisher Scientific), 1% Non-Essential Amino Acids (11140, Thermo Fisher Scientific), and 1 ng/mL basic fibroblastic growth factor (bFGF, 100-18B, PeproTech, London, UK) at 37 °C and 5% CO₂. After 9 days, cells were detached using 0.25% trypsin-EDTA (25200, Thermo Fisher Scientific) and directly used for experiments at passage 5.

Two-dimensional monocyte and mesenchymal stromal cell mono-cultures

For 2D MC and MSC mono-cultures, films were pre-wetted overnight at 37 °C in osteoclast control medium (α -MEM (41061, Thermo Fisher Scientific), 10% human platelet lysate (hPL, PE20612, PL BioScience, Aachen, Germany) and 1% anti-anti) and osteogenic control medium (lg-DMEM (22320, Thermo Fisher Scientific), 10% hPL and 1% anti-anti). Before seeding, medium was removed, and cells were seeded by pipetting 5 μ l of cell suspension (1.5×10^5 cells/5 μ l for MCs and 2.5×10^4 cells/5 μ l for MSCs) onto the films. Cells were allowed to attach for 90 min at 37 °C and every 20 minutes a small droplet of the respective control medium was added to prevent for drying of the films. MCs were first cultured in priming medium (osteoclast control medium + 50 ng/ml macrophage colony-stimulating factor (M-CSF, 300-25, PeproTech)). After 48 hours, priming medium was replaced by osteoclast medium (priming medium + 50 ng/ml receptor activator of nuclear factor κ B ligand (RANKL, 310-01, PeproTech)) to induce osteoclastic differentiation. MSCs were stimulated to undergo osteogenic differentiation with osteogenic medium (osteogenic control medium + 10 mM β -glycerophosphate (G9422, Sigma-Aldrich), 50 μ g/ml ascorbic acid-2-phosphate (A8960, Sigma Aldrich), and 100 nM dexamethasone (D4902, Sigma-Aldrich)). Cells were kept in culture for 7 days at 37 °C and 5% CO₂, medium was replaced on day 2 and 5 and medium samples were collected and stored at -80 °C. Films were sacrificed for analyses after 2 days and 7 days of culture.

Three-dimensional monocyte-mesenchymal stromal cell co-culture

Scaffolds were pre-wetted overnight at 37 °C in osteoclast control medium. Before seeding, medium was removed, and cells were resuspended in osteoclast control medium (2.5×10^6 MCs and 5×10^5 MSCs/20 μ l) and seeded by pipetting 20 μ l of cell suspension onto the scaffolds. Cells were allowed to attach for 90 min at 37 °C and every 20 minutes a small droplet of osteoclast control medium was added to prevent for drying of the scaffolds. The cell-loaded scaffolds were statically cultured for 6 weeks at 37 °C and 5% CO₂ in custom-made bioreactors, which allowed for μ CT scanning during the culture period. Cells were cultured in osteoclast medium for the first 3 weeks (priming medium for the first 48 h whereafter medium was replaced by osteoclast medium). After 3 weeks, medium was switched to osteogenic medium to stimulate osteogenic differentiation. Medium was replaced 3x per week and medium samples were

collected weekly and stored at $-80\text{ }^{\circ}\text{C}$. Constructs were sacrificed for analyses after 3 weeks (day 21) and after 6 weeks (day 42) of culture.

7.5.4 Analyses

Contact angle measurements

Water contact angles were measured for SF films w/o pAsp and w/5% pAsp on a Dataphysics OCA30 contact angle goniometer ($N = 5$ per group). A $2\text{ }\mu\text{l}$ droplet of UPW was deposited on the films and after approximately 2 s the contact angles were determined by fitting the contour of the droplet using OCA20 software.

Mineral precipitations in medium

Mineralization solution samples were collected from mineralized films after 1 week and 2 weeks of mineralization ($N = 8$ per condition). Mineral precipitation in the mineralization solution was determined by measuring the optical density of $100\text{ }\mu\text{l}$ sample in a 96-wells assay plate at 600 nm using a plate reader (SynergyTM HTX, Biotek).

Calcium assay

Films ($N = 5$ per condition) were lyophilized and incubated for 48 h in 5 wt% trichloroacetic acid (TCA, T6399, Sigma-Aldrich). Scaffolds ($N = 5$ per condition) were lyophilized, weighted, disintegrated in 5 wt% trichloroacetic using 2 steel balls and a mini-beadbeaterTM (Biospec, Bartlesville, OK, USA), and subsequently incubated for 48 h. After incubation, a calcium assay (Stanbio, 0150-250, Block Scientific, Bellport, NY, USA) was performed to quantify calcium content in both films and scaffolds according to the manufacturer's instructions. Briefly, $95\text{ }\mu\text{l}$ Cresolphthalein complexone reaction mixture was added to $5\text{ }\mu\text{l}$ sample and incubated at room temperature for 1 min. Absorbance was measured at 550 nm with a plate reader and absorbance values were converted to calcium concentrations using standard curve absorbance values.

Mechanical analyses

Mechanical tests of films ($N = 5$ per condition) were performed with a Piuma nanoindenter (Optics 11, Amsterdam, The Netherlands) equipped with a spherical indenter tip probe with a radius of $29.1\text{ }\mu\text{m}$ and a stiffness of 204.6 N/m (p190853, Optics 11). Films were tested in PBS and an indentation of $10\text{ }\mu\text{m}$ depth was performed at 4 random locations per film and the Young's modulus was derived by fitting the load-depth curves to the Hertzian contact model between 0% and 30% of the maximum load point, assuming a Poisson's ratio of 0.4.(397,398) Scaffolds ($N = 5$ per condition) were mechanically tested in PBS by a full unconfined compression test using a 500 N load cell on a Criterion 42 mechanical test system (MTS, Berlin, Germany). Samples were compressed at a rate of 17% displacement/min until a displacement of 60% from the sample height was reached. The Young's modulus was derived by a linear fit to the

load-displacement curves between 2% and 10% displacement using MATLAB (version 2019b, The MathWorks Inc., Natick, MA, USA).

Scanning electron microscopy

Samples ($N = 3-4$ per experiment, time point, and condition) were fixed in 2.5% glutaraldehyde in 0.1 M sodium cacodylate buffer (CB) for 4 h and then washed in CB. For the characterization of (mineralized) scaffolds, both 3D samples and cross-sections were prepared. For cross-sections, scaffolds were after fixation soaked for 15 minutes in each 5% (w/v) sucrose and 35% (w/v) sucrose in PBS. Scaffolds were embedded in Tissue Tek® (Sakura) and frozen with liquid N₂. Cryosections were prepared with a thickness of 5 μm on 10 x 10 mm indium tin oxide (ITO) coated glass slides (576352, Sigma-Aldrich). Tissue Tek® was removed by washing with distilled water. Co-cultured scaffolds ($N = 2$ out of 4 per time point and condition) were stained and imaged with confocal microscopy as described below before dehydration. All samples were dehydrated with graded ethanol series (37%, 67%, 96%, 3 x 100%, 15 minutes each), followed by a hexamethyldisilazane (HDMS)/ethanol series (1:2, 1:1, 2:1, 3 x 100% HDMS, 15 minutes each). Samples were coated with 20 nm gold and imaging was performed in high vacuum, at 10 mm working distance, with a 5kV electron beam (Quanta 600F, FEI, Eindhoven, The Netherlands).

Alizarin red

Alizarin red staining was performed on films, cross-sections of films, and cross-sections of scaffolds ($N = 3$ per experiment and condition). Samples were fixed overnight in 3.7% neutral buffered formaldehyde and washed twice with PBS. Samples for cross-sections were prepared as described above (Section SEM) and cryosections were sliced with a thickness of 5 μm on EpreDia™ SuperFrost Plus™ Adhesion slides (Fisher Scientific, Breda, The Netherlands). Samples were washed in distilled water and stained for 15 min in 2% w/v Alizarin Red (ab146374, Abcam, Cambridge, UK) in distilled water at a pH of ~4.2. Films were directly washed in distilled water and imaged upon staining. Cross-sections were first dehydrated in pure acetone, acetone/xylene (1:1) and pure xylene, and mounted with Entellan™ (1.07960, Sigma-Aldrich). Samples were imaged with bright field microscopy (Zeiss Axio Observer Z1 with a 20x/0.8 Plan-Apochromat objective or a 5x/0.13 EC Epiplan-Neofluar objective).

Micro-computed tomography

For μCT scanning, wet and dry mineralized scaffolds ($N = 5$ per condition) and co-cultured constructs ($N = 8$ per condition) were scanned and analyzed with a μCT100 imaging system (Scanco Medical, Brüttisellen, Switzerland). Scanning was performed with an energy level of 45 kV_p, intensity of 200 μA, integration time of 300 ms and with twofold frame averaging. To reduce part of the noise, a constrained Gaussian filter was

applied to all scans with filter support 1 and filter width sigma 0.8 voxel. For mineralized scaffolds (both wet and dry), scanning was performed at an isotropic resolution of 11.4 μm . Filtered images were segmented, for wet scaffolds to detect mineralization (global threshold of 27% of the maximum grayscale value) and for dry scaffolds to study the morphology (global threshold of 22% of the maximum grayscale value). Unconnected objects smaller than 30 voxels were removed through component labeling. Morphology parameters were computed from dry scaffolds using the scanner manufacturer's image processing language (IPL) (131). To determine the pore size distribution, the image background was filled with largest possible spheres of which the diameter was derived. To quantify the degree of connectivity between trabecular-like structures, the mean connectivity density was calculated per scaffold according to a previously described method (389). In addition, porosity, mean trabecular thickness, mean trabecular space and average trabecular number per mm were derived per scaffold after triangulation of segmented scaffolds using the plate model. To track mineralization, co-cultured scaffolds were scanned weekly after an initial baseline scan (day 2) at an isotropic resolution of 17.2 μm . Filtered scans were segmented at a global threshold of 24% of the maximum grayscale value and unconnected objects smaller than 30 voxels were removed through component labelling. In addition, follow-up images of the radiopaque mineralized co-cultured scaffolds were registered to baseline images such that voxels at the surface of the scaffold were categorized into resorption site, formation site, or unchanged site (390). The scaffold was segmented at a global threshold of 24% of the maximum grayscale value and remodeled scaffold surface was segmented at a global threshold of 7.5% of the maximum grayscale value, which was chosen after registration of cell-free construct images in such a way that resorption and formation were below $\sim 1.5\%$ of the total volume. To reduce noise, only a minimum cluster of 2 resorbed or formed voxels were included in the analyses, meaning that only resorption and formation sites of more than $\sim 30 \mu\text{m}$ in length could be detected.

Raman microscopy

Scaffold cross-sections were analyzed with Raman Microscopy. Scaffolds ($N = 3$) were soaked for 15 minutes in each 5% (w/v) sucrose and 35% (w/v) sucrose in phosphate buffered saline (PBS). Samples were embedded in Tissue Tek® (Sakura) and quickly frozen with liquid N_2 . Cryosections were prepared with a thickness of 10 μm on microscope glasses covered with aluminum foil. Sections were washed three times with distilled water and air dried. Raman microscopy was subsequently performed on a Witec Alpha 300 R instrument (Witec, Ulm, Germany). Spectra were obtained using a 457 nm excitation laser at 8 mW. The light was split through a 600 mm^{-1} grating resulting in a spectral resolution of 2.8 cm^{-1} . Spectral imaging was performed at a resolution of 1 μm at an exposure time of 1 s. The obtained data were analyzed using the Witec Project 5

software (Witec). Samples were background corrected with the automatic shape function in the software, using shape size 400. Component analysis was subsequently performed, and the two or three major components were presented. The spectra are formed by averaging all the pixels containing the unique chemical signature. After extraction the data was transferred to Origin (Origin Pro 2021, OriginLab Corporation, Northampton, MA, USA) where the spectra were normalized to the Amide I 1660 cm^{-1} peak for visualization.

X-ray photoelectron spectroscopy

XPS spectra were obtained of air-dried scaffolds using a Thermo Scientific K-Alpha spectrometer (Thermo Fisher Scientific) equipped with a 180° double-focusing hemispherical analyzer with a 128-channel detector that uses an aluminum anode (Al $K\alpha$, 1486.7 eV, 72 W) and monochromatic, small-spot X-ray source. The survey scans used a pass energy of 200 eV and the atomic region scans 50 eV. The atom compositions were quantified from the survey spectra and the ratio of different carbon bonds were determined from the carbon region spectra using CasaXPS software (version 2.3.23).

Biochemical content analyses

Lyophilized mono-cultured films ($N = 5$ per condition) and co-cultured constructs ($N = 6$ per time point and per condition) were digested overnight in papain digestion buffer (containing 100 mmol phosphate buffer, 5 mmol L-cysteine, 5 mmol EDTA and 140 $\mu\text{g}/\text{ml}$ papain (P4762, Sigma-Aldrich)) at 60°C . DNA was quantified using the Qubit Quantification Platform (Invitrogen) with the high sensitivity assay, according to the manufacturer's instructions. GAG content in co-cultured constructs was measured using a dimethyl methylene blue (DMMB) assay (157) with shark cartilage chondroitin sulfate (C4284, Sigma-Aldrich) as a reference. Absorbance was read at 540 nm and 595 nm using a plate reader. Absorbance values were subtracted from each other (540-595) and converted to GAG content using standard curve absorbance values.

Lactate dehydrogenase activity

LDH activity was measured over time in cell supernatants of mono-cultured films ($N = 5$) and co-cultured constructs ($N = 6 - 12$ per condition, 3 samples per bioreactor containing 4 scaffolds). A 100 μl supernatant sample or NADH (10107735001, Sigma-Aldrich) standard was incubated with 100 μl LDH reaction mixture (11644793001, Sigma-Aldrich) in 96-wells assay plates. Absorbance was measured after 5-, 10- and 20-min at 490 nm, and LDH activity was calculated between 5- and 20- min reaction, using standard curve absorbance values.

PrestoBlue™ assay

Mono-cultured films were incubated with a 10% v/v PrestoBlue™ (A13262, Thermo Fisher Scientific) in osteogenic (for MSCs) or osteoclast (for MCs) control medium solution for 1 h at 37 °C in the dark. Fluorescence was measured with a plate reader (excitation: 530/25 nm, emission 590/35 nm). Measured fluorescence was corrected for blank medium samples.

Tartrate resistant acid phosphatase activity

TRAP was measured over time in cell supernatants of co-cultured constructs ($N = 6 - 12$ per condition, 3 samples per bioreactor containing 4 scaffolds). A 10 μ l supernatant sample or p-nitrophenol standard was incubated with 90 μ l p-nitrophenyl phosphate buffer (1 mg/ml p-nitrophenyl phosphate disodium hexahydrate (71768, Sigma-Aldrich), 0.1 M sodium acetate, 0.1% Triton X-100 and 30 μ l/ml tartrate solution (3873, Sigma-Aldrich) in PBS) in 96-wells assay plates for 90 min at 37 °C. To stop the reaction, 100 μ l 0.3 M NaOH was added. Absorbance was read at 405 nm using a plate reader and absorbance values were converted to TRAP activity (converted p-nitrophenyl phosphate in nmol/ml/min) using standard curve absorbance values.

Alkaline phosphatase activity

Co-cultured constructs ($N = 6$ per time point and per condition) were washed in PBS and disintegrated using 2 steel balls and a mini-beadbeater™ (Biospec, Bartlesville, OK, USA) in cell lysis buffer containing 0.2% (v/v) Triton X-100 and 5 mM MgCl₂. ALP activity in cell lysates was determined by adding 20 μ l of 0.75 M 2-amino-2-methyl-1-propanol (A65182, Sigma-Aldrich) to 80 μ l sample in 96-wells assay plates. Subsequently, 100 μ l substrate solution (10 mM p-nitrophenyl-phosphate (71768, Sigma-Aldrich) in 0.75 M 2-amino-2-methyl-1-propanol) was added and wells were incubated at room temperature for 15 minutes. To stop the reaction, 100 μ l 0.2 M NaOH was added. Absorbance was measured with a plate reader at 450 nm and these values were converted to ALP activity (converted p-nitrophenyl phosphate in μ mol/ml/min) using standard curve absorbance values.

Pro-Collagen 1 C-Terminal Propeptide quantification

PICP as collagen formation product was quantified in cell supernatants of co-cultured constructs from day 21 and day 42 using an enzyme-linked immunosorbent assay (ELISA, MBS2502579, MyBioSource, San Diego, CA, USA) according to the manufacturer's protocol. Samples were added to anti-human PICP coated microwells. After 90 min incubation at 37 °C, samples were replaced by biotinylated antibody solution followed by 60 min incubation at 37 °C. After thorough washing, HRP-conjugate solution was added, and plates were incubated for 30 min at 37 °C. Wells were again washed, and substrate reagent was added followed by 15 min incubation in the

dark at 37 °C. To stop the reaction, stop solution was added and absorbance was measured at 450 nm in a plate reader. Absorbance values were converted to PICP concentrations using standard curve absorbance values.

(Immuno)histochemical analyses

Mono-cultured films after 7 days of culture ($N = 3$ per condition) were stained with DAPI and Phalloidin to visualize cell nuclei and the actin cytoskeleton, respectively. In short, films were fixed in 3.7% neutral buffered formaldehyde for 15 min, permeabilized in 0.5% Triton X-100 in PBS for 10 min and blocked in 2% BSA in PBS for 30 min. Cells were incubated with 0.1 µg/ml DAPI (D9542, Sigma-Aldrich) and 50 pmol Atto 647-conjugated Phalloidin (65906, Sigma-Aldrich) in PBS for 1 h. As some films had a curved surface, z-stacks were taken with a confocal laser scanning microscope (Leica TCS SP8X, 20x/0.4 HC PL Fluotar L objective). After background removal, to reduce autofluorescence from SF, z-stacks were converted to maximum intensity projections using Fiji (127).

Co-cultured scaffolds ($N = 2$ per time point and per condition) that were fixed for SEM analysis, were washed in PBS, permeabilized for 30 min in 0.5% Triton X-100 in PBS and stained overnight with 1 µmol/mL CNA35-mCherry (130) at 4 °C to visualize collagen. After washing with PBS, samples were incubated for 1 h with 0.1 µg/ml DAPI and 50 pmol Atto 488-conjugated Phalloidin (49409, Sigma-Aldrich). Samples were washed and imaged in PBS and z-stacks were acquired with a confocal laser scanning microscope (Leica TCS SP8X, 20x/0.75 HC PL APO CS2 objective). Z-stacks were converted to maximum intensity projections using Fiji (127).

Co-cultured scaffolds ($N = 4$ per time point and per condition) were prepared for cryosections by soaking them for 15 minutes in each 5% (w/v) sucrose and 35% (w/v) sucrose in phosphate buffered saline (PBS). Samples were embedded in Tissue Tek® (Sakura) and quickly frozen with liquid N₂. Cryosections were prepared with a thickness of 30 µm for antibody stainings and with a thickness of 5 µm for alcian blue staining. Upon staining, sections were fixed for 15 minutes in 3.7% neutral buffered formaldehyde and washed twice with PBS.

To visualize proteoglycan deposition, sections were stained in 1% w/v alcian blue (A5268, Sigma-Aldrich) in 3% acetic acid solution (pH 2.5) for 30 min. After washing in running distilled water for 5 min, sections were placed in Mayer's Hematoxylin solution for 10 min and washed in running tap water for 10 min. All sections were dehydrated in one change of 70% and 96% EtOH, three changes of 100% EtOH, and two changes of xylene. Sections were mounted with Entellan (107961 Sigma-Aldrich)

and imaged with a bright field microscope (Zeiss Axio Observer Z1, Plan-Apochromat 100x/1.40 objective).

To study osteogenic differentiation, sections were stained with DAPI, Atto 488-conjugated Phalloidin, RUNX2 and osteopontin. To study osteoclastic differentiation, sections were stained with DAPI, Atto 647-conjugated Phalloidin, Cathepsin K, and integrin- β_3 . Briefly, sections were permeabilized in 0.5% Triton X-100 in PBS for 10 min and blocked in 10% normal goat serum in PBS for 30 min. Primary antibodies were incubated overnight at 4 °C om 1% normal goat serum in PBS, secondary antibodies were incubated with 1 μ g/ml DAPI and 50 pmol Phalloidin in PBS for 1 h at room temperature. Antibodies are listed in **Table S7.1**. Z-stacks were acquired with a laser scanning microscope (Leica TCS SP8X, 63x/1.4 HC PL Apo CS2 objective). Z-stacks were converted to maximum intensity projections using Fiji (127).

7.5.5 Statistical analyses

Statistical analyses were performed, and graphs were prepared in GraphPad Prism (version 9.3.0, GraphPad, La Jolla, CA, USA) and R (version 4.1.2) (133). Data were tested for normality in distributions and equal variances using Shapiro-Wilk tests and Levene's tests, respectively. When these assumptions were met, mean \pm standard deviation are presented, and to test for differences, an independent t-test (for the comparison of two groups), one-way ANOVA followed by Holm-Šidák's post hoc method with adjusted p -values for multiple comparisons (for the comparison >2 groups), or a two-way ANOVA followed by Tukey's post hoc tests with adjusted p -value for multiple comparisons (for comparisons between groups over a period) were performed. Other data are presented as median \pm interquartile range and were tested for differences with non-parametric Mann-Whitney U tests or Kruskal-Wallis tests with Dunn's post hoc tests with adjusted p -value for multiple comparisons. With a p -value of <0.05 differences were considered statistically significant.

Author contributions

B.d.W., A.A., N.S., K.I. and S.H. contributed to conception, methodology and design of the study. B.d.W. performed the experiments. B.d.W., R.v.d.M. and P.B. contributed to the analyses of the experimental results. B.d.W. wrote the original draft of the manuscript. R.v.d.M. contributed to Figure 7.4 and Figure S7.2. PB contributed to Figure S7.3. Other figures were prepared by BdW. All authors contributed to manuscript revision and approved the submitted version. A.A., N.S., K.I. and S.H. contributed in the supervision. S.H. acquired funding for this research.

Acknowledgement

The authors thank Dewy van der Valk and Jasper Aarts for their help with the chemical characterization of the samples and Bert van Rietbergen for his support with the μ CT analyses. The authors gratefully acknowledge the financial support for B.d.W. and S.H. by the research program TTW with project number TTW 016.Vidi.188.021 to S.H., which is financed by the Netherlands Organization for Scientific Research (NWO). R.v.d.M, N.S. and A.A. were supported by the European Research Council (ERC) Advanced Investigator grant (H2020-ERC-2017-ADV-788982-COLMIN). A.A. was supported by the NWO (VI.Veni.192.094).

Supplementary information

To check for the presence of poly aspartic acid (pAsp) in silk fibroin (SF) w/5% pAsp films, films were stained with the cationic dye alcian blue to allow for visualization of the negatively charged pAsp (**Figure S7.1**).

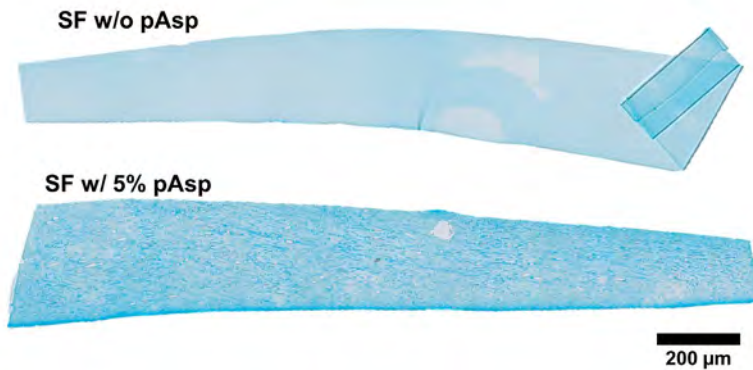


Figure S7.1. Plain silk fibroin (SF) film and SF film with 5 wt% poly-aspartic acid (pAsp) stained with alcian blue to visualize the negatively charged pAsp.

The presence of a small amount of pAsp in the SF material was also confirmed by chemical analysis. Raman spectroscopy measurements revealed a small peak at 1783 cm^{-1} , suggesting the presence of pAsp (**Figure S7.2**).

Raman spectroscopy non-mineralized silk fibroin

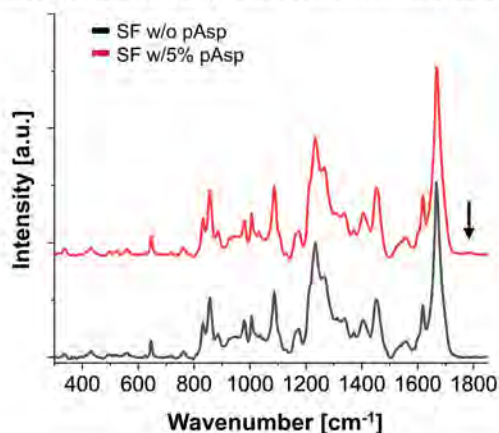


Figure S7.2. Comparison of non-mineralized silk fibroin (SF) in the presence (red) and absence (black) of poly-aspartic acid (pAsp). The spectra are near identical apart from a small peak at 1783 cm^{-1} , which indicates the presence of pAsp. Shown spectra are average spectra of a $30\times 30\text{ }\mu\text{m}$ area scans (total 900 spectra) for both samples.

X-ray photoelectron spectroscopy (XPS) measurements revealed a carbon peak with a wider shape, which is likely attributed to the carboxyl group in pAsp. XPS measurements also revealed the presence of calcium, phosphate and pAsp in both mineralized SF w/o pAsp and SF w/5% pAsp scaffolds. The presence of pAsp was observed by the carbon peak with wider shape relative to non-mineralized SF w/o pAsp scaffolds indicative for the presence of the carboxyl group of pAsp (**Figure S7.3**).

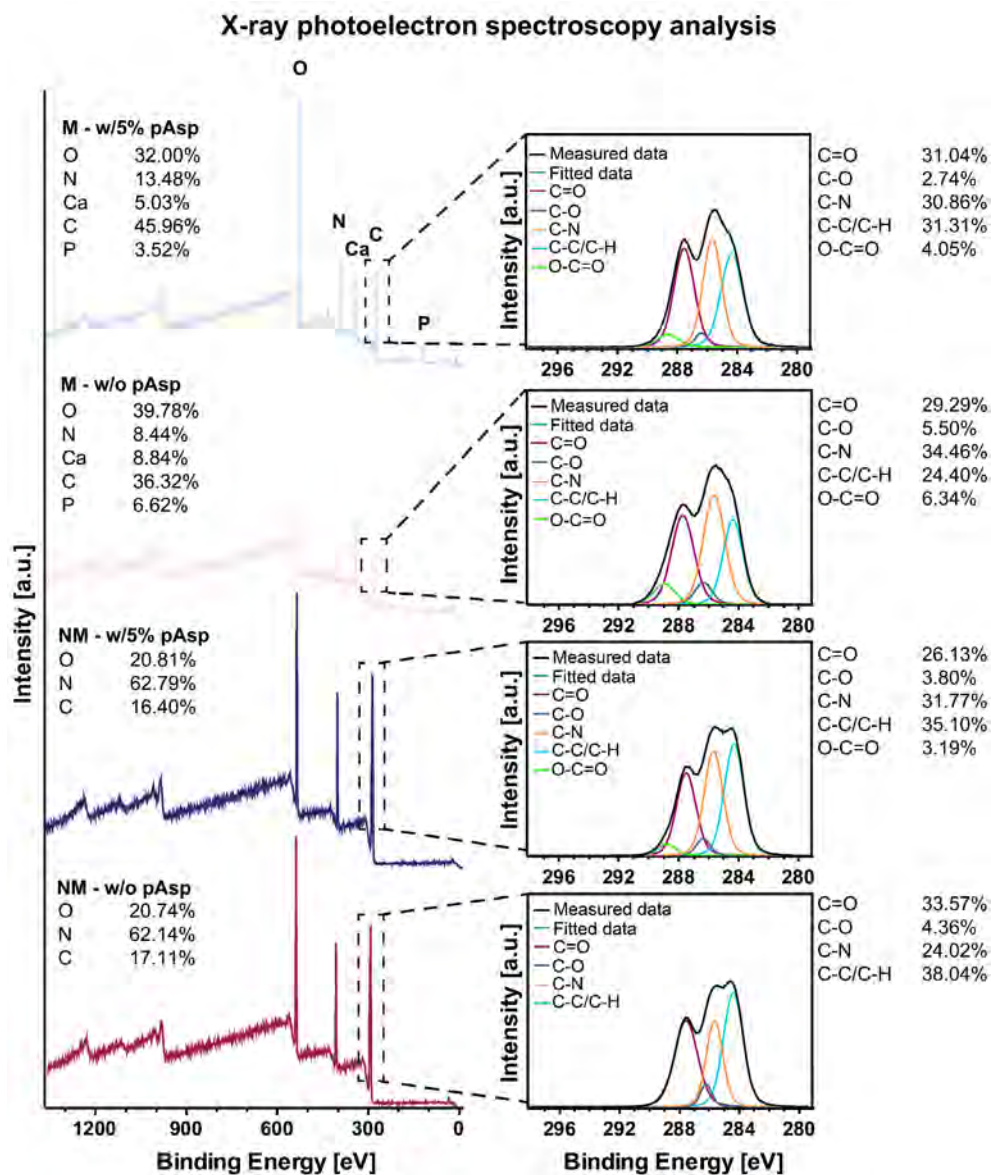


Figure S7.3. Comparison of X-ray photoelectron spectroscopy (XPS) measurements from mineralized and non-mineralized silk fibroin (SF) scaffolds w/o poly-aspartic acid (pAsp) and w/5% pAsp. Left panel presents the survey spectra with identified elements for each scaffold. Right panel present the carbon spectra, which were decomposed into the chemical bonds present in the different scaffolds.

To check for the presence of calcium in films and their cross-sections, an alizarin red staining was performed (**Figure S7.4**).

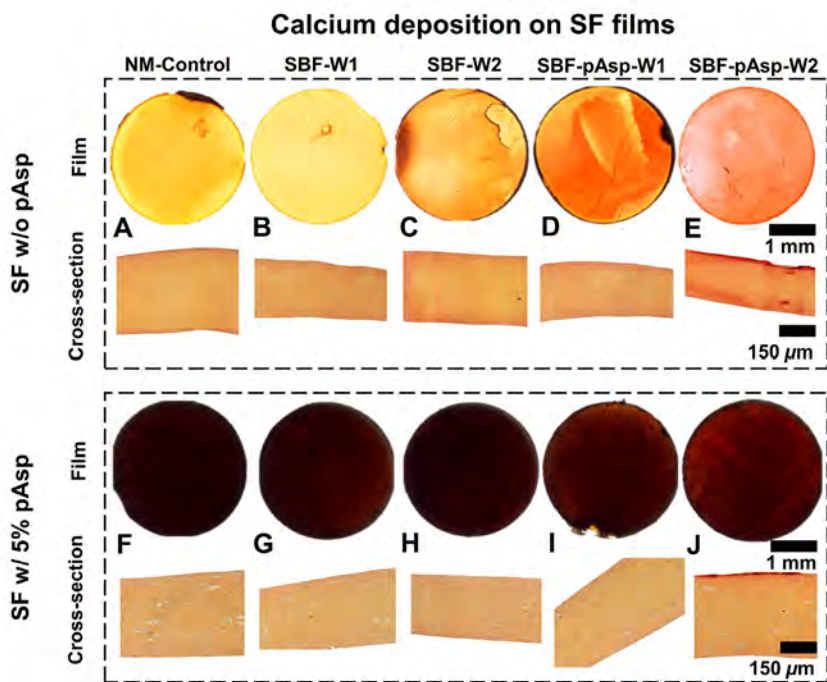


Figure S7.4. Calcium visualization with alizarin red staining. A clear red staining was observed on top of films mineralized with poly-aspartic acid (pAsp) in the mineralization solution after 2 weeks (cross-sections, **E+J**). In these groups, only mineralized silk fibroin (SF) w/o pAsp films showed red staining inside the film indicating mineral infiltration into the films (Figure S2E, cross-section). The films with pAsp in the material where less transparent and also non-mineralized (NM) films appeared to bind the stain. By preparing cross-sections, differences within this group became clearer. Abbreviations: week (W), simulated body fluid (SBF).

Because of the radiolucent nature of SF when immersed in water, mineralization could be localized with micro-computed tomography (μ CT) scanning of the scaffolds. By drying the mineralized scaffolds, their 3D morphology could also be characterized after μ CT scanning (**Figure S7.5**).

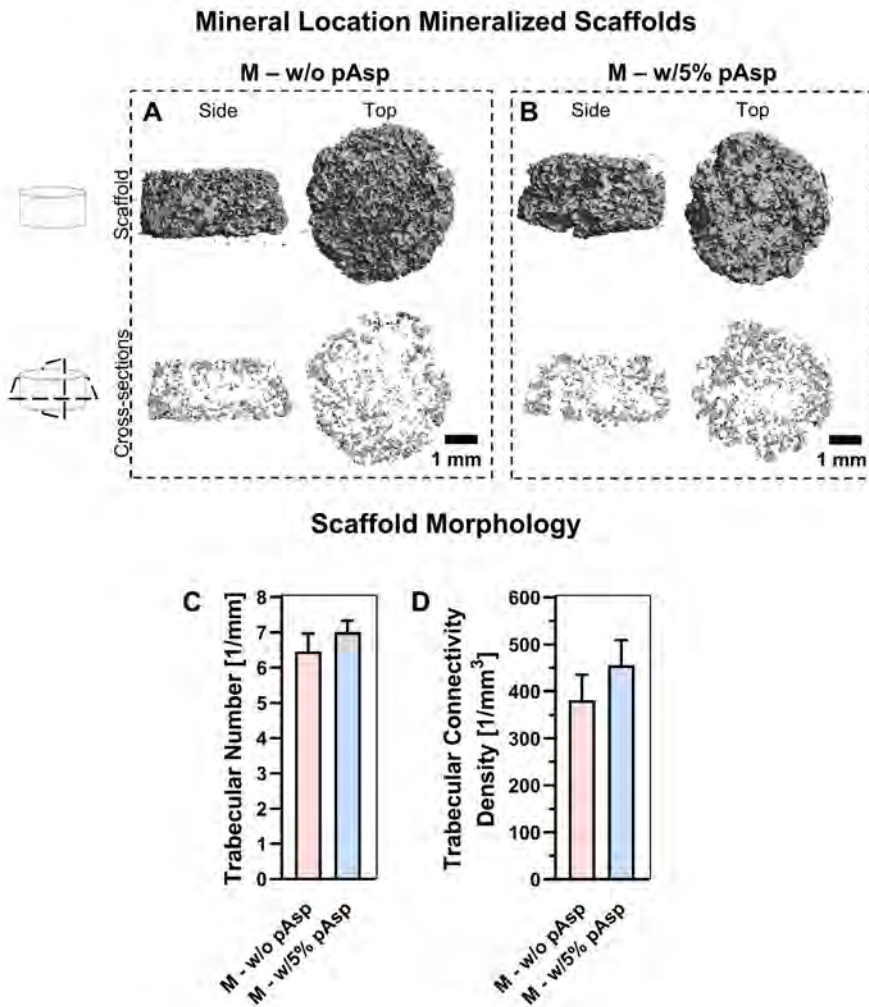


Figure S7.5. Morphological analyses of mineralized (M) silk fibroin (SF) scaffolds. (A) Mineral location visualized with μ CT for plain SF scaffolds and (B) for SF with 5% poly-aspartic acid (pAsp) in the scaffold. Cross-sections are optical slices of the whole scaffolds. No clear differences were observed between the two materials in terms of mineral distribution, (C) trabecular number (per mm length), and (D) the trabecular connectivity density, both *ns* (Independent t-test).

Longitudinal μ CT scanning was performed to track the remodeling dynamics. The influence of scanning on cytotoxicity was also evaluated (Figure S7.6).

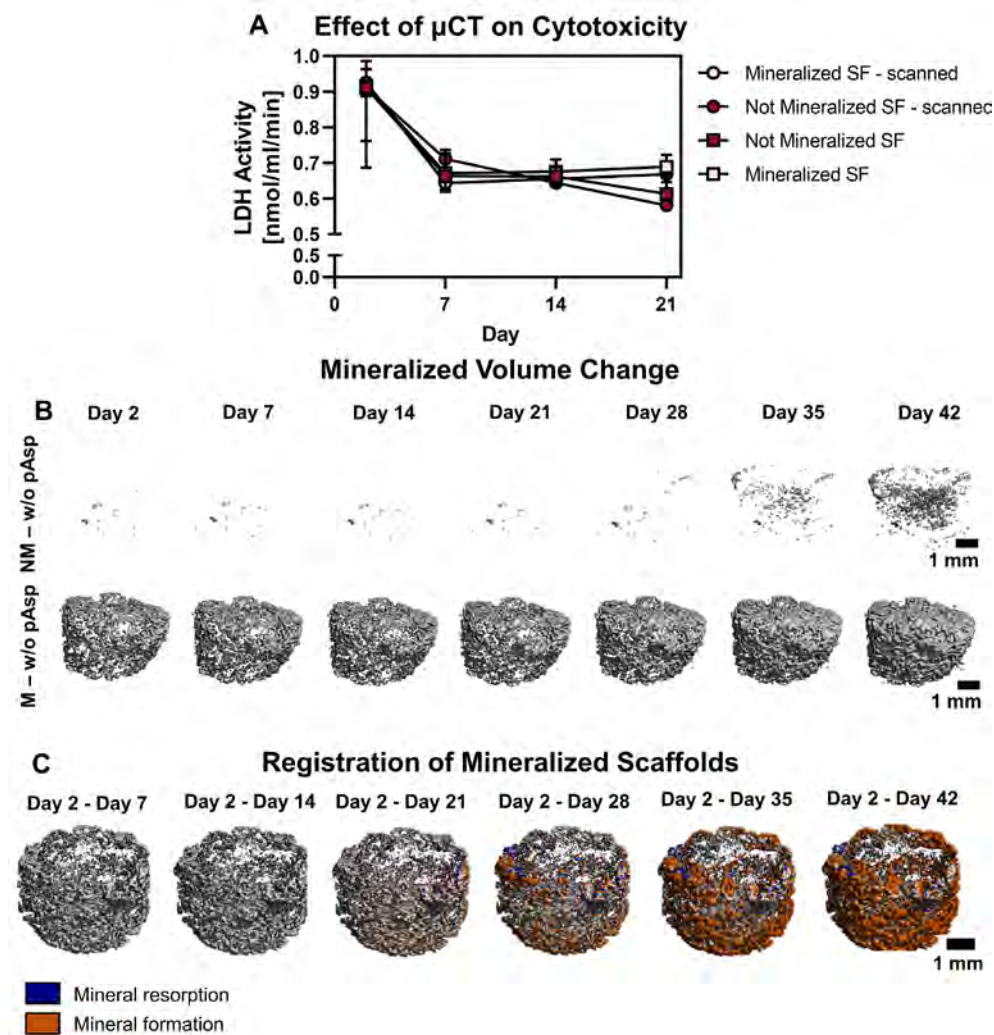


Figure S7.6. Longitudinal micro-computed tomography (μ CT) scanning analyses. First, the influence of scanning on cell death was evaluated over 21 days (A). No differences between scanned and unscanned constructs were found, μ CT scanning was therefore considered as a harmless method to track *in vitro* remodeling. Scans were segmented (B) and registered (C) to obtain information about mineralized volume change and resorption and formation sites, respectively.

A statistically significant higher sulphated glycosaminoglycan (GAG) content was found on day 21 of culture. GAGs were therefore visualized with an alcian blue staining. These GAGs were visualized between the trabecular-like structures (**Figure S7.7**).

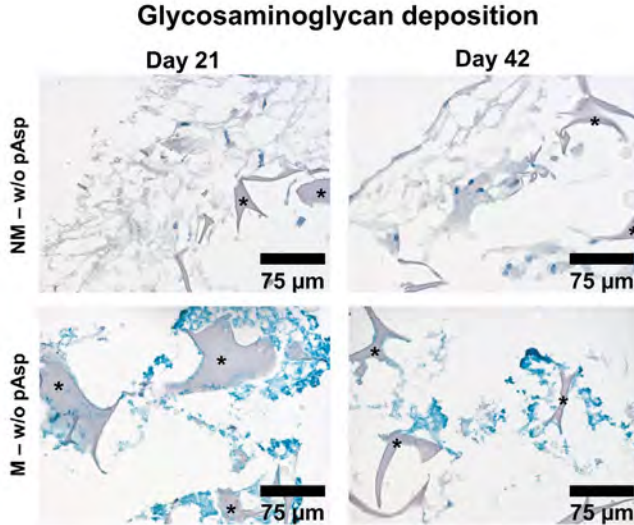


Figure S7.7. Glycosaminoglycan (GAG) visualization with alcian blue staining. GAGs were observed between the trabecular-like structures in mineralized (M) silk fibroin (SF) scaffolds on day 21 and 42. Asterisks indicate the scaffold trabeculae. Abbreviations: poly-aspartic acid (pAsp), non-mineralized (NM).

The antibodies that were used for immunofluorescent stainings are listed in **Table S7.1**.

Table S7.1. List of antibodies that were used in this study.

Antigen	Supplier	Catalogue No.	Conjugate	Species	Dilution
RUNX2	Abcam	ab23981		Rabbit	1:500
Osteopontin	Thermo Fisher	14-9096-82		Mouse	1:200
Cathepsin K	Abcam	Ab37259		Mouse	1:200
Integrin- β 3	Abcam	Ab227702		Rabbit	1:200
Anti-mouse IgG1	Molecular Probes	A21240	Alexa 647	Goat	1:200
Anti-Rabbit IgG	Molecular Probes	A21428	Alexa 555	Goat	1:200
Anti-mouse IgG2b	Molecular Probes	A21141	Alexa 488	Goat	1:200

Abbreviations: runt-related transcription factor 2 (RUNX2)

8

The impact of culture variables on human *in vitro* bone remodeling; a design of experiments approach

This chapter is based on:

Bregje W.M. de Wildt¹, Lizzy A.B. Cuypers^{1,2}, Esther E.A. Cramer¹, Annelieke S. Wentzel¹, Keita Ito¹, Sandra Hofmann¹

1. Orthopaedic Biomechanics, Department of Biomedical Engineering and Institute for Complex Molecular Systems (ICMS), Eindhoven University of Technology, Eindhoven, The Netherlands.

2. Department of Regenerative Biomaterials, Radboud University Medical Center, Nijmegen, The Netherlands.

In preparation

Abstract

Human *in vitro* bone remodeling models, using osteoclast-osteoblast co-cultures, could facilitate the investigation of human healthy (*i.e.*, balanced) and pathological (*i.e.*, unbalanced) bone remodeling while addressing the principle of reduction, refinement, and replacement of animal experiments. Although current *in vitro* osteoclast-osteoblast co-cultures have improved our understanding of bone remodeling, they lack culture method and outcome measurement standardization, hampering reproducibility and translatability. Therefore, *in vitro* bone remodeling models could benefit from a thorough evaluation of the impact of culture variables on functional and translatable outcome measures, with the aim to reach ‘healthy’ balanced osteoclast and osteoblast activity. Using a resolution III fractional factorial design, we identified the main effects of commonly used culture variables on bone turnover markers in a robust *in vitro* human bone remodeling model. Our model was able to capture physiological quantitative resorption – formation coupling along all conditions, which could be enhanced by external stimuli. Especially culture conditions of run 1 and 4 show promising results, where run 1 conditions could be used as high bone turnover system and run 4 as self-regulating system as the addition of osteoclastic and osteogenic differentiation factors was not required for remodeling. The results generated with our *in vitro* model allow for better translation between *in vitro* studies and towards *in vivo* studies, for improved preclinical bone remodeling drug development.

8.1 Introduction

Bone is a highly dynamic tissue continuously remodeled by bone resorbing osteoclasts, bone forming osteoblasts, and regulating osteocytes. Physiological or healthy bone remodeling involves balanced formation and resorption. A shift in this balance, towards more resorption or formation, is a hallmark for bone pathologies like osteoporosis or osteopetrosis, respectively. Studies of these bone pathologies and their treatment development are routinely performed in animal models. These animal models often represent human physiology insufficiently, which is likely one of the reasons that only 8-10% of preclinically developed drugs are approved for regular clinical use (23–25). Human *in vitro* bone remodeling models could facilitate the investigation of human healthy and pathological bone remodeling while addressing the principle of reduction, refinement, and replacement of animal experiments (3Rs) (7,111).

A co-culture of osteoclasts and osteoblasts is minimally needed to mimic the bone remodeling process *in vitro* (36). For these co-cultures, human monocytes (hMCs) and mesenchymal stromal cells (hMSCs) are most frequently used as progenitor cells which are in culture differentiated into osteoclasts and osteoblasts (and eventually osteocytes), respectively (43). To stimulate hMCs and hMSCs to undergo differentiation and subsequently study *in vitro* remodeling, a variety of culture conditions and outcome measures are used which differ for each research group and/or study aim (36,43). Variations in culture protocols include *e.g.*, different cell ratios, different base media, the use of osteogenic/osteoclast supplements and their respective concentrations, and the application of mechanical load (43). These culture variables could lead to unequal stimulation of osteoblasts and osteoclasts which might cause an unhealthy resorption-formation balance. Moreover, outcome measures of current models often include only the evaluation of osteoclast and/or osteoblast markers with *e.g.*, gene expression analysis or enzymatic activity assays rather than their functionality to resorb and form a bone-like extracellular matrix *in vitro* (43), which is mostly the main outcome measure for *in vivo* studies (*i.e.*, the evaluation of bone structure change using X-ray based methods). Thus, although current *in vitro* osteoclast-osteoblast co-cultures have improved our understanding of bone remodeling, they lack culture method and outcome measurement standardization, hampering reproducibility and translatability to *in vivo* animal models and *in vivo* human data. In this regard, *in vitro* bone remodeling models could benefit from a thorough evaluation of the impact of culture variables on functional and translatable outcome measures, with the aim to reach 'healthy' balanced osteoclast and osteoblast activity.

Researchers have already attempted to study the influences of culture variables on human osteoblast-osteoclast co-cultures. For example, studies looked at the influence of cell ratio on osteoclast formation (217), osteogenic factor addition and timing on osteogenic and osteoclastic differentiation (391,392), and the replacement of the culture supplement fetal bovine serum (FBS) by serum free medium (393), or human platelet lysate (hPL) (183) on osteoclastic resorption. As such, most studies analyze the influence of only one culture variable on *in vitro* remodeling outcomes while a specific combination of multiple variables might lead to improved results. A fractional factorial design of experiments (DoE) approach could facilitate the time-efficient evaluation of the impact of multiple culture variables on *in vitro* remodeling outcomes (394). While regularly used in most engineering fields, the DoE approach is barely employed for bioengineering. For bioengineering, DoE have been employed for *e.g.*, the optimization of biomaterials (395,396), or the optimization of culture conditions for improved human pluripotent stem cell expansion (397), osteogenic differentiation of adipose derived hMSCs (239), or vascular network formation in bone-like constructs (398). In this study, we used a fractional factorial design to evaluate the impact of culture variables on functional and translatable outcome measures in an *in vitro* remodeling model (**Figure 8.1**) (**Chapter 7**). As such, the influence of commonly used culture variables (43), including base medium, cell ratio, mechanical loading, hPL concentration, osteogenic differentiation factors, osteoclast differentiation factors and 1,25-dihydroxyvitamin D₃, on mainly non-destructive bone remodeling outcomes was evaluated over a period of 28 days. Outcome measures included sequential (registered) micro-computed tomography (μ CT) images and the longitudinal evaluation of resorption by tartrate-resistant acid phosphatase (TRAP) and cathepsin K quantification, and formation by alkaline phosphatase (ALP) and pro-collagen 1 c-terminal propeptide (PICP) quantification as commonly used bone turnover biomarkers (399). Besides, cell metabolic activity and cell death were longitudinally monitored. With this study, we aimed at finding culture conditions that equally support osteoclastic and osteogenic differentiation of hMCs and hMCSs, respectively, followed by balanced *in vitro* remodeling.

8.2 Materials and Methods

8.2.1 Factor selection and experimental matrix creation

To select the parameters to be tested in the DoE set-up, a database, as part of a systematic review, with culture conditions of all identified *in vitro* bone remodeling models was consulted (43).

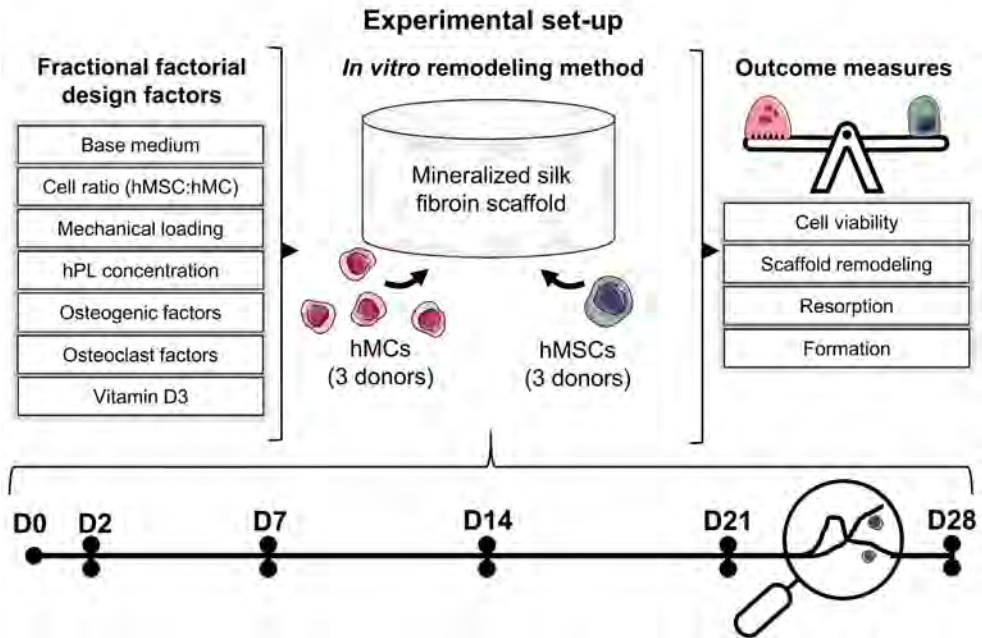


Figure 8.1. A fractional factorial design was used to study the influences of the culture variables (base medium, cell ratio, mechanical loading, hPL concentration, osteogenic differentiation factors and 1,25-dihydroxyvitamin D3) on cell viability, scaffold remodeling balance, osteoclastic resorption and osteoblastic formation in an *in vitro* bone remodeling model. A co-culture of hMCs and hMSCs was maintained for a period of 28 days during which remodeling was tracked non-destructively. Abbreviations: human platelet lysate (hPL), human monocytes (hMCs), human mesenchymal stromal cells (hMSCs), day (D). The figure was modified from Servier Medical Art, licensed under a Creative Commons Attribution 3.0 Generic License (<http://smart.servier.com/>, accessed on 8 July 2021).

From this database, the following culture variables were identified: culture substrate/material, cell type, seeding density, base medium, co-culture cell ratio, biomechanical environment, serum supplement, osteogenic differentiation factors (*i.e.*, dexamethasone, β -glycerophosphate and ascorbic acid), osteoclast differentiation factors (*i.e.*, receptor activator of nuclear factor κ B ligand (RANKL) and macrophage colony-stimulating factor (M-CSF)), and the use of additional factors of which 1,25-dihydroxyvitamin D3 was most commonly used. For this study, the influence of culture substrate/material, cell type and their seeding densities were not included as these factors form the base of our *in vitro* model that was used to study the effect of the other factors (**Chapter 7**). For the other factors, two levels (*i.e.*, low stimulation and high stimulation) were assigned (**Table 8.1**). For base medium, levels were α -MEM and DMEM as most commonly used co-culture base media (43). For cell ratio, ratios of 1:2 and 1:5 (hMSCs : hMCs) were included. For mechanical loading, static and dynamic

loading were included, using a custom made spinner flask bioreactor at 300 RPM to apply fluid shear stress (90). As a serum supplement, hPL was used at 5% and 10% concentration since the most commonly used FBS can inhibit osteoclast resorption (183,393). For osteogenic supplements, ascorbic acid was used in all conditions as a requirement for collagen synthesis. Dexamethasone was added in a low concentration of 10 nM, which is a commonly used concentration for co-cultures and believed to be the physiological glucocorticoid concentration known to stimulate osteogenesis and osteoclastogenesis (254,255). The other commonly used co-culture dexamethasone concentration of 100 nM was used for high stimulation (43). β -glycerophosphate was only added in the high stimulation condition at the most commonly used concentration of 10 mM (43). As the material used in this study contained hydroxyapatite, resorption was expected to release sufficient phosphate for osteogenic differentiation and mineralization. M-CSF and RANKL were only added in high stimulation conditions at commonly used concentrations of 50 ng/ml (43). The concentration of 1,25-dihydroxyvitamin D3 was set at the common concentration 10 nM in high stimulation conditions, whereas in low stimulation conditions no 1,25-dihydroxyvitamin D3 was added (**Table 8.1**).

Table 8.1. Evaluated factors and their corresponding levels.

	Factor	Level		Unit	
		Low	High		
A	Base medium	<i>a</i> -MEM	DMEM	-	
B	Cell ratio	1:2	1:5	-	
C	Mechanical loading*	0	300	RPM	
D	hPL concentration	5	10	%	
E	Osteogenic factors**	Dexamethasone	10	100	nM
		β -glycerophosphate	0	10	mM
F	Osteoclast factors	M-CSF	0	50	ng/ml
		RANKL***	0	50	ng/ml
G	1,25-dihydroxyvitamin D3	0	10	nM	

Abbreviations: human platelet lysate (hPL), macrophage colony-stimulating factor (M-CSF), receptor activator of nuclear factor κ B ligand (RANKL). *applied from day 2 in culture, **ascorbic acid was present in all cultures, ***added from day 2 in culture

For the resulting 7 factors with 2 levels, a resolution III fractional factorial design was randomly created using R (version 4.1.2) (133) with the Rcmdr DoE plugin (version 0.12-3, Ulrike Grömping) (400), leading to 8 experimental runs (**Table 8.2**). Resolution \geq III designs are considered appropriate for screening purposes. An additional run was included in which all factors had level low, which served as a negative control (run 9), a positive control (all factors level high) was already part of the design (run 7) (**Table 8.2**).

Table 8.2. Experimental matrix

Run	A	B	C	D	E	F	G
1	α -MEM	1:5	Dynamic	5% hPL		OCL fact	
2	α -MEM	1:5	Static	5% hPL	OG fact		vitD3
3	DMEM	1:5	Static	10% hPL			
4	α -MEM	1:2	Dynamic	10% hPL			vitD3
5	DMEM	1:2	Static	5% hPL		OCL fact	vitD3
6	DMEM	1:2	Dynamic	5% hPL	OG fact		
7	DMEM	1:5	Dynamic	10% hPL	OG fact	OCL fact	vitD3
8	α -MEM	1:2	Static	10% hPL	OG fact	OCL fact	
9	α -MEM	1:2	Static	5% hPL			

Abbreviations: human platelet lysate (hPL), osteogenic differentiation factors (OG fact), osteoclast differentiation factors (OCL fact), 1,25-dihydroxyvitamin D3 (vitD3). A = base medium, B = cell ratio, C = mechanical loading, D = human platelet lysate concentration, E = osteogenic factors, F = osteoclast factors, G = 1,25-dihydroxyvitamin D3

8.2.2 Scaffold fabrication

Bombyx mori L. silkworm cocoons were degummed by boiling them in 0.2 M Na₂CO₃ (S-7795, Sigma-Aldrich, Zwijndrecht, The Netherlands) for 1 h. Air-dried silk fibroin (SF) was dissolved in 9 M LiBr (199870025, Acros, Thermo Fisher Scientific, Breda, The Netherlands), filtered, and dialyzed against ultra-pure water (UPW) for 36 h using SnakeSkin Dialysis Tubing (molecular weight cut-off: 3.5 K, 11532541, Thermo Fisher Scientific). The dialyzed SF solution was frozen at -80 °C and lyophilized for 7 days. Lyophilized SF was dissolved in hexafluoro-2-propanol (003409, Fluorochem, Hadfield, UK) at a concentration of 17% (w/v) and casted in scaffold molds containing NaCl granules with a size of 250–300 μ m as template for the pores. Molds were covered to improve the SF blending with the granules. After 3 h, covers were removed from molds, and hexafluoro-2-propanol was allowed to evaporate for 7 days whereafter β -sheets were induced by submerging SF-salt blocks in 90% MeOH for 30 min. SF-salt blocks were cut into discs of 3 mm height with a Accutom-5 (04946133, Struer, Cleveland, OH, USA). NaCl was dissolved for 48 h from the scaffolds in UPW, resulting in porous sponges. From these sponges, scaffolds were punched with a 5 mm diameter biopsy punch.

8.2.3 Scaffold mineralization

SF scaffolds were mineralized as described in **Chapter 7**, using a mineralization solution with 10x SBF (356) and 100 μ g/ml poly-aspartic acid (pAsp, P3418, Sigma-Aldrich). Briefly, a 10x SBF stock was prepared. Just prior to mineralization, mineralization solution was prepared by adding 100 μ g/ml pAsp to 10x SBF, followed by the addition of NaHCO₃ until a final concentration of 10 mM, both under vigorous steering.

Scaffolds were incubated with 8.6 ml mineralization solution for 2 weeks at 37 °C on an orbital shaker at 150 RPM in mineralization solution with a solution replenishment after 1 week. After mineralization, scaffolds were washed 3 x 15 min in an excess of UPW. Scaffolds were sterilized by autoclaving in phosphate buffered saline (PBS) at 121 °C for 20 min.

8.2.4 Cell culture experiments

Monocyte isolation

Peripheral blood mononuclear cells (PBMCs) were isolated from human peripheral blood buffy coats (Sanquin, Eindhoven, The Netherlands; collected under their institutional guidelines and with informed consent per Declaration of Helsinki) of three healthy donors. The buffy coats (~50 ml each) were diluted with 0.6% w/v sodium citrate in PBS (citrate-PBS) until a final volume of 200 ml and layered per 25 ml on top of 10 ml Lymphoprep™ (07851, StemCell technologies, Köln, Germany) in 50 ml centrifugal tubes. After density gradient centrifugation (20 min at 800x g, lowest break), PBMCs were collected, resuspended in citrate-PBS, and washed four times in citrate-PBS supplemented with 0.01% bovine serum albumin (BSA, 10735086001, Merck KGaA, Darmstadt, Germany). PBMCs were frozen at 10⁵ cells/ml in freezing medium containing RPMI-1640 (RPMI, A10491, Thermo Fisher Scientific), 20% fetal bovine serum (FBS, BCBV7611, Sigma-Aldrich) and 10% dimethyl sulfoxide (DMSO, 1.02952.1000, VWR, Radnor, PA, USA) and stored in liquid nitrogen until further use. Before hMC isolation, PBMCs were thawed, collected in hMC isolation medium containing RPMI, 10% FBS (BCBV7611, Sigma-Aldrich) and 1% penicillin-streptomycin (p/s, 15070063, Thermo Fisher Scientific), and after centrifugation resuspended in isolation buffer (0.5% w/v BSA in 2mM EDTA-PBS). hMCs were enriched from PBMCs with manual magnetic activated cell separation (MACS) using the Pan Monocyte Isolation Kit (130-096-537, Miltenyi Biotec, Leiden, Netherlands) and LS columns (130-042-401, Miltenyi Biotec) according to the manufacturer's protocol, and directly used for experiments.

hMSC isolation and expansion

hMSCs were isolated from human bone marrow of three healthy donors (1M-125, Lonza, Walkersville, MD, USA, collected under their institutional guidelines and with informed consent) and characterized for surface markers and multilineage differentiation, as previously described (124). Bone marrow-derived hMSCs (hBMSCs) were frozen at passage 4 with 5*10⁶ cells/ml in freezing medium containing FBS (BCBV7611, Sigma-Aldrich) with 10% DMSO and stored in liquid nitrogen until further use. Before experiments, hBMSCs were thawed, collected in high glucose DMEM (hg-DMEM, 41966, Thermo Fisher Scientific), seeded at a density of 2.5*10³

cells/cm² and expanded in expansion medium containing hg-DMEM, 10% FBS (BCBV7611, Sigma-Aldrich), 1% Antibiotic Antimycotic (anti-anti, 15240, Thermo Fisher Scientific), 1% Non-Essential Amino Acids (11140, Thermo Fisher Scientific), and 1 ng/ml basic fibroblast growth factor (bFGF, 100-18B, PeproTech, London, UK) at 37 °C and 5% CO₂. After 7-10 days, at around 80% confluence, cells were detached using 0.25% trypsin-EDTA (25200, Thermo Fisher Scientific) and seeded onto scaffolds at passage 4 or 5.

hMC-hBMSC co-culture on mineralized SF scaffolds

hBMSCs were seeded at a density of 0.5×10^6 cells per scaffold and seeding was performed dynamically (125) in 50 ml tubes on an orbital shaker at 150 RPM in expansion medium. After 6 hours, scaffolds were transferred to 24-wells plates and hMCs were seeded in hMC isolation medium at a density of 1×10^6 or 2.5×10^6 cells/20 μ l (dependent on the experimental run) by pipetting 20 μ l of cell suspension onto the scaffolds. Cells were allowed to attach for 90 min at 37 °C and every 20 minutes a small droplet of medium from the respective experimental run was added. Per experimental run, 4 different hMC and hBMSC donor combinations (1 – 3 repeats per donor combination) were seeded on $N = 8$ scaffolds. The cell-loaded scaffolds were subsequently placed in custom-made spinner flask bioreactors (4 scaffolds per bioreactor, 2 bioreactors per experimental run) and cultured statically or dynamically for 28 days at 37 °C and 5% CO₂ in their respective medium (**Table S8.1** and **Table S8.2**). Medium was replaced 3x per week and medium samples were collected on day 2 and weekly from day 7 and stored at -80 °C. Constructs were sacrificed for analyses after 28 days of culture.

8.2.5 Analyses

μ CT

On day 2, 7, 14, 21 and 28, scaffolds ($N = 8$ per run) were scanned and later analyzed with a μ CT100 imaging system (Scanco Medical, Brüttisellen, Switzerland). Scanning was performed with an energy level of 45 kVp, intensity of 200 μ A, integration time of 300 ms and with twofold frame averaging. To reduce part of the noise, a constrained Gaussian filter was applied to all scans with filter support 1 and filter width sigma 0.8 voxel. Follow-up images were registered to the image of the previous time point, such that voxels at the surface of the scaffold were categorized into resorption site, formation site, or unchanged/quiescent site (390). The scaffold was segmented at a global threshold of 24% of the maximum grayscale value and remodeled scaffold surface was segmented at a global threshold of 7.5% of the maximum grayscale value. This threshold was chosen after registration of cell-free construct images in such a way that resorption and formation were below $\sim 1.5\%$ of the total volume to ensure that remodeled volume

was caused by the cells instead of by noise. To further reduce noise, only a minimum cluster of 2 resorbed or formed voxels were included in the analyses. For illustration purposes, day 28 images were also registered to day 2 images for the total resorption and formation visualization.

PrestoBlue™ assay

On day 2, 7, 14, 21 and 28, scaffolds were incubated with 10% v/v PrestoBlue™ (A13262, Thermo Fisher Scientific) in their respective medium (without supplementation of 1,25-dihydroxyvitamin D₃, osteogenic or osteoclast factors) within their bioreactors for 25 min at 37 °C in the dark. Samples ($N = 8$, 4 technical repeats from 2 bioreactors with each 4 scaffolds per run) were pipetted in duplo in black 96-wells assay plates. Fluorescence (excitation: 530/25 nm, emission 590/35 nm) was measured with a plate reader (Synergy™ HTX, Biotek). Measured fluorescence was corrected for blank medium samples.

Lactate dehydrogenase activity (LDH)

On cell supernatants from day 2, 7, 14, 21 and 28, LDH activity was measured ($N = 8$, 4 technical repeats from 2 bioreactors with each 4 scaffolds per run). A 100 μ l supernatant sample or NADH (10107735001, Sigma-Aldrich) standard was in duplo incubated with 100 μ l LDH reaction mixture (11644793001, Sigma-Aldrich) in 96-wells assay plates. Absorbance was measured after 5-, 10- and 20- min at 490 nm using a plate reader, and LDH activity was calculated between the 10- and 20- min reactions, using standard curve absorbance values.

TRAP activity

On cell supernatants from day 2, 7, 14, 21 and 28, TRAP activity was quantified ($N = 8$, 4 technical repeats from 2 bioreactors with each 4 scaffolds per run). A 10 μ l supernatant sample or p-nitrophenol standard was in duplicate incubated with 90 μ l p-nitrophenyl phosphate buffer (1 mg/ml p-nitrophenyl phosphate disodium hexahydrate (71768, Sigma-Aldrich), 0.1 M sodium acetate, 0.1% Triton X-100 and 30 μ l/ml tartrate solution (3873, Sigma-Aldrich) in PBS) in 96-wells assay plates for 90 min at 37 °C. To stop the reaction, 100 μ l 0.3 M NaOH was added. Absorbance was read at 405 nm using a plate reader and absorbance values were converted to TRAP activity (converted p-nitrophenyl phosphate in nmol/ml/min) using standard curve absorbance values.

Cathepsin K activity

On cell supernatants from day 2, 7, 14, 21 and 28, Cathepsin K activity was quantified ($N = 8$, 4 technical repeats from 2 bioreactors with each 4 scaffolds per run). A 50 μ l supernatant sample or aminomethylcoumarin (A9891, Sigma-Aldrich) standard was in duplo incubated with 50 μ l substrate working solution (100 μ M Z-LR-AMC (BML-

P229-0010, Enzo Life Sciences, Bruxelles, Belgium), 0.1 M sodium acetate trihydrate, 4 mM EDTA and 4 mM DTT at pH 5.5 in UPW) in 96-wells assay plates for 30 min at 37 °C. Fluorescence (excitation: 360/40 nm, emission 460/40 nm) was measured with a plate reader and values were converted to Cathepsin K activity (converted Z-LR-AMC in $\mu\text{mol}/\text{ml}/\text{min}$) using standard curve fluorescence values.

PICP quantification

On cell supernatants from day 2, 7, 14, 21 and 28, PICP as collagen formation product was quantified using an enzyme-linked immunosorbent assay (ELISA, MBS2502579, MyBioSource, San Diego, CA, USA) according to the manufacturer's protocol. Samples ($N = 2$, one sample per bioreactors with each 4 scaffolds per run) were added in triplicate to anti-human PICP coated microwells. After 90 min incubation at 37 °C, samples were replaced by biotinylated antibody solution followed by 60 min incubation at 37 °C. After thorough washing, HRP-conjugate solution was added, and plates were incubated for 30 min at 37 °C. Wells were again washed, and substrate reagent was added followed by 15 min incubation in the dark at 37 °C. To stop the reaction, stop solution was added and absorbance was measured at 450 nm in a plate reader. Absorbance values were converted to PICP concentrations using standard curve absorbance values.

Alkaline phosphatase activity

On day 28, scaffolds ($N = 4$ per run) were washed in PBS and disintegrated using 2 steel balls and a mini-beadbeaterTM (Biospec, Bartlesville, OK, USA) in 500 μl cell lysis buffer containing 0.2% (v/v) Triton X-100 and 5 mM MgCl_2 . ALP activity in cell lysates was determined by adding 20 μl of 0.75 M 2-amino-2-methyl-1-propanol (A65182, Sigma-Aldrich) to 80 μl sample in 96-wells assay plates. Subsequently, 100 μl substrate solution (10 mM p-nitrophenyl-phosphate (71768, Sigma-Aldrich) in 0.75 M 2-amino-2-methyl-1-propanol) was added and wells were incubated at room temperature for 15 minutes. To stop the reaction, 100 μl 0.2 M NaOH was added. Absorbance was measured with a plate reader at 450 nm and these values were converted to ALP activity (converted p-nitrophenyl phosphate in $\mu\text{mol}/\text{ml}/\text{min}$) using standard curve absorbance values.

Scanning electron microscopy (SEM)

On day 28, scaffolds ($N = 1-3$ per run) were fixed in 2.5% glutaraldehyde in 0.1 M sodium cacodylate buffer (CB) for 4 h and then washed in CB. Samples were dehydrated with graded ethanol series (37%, 67%, 96%, 3 x 100%, 15 minutes each), followed by a hexamethyldisilazane (HDMS)/ethanol series (1:2, 1:1, 2:1, 3 x 100% HDMS, 15 minutes each). Samples were coated with 20 nm gold and imaging was performed in

high vacuum, at 10 mm working distance, with a 5kV electron beam (Quanta 600F, FEI, Eindhoven, The Netherlands).

Histochemical analysis and confocal microscopy

On day 28, scaffolds ($N = 1-3$ per run) were fixed overnight in 3.7% neutral buffered formaldehyde, washed in PBS, permeabilized for 30 min in 0.5% Triton X-100 in PBS and stained overnight with 1 $\mu\text{mol/mL}$ CNA35-OG488 (132) and 0.2 nmol/ml OsteoSense™ 680 (NEV10020EX, PerkinElmer, Waltham, MA, USA) at 4 °C to visualize collagen and hydroxyapatite, respectively. After washing with PBS, samples were incubated for 1 h with 1 $\mu\text{g/ml}$ DAPI and 50 pmol Atto 550-conjugated Phalloidin (19083, Sigma-Aldrich). Samples were washed and imaged in PBS images were acquired with a confocal laser scanning microscope (Leica TCS SP8X, 40x/0.95 HC PL APO objective).

8.2.6 Statistical analyses

Statistical analyses were performed, and graphs were prepared in GraphPad Prism (version 9.3.0, GraphPad, La Jolla, CA, USA) and R (version 4.1.2) (133) with the Rcmdr DoE plugin (version 0.12-3, Ulrike Grömping) (400). Statistical analyses were only done for day 21 data, as osteoclasts have a limited lifespan of about 14-21 days (232,289), and osteogenesis takes about 14-21 days (401). ALP data was analyzed at day 28, as endpoint analysis. For the comparison between different experimental runs, data were tested for normality in distributions and equal variances using Shapiro-Wilk tests and Levene's tests, respectively. When these assumptions were met, mean \pm standard deviation are presented and a one-way ANOVA was performed followed by Holm-Šidák's post hoc tests with adjusted p -values for multiple comparisons, in which experimental runs were pairwise compared with the negative (run 9) and positive (run 7) control. Other data are presented as median \pm interquartile range and were tested for differences with the non-parametric Kruskal-Wallis test with Dunn's post hoc tests with adjusted p -value for pairwise comparisons with the positive and negative control. To quantify the resorption-formation coupling, a spearman correlation coefficient was calculated for the μCT outcomes resorbed mineralized volume – formed mineralized volume and for the supernatant outcomes TRAP activity – PICP concentration. As part of the fractional factorial design analysis, factor main effect plots and effect normal plots were prepared for effect visualization and factor significance (400), respectively. Due to failed μCT registration, some experimental runs missed 1 – 2 out of 8 samples for mineral formation and resorption quantification. To allow for a balanced factorial design analysis, the average of the respective experimental runs was included as additional samples. A p -value of <0.05 was considered statistically significant.

8.3 Results

8.3.1 Cell viability

From day 7 to day 28, metabolic activity increased for all experimental runs (**Figure 8.2A**). When comparing the metabolic activity on day 21 of each run with the metabolic activity of the positive and negative control, a statistically significant lower metabolic activity was found in the positive control (run 7) when compared with run 1, 2, 3 and the negative control (run 9) (**Figure 8.2B**). The negative control also had a statistically significant higher metabolic activity than run 4 (**Figure 8.2B**). LDH activity in the supernatant, as a measure for cell death, initially decreased for most experimental runs while towards day 21 it tended to stabilize or increase slightly (**Figure 8.2C**). While the metabolic activity was relatively low in the positive control, a statistically significant higher day 21 LDH activity was found when comparing the positive control with run 1, 4, 5 and the negative control (run 9) (**Figure 8.2D**). Overall, cell death was lowest in the negative control with a statistically significant difference when comparing to run 3 and 8 (**Figure 8.2D**). Factor main effect plots indicated the influence of the culture variables and their corresponding levels on metabolic activity and cell death (**Figure 8.2E**). No significant contribution to metabolic activity nor cell death was found from one of the factors. From the metabolic activity main effect plots and normal effect plots, a high cell ratio (1:5) tended to positively influence metabolic activity (**Figure 8.2E** and **Figure S8.1**). Interestingly, all other factors seemed to negatively impact metabolic activity when high stimulation was applied (**Figure 8.2E** and **Figure S8.1**). A high concentration of hPL tended to increase LDH activity (**Figure 8.2E** and **Figure S8.1**), likely caused by the presence of LDH in human platelets (402).

8.3.2 Scaffold remodeling

When visualizing mineral resorption and formation sites after registration of day 28 μ CT images to day 2 images, remodeling was observed in all experimental runs (**Figure 8.3A**). While in the negative control (run 9) limited remodeling was observed, the positive control (run 7) showed extensive remodeling with mostly mineral formation (**Figure 8.3A**). Quantification of the percentage formed, resorbed and quiescent (unremodeled) mineral between day 2 - 7, 7 - 14, 14 - 21, and 21 - 28, allowed for calculating the balance between formed and resorbed mineral (*i.e.*, mineral formation – mineral resorption) (**Figure 8.3B**). Remarkably, in all experimental runs more formation than resorption was observed for most time points (**Figure 8.3B**). Over time, the negative control (run 9) showed most balanced remodeling with limited net resorption or formation, while in the positive control (run 7) a relatively high net formation was observed at all time points (**Figure 8.3B**).

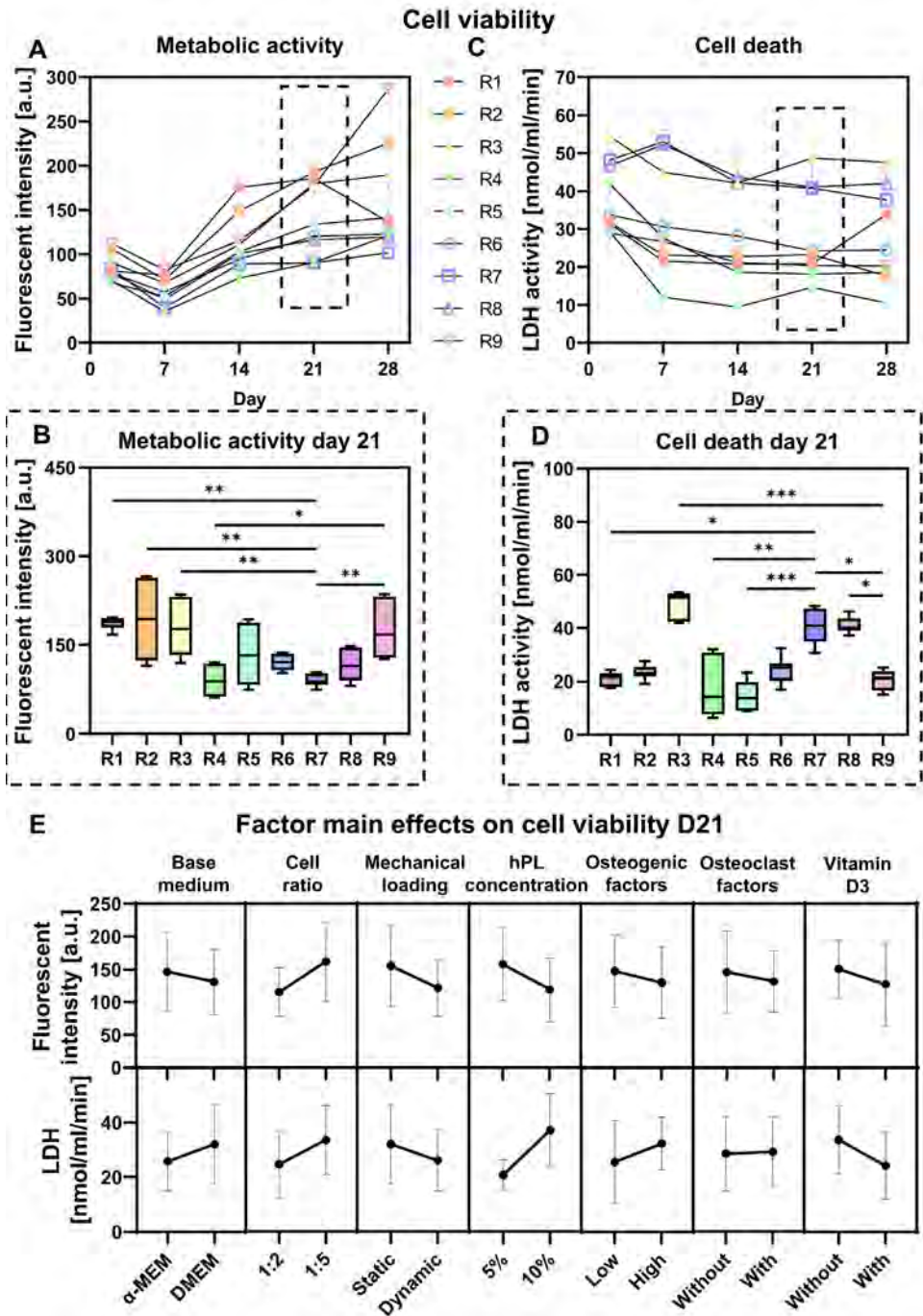


Figure 8.2. Cell viability testing of experimental runs. (A) Metabolic activity measurements using PrestoBlue™ on day 2, 7, 14, 21, and 28. (B) Day 21 metabolic activity measurements, $p < 0.05$ (Kruskal-

Wallis and Dunn's post hoc tests). (C) Cell death measured by LDH release in the medium on day 2, 7, 14, 21, and 28. (D) Day 21 cell death measurements, $p < 0.05$ (Kruskal-Wallis and Dunn's post hoc tests). (E) Factor main effects and standard deviations on day 21 cell viability outcome measures. (* $p < 0.05$, ** $p < 0.01$, *** $p < 0.001$). Abbreviations: lactate dehydrogenase activity (LDH), run (R), human platelet lysate (hPL).

From day 14 - 21, there was indeed a significantly higher net formation in the positive control when compared to run 3, 5, 8, and the negative control (**Figure 8.3C**). In addition to the positive control, run 6 also had a significantly higher net formation than the negative control (**Figure 8.3C**). Comparison of the quiescent scaffold mineralized volume revealed that most scaffold was remodeled in the initial 21 days, observed by a small increase in quiescent volume after day 21 consistent for all experimental runs (**Figure 8.3D**). Overall, most scaffold remodeling seemed to take place in the positive control and least remodeling in the negative control (**Figure 8.3D**). From day 14 - 21, least quiescent scaffold mineralized volume was observed in run 1, with statistically significant less quiescent volume than the negative control (run 9) (**Figure 8.3E**).

8.3.3 Osteoclastic resorption

Over the culture period, experimental run 1 showed consistently most resorbed mineralized volume (**Figure 8.4A**). In both the positive (run 7) and negative (run 9) controls, limited resorption was observed (**Figure 8.4A**). When comparing the resorbed mineralized volume from day 14 - 21, statistically significant more mineral resorption was observed in experimental run 1 when compared with the positive control (**Figure 8.4B**). Interestingly, although not significant, the osteoclast factor-lacking run 4 also showed a relatively high resorbed mineralized volume. For run 1 and 4, the high resorbed mineralized volume was reflected in a relatively high TRAP activity and for run 1 also Cathepsin K activity (**Figure 8.4C+E**). Although limited resorbed mineralized volume was observed for the positive control (run 7), a relatively high TRAP activity was measured (**Figure 8.4C**). On day 21, when compared to the negative control (run 9), a statistically significant higher TRAP activity was measured in run 1 and 7 (**Figure 8.4D**). When compared to the positive control (run 7), a statistically significant lower TRAP activity was found in run 2 and 5 (**Figure 8.4D**). In line with the TRAP activity measurements, highest cathepsin K activity was found for experimental run 1, with a statistically significant difference with both positive and negative control (**Figure 8.4F**). From SEM images, osteoclast-like cells were observed in run 1 - 8 (**Figure 8.4G**). No apparent osteoclast-like cells (*i.e.*, $>10 \mu\text{m}$ in diameter and a ruffled border) were found in the negative control (run 9). In run 1 and 7, relatively large osteoclast-like cells were observed and in run 1 these cells were found in groups. Osteoclast-like cells in other experimental runs were generally smaller than osteoclast-like cells found in run 1 and 7 (**Figure 8.4G**).

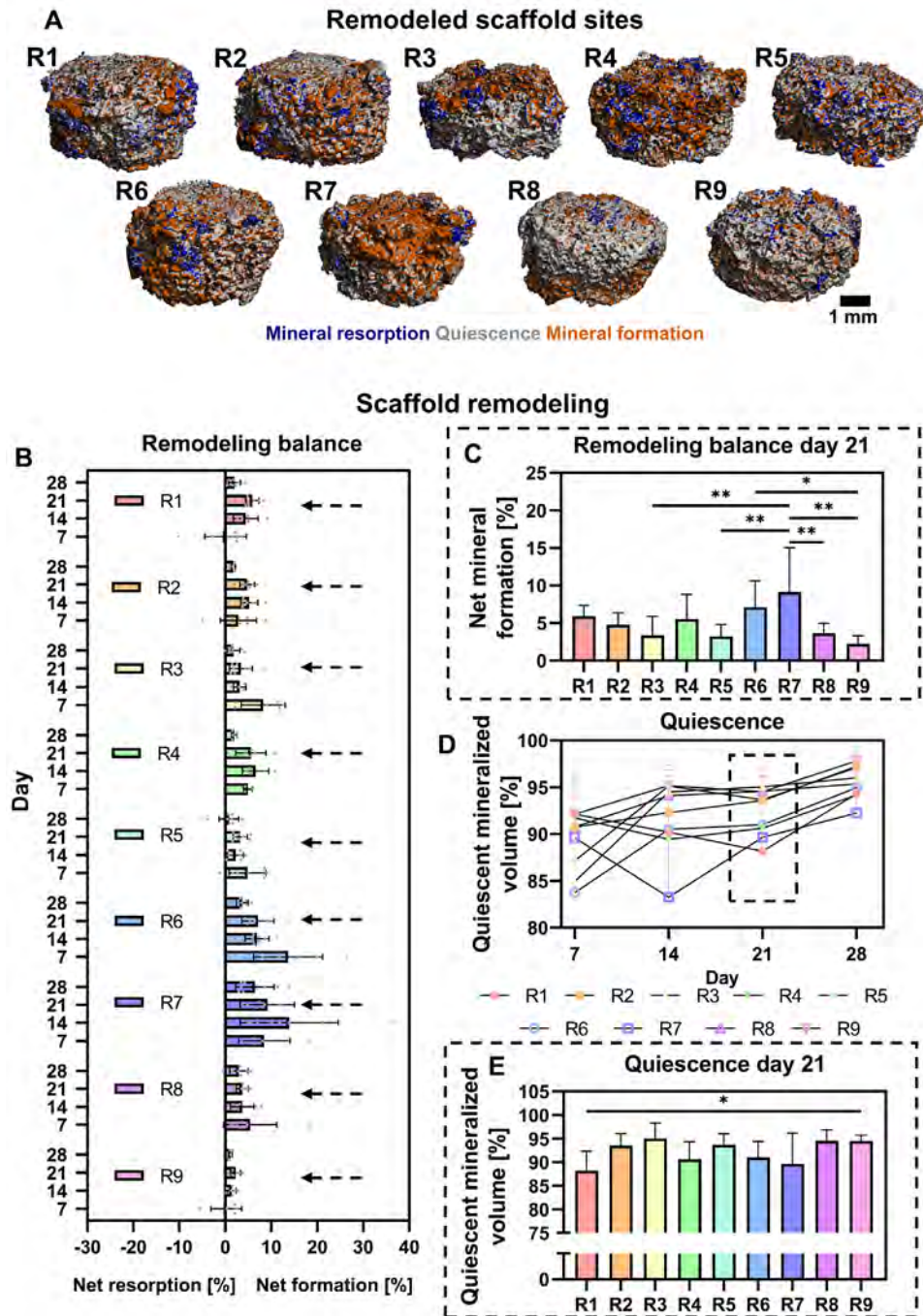


Figure 8.3. Scaffold remodeling of experimental runs. (A) Remodeled scaffolds sites between day 2 and 28, obtained with μ CT. (B) μ CT based formed mineral – resorbed mineral as measure for remodeling

balance of day 2-7, 7-14, 14-21, and 21-28. (C) Day 14-21 remodeling balance, $p < 0.05$ (One-way ANOVA and Holm-Šidák's post hoc tests). (D) μ CT based quiescent mineral or unremodeled scaffold mineral of day 2-7, 7-14, 14-21, and 21-28. (E) Day 14-21 quiescent mineral, $p < 0.05$ (One-way ANOVA and Holm-Šidák's post hoc tests). (* $p < 0.05$, ** $p < 0.01$). Abbreviations: run (R).

Factor main effect plots indicated the influence of the culture variables and their corresponding levels on mineral resorption, TRAP activity and cathepsin K activity (**Figure 8.5**). No significant contribution to mineral resorption, TRAP activity or cathepsin K activity was found from one of the factors. From the main effect plots and normal effect plots, mechanical loading tended to positively influence mineral resorption and TRAP activity, while the addition of high concentrations of osteogenic supplements tended to negatively influence mineral resorption (**Figure 8.5** and **Figure S8.2**). Overall, factor main effect plots showed a similar trend for almost each resorption outcome measure (**Figure 8.5**). Only TRAP activity was positively influenced by a high concentration of hPL while resorbed mineral and cathepsin K were negatively influenced by a high concentration of hPL (**Figure 8.5**). This might be explained by the presence of TRAP in hPL (183).

8.3.4 Osteoblastic formation

When evaluating formed mineralized volume over time, the positive control (run 7) tended to have consistently high mineral formation while in the negative control (run 9), a relatively low formed mineralized volume was observed (**Figure 8.6A**). On day 21, only for run 1 a statistically significant higher formed mineralized volume was observed when compared to the negative control (**Figure 8.6B**). Similar trends were observed for collagen type I formation, measured by PICP release in the cell supernatant. Where most mineral formation was observed in run 1 and 7, also highest collagen type I formation was observed in these conditions (**Figure 8.6C+D**). In the negative control, limited collagen type I formation was observed. ALP activity measurements on the cell lysate of day 28 revealed highest ALP activity in the positive control and lowest in the negative control (**Figure 8.6E**). For the positive control, a statistically significant higher ALP activity was observed when compared to the ALP activity of run 5 and the negative control. Visualization of the constructs with confocal microscopy demonstrated collagen formation in run 1, 3, 4, 5 and 6 (**Figure 8.6F**). Remarkably, although relatively high PICP was observed in the positive control, almost no collagen was observed in the microscopy samples (**Figure 8.6F**). In all conditions, hydroxyapatite was mainly observed on the SF scaffold trabeculae rather than in the by the cells produced extracellular matrix (**Figure 8.6F**). In run 8 and 9, limited numbers of cells were observed (**Figure 8.6F**).

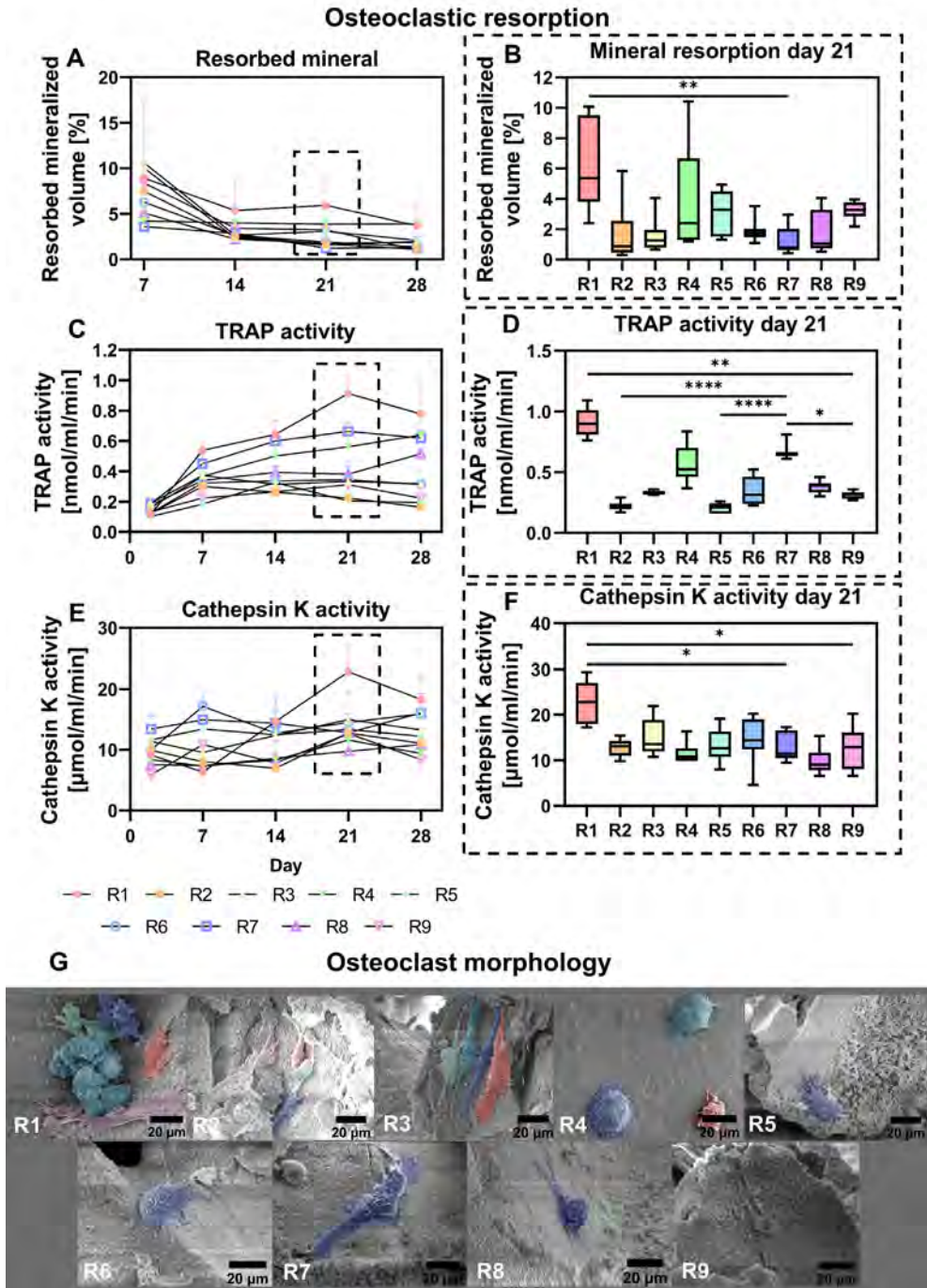


Figure 8.4. Osteoclastic resorption of experimental runs. **(A)** μCT based resorbed mineral of day 2-7, 7-14, 14-21, and 21-28. **(B)** Day 14-21 resorbed mineral, $p < 0.05$ (Kruskal-Wallis and Dunn's post hoc tests).

(C) TRAP activity in the medium on day 2, 7, 14, 21, and 28. (D) Day 21 TRAP activity measurements, $p < 0.05$ (Kruskal-Wallis and Dunn's post hoc tests). (E) Cathepsin K activity in the medium on day 2, 7, 14, 21, and 28. (F) Day 21 cathepsin K activity measurements, $p < 0.05$ (Kruskal-Wallis and Dunn's post hoc tests). (G) Visualization of osteoclast-like cells on day 28 with SEM. ($*p < 0.05$, $**p < 0.01$, $***p < 0.0001$). Abbreviations: tartrate-resistant acid phosphatase (TRAP), run (R), scanning electron microscopy (SEM).

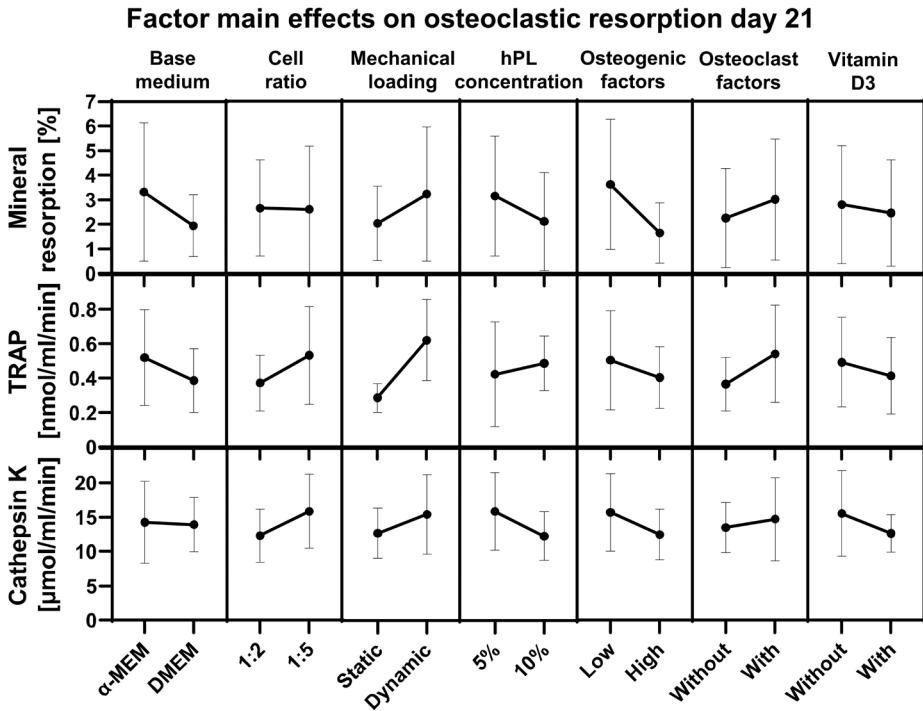


Figure 8.5. Factor main effects and standard deviations on day 21 osteoclastic resorption outcome measures.

Factor main effect plots indicated the influence of the culture variables and their corresponding levels on mineral formation, collagen type I formation measured by PICP, and ALP activity (Figure 8.7A). No significant contribution to mineral formation, collagen type I formation, and ALP activity was found from one of the factors. From the main effect plots and normal effect plots, mechanical loading tended to positively influence mineral formation and collagen type I formation (Figure 8.7A and Figure S8.2). Other factors did not seem to influence mineral formation (Figure 8.7A and Figure S8.2). ALP activity tended to be positively influenced by high concentrations of osteogenic supplements (Figure 8.7A and Figure S8.2).

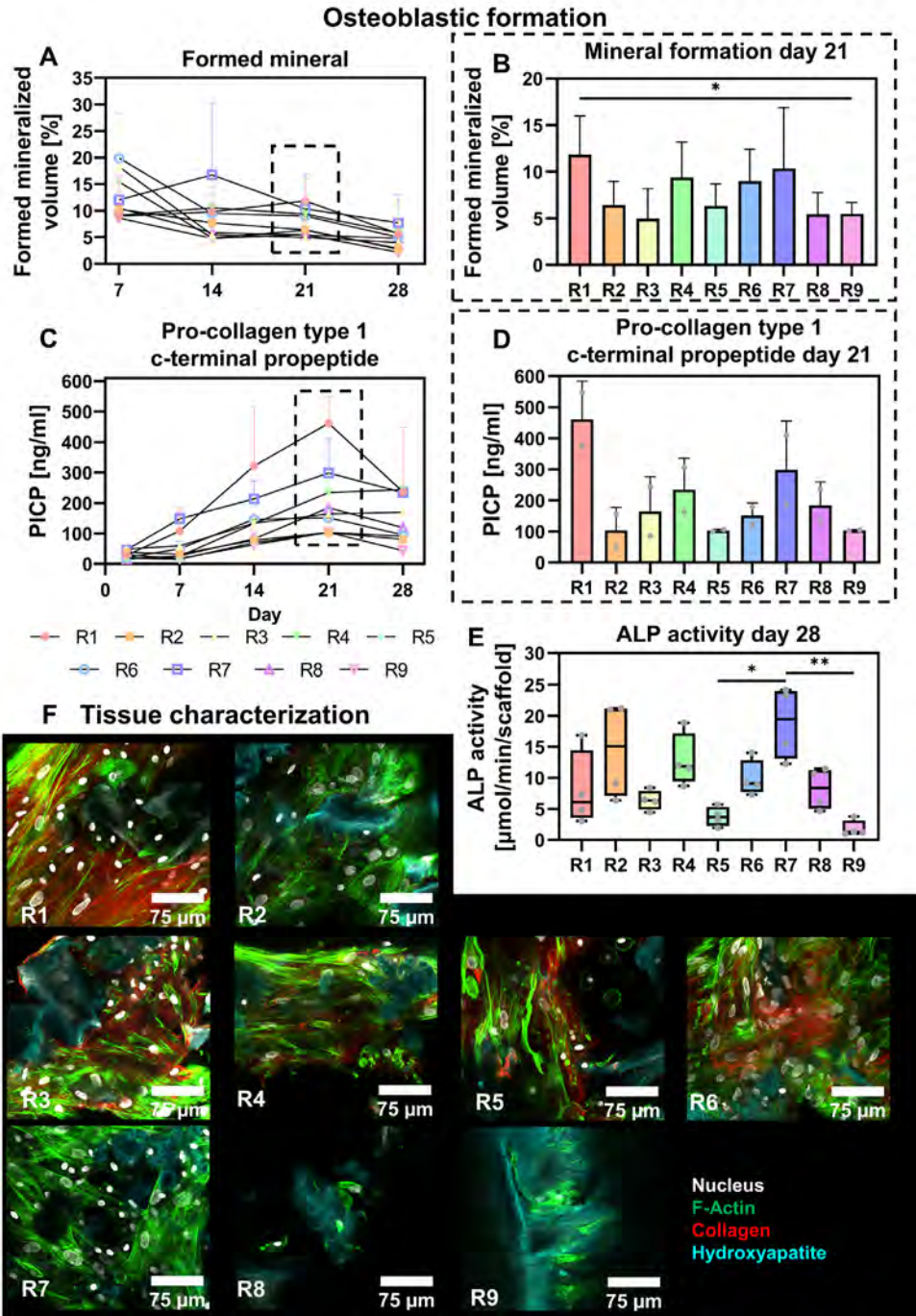


Figure 8.6. Osteoblastic formation of experimental runs. (A) μ CT based formed mineral of day 2-7, 7-14, 14-21, and 21-28. (B) Day 14-21 formed mineral, $p < 0.05$ (One-way ANOVA and Holm-Šidák's post hoc

tests). (C) PICP release in medium from day 2, 7, 14, 21, and 28. (D) Day 21 PICP release measurements. (E) ALP activity in cell lysates on day 28, $p < 0.05$ (Kruskal-Wallis and Dunn's post hoc tests). (F) Visualization of bone-like tissue in cultured constructs on day 28 with confocal microscopy, stained for collagen (red), F-Actin (green), hydroxyapatite (cyan), and the nucleus (gray). (* $p < 0.05$, ** $p < 0.01$). Abbreviations: pro-collagen 1 c-terminal propeptide (PICP), alkaline phosphatase (ALP), run (R).

As mineral formation was relatively high in groups where mineral resorption was elevated in the absence of high stimulation with osteogenic factors, we investigated the coupling between resorption and formation markers (**Figure 8.7B+C**). Interestingly, a strong positive correlation ($r = 0.81, p < 0.0001$) was observed between the osteoclastic resorption marker TRAP and the collagen formation marker PICP (**Figure 8.7B**). In line with these results, main effect plots and normal effect plots for TRAP activity and PICP concentration followed a similar pattern (**Figure 8.5, Figure 8.7A and Figure S8.2**), which could suggest an influence of osteoclastic differentiation and/or TRAP activity on osteoblastic collagen formation. When investigating the coupling between mineral resorption and formation, a moderate positive correlation ($r = 0.59, p < 0.0001$) was found (**Figure 8.7C**). When splitting the data into high and low stimulation with osteogenic factors, a weak positive ($r = 0.38, p < 0.05$) correlation between mineral resorption and formation was found in highly stimulated scaffolds whereas a strong positive correlation ($r = 0.80, p < 0.0001$) was found when low stimulation was applied (**Figure 8.7C**). This indicates that resorption - formation coupling can be disturbed by high stimulation with osteogenic factors.

8.4 Discussion

Human *in vitro* bone remodeling models, using osteoclast-osteoblast co-cultures, could facilitate the investigation of human healthy (*i.e.*, balanced) and pathological (*i.e.*, unbalanced) bone remodeling while addressing the principle of 3Rs for animal experiments (7,111). Although current *in vitro* osteoclast-osteoblast co-cultures have improved our understanding of bone remodeling, they lack culture method and outcome measurement standardization, hampering reproducibility and translatability to *in vivo* animal models and *in vivo* human data. In this regard, *in vitro* bone remodeling models could benefit from a thorough evaluation of the impact of culture variables on functional and translatable outcome measures, with the aim to reach 'healthy' balanced osteoclast and osteoblast activity. Using a resolution III fractional factorial design, we identified the main effects of commonly used culture variables at high and low stimulation on mineral resorption, mineral formation and a multitude of bone turnover biomarkers in our *in vitro* human bone remodeling model.

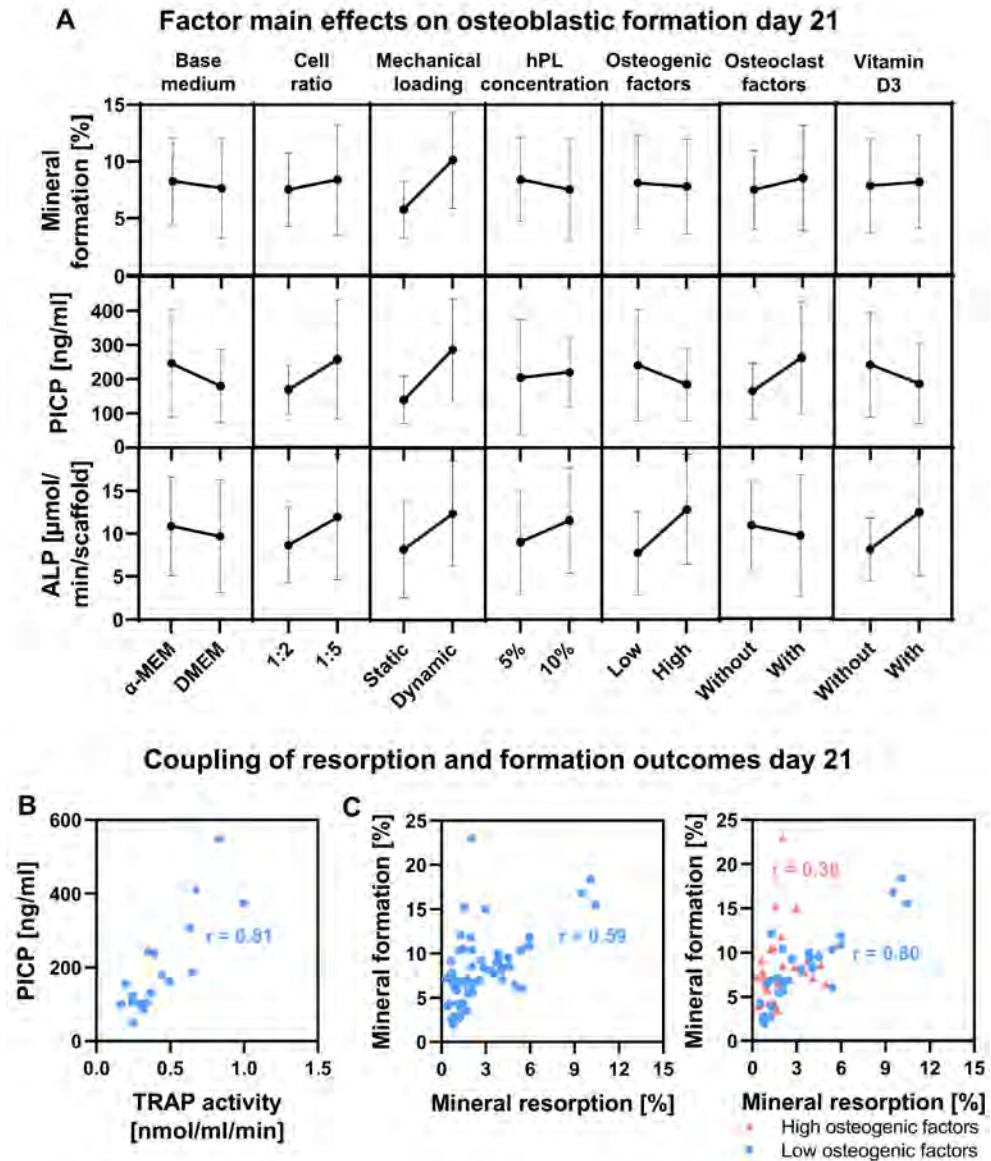


Figure 8.7. (A) Factor main effects and standard deviations on day 21 osteoblastic formation outcome measures. Correlation/coupling of resorption and formation outcomes for (B) organic matrix resorption and formation (TRAP and PICP), and (C) inorganic matrix resorption and formation, in the presence and absence of high stimulation with osteogenic differentiation factors. Abbreviations: human platelet lysate (hPL), tartrate-resistant acid phosphatase (TRAP), pro-collagen 1 c-terminal propeptide (PICP).

We first evaluated the influence of culture variables on cell viability. None of the factors had a significant influence on cell metabolic activity or cell death. The absence of

significant factors indicates that a combination of multiple factors contributed to the found differences between the experimental runs. As such, metabolic activity tended to decrease with high stimulation of all factors other than cell ratio. As the seeding density of hBMSCs remained constant over the different experimental runs, a higher cell ratio led to an increase in hMC density and thereby likely positively influencing cell metabolic activity. The negative influence on metabolic activity of the other culture variables with high stimulation might be explained by differences in energy metabolism of undifferentiated and differentiated progenitor cells. In this study, metabolic activity was measured by the reduction of resazurin to fluorescent resorufin by aerobic respiration. In contrast to our results, osteogenic differentiation of hMSCs has shown to increase the portion of aerobic respiration to the cells' energy metabolism (403). Moreover, osteoclast differentiation is associated with increased mitochondrial biosynthesis and oxygen consumption rate, likely enhancing aerobic respiration (404,405). Thus, osteogenic and osteoclastic differentiation were expected to increase metabolic activity. Although high stimulation did not always lead to improved cell differentiation, one hypothesis for this contradiction might be that limited exogenous factor stimulation enhances endogenous factor production. To confirm this hypothesis, further cell secretome quantification using for example multiplex ELISA is required. If cells with limited stimulation are indeed producing more endogenous factors, limited stimulation might be essential to create self-regulating models.

In our effort to mimic healthy (balanced) remodeling *in vitro*, the influences of culture variables on bone turnover parameters were evaluated. Although the negative control showed most balanced resorption and formation, limited remodeling could be detected, while the ability to capture remodeling is imperative for *in vitro* remodeling models. On the other hand, the positive control showed least balanced resorption and formation, with a relatively high net formation and low volume of quiescent mineral. As such, both low and high stimulation are non-optimal to mimic bone homeostasis *in vitro*. With the least quiescent mineral, experimental run 1 stood out. When evaluating the resorption dynamics of this experimental run, most mineral resorption and highest activity of matrix degradation enzymes TRAP and Cathepsin K were measured, and typical osteoclast-like cells were identified. Therefore, run 1 is considered most optimal for *in vitro* bone resorption. Remarkably, in terms of osteoblastic formation, run 1 also showed most mineral and collagen type I formation. Only for osteogenic differentiation, measured by ALP activity in the cell lysates, run 1 showed levels in between the positive and negative control. The main effects indicated a positive influence of high stimulation with osteogenic differentiation factors on ALP activity, while run 1 was cultured with low stimulation with osteogenic supplements. However, to only measure cell-derived ALP, ALP activity was measured on the cell lysate after 4 weeks instead of tracked over

time. As such, possible down regulations in ALP activity due to osteoblast maturation after 4 weeks could not be excluded (128).

Another experimental run of interest was run 4. In this condition, co-cultures were performed in the absence of high stimulation with osteoclastic and osteogenic differentiation factors, but in the presence of 1,25-dihydroxyvitamin D3. Even in the absence of differentiation factors, relatively high levels of mineral resorption, TRAP activity, mineral formation, collagen type I production, and ALP activity were found. Thus far, the use of exogenous osteoclast differentiation factors (*i.e.*, RANKL and M-CSF) in osteoclast-osteoblast co-cultures appears often crucial for the development of functional osteoclasts (7), while exogenous application of these factors could overrule the natural RANKL/osteoprotegerin (OPG) ratio as important regulator in healthy and pathological bone remodeling (7,406). When no differentiation factors were used in human PBMC-osteoblast co-cultures, no osteoclastic differentiation of PBMCs was observed (226). Other researchers found that when human PBMCs and hBMSCs were co-cultured on osteoblast derived matrix in the absence of osteogenic and osteoclastic differentiation factors, resorption was comparable to PBMC mono-cultures treated with M-CSF and RANKL (343). Moreover, before the discovery of RANKL and the ability to clone this factor, stomal cells and osteoblasts were used as a tool for osteoclastic differentiation *in vitro* (212). We therefore believe that osteoclastic differentiation in osteoclast-osteoblast co-culture in the absence of exogenous RANKL is possible under the correct circumstances. With the use of 1,25-dihydroxyvitamin D3 in experimental run 4, RANKL expression by hMSCs/osteoblasts and subsequent osteoclastic differentiation might have been stimulated as earlier demonstrated (212,263). It would be interesting to quantify M-CSF, RANKL and OPG produced in the experimental runs to investigate the influence of 1,25-dihydroxyvitamin D3 on the osteoclastic differentiation potential in our co-cultures, with the ambition to circumvent the use of exogenous osteoclastic differentiation factors in future.

The enhanced resorption and formation in experimental run 1 raised the expectation that resorption and formation were coupled in our *in vitro* model. Indeed, resorption and formation were correlated for both mineral resorption/formation and organic matrix resorption/formation. By adding an exogeneous phosphate source to the model (β -glycerophosphate), mineral resorption – formation coupling was disturbed. Most likely, osteoclasts released sufficient calcium phosphate from the mineralized scaffold for subsequent formation. *In vivo*, coupling includes communication through secreted and cell-bound factors, topographical cues, and the release of growth factors from the bone matrix, with the main goal to replace the resorbed bone volume by an equal volume of new bone (95,234,407). In addition, osteocytes as well as osteoclast and

osteoblast progenitors contribute to this coupling, which likely change their contribution during their differentiation towards mature osteoclasts and osteoblasts (408,409). As such, coupling is a highly complex process, and it is expected that not all coupling aspects are present in our model. More specifically, the release of growth factors from the matrix/scaffold and the contribution of osteocytes are likely lacking. To enable coupling through growth factor release, *in vitro* remodeling models could be developed on decellularized bone tissue (34,410). To additionally involve osteocytes into the bone remodeling process *in vitro*, a long-term pre-culture in which osteoprogenitors differentiate into osteocytes while they develop their mineralized niche (116,259), or the use of cell-lines might be required, due to challenges with primary osteocyte isolation and subsequent culture (411). To combine the presence of a growth-factor containing bone matrix and osteocytes, osteocytes could also be cultured in their native niche using human trabecular bone specimens (411). In this study we found quantitative coupling between resorption and formation at the tissue level. To further validate coupling in our *in vitro* model, it would be interesting to study coupling qualitatively at the level of the individual resorption pits to see whether formation takes place on previously resorbed surfaces like in the model of A. Hikita *et al.*, (2015) (230). Nevertheless, quantitative coupling was observed along all conditions, indicating some endogenous regulation in all conditions which can be enhanced by external stimuli.

The application of mechanical loading tended to be the most influential factor on both resorption and formation outcomes. While mechanical loading in terms of fluid flow induced shear stress has, in line with our results, been shown to stimulate mineralization and collagen formation in similar settings (90,116), its clear effect on resorption outcomes was unexpected. *In vivo*, bone remodeling and adaptation is regulated by osteocytes under influence of interstitial fluid flow through the lacuno-canalicular network (114). Osteocytes that sense mechanical loading could inhibit osteoclastic differentiation both directly and indirectly (412). The direct influence of mechanical loading on osteoclast differentiation is relatively unknown with *in vitro* both positive (413) and negative (414,415) influences reported in literature. As mentioned above, the contribution of osteocytes and thereby their inhibitory influence on resorption under influence of mechanical loading is likely lacking. Another explanation for the enhanced resorption under influence of mechanical loading could be the improved mass transport when fluid flow was applied. It would therefore be interesting to study the interaction between osteoclastic differentiation factors and mechanical loading within our model, to check whether the likely improved distribution of osteoclastic differentiation factors indeed leads to increased osteoclastic differentiation.

A limitation of the current study is the resolution of the fractional factorial design. With the use of a resolution III design, only an influence of factor main effects could be provided. Moreover, some of these main effects are confounded with interaction effects, which complicates outcome interpretation. In our evaluation, we did not find significant contributions of specific factors to cell viability and bone turnover outcomes. Nevertheless, clear differences between experimental runs were observed. This suggests that a combination of multiple factors contributed to the found differences between experimental runs. Additionally, by both using three different hMC and hBMSC donors, and three different methods for each resorption and formation, we here present a robust evaluation of the influence of culture variables on *in vitro* bone remodeling.

8.5 Conclusion

Taken together, with the aim to mimic healthy balanced bone remodeling *in vitro*, we have identified the influences of commonly used culture variables on translatable bone turnover parameters in a human bone remodeling model. We herewith present a robust *in vitro* bone remodeling model, that was able to capture physiological quantitative resorption – formation coupling along all conditions, which could be enhanced by external stimuli. As such, *in vitro* remodeling (*i.e.*, resorption and formation) was enhanced by the application of mechanical loading. Moreover, high stimulation with osteogenic differentiation factors disturbed mineral resorption – formation coupling. Especially culture conditions of run 1 and 4 show promising results, where run 1 conditions could be used as high bone turnover system and run 4 as self-regulating system as the addition of osteoclastic and osteogenic differentiation factors was not required for remodeling. The results generated with our *in vitro* model allow for better translation between *in vitro* studies and towards *in vivo* studies, for improved preclinical bone remodeling drug development.

Author Contributions

B.d.W., L.C., K.I. and S.H. contributed to conception and design of the study. B.d.W., L.C., E.C. and S.H. contributed to the methodology. B.d.W. performed the experiments. B.d.W. and A.W. analyzed the experimental results. B.d.W. wrote the original draft of the manuscript. B.d.W., K.I. and S.H. were involved in supervision. All authors contributed to manuscript revision and approved the submitted version. B.d.W. and S.H. acquired funding for this research.

Acknowledgement

This work is part of the research program TTW with project number TTW 016.Vidi.188.021, which is (partly) financed by the Netherlands Organization for Scientific Research (NWO). This research was also financially supported by the Gravitation Program “Materials Driven Regeneration”, funded by the Netherlands Organization for Scientific Research (024.003.013).

Supplementary information

Each experimental run in the fractional factorial design had a unique medium composition (**Table S8.1** and **Table S8.2**).

Table S8.1. Medium compositions for different experimental runs.

	Base medium	hPL	Anti-anti	HEPES	L-Glut	Ascorbic acid	β -GP	Dex	RANKL*	M-CSF	vit D3
R1	94% α -MEM	5%	1%	25 mM		50 μ g/ml		10 nM	50 ng/ml	50 ng/ml	
R2	94% α -MEM	5%	1%	25 mM		50 μ g/ml	10 mM	100 nM			10 nM
R3	89% DMEM	10%	1%	25 mM	4mM	50 μ g/ml		10 nM			
R4	89% α -MEM	10%	1%	25 mM		50 μ g/ml		10 nM			10 nM
R5	94% DMEM	5%	1%	25 mM	4mM	50 μ g/ml		10 nM	50 ng/ml	50 ng/ml	10 nM
R6	94% DMEM	5%	1%	25 mM	4mM	50 μ g/ml	10 mM	100 nM			
R7	89% DMEM	10%	1%	25 mM	4mM	50 μ g/ml	10 mM	100 nM	50 ng/ml	50 ng/ml	10 nM
R8	89% α -MEM	10%	1%	25 mM		50 μ g/ml	10 mM	100 nM	50 ng/ml	50 ng/ml	
R9	94% α -MEM	5%	1%	25 mM		50 μ g/ml		10 nM			

Abbreviations: run (R), human platelet lysate (hPL), antibiotic antimycotic (anti-anti), L-glutamine (L-glut), β -glycerophosphate (β -GIP), dexamethasone (dex), macrophage colony-stimulating factor (M-CSF), receptor activator of nuclear factor κ B ligand (RANKL), 1,25-dihydroxyvitamin D3 (vit D3). *Applied from day 2 in culture.

Table S8.2. Medium components and suppliers.

Medium component	Supplier
α -MEM	41061, Thermo Fisher Scientific, Breda, The Netherlands
DMEM	11880, Thermo Fisher Scientific
hPL	PE20612, PL BioScience, Aachen, Germany
Anti-anti	15240, Thermo Fisher Scientific
HEPES	15630, Thermo Fisher Scientific
L-glutamine	X0550-100, Biowest, Nuaille, France
Ascorbic acid-2-phosphate	A8960, Sigma Aldrich, Zwijndrecht, The Netherlands
β -glycerophosphate	G9422, Sigma-Aldrich
Dexamethasone	D4902, Sigma-Aldrich
RANKL	310-01, PeproTech, London, UK
M-CSF	300-25, PeproTech
1,25-dihydroxyvitamin D3	D1530, Sigma-Aldrich

Abbreviations: human platelet lysate (hPL), antibiotic antimycotic (anti-anti), macrophage colony-stimulating factor (M-CSF), receptor activator of nuclear factor κ B ligand (RANKL).

Normal effect plots were generated to visualize the effect size and direction of each factor on cell viability (**Figure S8.1**) and bone turnover outcomes (**Figure S8.2**).

Normal effect plots for cell viability

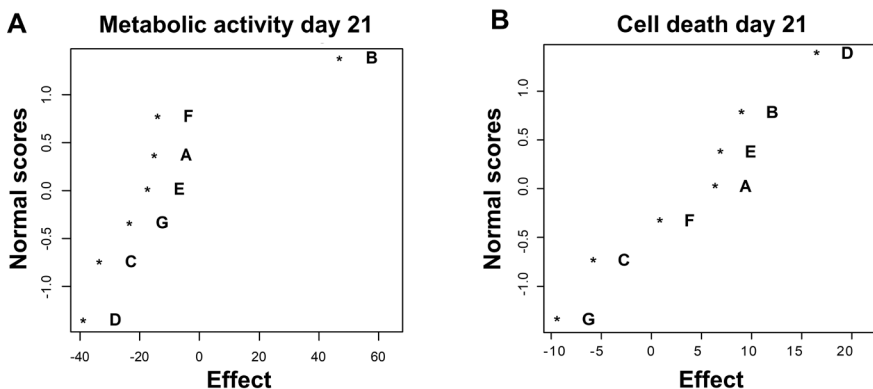


Figure S8.1. Normal effect plots for cell viability outcomes. **(A)** Normal effect plot for day 21 metabolic activity, indicating a non-significant positive effect of a high cell ratio on metabolic activity. **(B)** Normal

effect plot for day 21 cell death. A = base medium, B = cell ratio, C = mechanical loading, D = human platelet lysate concentration, E = osteogenic factors, F = osteoclast factors, F = 1,25-dihydroxyvitamin D3

Normal effect plots for resorption

Normal effect plots for formation

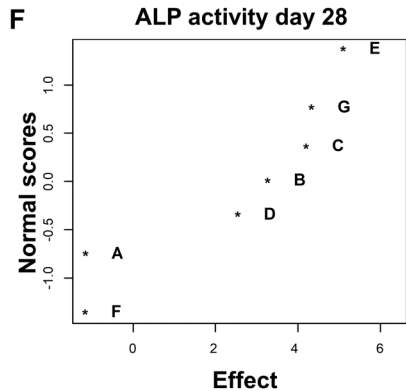
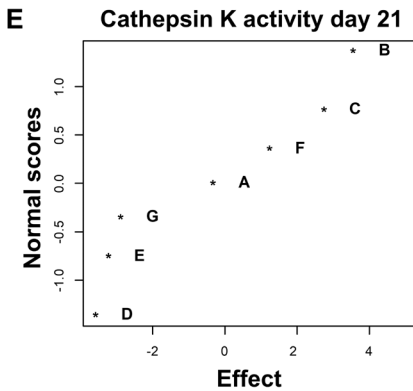
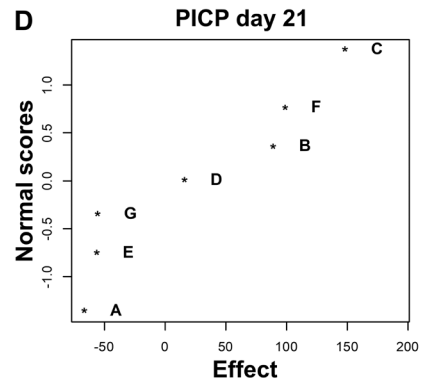
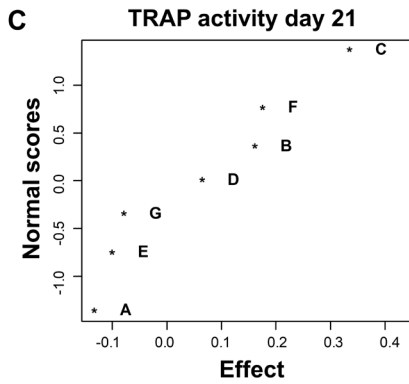
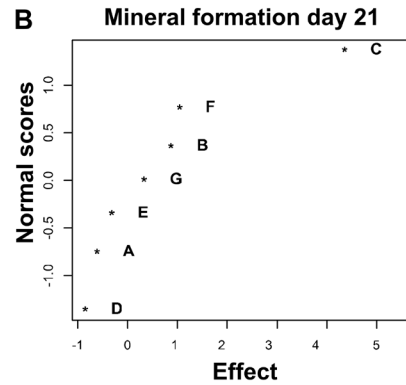
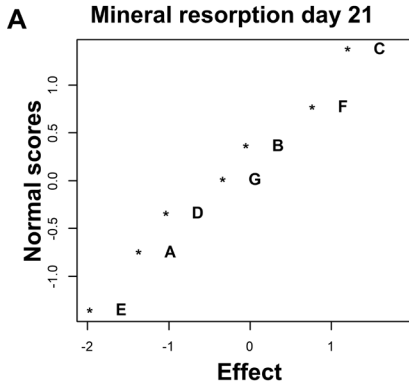


Figure S8.2. Normal effect plots for bone turnover outcomes. (A) Normal effect plot for day 21 mineral resorption. (B) Normal effect plot for day 21 mineral formation, indicating a non-significant positive effect

of high stimulation with mechanical loading on mineral formation. **(C)** Normal effect plot of day 21 TRAP activity. **(D)** Normal effect plot of day 21 PICP. **(E)** Normal effect plot of day 21 Cathepsin K activity. **(F)** Normal effect plot of day 28 ALP activity. A = base medium, B = cell ratio, C = mechanical loading, D = human platelet lysate concentration, E = osteogenic factors, F = osteoclast factors, F = 1,25-dihydroxyvitamin D₃. Abbreviation: tartrate-resistant acid phosphatase (TRAP), pro-collagen 1 c-terminal propeptide (PICP), alkaline phosphatase (ALP).

9

General discussion

A part of this chapter is based on:

Sana Ansari^{1,2,†}, **Bregje W.M. de Wildt**^{1,2,†}, Michelle A.M. Vis^{1,2}, Carolina E. de Korte¹, Keita Ito^{1,2}, Sandra Hofmann^{1,2}, Yuana Yuana³

1. Orthopaedic Biomechanics, Department of Biomedical Engineering, Eindhoven University of Technology, Eindhoven, The Netherlands.
2. Institute for Complex Molecular Systems (ICMS), Eindhoven University of Technology, Eindhoven, The Netherlands.
3. Department of Biomedical Engineering, Eindhoven University of Technology, Eindhoven, The Netherlands.

†Authors contributed equally

9.1 Rationale and main findings

Since the 1990s, bone tissue engineering has traditionally been focusing on developing grafts for patients with large bone defects, making use of scaffolds, progenitor cells, biochemical and biomechanical stimuli. While engineered bone-like tissues proved of limited success for human bone regeneration, their development has advanced our ability to manipulate cells and engineer materials. To improve preclinical treatment development and to replace, reduce, and refine animal experiments, bone tissue engineering strategies are increasingly applied for the creation of *in vitro* models to study human bone in health and disease. This change in focus; from bone regeneration to *in vitro* models, has brought new challenges for researchers of which some are addressed in this thesis (Figure 9.1).

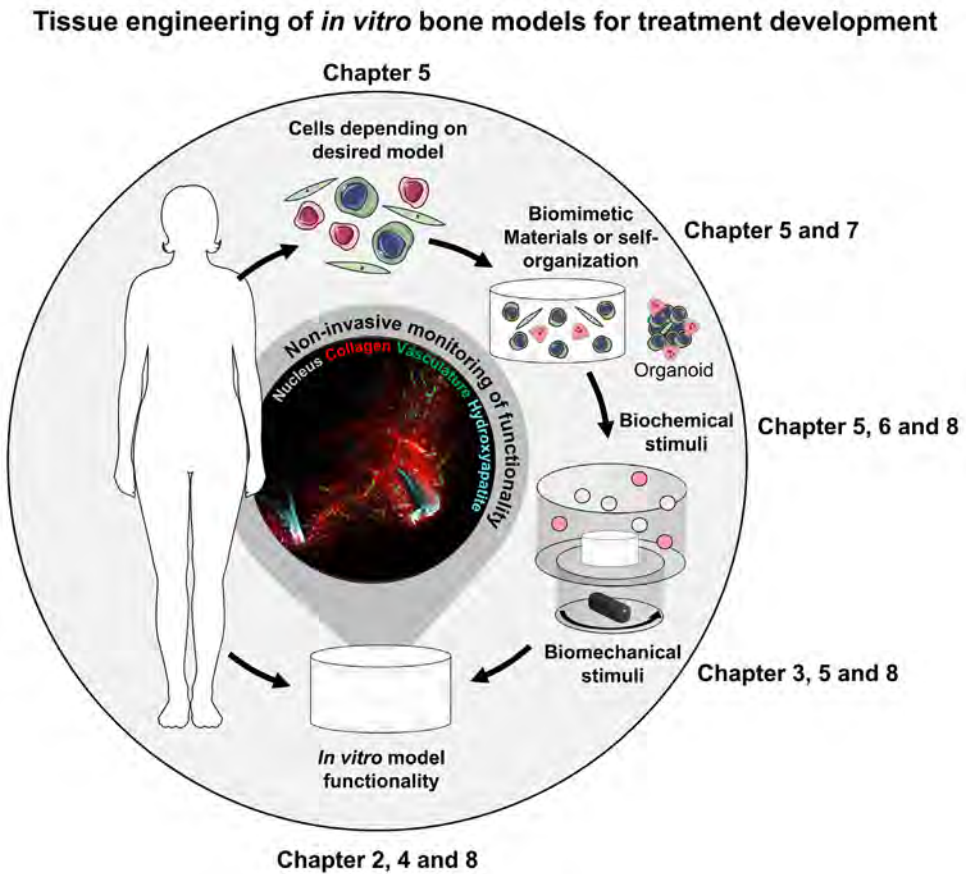


Figure 9.1. Tissue engineering approach to create 3D *in vitro* bone models. Around the central circle, the chapters in which the *in vitro* modeling parameters were addressed are indicated. The figure was modified

from Servier Medical Art, licensed under a Creative Common Attribution 3.0 Generic License (<http://smart.servier.com>, accessed on 15 July 2022).

The first part of this thesis was focused on the development of *in vitro* models for evaluating human bone formation and regeneration. In **Chapter 2** we described the bone extracellular matrix (ECM) based on the most recent advances on bone structure from the nanometer scale to the micrometer scale, which were used to provide recommendations on the to be engineered ECM for *in vitro* bone models. These recommendations include uniformly organized collagen fibrils with interconnected intrafibrillar and extrafibrillar mineral crystals on the nanometer scale, and a dense and anisotropic collagen network that is highly mineralized on the micrometer scale. In **Chapter 3**, an *in vitro* platform to study bone formation under the influence of curvature and no fluid flow or directional fluid flow was developed and an initial attempt in three-dimensions (3D) was made to improve the resemblance of *in vitro* produced bone-like ECM to the physiological bone ECM on the micrometer scale. Based on the results obtained within this study, supported by existing literature, we believe that anisotropy in 3D might be guided by curvature, while collagen network density can be increased through the application of fluid shear stress. The *in vitro* platform as described in **Chapter 3** was subsequently extended with endothelial cells and used as critically sized defect model to enable the *in vitro* investigation of material-driven bone regeneration in **Chapter 4**. After a model build-up phase of 4 weeks, in which vessel-like structures and a bone-like matrix were formed, materials (*i.e.*, a fibrin clot, blood clot mimic and soft callus mimic) were artificially implanted. Within this model, important hallmarks for *in situ* bone regeneration including cell migration, vascularization, and osteoinduction, were evaluated. While our model is still limited in the evaluation of immune responses, hallmarks of physiological bone regeneration were observed *in vitro*. These included the endothelial cell chemotaxis induced by the blood clot mimic and the mineralization of the soft callus mimics. As such, this *in vitro* model could contribute to improved pre-clinical evaluation of biomaterials for bone regeneration, while aiding to reduce the need for animal experiments.

The second part of this thesis was focused on advancing tissue engineering of *in vitro* human bone remodeling models. First, we identified after a systematic search all osteoclast-osteoblast co-cultures aiming at recapitulating bone remodeling *in vitro* that have been described in literature before 2020 in **Chapter 5**. From these studies, differences in cell-culture methods (culture substrate, mechanical loading, cell sources, culture medium, seeding density and cell-ratio) and resorption/formation analyses methods were mapped systematically, which underlined the variability between currently available *in vitro* remodeling models, hampering translation between *in vitro* models. One of the limitations of currently available *in vitro* bone remodeling models

identified in **Chapter 5** was the frequent use of fetal bovine serum (FBS). In **Chapter 6**, we therefore investigated whether FBS could be replaced by human platelet lysate (hPL) as a more physiologically relevant and xenogeneic-free medium supplement for *in vitro* human bone remodeling models. We found that hPL supported both osteoclastogenesis and osteogenesis, and when co-cultured, remodeling could be balanced by the hPL concentration. As such, we successfully found a xenogeneic-free replacement for FBS to increase the compliance of our *in vitro* model with the desire to replace, reduce, and refine animal experiments. Another limitation of currently available *in vitro* bone remodeling models identified in **Chapter 5** is the lack of studying cell-matrix interactions and model functionality; the ability of osteoclasts and osteoblasts to resorb and subsequently form a bone-like matrix. Inspired by collagen mineralization techniques, we developed a mineralized silk fibroin scaffold in **Chapter 7**. As a remodeling template, this scaffold facilitated the temporal investigation of both resorption by osteoclasts and formation by osteoblasts, which recapitulated the physiological bone remodeling cycle. This is of importance as these functional outcome measures need to be targeted for bone remodeling pathologies like osteoporosis. In **Chapter 8**, we utilized the model described in **Chapter 7** to address the translational issues identified in **Chapter 5**. A design of experiments set-up was used to study the influence of base medium, cell-ratio, hPL concentration, mechanical loading, osteogenic differentiation factors, osteoclastic differentiation factors, and 1,25-dihydroxyvitamin D3 on *in vitro* bone remodeling. Our model was able to capture physiological quantitative resorption – formation coupling along all conditions and across different cell donors, which could be enhanced by external stimuli. Culture conditions were identified to study high bone turnover, as well as conditions that promote self-regulation as the addition of osteoclastic and osteogenic differentiation factors was not required for remodeling. The results generated with our *in vitro* model allow for better translation between *in vitro* studies and towards *in vivo* studies, for improved preclinical bone remodeling drug development. Besides, our model was highly sensitive to alterations in culture conditions and thereby able to capture physiological aspects of human bone remodeling like increased formation with mechanical loading. As such, we have developed a functional *in vitro* bone remodeling model, which was partly validated by well-known physiological cell-responses.

9.2 Remaining challenges for *in vitro* bone models

9.2.1 Towards self-regulating *in vitro* models

A major challenge in the development of *in vitro* bone models is the need for non-physiological exogenous stimulation. For instance, *In vivo* bone remodeling is regulated

by communication through direct cell-cell contact as well as soluble factors. Among these soluble communication factors, secretory macrophage colony-stimulating factor (M-CSF), receptor activator of nuclear factor κ B ligand (RANKL) and osteoprotegerin (OPG) are factors produced by osteocytes, osteoblasts and their precursors that directly regulate osteoclastic differentiation and resorption (281). In turn, monocyte-derived macrophages and osteoclasts release soluble factors that are involved in osteogenic differentiation of mesenchymal stromal cells (408).

Besides these secreted differentiation factors, bone cells can also communicate through extracellular vesicles. Extracellular vesicles are phospholipid-enclosed nanoparticles containing a variety of lipids, proteins, genetic material (DNA/RNA), and minerals derived from their parent cells (416–419). Based on the current knowledge in the field, extracellular vesicles can be classified into three subtypes: (i) plasma membrane-derived ectosomes, (ii) endosome-originated exosomes, and (iii) apoptotic bodies (**Figure 9.2**) (419,420). Although initially considered as inert cellular debris, extracellular vesicles are now recognized as being important mediators in intercellular communication and many biological processes (420–422), including bone remodeling.

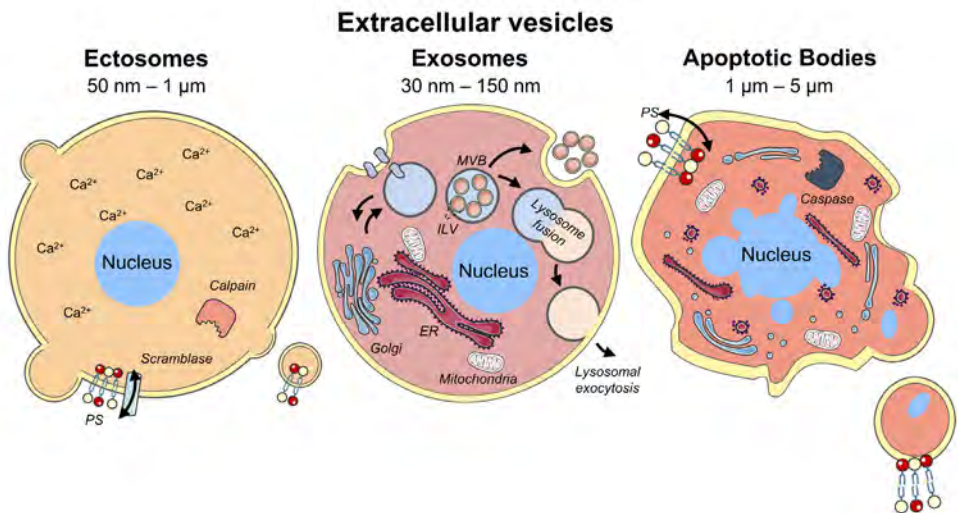


Figure 9.2. Subtypes of extracellular vesicles based on their possible biogenesis pathways. Extracellular vesicles can appear as ectosomes that bleb from the cell membrane, as exosomes that are formed inside the cell after endocytosis, or as apoptotic bodies that derive from cells undergoing apoptosis. Abbreviations: multi vesicular body (MVB), intra luminal vesicle (ILV), endoplasmic reticulum (ER), phosphatidylserine (PS). Figure was modified from Servier Medical Art, licensed under a Creative Common Attribution 3.0 Generic License. (<http://smart.servier.com>, accessed on 20 January 2021).

In terms of bone remodeling, Cappariello *et al.*, (2018) (423) found that osteoblasts pre-treated with parathyroid hormone generated extracellular vesicles carrying RANKL and demonstrated that these extracellular vesicles supported the survival of osteoclasts *in vitro* (423). *In vivo*, intraperitoneal injection of extracellular vesicles from wild-type osteoblasts into RANKL^{-/-} mice lacking tartrate-resistant acid phosphatase (TRAP) expression increased the presence of TRAP-positive cells in trabecular bone, which is indicative of osteoclastogenesis (423). Mature osteoblasts also release extracellular vesicles with specific characteristics involved in matrix mineralization. These extracellular vesicles are anchored to proteins of the surrounding ECM and are known as matrix vesicles (424,425). Osteoclasts and their precursors have also been described to generate extracellular vesicles with a diameter between 25 and 120 nm, similar to the size of exosomes (426). Their membranes are enriched with epithelial cell adhesion molecule, CD63, and receptor activator of nuclear factor κ B (RANK). Interestingly, RANK rich osteoclast-derived extracellular vesicles act as inhibitors of osteoclastogenesis through competitively decreasing the RANK-RANKL interaction with *e.g.*, osteoblasts (426,427). During bone remodeling, osteoclasts often undergo apoptosis at the end of the bone resorption phase and produce large amounts of apoptotic bodies (428). These vesicles promote osteogenesis via RANKL reverse signaling. It has been shown that osteocyte mechanosensitivity is encoded through unique intracellular calcium dynamics (429). Upon fluid flow, osteocytes showed a transient increase in intracellular calcium ions and these cells released a substantial amount of extracellular vesicles containing bone regulatory proteins such as sclerostin, RANKL, and OPG into the culture medium (429). Osteocytes also released extracellular vesicles containing micro RNA (miR)-218 which inhibited sclerostin and influenced the differentiation of osteoblasts (430) (**Table 9.1**).

Consequently, in theory osteoclastic and osteogenic differentiation and subsequent *in vitro* remodeling could be a self-regulating process, which is desired to enable the investigation of the influence of exogenous factors like drugs on bone turnover *in vitro*. In practice, proper osteoclastic differentiation under the sole influence of cells from the osteogenic lineage is challenging (7). The common practice in cell-culture is to replace the culture medium two or three times a week. As such, waste products are removed, and new nutrients are provided. This change in medium however also removes soluble communication factors and extracellular vesicles not bound to the ECM. Although in this thesis (**Chapter 8**) potential experimental conditions that could limit the need for exogenous differentiation factors were identified, it is expected that cell crosstalk and subsequent remodeling can be enhanced when soluble communication factors and extracellular vesicles are retained (136). Culture medium dialysis could facilitate in the retention of high molecular weight communication factors and extracellular vesicles

while allowing for diffusion of low molecular weight waste products and nutrients (**Figure 9.3**) (136,431). Such systems have the potential to improve the crosstalk mediated self-regulation of *in vitro* bone remodeling models.

Table 9.1. Cargo and function of extracellular vesicles derived from bone cells

Cell source of EVs	Cargo of EVs	Function of EVs
Osteoblast	<ol style="list-style-type: none"> 1. RANKL (423) 2. miR-1192, miR-680 and miR-302a (432) 3. miR-125b and miR-503 (433,434) 	<ol style="list-style-type: none"> 1. Supports survival of osteoclasts <i>in vitro</i> and osteoclastogenesis <i>in vivo</i>. 2. Promote osteogenic differentiation, as manifested by up-regulated expression of osteogenic marker genes RUNX2 and ALP, as well as enhanced matrix mineralization. 3. Have anti-osteoclastogenic activity.
Osteoclast	<ol style="list-style-type: none"> 1. RANK, EpCAM CD63 (426–428) 2. miR-214 (435,436) 	<ol style="list-style-type: none"> 1. Maintain bone homeostasis and promote osteogenesis through the RANK-RANKL reverse signaling. 2. Inhibits osteoblast activity <i>in vitro</i>.
Osteocyte	<ol style="list-style-type: none"> 1. LAMP1, sclerostin, RANKL and OPG (429) 2. miR-218 (430) 	<ol style="list-style-type: none"> 1. Attenuate bone formation <i>in vivo</i>. 2. Inhibits sclerostin and influences the differentiation of osteoblasts.

Abbreviations: extracellular vesicles (EVs), receptor activator of nuclear factor κ B ligand (RANKL), microRNA (miR), runt-related transcription factor 2 (RUNX2), alkaline phosphatase (ALP), receptor activator of nuclear factor κ B (RANK), epithelial cell adhesion molecule (EpCAM), Lysosomal-associated membrane protein 1 (LAMP1), osteoprotegerin (OPG).

9.2.2 Integration of systemic regulators of bone remodeling

Bone remodeling is not only regulated by osteoclast-osteoblast crosstalk and osteocytes. Bone is an endocrine organ that interacts through systemic factors with other organs including *e.g.*, muscles (437,438), kidneys (439), parathyroid glands (440), and the brain (441). For example, the chronic kidney disease nephrotic syndrome is associated with low levels of vitamin D, which can lead to a decrease in bone mineral density (442). In addition, postmenopausal estrogen deficiency in women is a major cause of osteoporosis (443). Moreover, sustained release of parathyroid hormone in hyperthyroidism can induce a catabolic response in bone (7). Currently, these

interactions are mainly studied in animal experiments *in vivo* or *in vitro* by testing the influence of for instance estrogen administration schemes on single bone cells (444). The use of estrogen in *in vitro* bone remodeling models is relatively unexplored. To improve physiological relevance, the use of such systemic factors like estrogen should be considered for *in vitro* bone remodeling models. To accomplish this, *in vitro* administration dosages and schemes need to be optimized first. After successful implementation into the culture conditions, estrogen might be removed again to mimic postmenopausal estrogen deficiency *in vitro* (7). Such model has great potential for the development of osteoporosis drugs. Other potential strategies involve multi-organ platforms to study the instant interaction of bone with other organs (410).

Towards engineering of self-regulating *in vitro* models

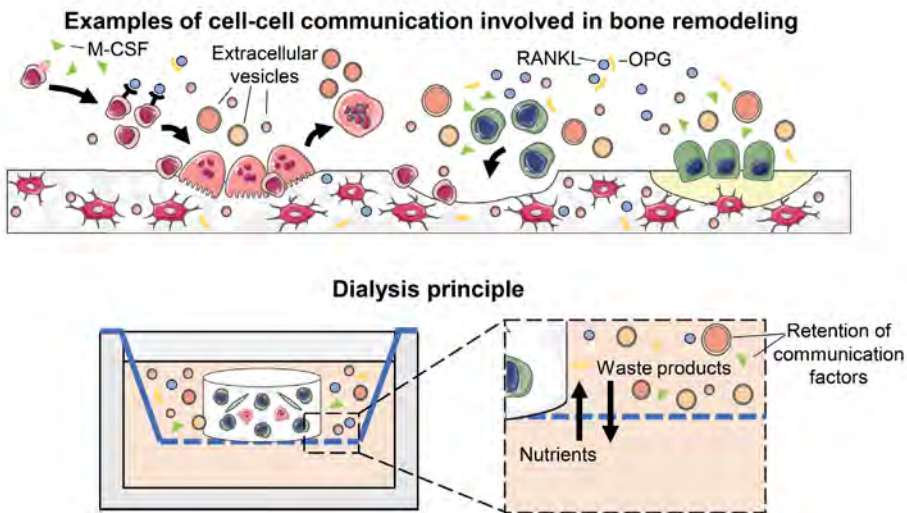


Figure 9.3. Examples of communication factors that regulate bone remodeling *in vivo* and how *in vitro* these communication factors might be retained during cell-culture medium refreshments. The medium in the bottom compartment can be replaced with fresh medium while medium in the top compartment is not changed. Dialysis of culture medium relies on the size of medium components. The dialysis membrane (dependent on the chosen molecular weight cut-off) allows for exchange of low molecular weight proteins, amino acids, vitamins, lactate, and ammonium, while high molecular weight components such as extracellular vesicles and growth factors are retained in the insert. Abbreviations: macrophage colony-stimulating factor (M-CSF), receptor activator of nuclear factor κ B ligand (RANKL), osteoprotegerin (OPG). The figure was adapted from (136) and modified with Servier Medical Art, licensed under a Creative Commons Attribution 3.0 Generic License (<http://smart.servier.com>, accessed on 15 July 2022).

While developing platforms to study the systemic regulation of bone remodeling, one should consider the applied culture medium. Ideally, cells are cultured in a medium of

which its composition is well known. In practice, osteoclast-osteoblast co-cultures are mostly performed in FBS containing medium of which its composition is unknown and varies from batch-to-batch (**Chapter 5**). The presence of alkaline phosphatase in FBS can, when combined with the osteogenic differentiation factor β -glycerophosphate, induce mineral precipitation in the absence of cells (137). In addition, it is known that FBS also contains some estrogen and parathyroid hormone (445,446). Furthermore, phenol red, which is often used in the base medium, has affinity to estrogen receptors. Although the binding affinity is relatively low, the concentration in culture medium is considerably high which can lead to occupation of estrogen receptors (243,244). In this thesis, we have attempted to circumvent the use of phenol red and FBS for our *in vitro* bone remodeling model by using phenol red free base medium and hPL as serum substitute (**Chapter 6**). Although it is expected that human platelets contain limited systemic factors that affect bone remodeling, its exact composition remains a black box. To facilitate reproducibility and control over *in vitro* bone models, the use of a defined serum-free medium is desired. While serum-free media are commercially being developed for often only one cell type, the use of serum-free medium for bone relevant co-cultures is to date relatively unexplored with (to our knowledge) one attempt for bone remodeling (393). Taken together, physiological and pathological relevance of *in vitro* bone models can be improved by implementation of systemic factors involved in bone (remodeling), which can only be tightly controlled in defined serum-free media.

9.2.3 Towards \geq triple cultures

In this thesis, co-cultures were used to mimic the processes of bone regeneration (**Chapter 4**) and remodeling (**Chapter 6-8**). Although we have shown that with these co-cultures essential physiological processes can be mimicked, *in vivo* many other cells are involved in regeneration and remodeling which were not included in our models. For example, a heterogeneous immune cell population and periosteal cells play a crucial role in physiological bone regeneration (447,448). Moreover, osteocytes orchestrate bone remodeling and adaptation *in vivo*, mainly under the influence of mechanical loading (114). However, increasing the number of cell types complicates cell-culture, requiring new optimization of culture conditions including timing of cell seeding and administration of medium supplements. Moreover, to additionally involve osteocytes into the bone remodeling process *in vitro*, a long-term pre-culture in which osteoprogenitors differentiate into osteocytes while they develop their mineralized niche (116,259), or the use of cell-lines might be required, due to challenges with primary osteocyte isolation and subsequent culture (411). To overcome this challenge, future studies could investigate combining osteoclast-osteoblast co-cultures with viable bone explant cultures (411), or towards osteocytes pre-differentiated mesenchymal stromal cells/osteoblasts seeded in an artificial bone-like matrix (265). Combining

osteoclast-osteoblast co-cultures with osteocytes would allow for studying the influence of osteocyte signaling on bone remodeling *in vitro*, which is crucial for studies on bone adaptation and likely endocrine bone pathologies (449).

9.2.4 Simplicity versus physiological relevance

For an *in vitro* model, a trade-off between simplicity and physiological relevance should be made. Many researchers have the desire to create models which closely mimic the *in vivo* situation (**Chapter 2**). However, increasing physiological relevance and therefore model complexity comes often at the expense of model handling and reproducibility, with its consequences for model translatability (450). Scalability and interlaboratory reproducibility become crucial when human *in vitro* models are used in translational research, like preclinical treatment development (245,451). As such, reproducible and therefore likely easily manufactured *in vitro* models are a potential way forward. Proper model validation could identify key model aspects needed to mimic the desired physiological process with for example a design of experiments approach described in **Chapter 8**. Although such *in vitro* models might be used in a high-throughput fashion in future, currently simpler and more short-term high-throughput screening platforms could identify potential treatment hits before more complex and physiologically relevant *in vitro* models are applied. Unfortunately, to this extent animal experiments likely remain a requirement in the preclinical research pipeline in the near future, as *in vitro* models remain hypothesis (*i.e.*, tissue aspect) driven and therefore less sensitive to complicated/unexpected treatment-host interactions (**Figure 9.4**) (451,452).

9.3 Towards refinement of the preclinical research pipeline

Although the replacement of animal experiments with human *in vitro* models remains challenging, their integration into the preclinical research pipeline might screen out treatments before they are tested in animal experiments, and thereby reducing the burden on animals for experimentation. While over the past decade many *in vitro* models and organoids have been developed, pharmaceutical companies have not yet widely adopted these types of technology (451). Successful integration of human *in vitro* models into the preclinical research pipeline likely relies on a multitude of model requirements, including the use of relevant biomarkers, model functionality, model validation, robustness and reproducibility, accessibility of cell/tissue source for model, manufacturability, etc. (extensively described by Jeong et al., (2018) (453)). To facilitate the application of developed *in vitro* models for drug or treatment development in future, academic researchers and pharmaceutical companies should collaborate already at early development stages to share knowledge and desired requirements (451). Additionally, a currently being explored strategy to further facilitate translation towards reduced animal

experimentation is the investigation of species differences in these developed sophisticated *in vitro* models. Data from animal *in vitro* and *in vivo* models can be compared, and their results might facilitate translation and extrapolation of human *in vitro* models to the human *in vivo* situation (44,454), in which computational models might account for exposure differences. However, to enable this translation, method standardization and translatable outcome measures (*i.e.*, established biomarkers measurable at multiple model levels) might be needed (44). As such, refinement of the preclinical research pipeline towards efficient and safe treatment development requires close collaboration of biologists, computational scientists, engineers and pharmaceutical companies (**Figure 9.4**).

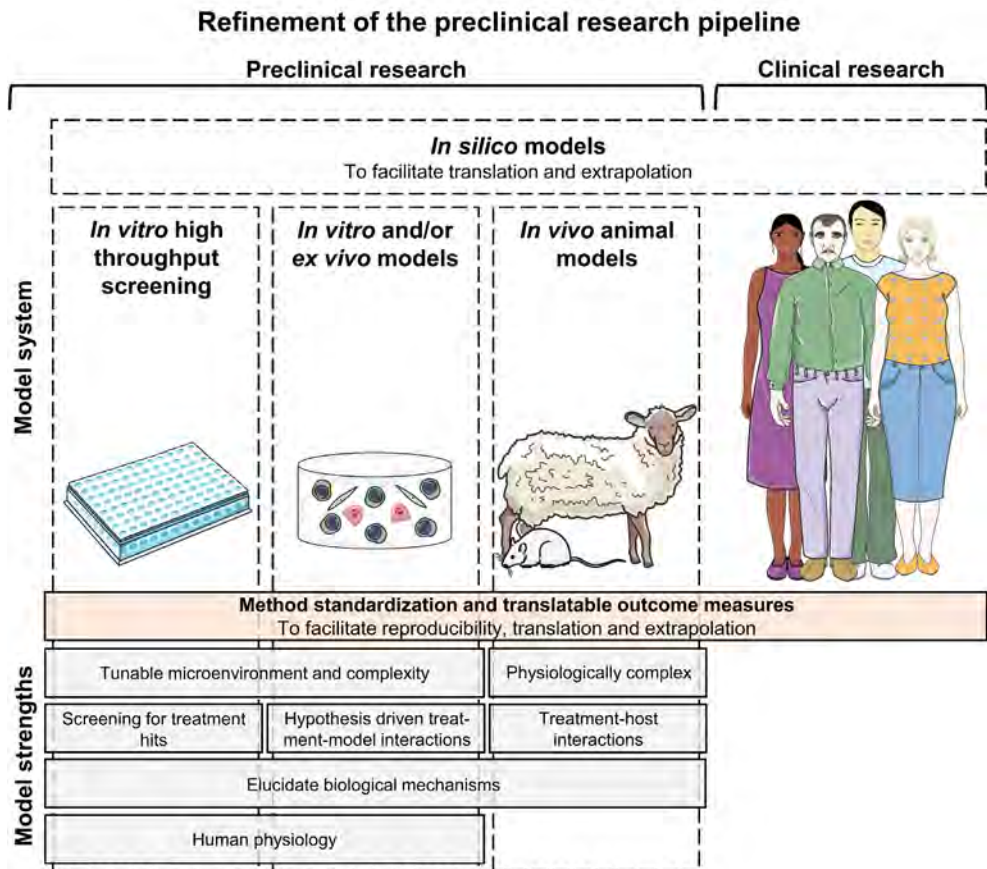


Figure 9.4. Proposed future way forward for the preclinical research pipeline in which *in vitro* high throughput screening platforms facilitate efficient screening for treatment hits, which are subsequently tested in human *in vitro* models that mimic certain aspects of human physiology more closely. For complex treatment-host interactions, animal models might still be required. Translation and extrapolation could be improved by method standardization, the use of standardized translatable outcome measures, and the

characterization of interspecies differences. In silico models can facilitate in translation and extrapolation of treatment effects, all to allow for safe but efficient preclinical treatment development. The figure was created with Servier Medical Art, licensed under a Creative Common Attribution 3.0 Generic License (<http://smart.servier.com>, accessed on 15 July 2022).

9.4 General conclusion

Taken together, in this thesis the tissue engineering paradigm has been extended to *in vitro* human bone models. Methods to improve biomimicry of the produced or to-be remodeled ECM as well as the cell-culture environment and analyses methods were refined. As a result, this thesis presents functionally validated *in vitro* models for the evaluation of crucial aspects of material-driven human bone regeneration and human bone remodeling by osteoclasts and osteoblasts, helping to advance preclinical *in vitro* bone treatment development while contributing to the desire to replace, refine, and reduce animal experiments.

Bibliography

1. Clarke B. Normal bone anatomy and physiology. *Clin J Am Soc Nephrol* (2008) 3:S131–S139. doi: 10.2215/CJN.04151206
2. Buckwalter JA, Glimcher MJ, Cooper RR, Recker R. Bone Biology. *J Bone Jt Surg* (1995) 77:1256–1275. doi: 10.2106/00004623-199508000-00019
3. Buck DW, Dumanian GA. Bone biology and physiology: Part I. The fundamentals. *Plast Reconstr Surg* (2012) 129:1314–1320. doi: 10.1097/PRS.0b013e31824eca94
4. Wolff J. *The Law of Bone Remodelling*. (1986).
5. Reznikov N, Shahar R, Weiner S. Bone hierarchical structure in three dimensions. *Acta Biomater* (2014) 10:3815–3826. doi: 10.1016/j.actbio.2014.05.024
6. Kohli N, Wright KT, Sammons RL, Jeys L, Snow M, Johnson WEB. An *in vitro* comparison of the incorporation, growth, and chondrogenic potential of human bone marrow versus adipose tissue mesenchymal stem cells in clinically relevant cell scaffolds used for cartilage repair. *Cartilage* (2015) 6:252–263. doi: 10.1177/1947603515589650
7. Owen R, Reilly GC. *In vitro* models of bone remodelling and associated disorders. *Front Bioeng Biotechnol* (2018) 6:134. doi: 10.3389/fbioe.2018.00134
8. Fernández-Tresguerres Hernández-Gil I, Angel Alobera Gracia M, del Canto Pingarrón M, Blanco Jerez L. Physiological bases of bone regeneration II. The remodeling process. *Med Oral Patol Oral Cir Bucal* (2006) 11:E151–E157.
9. Zaidi M. Skeletal remodeling in health and disease. *Nat Med* (2007) 13:791–801. doi: 10.1038/nm1593
10. Salari N, Ghasemi H, Mohammadi L, Behzadi M hasan, Rabieenia E, Shohaimi S, Mohammadi M. The global prevalence of osteoporosis in the world: a comprehensive systematic review and meta-analysis. *J Orthop Surg Res* (2021) 16:609. doi: 10.1186/s13018-021-02772-0
11. Stone KL, Seeley DG, Lui L-Y, Cauley JA, Ensrud K, Browner WS, Nevitt MC, Cummings SR. BMD at Multiple Sites and Risk of Fracture of Multiple Types: Long-Term Results From the Study of Osteoporotic Fractures. (2003). 1947–1954 p. doi: 10.1359/jbmr.2003.18.11.1947
12. Cauley JA. Public health impact of osteoporosis. *J Gerontol A Biol Sci Med Sci* (2013) 68:1243–1251. doi: 10.1093/gerona/glt093
13. Einhorn TA, Gerstenfeld LC. Fracture healing: mechanisms and interventions. *Nat Rev Rheumatol* (2015) 11:45–54. doi: 10.1038/nrrheum.2014.164
14. Dimitriou R, Jones E, McGonagle D, Giannoudis P V. Bone regeneration: current concepts and future directions. *BMC Med* (2011) 9:66. doi: 10.1186/1741-7015-9-66
15. Zura R, Xiong Z, Einhorn T, Watson JT, Ostrum RF, Prayson MJ, Della Rocca GJ, Mehta S, McKinley T, Wang Z, et al. Epidemiology of Fracture Nonunion in 18 Human Bones. *JAMA Surg* (2016) 151:e162775. doi: 10.1001/jamasurg.2016.2775
16. Mills LA, Aitken SA, Simpson AHRW. The risk of non-union per fracture: current myths and revised figures from a population of over 4 million adults. *Acta Orthop* (2017) 88:434–439. doi: 10.1080/17453674.2017.1321351
17. Koons GL, Diba M, Mikos AG. Materials design for bone-tissue engineering. *Nat Rev Mater* (2020) 5:584–603. doi: 10.1038/s41578-020-0204-2
18. Williams DF. “B.,” *The Williams Dictionary of Biomaterials*. Liverpool University Press (1999). p. 33–54 doi: 10.5949/UPO9781846314438.006
19. Caddeo S, Boffito M, Sartori S. Tissue engineering approaches in the design of healthy and

- pathological *in vitro* tissue models. *Front Bioeng Biotechnol* (2017) 5:40. doi: 10.3389/fbioe.2017.00040
20. Holmes A, Brown R, Shakesheff K. Engineering tissue alternatives to animals: applying tissue engineering to basic research and safety testing. *Regen Med* (2009) 4:579–592. doi: 10.2217/rme.09.26
 21. Cramer EEA, Ito K, Hofmann S. Ex vivo Bone Models and Their Potential in Preclinical Evaluation. *Curr Osteoporos Rep* (2021) 19:75–87. doi: 10.1007/s11914-020-00649-5
 22. Hulsart-Billström G, Dawson JI, Hofmann S, Müller R, Stoddart MJ, Alini M, Redl H, El Haj A, Brown R, Salih V, et al. A surprisingly poor correlation between *in vitro* and *in vivo* testing of biomaterials for bone regeneration: Results of a multicentre analysis. *Eur Cells Mater* (2016) 31:312–322. doi: 10.22203/eCM.v031a20
 23. Thomas DW, Burns J, Audette J, Adam Carroll, Dow-Hygelund C, Hay M. Clinical Development Success Rates 2006–2015. (2016).
 24. Thomas D, Chancellor D, Micklus A, LaFever S, Hay M, Chaudhuri S, Bowden R, Lo AW. Clinical Development Success Rates and Contributing Factors 2011–2020. (2021).
 25. Barré - Sinoussi F, Montagutelli X. Animal models are essential to biological research: issues and perspectives. *Futur Sci OA* (2015) 1:FSO63. doi: 10.4155/FSO.15.63
 26. Chen S, Chen X, Geng Z, Su J. The horizon of bone organoid: A perspective on construction and application. *Bioact Mater* (2022) 18:15–25. doi: 10.1016/j.bioactmat.2022.01.048
 27. Festing S, Wilkinson R. The ethics of animal research. *EMBO Rep* (2007) 8:526–530. doi: 10.1038/sj.embor.7400993
 28. Kabene S, Baadel S. Bioethics: a look at animal testing in medicine and cosmetics in the UK. *J Med Ethics Hist Med* (2019) 12: doi: 10.18502/jmehm.v12i15.1875
 29. Russell WMS, Burch RL. *The Principles of Humane Experimental Techniques*. London: Methuen & Co LTD (1959).
 30. Perier-Metz C, Corté L, Allena R, Checa S. A 3D in Silico Multi-Tissue Evolution Model Highlights the Relevance of Local Strain Accumulation in Bone Fracture Remodeling. *Front Bioeng Biotechnol* (2022) 10:835094. doi: 10.3389/fbioe.2022.835094
 31. Kameo Y, Miya Y, Hayashi M, Nakashima T, Adachi T. In silico experiments of bone remodeling explore metabolic diseases and their drug treatment. *Sci Adv* (2020) 6:eax0938. doi: 10.1126/sciadv.aax0938
 32. Andrés Sastre E, Nossin Y, Jansen I, Kops N, Intini C, Witte-Bouma J, van Rietbergen B, Hofmann S, Ridwan Y, Gleeson JP, et al. A new semi-orthotopic bone defect model for cell and biomaterial testing in regenerative medicine. *Biomaterials* (2021) 279:121187. doi: 10.1016/j.biomaterials.2021.121187
 33. Klüter T, Hassan R, Rasch A, Naujokat H, Wang F, Behrendt P, Lippross S, Gerdesmeyer L, Eglin D, Seekamp A, et al. An ex vivo bone defect model to evaluate bone substitutes and associated bone regeneration processes. *Tissue Eng Part C Methods* (2020) 26: doi: 10.1089/ten.TEC.2019.0274
 34. Park Y, Cheong E, Kwak J-G, Carpenter R, Shim J-H, Lee J. Trabecular bone organoid model for studying the regulation of localized bone remodeling. *Sci Adv* (2021) 7:eabd6495. doi: 10.1126/sciadv.abd6495
 35. Matziolis G, Tuischer J, Kasper G, Thompson M, Bartmeyer B, Krockner D, Perka C, Duda G. Simulation of Cell Differentiation in Fracture Healing: Mechanically Loaded Composite Scaffolds in a Novel Bioreactor System. *Tissue Eng* (2006) 12:201–208. doi: 10.1089/ten.2006.12.201
 36. Borciani G, Montalbano G, Baldini N, Cerqueni G, Vitale-Brovarone C, Ciapetti G. Co-Culture

- Systems of Osteoblasts and Osteoclasts: Simulating *in vitro* Bone Remodeling in Regenerative Approaches. *Acta Biomater* (2020) 108:22–45. doi: 10.1016/j.actbio.2020.03.043
37. Mattei G, Giusti S, Ahluwalia A. Design criteria for generating physiologically relevant *in vitro* models in bioreactors. *Processes* (2014) 2:548–569. doi: 10.3390/pr2030548
 38. Czekanska EM, Stoddart MJ, Ralphs JR, Richards RG, Hayes JS. A phenotypic comparison of osteoblast cell lines versus human primary osteoblasts for biomaterials testing. *J Biomed Mater Res - Part A* (2014) 102:2636–2643. doi: 10.1002/jbm.a.34937
 39. Bala Y, Seeman E. Bone's material constituents and their contribution to bone strength in health, disease, and treatment. *Calcif Tissue Int* (2015) 97:308–326. doi: 10.1007/s00223-015-9971-y
 40. Bishop N. Bone material properties in osteogenesis imperfecta. *J Bone Miner Res* (2016) 31:699–708. doi: 10.1002/jbmr.2835
 41. Karunaratne A, Xi L, Bentley L, Sykes D, Boyde A, Esapa CT, Terrill NJ, Brown SDM, Cox RD, Thakker R V, et al. Multiscale alterations in bone matrix quality increased fragility in steroid induced osteoporosis. *Bone* (2016) 84:15–24. doi: 10.1016/j.bone.2015.11.019
 42. Rogal J, Schlünder K, Loskill P. Developer's Guide to an Organ-on-Chip Model. *ACS Biomater Sci Eng* (2022) doi: 10.1021/acsbomaterials.1c01536
 43. Remmers SJA, de Wildt BWM, Vis MAM, Spaander ESR, de Vries RBM, Ito K, Hofmann S. Osteoblast-osteoclast co-cultures: A systematic review and map of available literature. *PLoS One* (2021) 16:e0257724. doi: 10.1371/journal.pone.0257724
 44. Mattes WB. *In vitro* to *in vivo* translation. *Curr Opin Toxicol* (2020) 23–24:114–118. doi: 10.1016/j.cotox.2020.09.001
 45. Hart NH, Nimphius S, Rantalainen T, Ireland A, Siafarikas A, Newton RU. Mechanical basis of bone strength: influence of bone material, bone structure and muscle action. *J Musculoskelet Neuronal Interact* (2017) 17:114–139.
 46. Strandring S, Ellis H, Healy JC, Johnson D, Williams A, Collins P, Wigley C, Berkovitz BK, Borley NR, Crossman AR, et al. *Gray's Anatomy, the anatomical basis of clinical practice*. Thirty-Nin. Churchill Livingstone (2005). 87–102 p.
 47. Bonewald LF. The amazing osteocyte. *J Bone Miner Res* (2011) 26:229–238. doi: 10.1002/jbmr.320
 48. Shrivats AR, Mcdermott MC, Hollinger JO. Bone tissue engineering: state of the union. *Drug Discov Today* (2014) 19:781–786. doi: 10.1016/j.drudis.2014.04.010
 49. Orgel JPRO, Irving TC, Miller A, Wess TJ. Microfibrillar structure of type I collagen in situ. *PNAS* (2006) 103:9001–9005. doi: 10.1073/pnas.0502718103
 50. Garnero P. The role of collagen organization on the properties of bone. *Calcif Tissue Int* (2015) 97:229–240. doi: 10.1007/s00223-015-9996-2
 51. Ascenzi A, Bonucci E. The tensile properties of single osteons. *Anat Rec* (1967) 158:375–386. doi: 10.1002/ar.1091580403
 52. Ascenzi A, Bonucci E. The compressive properties of single osteons. *Anat Rec* (1968) 161:377–392. doi: 10.1002/ar.1091610309
 53. Wang Y, Azaïs T, Robin M, Vallée A, Catania C, Legriel P, Pehau-Arnaudet G, Babonneau F, Giraud-Guille M, Nassif N. The predominant role of collagen in the nucleation, growth, structure and orientation of bone apatite. *Nat Mater* (2012) 11:724–733. doi: 10.1038/nmat3362
 54. Kim D, Lee B, Thomopoulos S, Jun Y-S. The role of confined collagen geometry in decreasing nucleation energy barriers to intrafibrillar mineralization. *Nat Commun* (2018) 9:962. doi: 10.1038/s41467-018-03041-1
 55. Weiner S, Wagner DH. The material bone: structure-mechanical function relations. *Annu Rev*

- Mater Sci* (1998) 28:271–298. doi: 10.1146/annurev.matsci.28.1.271
56. Shapiro F. Bone development and its relation to fracture repair. The role of mesenchymal osteoblasts and surface osteoblasts. *Eur Cells Mater* (2008) 15:53–76. doi: 10.22203/eCM.v015a05
 57. Gorski JP. Biomineralization of bone: a fresh view of the roles of non-collagenous proteins. *Front Biosci (Landmark Ed)* (2011) 16:2598–2621.
 58. Kalamajski S, Oldberg A. The role of small leucine-rich proteoglycans in collagen fibrillogenesis. *Matrix Biol* (2010) 29:248–253. doi: 10.1016/j.matbio.2010.01.001
 59. Chow WY, Rakesh R, Muller KH, Reid DG, Skepper JN, Wong WC, Brooks RA, Green M, Bihan D, Farndale RW, et al. NMR spectroscopy of native and *in vitro* tissues implicates polyADP ribose in biomineralization. *Science* (2014) 344:742–746. doi: 10.1126/science.1248167 746
 60. Ghazanfari S, Khademhosseini A, Smit TH. Mechanisms of lamellar collagen formation in connective tissues. *Biomaterials* (2016) 97:74–84. doi: 10.1016/j.biomaterials.2016.04.028
 61. Poellmann MJ, Estrada JB, Boudou T, Berent ZT, Franck C, Johnson AJW, Asme M, Estrada JB, Boudou T, Berent ZT, et al. Differences in morphology and traction generation of cell lines representing different stages of osteogenesis. *J Biomech Eng* (2015) 137: doi: 10.1115/1.4031848
 62. Matsugaki A, Isobe Y, Saku T, Nakano T. Quantitative regulation of bone-mimetic, oriented collagen/apatite matrix structure depends on the degree of osteoblast alignment on oriented collagen substrates. *J Biomed Mater Res A* (2015) 103A:489–499. doi: 10.1002/jbm.a.35189
 63. Ozasa R, Matsugaki A, Isobe Y, Saku T, Yun HS, Nakano T. Construction of human induced pluripotent stem cell-derived oriented bone matrix microstructure by using *in vitro* engineered anisotropic culture model. *J Biomed Mater Res A* (2018) 106A:360–369. doi: 10.1002/jbm.a.36238
 64. Callens SJP, Fan D, Hengel IAJ van, Fratila-apachitei LE, Zadpoor AA. Emergent collective organization of bone cells in complex curvature fields. *BioRxiv* (2020) doi: 10.1101/2020.10.28.358572
 65. Bidan CM, Kommareddy KP, Rumpler M, Kollmannsberger P, Bréchet YJM, Fratzl P, Dunlop JWC. How linear tension converts to curvature: Geometric control of bone tissue growth. *PLoS One* (2012) 7:e36336. doi: 10.1371/journal.pone.0036336
 66. Matsugaki A, Fujiwara N, Nakano T. Continuous cyclic stretch induces osteoblast alignment and formation of anisotropic collagen fiber matrix. *Acta Biomater* (2013) 9:7227–7235. doi: 10.1016/j.actbio.2013.03.015
 67. Xu H, Duan J, Ren L, Yang P, Yang R, Li W, Shang P, Jiang JX. Impact of flow shear stress on morphology of osteoblast-like IDG-SW3 cells. *J Bone Min Metab* (2018) 36:529–536. doi: 10.1007/s00774-017-0870-3
 68. Saeidi N, Karmelek K, Paten J, Zareian R, DiMasi E, Ruberti J. Molecular crowding of collagen: a pathway to produce highly organized collagenous structures. *Biomaterials* (2012) 33:7366–7374. doi: 10.1016/j.biomaterials.2012.06.041
 69. Nassif N, Belamie E, Davidson P, Panine P, Mosser G, Fratzl P. Self-assembled collagen - apatite matrix with bone-like hierarchy. *Chem Mater* (2010) 22:3307–3309. doi: 10.1021/cm903594n
 70. Wingender B, Bradley P, Saxena N, Ruberti JW, Gower L. Biomimetic organization of collagen matrices to template bone-like microstructures. *Matrix Biol* (2016) 52–54:384–396. doi: 10.1016/j.matbio.2016.02.004
 71. Giraud-Guille M-M. Liquid crystallinity in condensed type I collagen solutions. A clue to the packing of collagen in extracellular matrices. *J Mol Biol* (1992) 224:861–873. doi: 10.1016/0022-2836(92)90567-4
 72. Tang M, Ding S, Min X, Jiao Y, Li L, Li H, Zhou C. Collagen films with stabilized liquid

- crystalline phases and concerns on osteoblast behaviors. *Mater Sci Eng C* (2016) 58:977–985. doi: 10.1016/j.msec.2015.09.058
73. Paten JA, Siadat SM, Susilo ME, Ismail EN, Stoner JL, Rothstein JP, Ruberti JW. Flow-induced crystallization of collagen: a potentially critical mechanism in early tissue formation. *ACS Nano* (2016) 10:5027–5040. doi: 10.1021/acsnano.5b07756
 74. Bhole AP, Flynn BP, Lines M, Saeidi N, Dimarzio CA, Ruberti JW. Mechanical strain enhances survivability of collagen micronetworks in the presence of collagenase: implications for load-bearing matrix growth and stability. *Phil Trans R Soc A* (2009) 367:3339–3362. doi: 10.1098/rsta.2009.0093
 75. Jonge N De, Foolen J, Brugmans MCP, So SHM. Degree of scaffold degradation influences collagen (re)orientation in engineered tissues. *Tissue Eng Part A* (2014) 20:1747–1757. doi: 10.1089/ten.tea.2013.0517
 76. Rubin MA, Jasiuk I, Taylor J, Rubin J, Ganey T, Apkarian RP. TEM analysis of the nanostructure of normal and osteoporotic human trabecular bone. *Bone* (2003) 33:270–282. doi: 10.1016/S8756-3282(03)00194-7
 77. Schwarcz HP, McNally EA, Botton GA. Dark-field transmission electron microscopy of cortical bone reveals details of extrafibrillar crystals. *J Struct Biol* (2014) 188:240–248. doi: 10.1016/j.jsb.2014.10.005
 78. Reznikov N, Bilton M, Lari L, Stevens MM, Kröger R. Fractal-like hierarchical organization of bone begins at the nanoscale. *Science* (2018) 360:eaao2189. doi: 10.1126/science.aao2189
 79. Chen P, Toroian D, Price PA, Mckittrick J. Minerals form a continuum phase in mature cancellous bone. *Calcif Tissue Int* (2011) 88:351–361. doi: 10.1007/s00223-011-9462-8
 80. Nair AK, Gautieri A, Chang S, Buehler MJ. Molecular mechanics of mineralized collagen fibrils in bone. *Nat Commun* (2013) 4:1724. doi: 10.1038/ncomms2720
 81. Shao C, Zhao R, Jiang S, Yao S, Wu Z, Jin B, Yang Y, Pan H, Tang R. Citrate improves collagen mineralization via interface wetting: a physicochemical understanding of biomineralization control. *Adv Mater* (2018) 30:1–7. doi: 10.1002/adma.201704876
 82. Davies E, Müller KH, Ching W, Pickard CJ, Reid DG, Skepper JN, Duer MJ. Citrate bridges between mineral platelets in bone. *PNAS* (2014) 111:E1354–E1363. doi: 10.1073/pnas.1315080111
 83. Franklin RB, Chellaiah M, Zou J, Reynolds MA, Leslie C. Evidence that osteoblasts are specialized citrate-producing cells that provide the citrate for incorporation into the structure of bone. *Open Bone J* (2014) 6:1–7. doi: 10.2174/1876525401406010001
 84. Chen H, Wang Y, Dai H, Tian X, Cui Z-K, Chen Z, Hu L, Song Q, Liu A, Zhang Z, et al. Bone and plasma citrate is reduced in osteoporosis. *Bone* (2018) 114:189–197. doi: 10.1016/j.bone.2018.06.014
 85. Poundarik AA, Boskey A, Gundberg C, Vashishth D. Biomolecular regulation, composition and nanoarchitecture of bone mineral. *Sci Rep* (2018) 8:1–8. doi: 10.1038/s41598-018-19253-w
 86. Vetsch JR, Paulsen SJ, Müller R, Hofmann S. Effect of fetal bovine serum on mineralization in silk fibroin scaffolds. *Acta Biomater* (2015) 13:277–285. doi: 10.1016/j.actbio.2014.11.025
 87. Samal SK, Dash M, Declercq HA, Gheysens T, Dendooven J, Voort P Van Der, Cornelissen R, Dubruel P, Kaplan DL. Enzymatic mineralization of silk scaffolds. *Macromol Biosci* (2014) 14:991–1003. doi: 10.1002/mabi.201300513
 88. Wittkowske C, Reilly GC, Lacroix D, Perrault CM. *In vitro* bone cell models: impact of fluid shear stress on bone formation. *Front Bioeng Biotechnol* (2016) 4: doi: 10.3389/fbioe.2016.00087
 89. Vetsch JR, Betts DC, Müller R, Hofmann S. Flow velocity-driven differentiation of human mesenchymal stromal cells in silk fibroin scaffolds: A combined experimental and computational



- approach. *PLoS One* (2017) 12:1–17. doi: 10.1371/journal.pone.0180781
90. Melke J, Zhao F, Rietbergen B, Ito K, Hofmann S. Localisation of mineralised tissue in a complex spinner flask environment correlates with predicted wall shear stress level localisation. *Eur Cells Mater* (2018) 36:57–68. doi: 10.22203/eCM.v036a05
 91. Kohli N, Ho S, Brown SJ, Sawadkar P, Sharma V, Snow M, García-Gareta E. Bone remodelling *in vitro*: Where are we headed? - A review on the current understanding of physiological bone remodelling and inflammation and the strategies for testing biomaterials *in vitro*. *Bone* (2018) 110:38–46. doi: 10.1016/j.bone.2018.01.015
 92. Aubin JE. Advances in the osteoblast lineage. *Biochem Cell Biol* (1998) 76:899–910. doi: 10.1139/bcb-76-6-899
 93. Ninomiya K, Miyamoto T, Imai J, Fujita N, Suzuki T, Iwasaki R, Yagi M, Watanabe S, Toyama Y, Suda T. Osteoclastic activity induces osteomodulin expression in osteoblasts. *Biochem Biophys Res Commun* (2007) 362:460–466. doi: 10.1016/j.bbrc.2007.07.193
 94. Nudelman F, Lausch AJ, Sommerdijk NAJM, Sone ED. *In vitro* models of collagen biomineralization. *J Struct Biol* (2013) 183:258–269. doi: 10.1016/j.jsb.2013.04.003
 95. Sims NA, Martin TJ. Coupling signals between the osteoclast and osteoblast: how are messages transmitted between these temporary visitors to the bone surface? *Front Endocrinol (Lausanne)* (2015) 6:1–5. doi: 10.3389/fendo.2015.00041
 96. Lerner UH, Kindstedt E, Lundberg P. The critical interplay between bone resorbing and bone forming cells. *J Clin Periodontol* (2019) doi: 10.1111/jcpe.13051
 97. Luukkonen J, Hilli M, Nakamura M, Ritamo I, Valmu L, Kauppinen K, Tuukkanen J, Lehenkari P. Osteoclasts secrete osteopontin into resorption lacunae during bone resorption. *Histochem Cell Biol* (2019) 151:475–487. doi: 10.1007/s00418-019-01770-y
 98. Kerschnitzki M, Wagermaier W, Roschger P, Seto J, Shahar R, Duda GN, Mundlos S, Fratzl P. The organization of the osteocyte network mirrors the extracellular matrix orientation in bone. *J Struct Biol* (2011) 173:303–311. doi: 10.1016/j.jsb.2010.11.014
 99. Liu Y, Luo D, Wang T. Hierarchical structures of bone and bioinspired bone tissue engineering. *Small* (2016) 12:4611–4632. doi: 10.1002/sml.201600626
 100. Thompson EM, Matsiko A, Farrell E, Kelly DJ, O'Brien FJ. Recapitulating endochondral ossification: a promising route to *in vivo* bone regeneration. *J Tissue Eng Regen Med* (2015) 9:889–902. doi: 10.1002/term.1918
 101. Freeman FE, Schiavi J, Brennan MA, Owens P, Layrolle P, McNamara LM. Mimicking the biochemical and mechanical extracellular environment of the endochondral ossification process to enhance the *in vitro* mineralization potential of human mesenchymal stem cells. *Tissue Eng Part A* (2017) 23:1466–1478. doi: 10.1089/ten.tea.2017.0052
 102. Georgiadis M, Müller R, Schneider P. Techniques to assess bone ultrastructure organization: orientation and arrangement of mineralized collagen fibrils. *J R Soc Interface* (2016) 13: doi: 10.1098/rsif.2016.0088
 103. Jonge N de, Kanters FMW, Baaijens FPT, Bouten CVC. Strain-induced collagen organization at the micro-level in fibrin-based engineered tissue constructs. *Ann Biomed Eng* (2013) 41:763–774. doi: 10.1007/s10439-012-0704-3
 104. Scimeca M, Bischetti S, Lamsira HK, Bonfiglio R, Bonanno E. Energy Dispersive X-ray (EDX) microanalysis: A powerful tool in biomedical research and diagnosis. *Eur J Histochem* (2018) 62: doi: 10.4081/ejh.2018.2841
 105. Tadano S, Giri B. X-ray diffraction as a promising tool to characterize bone nanocomposites. *Sci Technol Adv Mater* (2011) 12: doi: 10.1088/1468-6996/12/6/064708
 106. Jalili-Firoozinezhad S, Martin I, Scherberich A. Bimodal morphological analyses of native and

- engineered tissues. *Mater Sci Eng C* (2017) 76:543–550. doi: 10.1016/j.msec.2017.03.140
107. De Boer P, Hoogenboom JP, Giepmans BNG. Correlated light and electron microscopy: Ultrastructure lights up! *Nat Methods* (2015) 12:503–513. doi: 10.1038/nMeth.3400
 108. Stalder AK, Ilgenstein B, Chicherova N, Deyhle H, Beckmann F, Müller B, Hieber SE. Combined use of micro computed tomography and histology to evaluate the regenerative capacity of bone grafting materials. *Int J Mater Res* (2014) 105:679–691. doi: 10.3139/146.111050
 109. Reznikov N, Shahar R, Weiner S. Three-dimensional structure of human lamellar bone: The presence of two different materials and new insights into the hierarchical organization. *Bone* (2014) 59:93–104. doi: 10.1016/j.bone.2013.10.023
 110. de Wildt BWM, Ansari S, Sommerdijk NAJM, Ito K, Akiva A, Hofmann S. From bone regeneration to three-dimensional *in vitro* models: tissue engineering of organized bone extracellular matrix. *Curr Opin Biomed Eng* (2019) 10:107–115. doi: 10.1016/j.cobme.2019.05.005
 111. Balls M, Goldberg AM, Fentem JH, Broadhead CL, Burch RL, Festing RL, Frazier J. The Three Rs: The Way Forward. *ATLA* (1995) 23:838–866.
 112. Matsugaki A, Kimura Y, Watanabe R, Nakamura F, Takehana R, Nakano T. Impaired alignment of bone matrix microstructure associated with disorganized osteoblast arrangement in malignant melanoma metastasis. *Biomolecules* (2021) 11:131. doi: 10.3390/biom11020131
 113. Hadida M, Marchat D. Strategy for achieving standardized bone models. *Biotechnol Bioeng* (2020) 117:251–271. doi: 10.1002/bit.27171
 114. Burger EH, Klein-Nulend J. Mechanotransduction in bone — role of the lacuno-canalicular network. *FASEB J* (1999) 13:S101–S112.
 115. Ishimoto T, Kawahara K, Matsugaki A, Kamioka H, Nakano T. Quantitative Evaluation of Osteocyte Morphology and Bone Anisotropic Extracellular Matrix in Rat Femur. *Calcif Tissue Int* (2021) 109:434–444. doi: 10.1007/s00223-021-00852-1
 116. Akiva A, Melke J, Ansari S, Liv N, van der Meijden R, van Erp M, Zhao F, Stout M, Nijhuis WH, de Heus C, et al. An Organoid for Woven Bone. *Adv Funct Mater* (2021) 31:2010524. doi: 10.1002/adfm.202010524
 117. Vetsch JR, Müller R, Hofmann S. The influence of curvature on threedimensional mineralized matrix formation under static and perfused conditions: An *in vitro* bioreactor model. *J R Soc Interface* (2016) 13:20160425. doi: 10.1098/rsif.2016.0425
 118. Rumpler M, Woesz A, Dunlop JWC, Van Dongen JT, Fratzl P. The effect of geometry on three-dimensional tissue growth. *J R Soc Interface* (2008) 5:1173–1180. doi: 10.1098/rsif.2008.0064
 119. Ehrig S, Schamberger B, Bidan CM, West A, Jacobi C, Lam K, Kollmannsberger P, Petersen A, Tomancak P, Kommareddy K, et al. Surface tension determines tissue shape and growth kinetics. *Sci Adv* (2019) 5:9394–9405. doi: 10.1126/sciadv.aav9394
 120. Callens SJP, Uyttendaele RJC, Fratila-Apachitei LE, Zadpoor AA. Substrate curvature as a cue to guide spatiotemporal cell and tissue organization. *Biomaterials* (2020) 232:119739. doi: 10.1016/j.biomaterials.2019.119739
 121. Ansari S, Ito K, Hofmann S. Cell Sources for Human *In vitro* Bone Models. *Curr Osteoporos Rep* (2021) 19:88–100. doi: 10.1007/s11914-020-00648-6
 122. Zhao F, Melke J, Ito K, Rietbergen B Van, Hofmann S. A multiscale computational fluid dynamics approach to simulate the micro - fluidic environment within a tissue engineering scaffold with highly irregular pore geometry. *Biomech Model Mechanobiol* (2019) 18:1965–1977. doi: 10.1007/s10237-019-01188-4
 123. Maisonneuve BGC, Roux DCD, Thorn P, Cooper-White JJ. Effects of cell density and biomacromolecule addition on the flow behavior of concentrated mesenchymal cell

- suspensions. *Biomacromolecules* (2013) 14:4388–4397. doi: 10.1021/bm401335g
124. Hofmann S, Hagenmüller H, Koch AM, Müller R, Vunjak-Novakovic G, Kaplan DL, Merkle HP, Meinel L. Control of *in vitro* tissue-engineered bone-like structures using human mesenchymal stem cells and porous silk scaffolds. *Biomaterials* (2007) 28:1152–1162. doi: 10.1016/j.biomaterials.2006.10.019
 125. Melke J, Zhao F, Ito K, Hofmann S. Orbital seeding of mesenchymal stromal cells increases osteogenic differentiation and bone - like tissue formation. *J Orthop Res* (2019) 2020:1–10. doi: 10.1002/jor.24583
 126. Mccooy RJ, Brien FJO. Influence of Shear Stress in Perfusion Bioreactor Cultures for the Development of Three-Dimensional Bone Tissue Constructs : A Review. *Tissue Eng Part B* (2010) 16:587–601. doi: 10.1089/ten.teb.2010.0370
 127. Schindelin J, Arganda-Carreras I, Frise E, Kaynig V, Longair M, Pietzsch T, Preibisch S, Rueden C, Saalfeld S, Schmid B, et al. Fiji: An open-source platform for biological-image analysis. *Nat Methods* (2012) 9:676–682. doi: 10.1038/nmeth.2019
 128. Rutkovskiy A, Stenslokken K-O, Vaage IJ. Osteoblast Differentiation at a Glance. *Med Sci Monit Basic Res* (2016) 22:95–106. doi: 10.12659/MSMBR.901142
 129. Franz-odendaal TA, Hall BK, Witten PE. Buried Alive : How Osteoblasts Become Osteocytes. *Dev Dyn* (2006) 235:176–190. doi: 10.1002/dvdy.20603
 130. Huszar G, Maiocco J, Naftolin F. Monitoring of collagen and collagen fragments in chromatography of protein mixtures. *Anal Biochem* (1980) 105:424–429. doi: 10.1016/0003-2697(80)90481-9
 131. Boussein ML, Boyd SK, Christiansen BA, Guldberg RE, Jepsen KJ, Müller R. Guidelines for assessment of bone microstructure in rodents using micro-computed tomography. *J Bone Miner Res* (2010) 25:1468–1486. doi: 10.1002/jbmr.141
 132. Aper SJA, Van Spreuwel ACC, Van Turnhout MC, Van Der Linden AJ, Pieters PA, Van Der Zon NLL, De La Rambelje SL, Bouten CVC, Merckx M. Colorful protein-based fluorescent probes for collagen imaging. *PLoS One* (2014) 9:e114983. doi: 10.1371/journal.pone.0114983
 133. R Core Team. R: A language and environment for statistical computing. R Foundation for Statistical Computing, Vienna, Austria. (2020) <http://www.r-project.org/index.html>
 134. Zhao F, Lacroix D, Ito K, van Rietbergen B, Hofmann S. Changes in scaffold porosity during bone tissue engineering in perfusion bioreactors considerably affect cellular mechanical stimulation for mineralization. *Bone Reports* (2020) 12:100265. doi: 10.1016/j.bonr.2020.100265
 135. Giorgi M, Verbruggen SW, Lacroix D. In silico bone mechanobiology: modeling a multifaceted biological system. *WTREs Syst Biol Med* (2016) 8:485–505. doi: 10.1002/wsbm.1356
 136. Vis MAM, Ito K, Hofmann S. Impact of Culture Medium on Cellular Interactions in *in vitro* Co-culture Systems. *Front Bioeng Biotechnol* (2020) 8:911. doi: 10.3389/fbioe.2020.00911
 137. Ansari S, Ito K, Hofmann S. Alkaline Phosphatase Activity of Serum Affects Osteogenic Differentiation Cultures. *ACS Omega* (2022) 15:12724–12733. doi: 10.1021/acsomega.1c07225
 138. Bidan CM, Kommareddy KP, Rumpler M, Kollmannsberger P, Fratzl P, Dunlop JWC. Geometry as a Factor for Tissue Growth: Towards Shape Optimization of Tissue Engineering Scaffolds. *Adv Healthc Mater* (2013) 2:186–194. doi: 10.1002/adhm.201200159
 139. Kommareddy KP, Lange C, Rumpler M, Dunlop JWC, Manjubala I, Cui J, Kratz K, Lendlein A, Fratzl P. Two stages in three-dimensional *in vitro* growth of tissue generated by osteoblastlike cells. *Biointerphases* (2010) 5:45–52. doi: 10.1116/1.3431524
 140. Matsuzaka T, Matsugaki A, Nakano T. Control of osteoblast arrangement by osteocyte mechanoresponse through prostaglandin E2 signaling under oscillatory fluid flow stimuli. *Biomaterials* (2021) 279:121203. doi: 10.1016/j.biomaterials.2021.121203

141. Smits AIPM, Bouten CVC. Tissue Engineering meets Immunoengineering: Prospective on Personalized In Situ Tissue Engineering Strategies. *Curr Opin Biomed Eng* (2018) 6:17–26. doi: 10.1016/j.cobme.2018.02.006
142. Cao S, Zhao Y, Hu Y, Zou L, Chen J. New perspectives: In-situ tissue engineering for bone repair scaffold. *Compos Part B* (2020) 202:108445. doi: 10.1016/j.compositesb.2020.108445
143. Spiller KL, Nassiri S, Witherell CE, Anfang RR, Ng J, Nakazawa KR, Yu T, Vunjak-Novakovic G. Sequential delivery of immunomodulatory cytokines to facilitate the M1-to-M2 transition of macrophages and enhance vascularization of bone scaffolds. *Biomaterials* (2015) 37:194–207. doi: 10.1016/j.biomaterials.2014.10.017
144. Sun T, Meng C, Ding Q, Yu K, Zhang X, Zhang W, Tian W, Zhang Q, Guo X, Wu B, et al. In situ bone regeneration with sequential delivery of aptamer and BMP2 from an ECM-based scaffold fabricated by cryogenic free-form extrusion. *Bioact Mater* (2021) 6:4163–4175. doi: 10.1016/j.bioactmat.2021.04.013
145. Omar O, Engstrand T, Kihlström L, Linder B, Åberg J, Shah FA, Palmquist A, Birgersson U, Elgali I, Pujari-Palmer M, et al. In situ bone regeneration of large cranial defects using synthetic ceramic implants with a tailored composition and design. *PNAS* (2020) 117:26660–26671. doi: 10.1073/pnas.2007635117
146. Gilchrist AE, Harley BAC. Engineered Tissue Models to Replicate Dynamic Interactions within the Hematopoietic Stem Cell Niche. *Adv Healthc Mater* (2022) 11:2102130. doi: 10.1002/adhm.202102130
147. Xiong Q, Zhang N, Zhang M, Wang M, Wang L, Fan Y, Lin CY. Engineer a pre-metastatic niched microenvironment to attract breast cancer cells by utilizing a 3D printed polycaprolactone/nano-hydroxyapatite osteogenic scaffold – An *in vitro* model system for proof of concept. *J Biomed Mater Res - Part B Appl Biomater* (2022) 110:1604–1614. doi: 10.1002/jbm.b.35021
148. Hankenson KD, Dishowitz M, Gray C, Schenker M. Angiogenesis in bone regeneration. *Injury* (2011) 42:556–561. doi: 10.1016/j.injury.2011.03.035
149. Verrier S, Alini M, Alsberg E, Buchman SR, Kelly D, Laschke MW, Menger MD, Murphy WL, Stegemann JP, Schütz M, et al. Tissue engineering and regenerative approaches to improving the healing of large bone defects. *Eur Cells Mater* (2016) 32:87–110. doi: 10.22203/eCM.v032a06
150. Shafiee S, Shariatzadeh S, Zafari A, Majd A, Niknejad H. Recent Advances on Cell-Based Co-Culture Strategies for Prevascularization in Tissue Engineering. *Front Bioeng Biotechnol* (2021) 9:745314. doi: 10.3389/fbioe.2021.745314
151. Pill K, Hofmann S, Redl H, Holthöner W. Vascularization mediated by mesenchymal stem cells from bone marrow and adipose tissue: A comparison. *Cell Regen* (2015) 4:8. doi: 10.1186/s13619-015-0025-8
152. Grosso A, Burger MG, Lunger A, Schaefer DJ, Banfi A, Di Maggio N. It takes two to tango: Coupling of angiogenesis and osteogenesis for bone regeneration. *Front Bioeng Biotechnol* (2017) 5:68. doi: 10.3389/fbioe.2017.00068
153. Pennings I, van Dijk LA, van Huuksloot J, Fledderus JO, Schepers K, Braat AK, Hsiao EC, Barriet E, Morales BM, Verhaar MC, et al. Effect of donor variation on osteogenesis and vasculogenesis in hydrogel cocultures. *J Tissue Eng Regen Med* (2019) 13:433–445. doi: 10.1002/term.2807
154. Klotz BJ, Lim KS, Chang YX, Soliman BG, Pennings I, Melchels FPW, Woodfield TBF, Rosenberg AJWP, Malda J, Gawlitta D. Engineering of a complex bone tissue model with endothelialised channels and capillary-like networks. *Eur Cells Mater* (2018) 35:335–349. doi: 10.22203/eCM.v035a23
155. Longoni A, Utomo L, Robinson A, Levato R, Rosenberg AJWP, Gawlitta D. Acceleration of Bone Regeneration Induced by a Soft-Callus Mimetic Material. *Adv Sci* (2022) 9:2103284. doi: 10.1002/advs.202103284

- 10.1002/advs.202103284
156. Ge J, Wood DK, Weingeist DM, Prasongtanakij S, Navasumrit P, Ruchirawat M, Engelward BP. Standard fluorescent imaging of live cells is highly genotoxic. *Cytom Part A* (2013) 83:552–560. doi: 10.1002/cyto.a.22291
 157. Farndale R, Sayers C, Barrett A. A direct spectrophotometric microassay for sulfated glycosaminoglycans in cartilage cultures. *Connect Tissue Res* (1982) 9:247–248.
 158. Scholman RC, Giovannone B, Hiddingh S, Meerding JM, Malvar Fernandez B, van Dijk MEA, Tempelman MJ, Prakken BJ, de Jager W. Effect of anticoagulants on 162 circulating immune related proteins in healthy subjects. *Cytokine* (2018) 106:114–124. doi: 10.1016/j.cyto.2017.10.021
 159. Babicki S, Arndt D, Marcu A, Liang Y, Grant JR, Maciejewski A, Wishart DS. Heatmapper: web-enabled heat mapping for all. *Nucleic Acids Res* (2016) 44:W147–W153. doi: 10.1093/NAR/GKW419
 160. Suen PK, Qin L. Sclerostin, an emerging therapeutic target for treating osteoporosis and osteoporotic fracture: A general review. *J Orthop Transl* (2016) 4:1–13. doi: 10.1016/j.jot.2015.08.004
 161. Arnott JA, Lambi AG, Mundy CM, Hendsi H, Pixley RA, Owen TA, Safadi FF, Popoff SN. The Role of Connective Tissue Growth Factor (CTGF/CCN2) in Skeletogenesis. *Crit Rev Eukaryot Gene Expr* (2011) 21:43–69. doi: 10.1615/critrevukargenexpr.v21.i1.40
 162. Wan J, Zhang G, Li X, Qiu X, Ouyang J, Dai J, Min S. Matrix Metalloproteinase 3: A Promoting and Destabilizing Factor in the Pathogenesis of Disease and Cell Differentiation. *Front Physiol* (2021) 12:663978. doi: 10.3389/fphys.2021.663978
 163. Paiva KBS, Granjeiro JM. “Matrix Metalloproteinases in Bone Resorption, Remodeling, and Repair.” *Progress in Molecular Biology and Translational Science*. Elsevier B.V. (2017). p. 203–303 doi: 10.1016/bs.pmbts.2017.05.001
 164. Ortega N, Behonick DJ, Werb Z. Matrix remodeling during endochondral ossification. *Trends Cell Biol* (2004) 14:86–93. doi: 10.1016/j.tcb.2003.12.003
 165. Bellido T, Delgado-Calle J. Ex Vivo Organ Cultures as Models to Study Bone Biology. *JBMR Plus* (2020) 4:e10345. doi: 10.1002/jbm4.10345
 166. Meng X, Xing Y, Li J, Deng C, Li Y, Ren X, Zhang D. Rebuilding the Vascular Network: *In vivo* and *in vitro* Approaches. *Front Cell Dev Biol* (2021) 9:639299. doi: 10.3389/fcell.2021.639299
 167. Watson EC, Adams RH. Biology of bone: The vasculature of the skeletal system. *Cold Spring Harb Perspect Med* (2018) 8:a031559. doi: 10.1101/cshperspect.a031559
 168. Stegen S, van Gestel N, Carmeliet G. Bringing new life to damaged bone: The importance of angiogenesis in bone repair and regeneration. *Bone* (2015) 70:19–27. doi: 10.1016/j.bone.2014.09.017
 169. Wehling M. Translational medicine: Can it really facilitate the transition of research “from bench to bedside”? *Eur J Clin Pharmacol* (2006) 62:91–95. doi: 10.1007/s00228-005-0060-4
 170. Wendler A, Wehling M. Translatability scoring in drug development: Eight case studies. *J Transl Med* (2012) 10:39. doi: 10.1186/1479-5876-10-39
 171. Yadav J, El Hassani M, Sodhi J, Lauschke VM, Hartman JH, Russell LE. Recent developments in *in vitro* and *in vivo* models for improved translation of preclinical pharmacokinetics and pharmacodynamics data. *Drug Metab Rev* (2021) 53:207–233. doi: 10.1080/03602532.2021.1922435
 172. Albeshri S, Alblaiheh A, Niazzy AA, Ramalingam S, Sundar C, Alghamdi HS. Biomarkers as independent predictors of bone regeneration around biomaterials: A systematic review of literature. *J Contemp Dent Pract* (2018) 19:605–6 18. doi: 10.5005/jp-journals-10024-2306

173. Kuo TR, Chen CH. Bone biomarker for the clinical assessment of osteoporosis: Recent developments and future perspectives. *Biomark Res* (2017) 5:18. doi: 10.1186/S40364-017-0097-4
174. Wang L, You X, Zhang L, Zhang C, Zou W. Mechanical regulation of bone remodeling. *Bone Res* (2022) 10:16. doi: 10.1038/s41413-022-00190-4
175. Ansari M. Bone tissue regeneration: biology, strategies and interface studies. *Prog Biomater* (2019) 8:223–237. doi: 10.1007/s40204-019-00125-z
176. Noori A, Ashrafi SJ, Vaez-Ghaemi R, Hatamian-Zaremi A, Webster TJ. A review of fibrin and fibrin composites for bone tissue engineering. *Int J Nanomedicine* (2017) 12:4937–4961. doi: 10.2147/IJN.S124671
177. Koolen MKE, Longoni A, Van Der Stok J, Van Der Jagt O, Gawlitta D, Weinans H. Complete regeneration of large bone defects in rats with commercially available fibrin loaded with BMP-2. *Eur Cells Mater* (2019) 38:94–105. doi: 10.22203/eCM.v038a08
178. Fan Q, Bai J, Shan H, Fei Z, Chen H, Xu J, Ma Q, Zhou X, Wang C. Implantable blood clot loaded with BMP-2 for regulation of osteoimmunology and enhancement of bone repair. *Bioact Mater* (2021) 6:4014–4026. doi: 10.1016/j.bioactmat.2021.04.008
179. Cheng A, Vantucci CE, Krishnan L, Ruehle MA, Kotanchek T, Wood LB, Roy K, Guldberg RE. Early systemic immune biomarkers predict bone regeneration after trauma. *PNAS* (2021) 118:e2017889118. doi: 10.1073/pnas.2017889118
180. Shah K, Majeed Z, Jonason J, O’Keefe RJ. The role of muscle in bone repair: The cells, signals, and tissue responses to injury. *Curr Osteoporos Rep* (2013) 11:130–135. doi: 10.1007/s11914-013-0146-3
181. Paul Neagu T, Țigliș M, Cocoloș I, Radu Jecan C. The relationship between periosteum and fracture healing. *Rom J Morphol Embryol* (2016) 57:1215–1220.
182. Betts DC, Müller R. Mechanical regulation of bone regeneration: Theories, models, and experiments. *Front Endocrinol (Lausanne)* (2014) 5:211. doi: 10.3389/fendo.2014.00211
183. de Wildt BWM, Ito K, Hofmann S. Human Platelet Lysate as Alternative of Fetal Bovine Serum for Enhanced Human *In vitro* Bone Resorption and Remodeling. *Front Immunol* (2022) 13:915277. doi: 10.3389/fimmu.2022.915277
184. Andrée B, Ichanti H, Kalies S, Heisterkamp A, Strauß S, Vogt PM, Haverich A, Hilfiker A. Formation of three-dimensional tubular endothelial cell networks under defined serum-free cell culture conditions in human collagen hydrogels. *Sci Rep* (2019) 9:5437. doi: 10.1038/s41598-019-41985-6
185. Ponte AL, Marais E, Gallay N, Langonné A, Delorme B, Hérault O, Charbord P, Domenech J. The *In vitro* Migration Capacity of Human Bone Marrow Mesenchymal Stem Cells: Comparison of Chemokine and Growth Factor Chemotactic Activities. *Stem Cells* (2007) 25:1737–1745. doi: 10.1634/stemcells.2007-0054
186. Gilbert W, Bragg R, Elmansi AM, McGee-Lawrence ME, Isales CM, Hamrick MW, Hill WD, Fulzele S. Stromal cell-derived factor-1 (CXCL12) and its role in bone and muscle biology. *Cytokine* (2019) 123:154783. doi: 10.1016/j.cyto.2019.154783
187. Yang F, Xue F, Guan J, Zhang Z, Yin J, Kang Q. Stromal-Cell-Derived Factor (SDF) 1-Alpha Overexpression Promotes Bone Regeneration by Osteogenesis and Angiogenesis in Osteonecrosis of the Femoral Head. *Cell Physiol Biochem* (2018) 46:2561–2575. doi: 10.1159/000489684
188. Yu X, Huang Y, Collin-Osdoby P, Osdoby P. Stromal Cell-Derived Factor-1 (SDF-1) Recruits Osteoclast Precursors by Inducing Chemotaxis, Matrix Metalloproteinase-9 (MMP-9) Activity, and Collagen Transmigration. (2003). 1404–1418 p. doi: 10.1359/jbmr.2003.18.8.1404
189. Li D qi, Wan Q long, Pathak JL, Li Z bing. Platelet-derived growth factor BB enhances osteoclast formation and osteoclast precursor cell chemotaxis. *J Bone Miner Metab* (2017) 35:355–



365. doi: 10.1007/s00774-016-0773-8
190. Zhang M, Yu W, Niibe K, Zhang W, Egusa H, Tang T, Jiang X. The effects of platelet-derived growth factor-BB on bone marrow stromal cell-mediated vascularized bone regeneration. *Stem Cells Int* (2018) 2018:3272098. doi: 10.1155/2018/3272098
191. Maes C, Coenegrachts L, Stockmans I, Daci E, Luttun A, Petryk A, Gopalakrishnan R, Moermans K, Smets N, Verfaillie CM, et al. Placental growth factor mediates mesenchymal cell development, cartilage turnover, and bone remodeling during fracture repair. *J Clin Invest* (2006) 116:1230–1242. doi: 10.1172/JCI26772
192. Yang Q, McHugh KP, Patntirapong S, Gu X, Wunderlich L, Hauschka P V. VEGF enhancement of osteoclast survival and bone resorption involves VEGF receptor-2 signaling and β 3-integrin. *Matrix Biol* (2008) 27:589–599. doi: 10.1016/j.matbio.2008.06.005
193. Liu Y, Berendsen AD, Jia S, Lotinun S, Baron R, Ferrara N, Olsen BR. Intracellular VEGF regulates the balance between osteoblast and adipocyte differentiation. *J Clin Invest* (2012) 122:3101–3113. doi: 10.1172/JCI61209
194. Zhou BO, Ding L, Morrison SJ. Hematopoietic stem and progenitor cells regulate the regeneration of their niche by secreting Angiopoietin-1. *Elife* (2015) 4:e05521. doi: 10.7554/eLife.05521
195. Yin J, Gong G, Sun C, Yin Z, Zhu C, Wang B, Hu Q, Zhu Y, Liu X. Angiopoietin 2 promotes angiogenesis in tissue-engineered bone and improves repair of bone defects by inducing autophagy. *Biomed Pharmacother* (2018) 105:932–939. doi: 10.1016/j.biopha.2018.06.078
196. Matilla L, Roncal C, Ibarrola J, Arrieta V, García-Penã A, Fernández-Celis A, Navarro A, Álvarez V, Gainza A, Orbe J, et al. A Role for MMP-10 (Matrix Metalloproteinase-10) in Calcific Aortic Valve Stenosis. *Arterioscler Thromb Vasc Biol* (2020) 1370–1382. doi: 10.1161/ATVBAHA.120.314143
197. Mao L, Yano M, Kawao N, Tamura Y, Okada K, Kaji H. Role of matrix metalloproteinase-10 in the BMP-2 inducing osteoblastic differentiation. *Endocr J Adv Publ* (2013) 60:1309–1319. doi: 10.1507/endocrj.Ej13-0270
198. Boyce BF, Xing L. Functions of RANKL/RANK/OPG in bone modeling and remodeling. *Arch Biochem Biophys* (2008) 473:139–146. doi: 10.1016/j.abb.2008.03.018
199. Fu YX, Gu JH, Zhang YR, Tong XS, Zhao HY, Yuan Y, Liu XZ, Bian JC, Liu ZP. Osteoprotegerin influences the bone resorption activity of osteoclasts. *Int J Mol Med* (2013) 31:1411–1417. doi: 10.3892/ijmm.2013.1329
200. Rodriguez D, Thula-Mata T, Toro E, Yeh Y, Holt C, Holliday L, Gower L. Multifunctional role of osteopontin in directing intrafibrillar mineralization of collagen and activation of osteoclasts. *Acta Biomater* (2014) 10:494–507. doi: 10.1016/j.actbio.2013.10.010
201. Terai K, Takano-Yamamoto T, Ohba Y, Hiura K, Sugimoto M, Sato M, Kawahata H, Inaguma N, Kitamura Y, Nomura S. Role of Osteopontin in Bone Remodeling Caused by Mechanical Stress. *J Bone Miner Res* (1999) 14:839–849. doi: 10.1359/jbmr.1999.14.6.839
202. Lin X, Patil S, Gao YG, Qian A. The Bone Extracellular Matrix in Bone Formation and Regeneration. *Front Pharmacol* (2020) 11:757. doi: 10.3389/fphar.2020.00757
203. Duchamp de Lageneste O, Colnot C. “Periostin in bone regeneration.” In: Kudo A, editor. *Periostin*. (2019). p. 49–59
204. Gramoun A, Azizi N, Sodek J, Heersche JNM, Nakchbandi I, Manolson MF. Fibronectin inhibits osteoclastogenesis while enhancing osteoclast activity via nitric oxide and interleukin-1 β -mediated signaling pathways. *J Cell Biochem* (2010) 111:1020–1034. doi: 10.1002/jcb.22791
205. Seiji Goda, Hiroshi Hayashi, Yosuke Ujii, Osamu Takeuchi, Reiko Komasa, Eisuke Domae, Kazuyo Yamamoto, Naoyuki Matsumoto, Takashi Ikeo. Fibronectin inhibited RANKL-induced differentiation into osteoclast. *J Oral Tissue Engin* (2014) 11:227–233. doi: 10.11223/jarde.11.227

206. Faia-Torres AB, Goren T, Ihalainen TO, Guimond-Lischer S, Charnley M, Rottmar M, Maniura-Weber K, Spencer ND, Reis RL, Textor M, et al. Regulation of human mesenchymal stem cell osteogenesis by specific surface density of fibronectin: A gradient study. *ACS Appl Mater Interfaces* (2015) 7:2367–2375. doi: 10.1021/am506951c
207. Feng X, McDonald JM. Disorders of Bone Remodeling. *Annu Rev Pathol* (2011) 6:121–145. doi: 10.1146/annurev-pathol-011110-130203
208. Burkhardt AM, Zlotnik A. Translating translational research: Mouse models of human disease. *Cell Mol Immunol* (2013) 10:373–374. doi: 10.1038/cmi.2013.19
209. Contopoulos-Ioannidis DG, Ntzani EE, Ioannidis JPA. Translation of highly promising basic science research into clinical applications. *Am J Med* (2003) 114:477–484. doi: 10.1016/S0002-9343(03)00013-5
210. Chambers TJ. Osteoblasts release osteoclasts from calcitonin-induced quiescence. *J Cell Sci* (1982) 57:247–260. doi: 10.1242/jcs.57.1.247
211. Takahashi N, Akatsu T, Udagawa N, Sasaki T, Yamaguchi A, Moseley JM, Martin TJ, Suda T. Osteoblastic cells are involved in osteoclast formation. *Endocrinology* (1988) 123:2600–2602. doi: 10.1210/endo-123-5-2600
212. Suda T, Takahashi N, Udagawa N, Jimi E, Gillespie MT, Martin TJ. Modulation of Osteoclast Differentiation and Function by the New Members of the Tumor Necrosis Factor Receptor and Ligand Families. *Endocr Rev* (1999) 20:345–357. doi: 10.1210/edrv.20.3.0367
213. de Vries RBM, Hooijmans CR, Langendam MW, van Luijk J, Leenaars M, Ritskes-Hoitinga M, Wever KE. A protocol format for the preparation, registration and publication of systematic reviews of animal intervention studies. *Evidence-based Preclin Med* (2015) 1:e00007. doi: 10.1002/ebm2.7
214. Remmers SJA, de Wildt BWM, Vis MAM, Spaander ESR, de Vries R, Hofmann S, Ito K. Osteoblast-osteoclast co-culture models of bone-remodelling: A systematic review protocol. (2020) doi: 10.5281/ZENODO.3969441
215. Ouzzani M, Hammady H, Fedorowicz Z, Elmagarmid A. Rayyan-a web and mobile app for systematic reviews. *Syst Rev* (2016) 5: doi: 10.1186/s13643-016-0384-4
216. Jemnitz K, Veres Z, Monostory K, Kóbori L, Vereczkey L. Interspecies differences in acetaminophen sensitivity of human, rat, and mouse primary hepatocytes. *Toxicol Vitro* (2008) 22:961–967. doi: 10.1016/j.tiv.2008.02.001
217. Jolly JJ, Chin K-Y, Fozzi Farhana Nur M, Alias E, Chua Hui K, Nuraini Wan Hasan W, Ima-Nirwana S. Optimization of the static human osteoblast/osteoclast co-culture system. *Iran J Med Sci* (2018) 43:208–213.
218. Bitar M, Brown RA, Salih V, Kidane AG, Knowles JC, Nazhat SN. Effect of cell density on osteoblastic differentiation and matrix degradation of biomimetic dense collagen scaffolds. *Biomacromolecules* (2008) 9:129–135. doi: 10.1021/bm701112w
219. Jones GL, Motta A, Marshall MJ, El Haj AJ, Cartmell SH. Osteoblast: Osteoclast co-cultures on silk fibroin, chitosan and PLLA films. *Biomaterials* (2009) 30:5376–5384. doi: 10.1016/j.biomaterials.2009.07.028
220. De Vries TJ, Schoenmaker T, Aerts D, Grevers LC, Souza PPC, Nazmi K, Van De Wiel MA, Ylstra B, Van Lent PL, Leenen PJM, et al. M-CSF priming of osteoclast precursors can cause osteoclastogenesis-insensitivity, which can be prevented and overcome on bone. *J Cell Physiol* (2015) 230:210–225. doi: 10.1002/jcp.24702
221. Kyllönen L, Haimi S, Mannerström B, Huhtala H, Rajala KM, Skottman H, Sándor GK, Miettinen S. Effects of different serum conditions on osteogenic differentiation of human adipose stem cells *in vitro*. *Stem Cell Res Ther* (2013) 4:17. doi: 10.1186/scrt165
222. Domaschke H, Gelinsky M, Burmeister B, Fleig R, Hanke T, Reinstorf A, Pompe W, Rösen-



- Wolff A. *In vitro* ossification and remodeling of mineralized collagen I scaffolds. *Tissue Eng* (2006) 12:949–958. doi: 10.1089/ten.2006.12.949
223. Lindner U, Kramer J, Rohwedel J, Schlenke P. Mesenchymal stem or stromal cells: Toward a better understanding of their biology? *Transfus Med Hemotherapy* (2010) 37:75–83. doi: 10.1159/000290897
224. Clarke MSFF, Sundaresan A, Vanderburg CR, Banigan MG, Pellis NR. A three-dimensional tissue culture model of bone formation utilizing rotational co-culture of human adult osteoblasts and osteoclasts. *Acta Biomater* (2013) 9:7908–7916. doi: 10.1016/j.actbio.2013.04.051
225. Kadow-Romacker A, Duda GN, Bormann N, Schmidmaier G, Wildemann B. Slight changes in the mechanical stimulation affects osteoblast-and osteoclast-like cells in co-culture. *Transfus Med Hemotherapy* (2013) 40:441–447. doi: 10.1159/000356284
226. Hammerl A, Diaz Cano CE, De-Juan-Pardo EM, van Griensven M, Poh PSP. A Growth Factor-Free Co-Culture System of Osteoblasts and Peripheral Blood Mononuclear Cells for the Evaluation of the Osteogenesis Potential of Melt-Electrowritten Polycaprolactone Scaffolds. *Int J Mol Sci* (2019) 20:1068. doi: 10.3390/ijms20051068
227. Bongio M, Lopa S, Gilardi M, Bersini S, Moretti M. A 3D vascularized bone remodeling model combining osteoblasts and osteoclasts in a CaP nanoparticle-enriched matrix. *Nanomedicine* (2016) 11:1073–1091. doi: 10.2217/nnm-2015-0021
228. Hayden RS, Quinn KP, Alonzo CA, Georgakoudi I, Kaplan DL. Quantitative Characterization of Mineralized Silk Film Remodeling during Long-Term Osteoblast-Osteoclast Co- Culture. *Biomaterials* (2014) 35:3794–3802. doi: 10.1016/j.biomaterials.2014.01.034
229. Hayden RS, Fortin J-P, Harwood B, Subramanian B, Quinn KP, Georgakoudi I, Kopin AS, Kaplan DL. Cell-tethered ligands modulate bone remodeling by osteoblasts and osteoclasts. *Adv Funct Mater* (2014) 24:472–479. doi: 10.1002/adfm.201302210
230. Hikita A, Imura T, Oshima Y, Saitou T, Yamamoto S, Imamura T. Analyses of bone modeling and remodeling using *in vitro* reconstitution system with two-photon microscopy. *Bone* (2015) 76:5–17. doi: 10.1016/j.bone.2015.02.030
231. Schröder HC, Wang XH, Wiens M, Diehl-Seifert B, Kropf K, Schloßmacher U, Müller WEG. Silicate modulates the cross-talk between osteoblasts (SaOS-2) and osteoclasts (RAW 264.7 cells): Inhibition of osteoclast growth and differentiation. *J Cell Biochem* (2012) 113:3197–3206. doi: 10.1002/jcb.24196
232. Manolagas SC. Birth and Death of Bone Cells: Basic Regulatory Mechanisms and Implications for the Pathogenesis and Treatment of Osteoporosis. *Endocr Rev* (2000) 21:115–137. doi: 10.1210/edrv.21.2.0395
233. Parfitt AM. The Spatial and Temporal Framework for Signal Traffic in Adult Human Bone. *J Cell Biochem* (1994) 55:273–286. doi: 10.1002/jcb.240550303
234. Sims NA, Martin TJ. Osteoclasts Provide Coupling Signals to Osteoblast Lineage Cells Through Multiple Mechanisms. *Annu Rev Physiol* (2020) 82:1–23. doi: 10.1146/annurev-physiol-021119-034425
235. Susa M, Luong-Nguyen N-H, Cappellen D, Zamurovic N, Gamse R, Kestrogen O. Human primary osteoclasts: *in vitro* generation and applications as pharmacological and clinical assay. *J Transl Med* (2004) 2:6. doi: 10.1186/1479-5876-2-6
236. Yang J, Qiao M, Li Y, Hu G, Song C, Xue L, Bai H, Yang J, Yang X. Expansion of a population of large monocytes (atypical monocytes) in peripheral blood of patients with acute exacerbations of chronic obstructive pulmonary diseases. *Mediators Inflamm* (2018) 2018:9031452. doi: 10.1155/2018/9031452
237. Wilkesmann S, Fellenberg J, Nawaz Q, Reible B, Moghaddam A, Boccaccini AR, Westhauser F. Primary osteoblasts, osteoblast precursor cells or osteoblast-like cell lines: Which human cell

- types are (most) suitable for characterizing 45S5-bioactive glass? *J Biomed Mater Res - Part A* (2020) 108:663–674. doi: 10.1002/jbm.a.36846
238. Abdallah D, Jourdain ML, Braux J, Guillaume C, Gangloff SC, Jacquot J, Velard F. An optimized method to generate human active osteoclasts from peripheral blood monocytes. *Front Immunol* (2018) 9:632. doi: 10.3389/fimmu.2018.00632
 239. Kuterbekov M, Machillot P, Baillet F, Jonas AM, Glinel K, Picart C. Design of experiments to assess the effect of culture parameters on the osteogenic differentiation of human adipose stromal cells. *Stem Cell Res Ther* (2019) 10:256. doi: 10.1186/s13287-019-1333-7
 240. Grossner T, Haberkorn U, Hofmann J, Gotterbarm T. Effects of Different Basal Cell Culture Media upon the Osteogenic Response of hMSCs Evaluated by 99mTc-HDP Labeling. *Int J Mol Sci* (2022) 23:6288. doi: 10.3390/ijms23116288
 241. Brauer A, Pohlemann T, Metzger W. Osteogenic differentiation of immature osteoblasts: Interplay of cell culture media and supplements. *Biotech Histochem* (2016) 91:161–169. doi: 10.3109/10520295.2015.1110254
 242. Ragab AA, Lavish SA, Banks MA, Goldberg VM, Greenfield EM. Osteoclast Differentiation Requires Ascorbic Acid. *J Bone Miner Res* (1998) 13:970–977. doi: 10.1359/jbmr.1998.13.6.970
 243. Welshons W V, Wolf MF, Murphy CS, Craig Jordan V. Estrogenic activity of phenol red. *Mol Cell Endocrinol* (1988) 57:169–178. doi: 10.1016/0303-7207(88)90072-x
 244. de Faria AN, Zancanela DC, Ramos AP, Torqueti MR, Ciancaglini P. Estrogen and phenol red free medium for osteoblast culture: study of the mineralization ability. *Cytotechnology* (2016) 68:1623–1632. doi: 10.1007/s10616-015-9844-2
 245. van der Valk J. Fetal bovine serum - a cell culture dilemma. *Science* (2022) 375:142–143. doi: 10.1126/science.abm1317
 246. van der Valk J, Bieback K, Buta C, Cochrane B, Dirks WG, Fu J, Hickman JJ, Hohensee C, Kolar R, Liebsch M, et al. Fetal Bovine Serum (FBS): Past - Present - Future. *ALTEX* (2018) 35:99–118. doi: 10.14573/altex.1705101
 247. Villasante A, Robinson ST, Cohen AR, Lock R, Guo XE, Vunjak-Novakovic G. Human Serum Enhances Biomimicry of Engineered Tissue Models of Bone and Cancer. *Front Bioeng Biotechnol* (2021) 9:658472. doi: 10.3389/fbioe.2021.658472
 248. Mbalaviele G, Jaiswal N, Meng A, Cheng L. Human Mesenchymal Stem Cells Promote Human Osteoclast Differentiation from CD34 Bone Marrow Hematopoietic Progenitors. *Endocrinology* (1999) 140:3736–3743. doi: 10.1210/endo.140.8.6880
 249. Takeyama S, Yoshimura Y, Deyama Y, Sugawara Y, Fukuda H, Matsumoto A. Phosphate decreases osteoclastogenesis in coculture of osteoblast and bone marrow. *Biochem Biophys Res Commun* (2001) 282:798–802. doi: 10.1006/bbrc.2001.4652
 250. Mozar A, Haren N, Chasseraud M, Louvet L, Mazière C, Wattel A, Mentaverri R, Morlière P, Kamel S, Brazier M, et al. High extracellular inorganic phosphate concentration inhibits RANK-RANKL signaling in osteoclast-like cells. *J Cell Physiol* (2008) 215:47–54. doi: 10.1002/jcp.21283
 251. Le Nihouannen D, Barralet JE, Fong JE, Komarova S V. Ascorbic acid accelerates osteoclast formation and death. *Bone* (2010) 46:1336–1343. doi: 10.1016/j.bone.2009.11.021
 252. Choi HK, Kim GJ, Yoo HS, Song DH, Chung KH, Lee KJ, Koo YT, An JH. Vitamin C activates osteoblastogenesis and inhibits osteoclastogenesis via Wnt/ β -catenin/ATF4 signaling pathways. *Nutrients* (2019) 11:506. doi: 10.3390/nu11030506
 253. Langenbach F, Handschel J. Effects of dexamethasone, ascorbic acid and β -glycerophosphate on the osteogenic differentiation of stem cells *in vitro*. *Stem Cell Res Ther* (2013) 4:117. doi: 10.1186/srct328
 254. Walsh S, Jordan GR, Jefferiss C, Stewart K, Beresford JN. High concentrations of

- dexamethasone suppress the proliferation but not the differentiation or further maturation of human osteoblast precursors *in vitro*: relevance to glucocorticoid-induced osteoporosis. *Rheumatology* (2001) 40:74–83. doi: 10.1093/rheumatology/40.1.74
255. Takuma A, Kaneda T, Sato T, Ninomiya S, Kumegawa M, Hakeda Y. Dexamethasone Enhances Osteoclast Formation Synergistically with Transforming Growth Factor- β by Stimulating the Priming of Osteoclast Progenitors for Differentiation into Osteoclasts. *J Biol Chem* (2003) 278:44667–44674. doi: 10.1074/jbc.M300213200
256. Zhou H, Cooper MS, Seibel MJ. Endogenous Glucocorticoids and Bone. *Bone Res* (2013) 2:107–119. doi: 10.4248/br201302001
257. Baker BM, Chen CS. Deconstructing the third dimension-how 3D culture microenvironments alter cellular cues. *J Cell Sci* (2012) 125:3015–3024. doi: 10.1242/jcs.079509
258. Hagenmüller H, Hofmann S, Kohler T, Merkle HP, Kaplan DL, Vunjak-Novakovic G, Müller R, Meinel L. Non-invasive time-lapsed monitoring and quantification of engineered bone-like tissue. *Ann Biomed Eng* (2007) 35:1657–1667. doi: 10.1007/s10439-007-9338-2
259. Remmers S, Mayer D, Melke J, Ito K, Hofmann S. Measuring Mineralised Tissue Formation and Resorption in a Human 3D Osteoblast-Osteoclast Co-Culture Model. *Eur Cells Mater* (2020) 40:189–202. doi: 10.22203/eCM.v040a12
260. Rossi E, Mracsko E, Papadimitropoulos A, Allafi N, Reinhardt D, Mehrkens A, Martin I, Knuesel I, Scherberich A. An *In vitro* Bone Model to Investigate the Role of Triggering Receptor Expressed on Myeloid Cells-2 in Bone Homeostasis. *Tissue Eng - Part C Methods* (2018) 24:391–398. doi: 10.1089/ten.tec.2018.0061
261. Krishnan V, Vogler EA, Sosnoski DM, Mastro AM. *In vitro* mimics of bone remodeling and the vicious cycle of cancer in bone. *J Cell Physiol* (2014) 229:453–462. doi: 10.1002/jcp.24464
262. Boanini E, Torricelli P, Sima F, Axente E, Fini M, Mihailescu IN, Bigi A. Strontium and zoledronate hydroxyapatites graded composite coatings for bone prostheses. *J Colloid Interface Sci* (2015) 448:1–7. doi: 10.1016/j.jcis.2015.01.088
263. Papadimitropoulos A, Scherberich A, Güven S, Theilgaard N, Crooijmans H, Santini F, Scheffler K, Zallone A, Martin I. A 3D *in vitro* bone organ model using human progenitor cells. *Eur Cells Mater* (2011) 21:445–458. doi: 10.22203/ecm.v021a33
264. Borciani G, Montalbano G, Baldini N, Vitale-Brovarone C, Ciapetti G. Protocol of Co-Culture of Human Osteoblasts and Osteoclasts to Test Biomaterials for Bone Tissue Engineering. *Methods Protoc* (2022) 5:8. doi: 10.3390/mps5010008
265. Bernhardt A, Skottke J, von Witzleben M, Gelinsky M. Triple culture of primary human osteoblasts, osteoclasts and osteocytes as an *in vitro* bone model. *Int J Mol Sci* (2021) 22:7316. doi: 10.3390/ijms22147316
266. Bryan N, Andrews KD, Loughran MJ, Rhodes NP, Hunt JA. Elucidating the contribution of the elemental composition of fetal calf serum to antigenic expression of primary human umbilical-vein endothelial cells *in vitro*. *Biosci Rep* (2011) 31:199–210. doi: 10.1042/BSR20100064
267. Piersma SR, Broxterman HJ, Kapci M, de Haas RR, Hoekman K, Verheul HMW, Jiménez CR. Proteomics of the TRAP-induced platelet releasate. *J Proteomics* (2009) 72:91–109. doi: 10.1016/j.jprot.2008.10.009
268. Barrientos S, Stojadinovic O, Golinko MS, Brem H, Tomic-Canic M. Growth factors and cytokines in wound healing. *Wound Repair Regen* (2008) 16:585–601. doi: 10.1111/j.1524-475X.2008.00410.x
269. Nurden AT. Platelets, inflammation and tissue regeneration. *Thromb Haemost* (2011) 105:13–33. doi: 10.1160/THS10-11-0720
270. Salari Sharif P, Abdollahi M. The Role of Platelets in Bone Remodeling. *Inflamm Allergy-Drug Targets* (2010) 9:393–399. doi: 10.2174/187152810793938044

271. Salamanna F, Maglio M, Sartori M, Tschon M, Fini M. Platelet Features and Derivatives in Osteoporosis : A Rational and Systematic Review on the Best Evidence. *Int J or Mol Sci* (2020) 21:1762. doi: 10.3390/ijms21051762
272. Chevallier N, Anagnostou F, Zilber S, Bodivit G, Maurin S, Barrault A, Bierling P, Hernigou P, Layrolle P, Rouard H. Osteoblastic differentiation of human mesenchymal stem cells with platelet lysate. *Biomaterials* (2010) 31:270–278. doi: 10.1016/j.biomaterials.2009.09.043
273. Viau S, Lagrange A, Chabrand L, Lorant J, Charrier M, Rouger K, Alvarez I, Eap S, Delorme B. A highly standardized and characterized human platelet lysate for efficient and reproducible expansion of human bone marrow mesenchymal stromal cells. *Cytotherapy* (2019) 21:738–754. doi: 10.1016/j.jcyt.2019.04.053
274. Xia W, Li H, Wang Z, Xu R, Fu Y, Zhang X, Ye X, Huang Y, Xiang AP, Yu W. Human platelet lysate supports ex vivo expansion and enhances osteogenic differentiation of human bone marrow-derived mesenchymal stem cells . *Cell Biol Int* (2011) 35:639–643. doi: 10.1042/cbi20100361
275. Guiotto M, Raffoul W, Hart AM, Riehle MO, Summa PG. Human platelet lysate to substitute fetal bovine serum in hMSC expansion for translational applications : a systematic review. *J Transl Med* (2020) 18:351. doi: 10.1186/s12967-020-02489-4
276. Karadjian M, Senger AS, Essers C, Wilkesmann S, Heller R, Fellenberg J, Simon R, Westhauser F. Human Platelet Lysate Can Replace Fetal Calf Serum as a Protein Source to Promote Expansion and Osteogenic Differentiation of Human Bone-Marrow-Derived Mesenchymal Stromal Cells. *Cells* (2020) 9:5–7. doi: 10.3390/cells9040918
277. Jafar H, Abuarqoub D, Ababneh N, Hasan M, Al-Sotari S, Aslam N, Kailani M, Ammouh M, Shraideh Z, Awidi A. hPL promotes osteogenic differentiation of stem cells in 3D scaffolds. *PLoS One* (2019) 14:e0215667. doi: 10.1371/journal.pone.0215667
278. Hemeda H, Giebel B, Wagner W. Evaluation of human platelet lysate versus fetal bovine serum for culture of mesenchymal stromal cells. *Cytotherapy* (2014) 16:170–180. doi: 10.1016/j.jcyt.2013.11.004
279. Burnouf T, Strunk D, Koh MBC, Schallmoser K. Human platelet lysate: Replacing fetal bovine serum as a gold standard for human cell propagation? *Biomaterials* (2016) 76:371–387. doi: 10.1016/j.biomaterials.2015.10.065
280. Agis H, Schröckmair S, Skorianz C, Fischer MB, Watzek G, Gruber R. Platelets increase while serum reduces the differentiation and activity of osteoclasts *in vitro*. *J Orthop Res* (2013) 31:1561–1569. doi: 10.1002/jor.22386
281. Kim JM, Lin C, Stavre Z, Greenblatt MB, Shim JH. Osteoblast-Osteoclast Communication and Bone Homeostasis. *Cells* (2020) 9:2073. doi: 10.3390/cells9092073
282. Udagawa N, Koide M, Nakamura M, Nakamichi Y, Yamashita T, Uehara S, Kobayashi Y, Furuya Y, Yasuda H, Fukuda C, et al. Osteoclast differentiation by RANKL and OPG signaling pathways. *J Bone Miner Metab* (2021) 39:19–26. doi: 10.1007/s00774-020-01162-6
283. Tylek T, Schilling T, Schlegelmilch K, Ries M, Rudert M, Jakob F, Groll J. Platelet lysate outperforms FCS and human serum for co-culture of primary human macrophages and hMSCs. *Sci Rep* (2019) 9:3533. doi: 10.1038/s41598-019-40190-9
284. Otsu N. A Threshold Selection Method from Gray-Level Histograms. *IEEE Trans Syst Man Cybern* (1979) 9:62–66. doi: 10.1109/TSMC.1979.4310076
285. Stirling DR, Swain-Bowden MJ, Lucas AM, Carpenter AE, Cimini BA, Goodman A. CellProfiler 4: improvements in speed, utility and usability. *BMC Bioinformatics* (2021) 22:433. doi: 10.1186/s12859-021-04344-9
286. Xiang B, Liu Y, Zhao W, Zhao H, Yu H. Extracellular calcium regulates the adhesion and migration of osteoclasts via integrin $\alpha\beta$ 3/Rho A/Cytoskeleton signaling. *Cell Biol Int* (2019)

- 43:1125–1136. doi: 10.1002/cbin.11033
287. Kanatani M, Sugimoto T, Kano J, Kanzawa M, Chihara K. Effect of high phosphate concentration on osteoclast differentiation as well as bone-resorbing activity. *J Cell Physiol* (2003) 196:180–189. doi: 10.1002/jcp.10270
288. Lees RL, Sabharwal VK, Heersche JNM. Resorptive State and Cell Size Influence Intracellular pH Regulation in Rabbit Osteoclasts Cultured on Collagen-Hydroxyapatite Films. *Bone* (2001) 28:187–194. doi: 10.1016/s8756-3282(00)00433-6
289. Weinstein RS, Manolagas SC. Apoptosis and Osteoporosis. *Am J Med* (2000) 108:153–164. doi: 10.1016/s0002-9343(99)00420-9
290. Delaisse JM, Sør K, Andersen TL, Rojek AM, Marcussen N. The Mechanism Switching the Osteoclast From Short to Long Duration Bone Resorption. *Front Cell Dev Biol* (2021) 9:644503. doi: 10.3389/fcell.2021.644503
291. Takeshita S, Kaji K, Kudo A. Identification and Characterization of the New Osteoclast Progenitor with Macrophage Phenotypes Being Able to Differentiate into Mature Osteoclasts. *J Bone Miner Res* (2000) 15:1477–1488. doi: 10.1359/jbmr.2000.15.8.1477
292. Xin Y, Liu Y, Liu D, Li J, Zhang C, Wang Y, Zheng S. New Function of RUNX2 in Regulating Osteoclast Differentiation via the AKT/NFATc1/CTSK Axis. *Calcif Tissue Int* (2020) 106:553–566. doi: 10.1007/s00223-020-00666-7
293. Bernhardt A, Koperski K, Schumacher M, Gelinsky M. Relevance of osteoclast-specific enzyme activities in cell-based *in vitro* resorption assays. *Eur Cells Mater* (2017) 33:28–42. doi: 10.22203/eCM.v033a03
294. Yunna C, Mengru H, Lei W, Weidong C. Macrophage M1/M2 polarization. *Eur J Pharmacol* (2020) 877:173090. doi: 10.1016/j.ejphar.2020.173090
295. McWhorter FY, Wang T, Nguyen P, Chung T, Liu WF. Modulation of macrophage phenotype by cell shape. *Proc Natl Acad Sci U S A* (2013) 110:17253–17258. doi: 10.1073/pnas.1308887110
296. Huang R, Wang X, Zhou Y, Xiao Y. RANKL-induced M1 macrophages are involved in bone formation. *Bone Res* (2017) 5:17019. doi: 10.1038/boneres.2017.19
297. Ichiro Nakamura, Mary F. Pilkington, Päivi T. Lakkakorpi, Lorraine Lipfert, Stephen M. Sims, S. Jeffrey Dixon, Gideon A. Rodan, Le T. Duong. Role of $\alpha v \beta 3$ integrin in osteoclast migration and formation of the sealing zone. *J Cell Sci* (1999) 122:3985–3993. doi: 10.1242/jcs.112.22.3985
298. Takegahara N, Kim H, Mizuno H, Sakaue-Sawano A, Miyawaki A, Tomura M, Kanagawa O, Ishii M, Choi Y. Involvement of receptor activator of nuclear factor- κ B ligand (RANKL)-induced incomplete cytokinesis in the polyploidization of osteoclasts. *J Biol Chem* (2016) 291:3439–3454. doi: 10.1074/jbc.M115.677427
299. Jansen IDC, Vermeer JAF, Bloemen V, Stap J, Everts V. Osteoclast fusion and fission. *Calcif Tissue Int* (2012) 90:515–522. doi: 10.1007/s00223-012-9600-y
300. McDonald MM, Khoo WH, Ng PY, Xiao Y, Zamerli J, Thatcher P, Kyaw W, Pathmanandavel K, Grootveld AK, Moran I, et al. Osteoclasts recycle via osteomorphs during RANKL-stimulated bone resorption. *Cell* (2021) 184:1330-1347.e13. doi: 10.1016/j.cell.2021.02.002
301. Zheng X, Baker H, Hancock WS, Fawaz F, McCaman M, Pungor E. Proteomic analysis for the assessment of different lots of fetal bovine serum as a raw material for cell culture. Part IV. Application of proteomics to the manufacture of biological drugs. *Biotechnol Prog* (2006) 22:1294–1300. doi: 10.1021/bp060121o
302. Astori G, Amati E, Bambi F, Bernardi M, Chierigato K, Schäfer R, Sella S, Rodeghiero F. Platelet lysate as a substitute for animal serum for the ex-vivo expansion of mesenchymal stem/stromal cells: Present and future. *Stem Cell Res Ther* (2016) 7:93. doi: 10.1186/s13287-016-0352-x

303. Barro L, Burnouf PA, Chou ML, Nebie O, Wu YW, Chen MS, Radosevic M, Knutson F, Burnouf T. Human platelet lysates for human cell propagation. *Platelets* (2021) 32:152–162. doi: 10.1080/09537104.2020.1849602
304. Yago T, Nanke Y, Ichikawa N, Kobashigawa T, Mogi M, Kamatani N, Kotake S. IL-17 induces osteoclastogenesis from human monocytes alone in the absence of osteoblasts, which is potently inhibited by anti-TNF- α antibody: A novel mechanism of osteoclastogenesis by IL-17. *J Cell Biochem* (2009) 108:947–955. doi: 10.1002/jcb.22326
305. Bastidas-Coral AP, Hogervorst JMA, Forouzanfar T, Kleverlaan CJ, Koolwijk P, Klein-Nulend J, Bakker AD. IL-6 counteracts the inhibitory effect of IL-4 on osteogenic differentiation of human adipose stem cells. *J Cell Physiol* (2019) 234:20520–20532. doi: 10.1002/jcp.28652
306. Irie A, Takami M, Kubo H, Sekino-Suzuki N, Kasahara K, Sanai Y. Heparin enhances osteoclastic bone resorption by inhibiting osteoprotegerin activity. *Bone* (2007) 41:165–174. doi: 10.1016/j.bone.2007.04.190
307. Laner-Plamberger S, Lener T, Schmid D, Streif DA, Salzer T, Öller M, Hauser-Kronberger C, Fischer T, Jacobs VR, Schallmoser K, et al. Mechanical fibrinogen-depletion supports heparin-free mesenchymal stem cell propagation in human platelet lysate. *J Transl Med* (2015) 13:354. doi: 10.1186/s12967-015-0717-4
308. Lee YM, Fujikado N, Manaka H, Yasuda H, Iwakura Y. IL-1 plays an important role in the bone metabolism under physiological conditions. *Int Immunol* (2010) 22:805–816. doi: 10.1093/intimm/dxq431
309. Osta B, Benedetti G, Miossec P. Classical and paradoxical effects of TNF- α on bone homeostasis. *Front Immunol* (2014) 5:48. doi: 10.3389/fimmu.2014.00048
310. Soysa NS, Alles N. Positive and negative regulators of osteoclast apoptosis. *Bone Reports* (2019) 11:100225. doi: 10.1016/j.bonr.2019.100225
311. Guo C, Yang XG, Wang F, Ma XY. IL-1 induces apoptosis and inhibits the osteoblast differentiation of MC3T3-E1 cells through the JNK and p38 MAPK pathways. *Int J Mol Med* (2016) 38:319–327. doi: 10.3892/ijmm.2016.2606
312. Ding J, Ghali O, Lencel P, Broux O, Chauveau C, Devedjian JC, Hardouin P, Magne D. TNF- α and IL-1 β inhibit RUNX2 and collagen expression but increase alkaline phosphatase activity and mineralization in human mesenchymal stem cells. *Life Sci* (2009) 84:499–504. doi: 10.1016/j.lfs.2009.01.013
313. Mangashetti LS, Khapli SM, Wani MR. IL-4 Inhibits Bone-Resorbing Activity of Mature Osteoclasts by Affecting NF- κ B and Ca²⁺ Signaling. *J Immunol* (2005) 175:917–925. doi: 10.4049/jimmunol.175.2.917
314. Bendixen AC, Shevde NK, Dienger KM, Willson TM, Funk CD, Pike JW. IL-4 inhibits osteoclast formation through a direct action on osteoclast precursors via peroxisome proliferator-activated receptor gamma 1. *PNAS* (2001) 98:2443–2448. doi: 10.1073/pnas.041493198
315. Bastidas-Coral AP, Bakker AD, Zandieh-Doulabi B, Kleverlaan CJ, Bravenboer N, Forouzanfar T, Klein-Nulend J. Cytokines TNF- α , IL-6, IL-17F, and IL-4 Differentially Affect Osteogenic Differentiation of Human Adipose Stem Cells. *Stem Cells Int* (2016) 2016:1318256. doi: 10.1155/2016/1318256
316. Takeuchi T, Yoshida H, Tanaka S. Role of interleukin-6 in bone destruction and bone repair in rheumatoid arthritis. *Autoimmun Rev* (2021) 20:102884. doi: 10.1016/j.autrev.2021.102884
317. O'Brien W, Fissel BM, Maeda Y, Yan J, Ge X, Gravallesse EM, Aliprantis AO, Charles JF. RANK-Independent Osteoclast Formation and Bone Erosion in Inflammatory Arthritis. *Arthritis Rheumatol* (2016) 68:2889–2900. doi: 10.1002/art.39837
318. Li Y, Bäckesjö CM, Haldosén LA, Lindgren U. IL-6 receptor expression and IL-6 effects change



- during osteoblast differentiation. *Cytokine* (2008) 43:165–173. doi: 10.1016/j.cyto.2008.05.007
319. Zhang Q, Chen B, Yan F, Guo J, Zhu X, Ma S, Yang W. Interleukin-10 inhibits bone resorption: A potential therapeutic strategy in periodontitis and other bone loss diseases. *Biomed Res Int* (2014) 2014:284836. doi: 10.1155/2014/284836
320. Chen E, Liu G, Zhou X, Zhang W, Wang C, Hu D, Xue D, Pan Z. Concentration-dependent, dual roles of IL-10 in the osteogenesis of human BMSCs via P38/MAPK and NF- κ B signaling pathways. *FASEB J* (2018) 32:4917–4929. doi: 10.1096/fj.201701256RRR
321. Lee Y. The role of interleukin-17 in bone metabolism and inflammatory skeletal diseases. *BMB Rep* (2013) 46:479–483. doi: 10.5483/BMBRep.2013.46.10.141
322. Huang H, Kim HJ, Chang EJ, Lee ZH, Hwang SJ, Kim HM, Lee Y, Kim HH. IL-17 stimulates the proliferation and differentiation of human mesenchymal stem cells: Implications for bone remodeling. *Cell Death Differ* (2009) 16:1332–1343. doi: 10.1038/cdd.2009.74
323. Singh A, Gill G, Kaur H, Amhmed M, Jakhu H. Role of osteopontin in bone remodeling and orthodontic tooth movement: a review. *Prog Orthod* (2018) 19: doi: 10.1186/s40510-018-0216-2
324. Ota K, Quint P, Ruan M, Pederson L, Westendorf JJ, Khosla S, Oursler MJ. TGF- β induces Wnt10b in osteoclasts from female mice to enhance coupling to osteoblasts. *Endocrinology* (2013) 154:3745–3752. doi: 10.1210/en.2013-1272
325. Hodge JM, Kirkland MA, Nicholson GC. Multiple roles of M-CSF in human osteoclastogenesis. *J Cell Biochem* (2007) 102:759–768. doi: 10.1002/jcb.21331
326. Lee MS, Kim HS, Yeon J-T, Choi S-W, Chun CH, Kwak HB, Oh J. GM-CSF Regulates Fusion of Mononuclear Osteoclasts into Bone-Resorbing Osteoclasts by Activating the Ras/ERK Pathway. *J Immunol* (2009) 183:3390–3399. doi: 10.4049/jimmunol.0804314
327. Del Angel-Mosqueda C, Gutiérrez-Puente Y, López-Lozano AP, Romero-Zavaleta RE, Mendiola-Jiménez A, Medina-De la Garza CE, Márquez-M M, De la Garza-Ramos MA. Epidermal growth factor enhances osteogenic differentiation of dental pulp stem cells *in vitro*. *Head Face Med* (2015) 11:29. doi: 10.1186/s13005-015-0086-5
328. Laflamme C, Curt S, Rouabhia M. Epidermal growth factor and bone morphogenetic proteins upregulate osteoblast proliferation and osteoblastic markers and inhibit bone nodule formation. *Arch Oral Biol* (2010) 55:689–701. doi: 10.1016/j.archoralbio.2010.06.010
329. Yi T, Lee HL, Cha JH, Ko S Il, Kim HJ, Shin HI, Woo KM, Ryoo HM, Kim GS, Baek JH. Epidermal growth factor receptor regulates osteoclast differentiation and survival through cross-talking with RANK signaling. *J Cell Physiol* (2008) 217:409–422. doi: 10.1002/jcp.21511
330. Irina Kratchmarova, Blagoy Blagoev, Mandana Haack-Sorensen, Moustapha Kassem, Matthias Mann. Mechanism of Divergent Growth Factor Effects in Mesenchymal Stem Cell Differentiation. *Science* (2005) 308:1472–1477. doi: 10.1126/science.1108408
331. Gupta RR, Yoo DJ, Hebert C, Niger C, Stains JP. Induction of an osteocyte-like phenotype by fibroblast growth factor-2. *Biochem Biophys Res Commun* (2010) 402:258–264. doi: 10.1016/j.bbrc.2010.10.011
332. Novais A, Chatzopoulou E, Chaussain C, Gorin C. The potential of fgf-2 in craniofacial bone tissue engineering: A review. *Cells* (2021) 10:932. doi: 10.3390/cells10040932
333. Jim E, Shuto T, Ikebe T, Jincushi S, Hirata M, Koca T. Basic Fibroblast Growth Factor Inhibits Osteoclast-Like Cell Formation. *J Cell Physiol* (1996) 168:395–402.
334. Binkert C, Demetriou M, Sukhu B, Szwercas M, Tenenbaum HC, Dennis JW. Regulation of Osteogenesis by Fetuin. *J or Biol Chem* (1999) 274:28514–28520. doi: 10.1074/jbc.274.40.28514
335. Brylka L, Jahnen-Dechent W. The role of fetuin-A in physiological and pathological mineralization. *Calcif Tissue Int* (2013) 93:355–364. doi: 10.1007/s00223-012-9690-6
336. Hung BP, Hutton DL, Kozielski KL, Bishop CJ, Naved B, Green JJ, Caplan AI, Gimble JM,

- Dorafshar AH, Grayson WL. Platelet-Derived Growth Factor BB Enhances Osteogenesis of Adipose-Derived but Not Bone Marrow-Derived Mesenchymal Stromal/Stem Cells. *Stem Cells* (2015) 33:2773–2784. doi: 10.1002/stem.2060
337. Lorget F, Kamel S, Mentaverri R, Wattel A, Naassila M, Maamer M, Brazier M. High extracellular calcium concentrations directly stimulate osteoclast apoptosis. *Biochem Biophys Res Commun* (2000) 268:899–903. doi: 10.1006/bbrc.2000.2229
338. Barradas AMC, Fernandes HAM, Groen N, Chai YC, Schrooten J, Van de Peppel J, Van Leeuwen JPTM, Van Blitterswijk CA, De Boer J. A calcium-induced signaling cascade leading to osteogenic differentiation of human bone marrow-derived mesenchymal stromal cells. *Biomaterials* (2012) 33:3205–3215. doi: 10.1016/j.biomaterials.2012.01.020
339. Lin H, Zhou Y, Lei Q, Lin D, Chen J, Wu C. Effect of inorganic phosphate on migration and osteogenic differentiation of bone marrow mesenchymal stem cells. *BMC Dev Biol* (2021) 21:1. doi: 10.1186/s12861-020-00229-x
340. Deng X, Liang LN, Zhu D, Zheng LP, Yu JH, Meng X ling, Zhao YN, Sun XX, Pan TW, Liu YQ. Wedelolactone inhibits osteoclastogenesis but enhances osteoblastogenesis through altering different semaphorins production. *Int Immunopharmacol* (2018) 60:41–49. doi: 10.1016/j.intimp.2018.04.037
341. Allison H, McNamara LM. Inhibition of osteoclastogenesis by mechanically stimulated osteoblasts is attenuated during estrogen deficiency. *Am J Physiol - Cell Physiol* (2019) 317:C969–C982. doi: 10.1152/ajpcell.00168.2019
342. Wu L, Feyerabend F, Schilling AF, Willumeit-Römer R, Luthringer BJC. Effects of extracellular magnesium extract on the proliferation and differentiation of human osteoblasts and osteoclasts in coculture. *Acta Biomater* (2015) 27:294–304. doi: 10.1016/j.actbio.2015.08.042
343. Schulze S, Wehrum D, Dieter P, Hempel U. A supplement-free osteoclast – osteoblast co-culture for pre-clinical application. *J Cell Physiol* (2018) 233:4391–4400. doi: 10.1002/jcp.26076
344. Lian WS, Ko JY, Chen YS, Ke HJ, Hsieh CK, Kuo CW, Wang SY, Huang BW, Tseng JG, Wang FS. MicroRNA-29a represses osteoclast formation and protects against osteoporosis by regulating PCAF-mediated RANKL and CXCL12. *Cell Death Dis* (2019) 10:705. doi: 10.1038/s41419-019-1942-1
345. Liu YQ, Han XF, Liu T, Cheng MC, Xiao H Bin. A cell-based model of bone remodeling for identifying activity of icarrin in the treatment of osteoporosis. *Biotechnol Lett* (2015) 37:219–226. doi: 10.1007/s10529-014-1661-8
346. Bernhardt A, Thieme S, Domaschke H, Springer A, Rösen-Wolff A, Gelinsky M. Crosstalk of osteoblast and osteoclast precursors on mineralized collagen-towards an *in vitro* model for bone remodeling. *J Biomed Mater Res - Part A* (2010) 95A:848–856. doi: 10.1002/jbm.a.32856
347. Shih YV, Varghese S. Tissue engineered bone mimetics to study bone disorders ex vivo: Role of bioinspired materials. *Biomaterials* (2019) 198:107–121. doi: 10.1016/j.biomaterials.2018.06.005
348. Scheinpflug J, Pfeiffenberger M, Damerau A, Schwarz F, Textor M, Lang A, Schulze F. Journey into bone models: A review. *Genes (Basel)* (2018) 9:247. doi: 10.3390/genes9050247
349. Popescu DC, Van Leeuwen ENM, Rossi NAA, Holder SJ, Jansen JA, Sommerdijk NAJM. Shaping amorphous calcium carbonate films into 2D model substrates for bone cell culture. *Angew Chemie - Int Ed* (2006) 45:1762–1767. doi: 10.1002/anie.200502602
350. Rico-Llanos GA, Borrego-González S, Moncayo-Donoso M, Becerra J, Visser R. Collagen type I biomaterials as scaffolds for bone tissue engineering. *Polymers (Basel)* (2021) 13:599. doi: 10.3390/polym13040599
351. Maher M, Castilho M, Yue Z, Glattauer V, Hughes TC, Ramshaw JAM, Wallace GG. Shaping collagen for engineering hard tissues: Towards a printomics approach. *Acta Biomater* (2021) 131:41–61. doi: 10.1016/j.actbio.2021.06.035

352. Melke J, Midha S, Ghosh S, Ito K, Hofmann S. Silk fibroin as biomaterial for bone tissue engineering. *Acta Biomater* (2016) 31:1–16. doi: 10.1016/j.actbio.2015.09.005
353. Marelli B, Ghezzi CE, Alessandrino A, Barralet JE, Freddi G, Nazhat SN. Silk fibroin derived polypeptide-induced biomineralization of collagen. *Biomaterials* (2012) 33:102–108. doi: 10.1016/j.biomaterials.2011.09.039
354. Shin K, Acri T, Geary S, Salem AK. Biomimetic Mineralization of Biomaterials Using Simulated Body Fluids for Bone Tissue Engineering and Regenerative Medicine <sup/>. *Tissue Eng Part A* (2017) 23:1169–1180. doi: 10.1089/ten.tea.2016.0556
355. Kokubo T, Takadama H. How useful is SBF in predicting *in vivo* bone bioactivity? *Biomaterials* (2006) 27:2907–2915. doi: 10.1016/j.biomaterials.2006.01.017
356. Tas AC, Bhaduri SB. Rapid coating of Ti6Al4V at room temperature with a calcium phosphate solution similar to 10x simulated body fluid. *J Mater Res* (2004) 19:2742–2749. doi: 10.1557/JMR.2004.0349
357. Olszta MJ, Cheng X, Jee SS, Kumar R, Kim YY, Kaufman MJ, Douglas EP, Gower LB. Bone structure and formation: A new perspective. *Mater Sci Eng R Reports* (2007) 58:77–116. doi: 10.1016/j.mser.2007.05.001
358. Wu R, Li H, Yang Y, Zheng Q, Li S, Chen Y. Bioactive Silk Fibroin-Based Hybrid Biomaterials for Musculoskeletal Engineering: Recent Progress and Perspectives. *ACS Appl Bio Mater* (2021) 4:6630–6646. doi: 10.1021/acsabm.1c00654
359. Li C, Jin HJ, Botsaris GD, Kaplan DL. Silk apatite composites from electrospun fibers. *J Mater Res* (2005) 20:3374–3384. doi: 10.1557/jmr.2005.0425
360. Ma XL, Li R, Ru L, Xu GW, Huang YP. Effect of polyaspartic acid on hydroxyapatite deposition in silk fibroin blend films. *Express Polym Lett* (2010) 4:321–327. doi: 10.3144/expresspolymlett.2010.40
361. Kim HJ, Kim U-J, Kim HS, Li C, Wada M, Leisk GG, Kaplan DL. Bone Tissue Engineering with Premineralized Silk Scaffolds. *Bone* (2008) 42:1226–1234. doi: doi:10.1016/j.bone.2008.02.007
362. Oosterlaken BM, Vena MP, de With G. *In vitro* Mineralization of Collagen. *Adv Mater* (2021) 33:2004418. doi: 10.1002/adma.202004418
363. Song Q, Jiao K, Tonggu L, Wang LG, Zhang SL, Yang YD, Zhang L, Bian JH, Hao DX, Wang CY, et al. Contribution of biomimetic collagen-ligand interaction to intrafibrillar mineralization. *Sci Adv* (2019) 5:eav9075.
364. Van Driessche AES, Kellermeier M, Benning LG, Gebauer D. *New Perspectives on Mineral Nucleation and Growth*. Van Driessche AES, Benning LG, editors. Cham: Springer International Publishing (2017). 7–10 p. doi: 10.1007/978-3-319-45669-0
365. Facchetti D, Hempel U, Martocq L, Smith AM, Koptuyg A, Surmenev RA, Surmeneva MA, Douglas TEL. Heparin enriched-wpi coating on ti6al4v increases hydrophilicity and improves proliferation and differentiation of human bone marrow stromal cells. *Int J Mol Sci* (2022) 23:139. doi: 10.3390/ijms23010139
366. Boyan BD, Lotz EM, Schwartz Z. Roughness and hydrophilicity as osteogenic biomimetic surface properties. *Tissue Eng - Part A* (2017) 23:1479–1489. doi: 10.1089/ten.tea.2017.0048
367. Bergara-Muguruza L, Mäkelä K, Yrjälä T, Salonen J, Yamashita K, Nakamura M. Surface Electric Fields Increase Human Osteoclast Resorption through Improved Wettability on Carbonate-Incorporated Apatite. *ACS Appl Mater Interfaces* (2021) 13:58270–58278. doi: 10.1021/acsami.1c14358
368. Shemesh M, Addadi L, Geiger B. Surface microtopography modulates sealing zone development in osteoclasts cultured on bone. *J R Soc Interface* (2017) 14:20160958. doi: 10.1098/rsif.2016.0958

369. Wang W, Caetano G, Ambler WS, Blaker JJ, Frade MA, Mandal P, Diver C, Bártolo P. Enhancing the hydrophilicity and cell attachment of 3D printed PCL/graphene scaffolds for bone tissue engineering. *Materials (Basel)* (2016) 9:992. doi: 10.3390/ma9120992
370. Ehtesabi H, Massah F. Improvement of hydrophilicity and cell attachment of polycaprolactone scaffolds using green synthesized carbon dots. *Mater Today Sustain* (2021) 13:100075. doi: 10.1016/j.mtsust.2021.100075
371. Ansari S, de Wildt BWM, Vis MAM, de Korte CE, Ito K, Hofmann S, Yuana Y. Matrix vesicles: Role in bone mineralization and potential use as therapeutics. *Pharmaceuticals* (2021) 14:289. doi: 10.3390/ph14040289
372. Mckee MD, Nanci A. Osteopontin and the Bone Remodeling Sequence. *Ann New York Acad Sci* (1995) 760:177–189. doi: 10.1111/j.1749-6632.1995.tb44629.x
373. Chellaiah MA, Kizer N, Biswas R, Alvarez U, Strauss-Schoenberger J, Rifas L, Rittling SR, Denhardt DT, Hruska KA. Osteopontin Deficiency Produces Osteoclast Dysfunction Due to Reduced CD44 Surface Expression. *Mol Biol Cell* (2003) 14:173–189. doi: 10.1091/mbc.E02-06
374. Halling Linder C, Ek-Rylander B, Krumpel M, Norgård M, Narisawa S, Millán JL, Andersson G, Magnusson P. Bone Alkaline Phosphatase and Tartrate-Resistant Acid Phosphatase: Potential Co-regulators of Bone Mineralization. *Calcif Tissue Int* (2017) 101:92–101. doi: 10.1007/s00223-017-0259-2
375. Scheuren AC, Vallaster P, Kuhn GA, Paul GR, Malhotra A, Kameo Y, Müller R. Mechano-Regulation of Trabecular Bone Adaptation Is Controlled by the Local *in vivo* Environment and Logarithmically Dependent on Loading Frequency. *Front Bioeng Biotechnol* (2020) 8:566346. doi: 10.3389/fbioe.2020.566346
376. Raggatt LJ, Partridge NC. Cellular and molecular mechanisms of bone remodeling. *J Biol Chem* (2010) 285:25103–25108. doi: 10.1074/jbc.R109.041087
377. Chen J, Sun T, You Y, Wu B, Wang X, Wu J. Proteoglycans and Glycosaminoglycans in Stem Cell Homeostasis and Bone Tissue Regeneration. *Front Cell Dev Biol* (2021) 9:760532. doi: 10.3389/fcell.2021.760532
378. Wojtas M, Lausch AJ, Sone ED. Glycosaminoglycans accelerate biomimetic collagen mineralization in a tissue-based *in vitro* model. *PNAS* (2020) 117:12636–12642. doi: 10.1073/pnas.1914899117
379. Tatara Y, Suto S, Itoh K. Novel roles of glycosaminoglycans in the degradation of type I collagen by cathepsin K. *Glycobiology* (2017) 27:1089–1098. doi: 10.1093/glycob/cwx083
380. Bi Y, Stuelten CH, Kilts T, Wadhwa S, Iozzo R V., Robey PG, Chen XD, Young MF. Extracellular matrix proteoglycans control the fate of bone marrow stromal cells. *J Biol Chem* (2005) 280:30481–30489. doi: 10.1074/jbc.M500573200
381. Jin Y, Kundu B, Cai Y, Kundu SC, Yao J. Bio-inspired mineralization of hydroxyapatite in 3D silk fibroin hydrogel for bone tissue engineering. *Colloids Surfaces B Biointerfaces* (2015) 134:339–345. doi: 10.1016/j.colsurfb.2015.07.015
382. Xu YF, Nudelman F, Eren ED, Wirix MJM, Cantaert B, Nijhuis WH, Hermida-Merino D, Portale G, Bomans PHH, Ottmann C, et al. Intermolecular channels direct crystal orientation in mineralized collagen. *Nat Commun* (2020) 11:5068. doi: 10.1038/s41467-020-18846-2
383. Engler AJ, Sen S, Sweeney HL, Discher DE. Matrix Elasticity Directs Stem Cell Lineage Specification. *Cell* (2006) 126:677–689. doi: 10.1016/j.cell.2006.06.044
384. Zvicer J, Medic A, Veljovic D, Jevtic S, Novak S, Obradovic B. Biomimetic characterization reveals enhancement of hydroxyapatite formation by fluid flow in gellan gum and bioactive glass composite scaffolds. *Polym Test* (2019) 76:464–472. doi: 10.1016/j.polymertesting.2019.04.004
385. Ren X, Zhou Q, Foulad D, Dewey MJ, Bischoff D, Miller TA, Yamaguchi DT, Harley BAC, Lee JC. Nanoparticulate mineralized collagen glycosaminoglycan materials directly and indirectly

- inhibit osteoclastogenesis and osteoclast activation. *J Tissue Eng Regen Med* (2019) 13:823–834. doi: 10.1002/term.2834
386. de Melo Pereira D, Davison N, Habibović P. Human osteoclast formation and resorptive function on biomineralized collagen. *Bioact Mater* (2022) 8:241–252. doi: 10.1016/j.bioactmat.2021.06.036
387. Ru J ying, Wang Y fen. Osteocyte apoptosis: the roles and key molecular mechanisms in resorption-related bone diseases. *Cell Death Dis* (2020) 11:846. doi: 10.1038/s41419-020-03059-8
388. Eriksen EF, Gundersen HJG, Melsen F, Mosekilde L, Eriksen EF. Reconstruction of the Formative Site in Iliac Trabecular Bone in 20 Normal Individuals Employing a Kinetic Model for Matrix and Mineral Apposition. *Bone Dis Rel Res* (1984) 5:243–252. doi: 10.1016/0221-8747(84)90066-3
389. Odgaard A, Gundersen HJG, Odgaard A. Quantification of Connectivity in Cancellous Bone, with Special Emphasis on 3-D Reconstructions. *Bone* (1993) 14:173–182. doi: 10.1016/8756-3282(93)90245-6
390. Christen P, Ito K, Ellouz R, Boutroy S, Sornay-rendu E, Chapurlat RD, Rietbergen B Van. Bone remodelling in humans is load-driven but not lazy. *Nat Commun* (2014) 5:4855. doi: 10.1038/ncomms5855
391. Heinemann C, Heinemann S, Worch H, Hanke T. Development of an osteoblast/osteoclast co-culture derived by human bone marrow stromal cells and human monocytes for biomaterials testing. *Eur Cells Mater* (2011) 21:80–93. doi: 10.22203/eCM.v021a07
392. Heinemann C, Heinemann S, Vater C, Worch H, Worch H, Hanke T. Influence of Osteogenic Supplements on the osteoclastogenesis of Human Monocytes. *J Dev Biol Tissue Eng* (2011) 3:55–61. doi: 10.5897/JDBTE.9000013
393. Atkins GJ, Kostakis P, Welldon KJ, Vincent C, Findlay DM, Zannettino ACW. Human trabecular bone-derived osteoblasts support human osteoclast formation *in vitro* in a defined, serum-free medium. *J Cell Physiol* (2005) 203:573–582. doi: 10.1002/jcp.20255
394. Antony J. “Fractional Factorial Designs.” *Design of Experiments for Engineers and Scientists*. Elsevier (2014). p. 87–112 doi: 10.1016/b978-0-08-099417-8.00007-9
395. Lam J, Carmichael ST, Lowry WE, Segura T. Hydrogel design of experiments methodology to optimize hydrogel for iPSC-NPC culture. *Adv Healthc Mater* (2015) 4:534–539. doi: 10.1002/adhm.201400410
396. Van Gaal RC, Vrethen AF, Van Sprang JF, Franssen PPKH, Van Turnhout MC, Dankers PYW. Biomaterial screening of protein coatings and peptide additives: Towards a simple synthetic mimic of a complex natural coating for a bio-artificial kidney. *Biomater Sci* (2021) 9:2209–2220. doi: 10.1039/d0bm01930e
397. Marinho PA, Chailangkarn T, Muotri AR. Systematic optimization of human pluripotent stem cells media using Design of Experiments. *Sci Rep* (2015) 5:09834. doi: 10.1038/srep09834
398. Bersini S, Gilardi M, Arrigoni C, Talò G, Zamai M, Zagra L, Caiola V, Moretti M. Human *in vitro* 3D co-culture model to engineer vascularized bone-mimicking tissues combining computational tools and statistical experimental approach. *Biomaterials* (2016) 76:157–172. doi: 10.1016/j.biomaterials.2015.10.057
399. Shetty S, Kapoor N, Bondu J, Thomas N, Paul T. Bone turnover markers: Emerging tool in the management of osteoporosis. *Indian J Endocrinol Metab* (2016) 20:846–852. doi: 10.4103/2230-8210.192914
400. Grömping U. Tutorial for designing experiments using the R package RcmdrPlugin.DoE. (2011).
401. Beck G. Gene Array Analysis of Osteoblast Differentiation Effect of Phosphorus on Bone and Mineral Metabolism View project. *Cell growth Differ* (2001) 12:61–83.

402. Hule V. Isoenzymes of lactic dehydrogenase is human platelets. *Clin Chim Acta* (1966) 13:431–434. doi: 10.1016/0009-8981(66)90233-6
403. Pattappa G, Heywood HK, de Bruijn JD, Lee DA. The metabolism of human mesenchymal stem cells during proliferation and differentiation. *J Cell Physiol* (2011) 226:2562–2570. doi: 10.1002/jcp.22605
404. Da W, Tao L, Zhu Y. The Role of Osteoclast Energy Metabolism in the Occurrence and Development of Osteoporosis. *Front Endocrinol (Lausanne)* (2021) 12:675385. doi: 10.3389/fendo.2021.675385
405. Kubatzky KF, Uhle F, Eigenbrod T. From macrophage to osteoclast – How metabolism determines function and activity. *Cytokine* (2018) 112:102–115. doi: 10.1016/j.cyto.2018.06.013
406. Wright HL, McCarthy HS, Middleton J, Marshall MJ. RANK, RANKL and osteoprotegerin in bone biology and disease. *Curr Rev Musculoskelet Med* (2009) 2:56–64. doi: 10.1007/s12178-009-9046-7
407. Sims NA, Martin TJ. Coupling the activities of bone formation and resorption: a multitude of signals within the basic multicellular unit. *Bonekey Rep* (2014) 3:481. doi: 10.1038/bonekey.2013.215
408. Stessuk T, Husch J, Hermens IA, Hofmann S, van den Beucken JJ. Osteogenic differentiation driven by osteoclasts and macrophages. *J Immunol Regen Med* (2021) 12:100044. doi: 10.1016/j.regen.2021.100044
409. Gori F, Hofbauer LC, Dunstan CR, Spelsberg TC, Khosla S, Riggs BL. The Expression of Osteoprotegerin and RANK Ligand and the Support of Osteoclast Formation by Stromal-Osteoblast Lineage Cells Is Developmentally Regulated*. *Endocrinology* (2000) 141:4768–4776. doi: 10.1210/endo.141.12.7840
410. Ronaldson-Bouchard K, Teles D, Yeager K, Tavakol DN, Zhao Y, Chramiec A, Tagore S, Summers M, Stylianou S, Tamargo M, et al. A multi-organ chip with matured tissue niches linked by vascular flow. *Nat Biomed Eng* (2022) 6:351–371. doi: 10.1038/s41551-022-00882-6
411. Shah KM, Stern MM, Stern AR, Pathak JL, Bravenboer N, Bakker AD. Osteocyte isolation and culture methods. *Bonekey Rep* (2016) 5:838. doi: 10.1038/bonekey.2016.65
412. You L, Temiyasathit S, Lee P, Kim CH, Tummala P, Yao W, Kingery W, Malone AM, Kwon RY, Jacobs CR. Osteocytes as mechanosensors in the inhibition of bone resorption due to mechanical loading. *Bone* (2008) 42:172–179. doi: 10.1016/j.bone.2007.09.047
413. Bratengeier C, Bakker AD, Fahlgrén A. Mechanical loading releases osteoclastogenesis-modulating factors through stimulation of the P2X7 receptor in hematopoietic progenitor cells. *J Cell Physiol* (2019) 234:13057–13067. doi: 10.1002/jcp.27976
414. Guo Y, Wang Y, Liu Y, Wang H, Guo C, Zhang X. Effect of the same mechanical loading on osteogenesis and osteoclastogenesis *in vitro*. *Chinese J Traumatol* (2015) 18:150–156. doi: 10.1016/j.cjte.2014.09.004
415. Gao Y, Li T, Sun Q, Ye C, Guo M, Chen Z, Chen J, Huo B. Migration and differentiation of osteoclast precursors under gradient fluid shear stress. *Biomech Model Mechanobiol* (2019) 18:1731–1744. doi: 10.1007/s10237-019-01171-z
416. Hasegawa T, Yamamoto T, Tsuchiya E, Hongo H, Tsuboi K, Kudo A, Abe M, Yoshida T, Nagai T, Khadiza N, et al. Ultrastructural and biochemical aspects of matrix vesicle-mediated mineralization. *Jpn Dent Sci Rev* (2017) 53:34–45. doi: 10.1016/j.jdsr.2016.09.002
417. Théry C, Witwer KW, Aikawa E, Alcaraz MJ, Anderson JD, Andriantsitohaina R, Antoniou A, Arab T, Archer F, Atkin-Smith GK, et al. Minimal information for studies of extracellular vesicles 2018 (MISEV2018): a position statement of the International Society for Extracellular Vesicles and update of the MISEV2014 guidelines. *J Extracell Vesicles* (2018) 7:1535750. doi: 10.1080/20013078.2018.1535750



418. Lötvall J, Hill AF, Hochberg F, Buzás EI, Vizio D Di, Gardiner C, Ghossein YS, Kurochkin I V., Mathivanan S, Quesenberry P, et al. Minimal experimental requirements for definition of extracellular vesicles and their functions: A position statement from the International Society for Extracellular Vesicles. *J Extracell Vesicles* (2014) 3:26913. doi: 10.3402/jev.v3.26913
419. György B, Szabó TG, Pásztói M, Pál Z, Misják P, Aradi B, László V, Pállinger É, Pap E, Kittel Á, et al. Membrane vesicles, current state-of-the-art: Emerging role of extracellular vesicles. *Cell Mol Life Sci* (2011) 68:2667–2688. doi: 10.1007/s00018-011-0689-3
420. Kalra H, Drummen GPC, Mathivanan S. Focus on extracellular vesicles: Introducing the next small big thing. *Int J Mol Sci* (2016) 17:170. doi: 10.3390/ijms17020170
421. Yuana Y, Sturk A, Nieuwland R. Extracellular vesicles in physiological and pathological conditions. *Blood Rev* (2013) 27:31–39. doi: 10.1016/j.blre.2012.12.002
422. El Andaloussi S, Mäger I, Breakefield XO, Wood MJA. Extracellular vesicles: Biology and emerging therapeutic opportunities. *Nat Rev Drug Discov* (2013) 12:347–357. doi: 10.1038/nrd3978
423. Cappariello A, Loftus A, Muraca M, Maurizi A, Rucci N, Teti A. Osteoblast-Derived Extracellular Vesicles Are Biological Tools for the Delivery of Active Molecules to Bone. *J Bone Miner Res* (2018) 33:517–533. doi: 10.1002/jbmr.3332
424. Hasegawa T. Ultrastructure and biological function of matrix vesicles in bone mineralization. *Histochem Cell Biol* (2018) 149:289–304. doi: 10.1007/s00418-018-1646-0
425. Shapiro IM, Landis WJ, Risbud M V. Matrix vesicles: Are they anchored exosomes? *Bone* (2015) 79:29–36. doi: 10.1016/j.bone.2015.05.013
426. Huynh N, Vonmoss L, Smith D, Rahman I, Felemban MF, Zuo J, Rody WJ, McHugh KP, Holliday LS. Characterization of regulatory extracellular vesicles from osteoclasts. *J Dent Res* (2016) 95:673–679. doi: 10.1177/0022034516633189
427. Yuan FL, Wu Q yuan, Miao ZN, Xu MH, Xu RS, Jiang DL, Ye JX, Chen F hu, Zhao MD, Wang HJ, et al. Osteoclast-derived Extracellular vesicles: Novel regulators of osteoclastogenesis and osteoclast-osteoblasts communication in bone remodeling. *Front Physiol* (2018) 9:628. doi: 10.3389/fphys.2018.00628
428. Ma Q, Liang M, Wu Y, Luo F, Ma Z, Dong S, Xu J, Dou C. Osteoclast-derived apoptotic bodies couple bone resorption and formation in bone remodeling. *Bone Res* (2021) 9:5. doi: 10.1038/s41413-020-00121-1
429. Morrell AE, Brown GN, Robinson ST, Sattler RL, Baik AD, Zhen G, Cao X, Bonewald LF, Jin W, Kam LC, et al. Mechanically induced Ca²⁺ oscillations in osteocytes release extracellular vesicles and enhance bone formation. *Bone Res* (2018) 6:6. doi: 10.1038/s41413-018-0007-x
430. Qin Y, Peng Y, Zhao W, Pan J, Ksiezak-Reding H, Cardozo C, Wu Y, Pajevic PD, Bonewald LF, Bauman WA, et al. Myostatin inhibits osteoblastic differentiation by suppressing osteocyte-derived exosomal microRNA-218: A novel mechanism in muscle-bone communication. *J Biol Chem* (2017) 292:11021–11033. doi: 10.1074/jbc.M116.770941
431. Shinohara M, Choi H, Ibuki M, Yabe SG, Okochi H, Miyajima A, Sakai Y. Endodermal differentiation of human induced pluripotent stem cells using simple dialysis culture system in suspension culture. *Regen Ther* (2019) 12:14–19. doi: 10.1016/j.reth.2019.05.004
432. Cui Y, Luan J, Li H, Zhou X, Han J. Exosomes derived from mineralizing osteoblasts promote ST2 cell osteogenic differentiation by alteration of microRNA expression. *FEBS Lett* (2016) 590:185–192. doi: 10.1002/1873-3468.12024
433. Chen C, Cheng P, Xie H, Zhou H De, Wu XP, Liao EY, Luo XH. MiR-503 regulates osteoclastogenesis via targeting RANK. *J Bone Miner Res* (2014) 29:338–347. doi: 10.1002/jbmr.2032
434. Minamizaki T, Nakao Y, Irie Y, Ahmed F, Itoh S, Sarmin N, Yoshioka H, Nobukiyo A,

- Fujimoto C, Nüda S, et al. The matrix vesicle cargo miR-125b accumulates in the bone matrix, inhibiting bone resorption in mice. *Commun Biol* (2020) 3:30. doi: 10.1038/s42003-020-0754-2
435. Sun W, Zhao C, Li Y, Wang L, Nie G, Peng J, Wang A, Zhang P, Tian W, Li Q, et al. Osteoclast-derived microRNA-containing exosomes selectively inhibit osteoblast activity. *Cell Discov* (2016) 2:16015. doi: 10.1038/celldisc.2016.15
436. Li D, Liu J, Guo B, Liang C, Dang L, Lu C, He X, Cheung HYS, Xu L, Lu C, et al. Osteoclast-derived exosomal miR-214-3p inhibits osteoblastic bone formation. *Nat Commun* (2016) 7:10872. doi: 10.1038/ncomms10872
437. Bakker AD, Jaspers RT. IL-6 and IGF-1 Signaling Within and Between Muscle and Bone: How Important is the mTOR Pathway for Bone Metabolism? *Curr Osteoporos Rep* (2015) 13:131–139. doi: 10.1007/s11914-015-0264-1
438. Maurel DB, Jähn K, Lara-Castillo N. Muscle-bone crosstalk: Emerging opportunities for novel therapeutic approaches to treat musculoskeletal pathologies. *Biomedicines* (2017) 5:62. doi: 10.3390/biomedicines5040062
439. Allison SJ. Bone and the kidney: It's complex. *Nat Rev Nephrol* (2013) 9:623. doi: 10.1038/nrneph.2013.184
440. Malluche HH, Koszewski N, Monier-Faugere MC, Williams JP, Mawad H. Influence of the parathyroid glands on bone metabolism. *Eur J Clin Invest* (2006) 36:23–33. doi: 10.1111/j.1365-2362.2006.01664.x
441. Rouseaud A, Moriceau S, Ramos-Brossier M, Oury F. Bone-brain crosstalk and potential associated diseases. *Horm Mol Biol Clin Investig* (2016) 28:69–83. doi: 10.1515/hmbci-2016-0030
442. Glenn DA, Denburg MR. Bone Health in Glomerular Kidney Disease. *Curr Osteoporos Rep* (2019) 17:570–579. doi: 10.1007/s11914-019-00531-z
443. Ji M, Yu Q. Primary osteoporosis in postmenopausal women. *Chronic Dis Transl Med* (2015) 1:9–13. doi: 10.1016/j.cdtm.2015.02.006
444. Schiavi J, Fodera DM, Brennan MA, McNamara LM. Estrogen depletion alters osteogenic differentiation and matrix production by osteoblasts *in vitro*. *Exp Cell Res* (2021) 408:112814. doi: 10.1016/j.yexcr.2021.112814
445. Milo GE, Malarkey WB, Powell JE, Blakeslee JR, Yohn DS. Effects of Steroid Hormones in Fetal Bovine Serum on Plating and Cloning of Human Cells *in vitro*. *In vitro* (1976) 12:23–30. doi: 10.1007/BF02832789
446. Baker M. Reproducibility: respect your cells! *Nature* (2016) 537:433–435. doi: 10.1210/en.2016-1297
447. Duchamp De Lageneste O, Julien A, Abou-Khalil R, Frangi G, Carvalho C, Cagnard N, Cordier C, Conway SJ, Colnot C. Periosteum contains skeletal stem cells with high bone regenerative potential controlled by Periostin. *Nat Commun* (2018) 9:773. doi: 10.1038/s41467-018-03124-z
448. Baht GS, Vi L, Alman BA. The Role of the Immune Cells in Fracture Healing. *Curr Osteoporos Rep* (2018) 16:138–145. doi: 10.1007/s11914-018-0423-2
449. Bonewald LF. The Role of the Osteocyte in Bone and Nonbone Disease. *Endocrinol Metab Clin North Am* (2017) 46:1–18. doi: 10.1016/j.ecl.2016.09.003
450. Oliveira CS, Leeuwenburgh S, Mano JF. New insights into the biomimetic design and biomedical applications of bioengineered bone microenvironments. *APL Bioeng* (2021) 5:041507. doi: 10.1063/5.0065152
451. Willyard C. Channeling chip power: Tissue chips are being put to the test by industry. *Nat Med* (2017) 23:138–140. doi: 10.1038/nm0217-138
452. Peneda Pacheco D, Suárez Vargas N, Visentin S, Petrini P. From tissue engineering to engineering tissues: The role and application of: The vitro models. *Biomater Sci* (2021) 9:70–83.

- doi: 10.1039/d0bm01097a
453. Jeong CG, Dal Negro G, Getsios S, Ekert JE. “Application of complex *in vitro* models (CIVMs) in drug discovery for safety testing and disease modeling,” *Microfluidic Cell Culture Systems*. Elsevier (2018). p. 121–158 doi: 10.1016/B978-0-12-813671-3.00005-0
454. Jang KJ, Otieno MA, Ronxhi J, Lim HK, Ewart L, Kodella KR, Petropolis DB, Kulkarni G, Rubins JE, Conegliano D, et al. Reproducing human and cross-species drug toxicities using a Liver-Chip. *Sci Transl Med* (2019) 11:eaax5516. doi: 10.1126/scitranslmed.aax5516

Summary

Since the 1990s, bone tissue engineering has traditionally been focusing on developing grafts for patients with large osseous defects, making use of scaffolds, progenitor cells, biochemical and biomechanical stimuli. By tuning these parameters, researchers have created bone-like tissues for transplantation. While these bone-like tissues proved of limited success for human bone regeneration, their development has advanced our ability to manipulate cells and engineer materials. To improve preclinical treatment development and to replace, reduce, and refine animal experiments (3Rs), bone tissue engineering strategies are increasingly applied for the creation of *in vitro* models to study human bone physiology and pathology. This change in focus; from bone regeneration to *in vitro* models, has brought new challenges for researchers of which some are addressed in this thesis.

One challenge is the creation of a bone-like tissue that actually resembles the physiological bone extracellular matrix (ECM). For bone regeneration, graft ECM organization is not imperative because of bone's innate capacity to regenerate and remodel upon implantation, and it has therefore received little attention. In physiological bone, organic (mainly collagen type I) and inorganic matrix (carbonated hydroxyapatite) are highly organized at multiple hierarchical levels. Changes in this structure are often a hallmark of bone pathology. *In vitro* models that aim at studying the bone ECM under influence of treatments should therefore improve their mimicry to physiological bone. In Chapter 2, we (i) give recommendations on the ECM requirements for three-dimensional (3D) *in vitro* bone models, (ii) review what has been achieved thus far, and (iii) suggest how this can be improved in future. One of these suggestions is the application of mechanical loading like directional fluid flow, which has been demonstrated to induce osteoblast alignment on two-dimensional substrates. *In vivo*, cells and collagen are however aligned in 3D and often with surface concavities. In Chapter 3, we therefore aimed at characterizing cell and tissue growth and orientation in a 3D concave “critically sized” channel with and without the application of directional fluid flow. ECM growth and organization was characterized up to 6 weeks. Based on the results obtained within this study, supported by existing literature, we believe that anisotropy in 3D might be guided by curvature, while collagen network density can be increased through the application of fluid shear stress. As full regeneration of the artificial defect was not accomplished in both static and dynamic cultures, we chose to use this “critically sized” defect model to enable the *in vitro* investigation of material-driven bone regeneration in Chapter 4. As graft vascularization is one the major challenges for successful bone regeneration *in vivo*, we extended the defect model with

a co-culture of mesenchymal stromal cells and endothelial cells. After a build-up phase of 4 weeks, in which vessel-like structures and a bone-like matrix were formed, materials (*i.e.*, a fibrin clot, blood clot mimic and soft callus mimic) were artificially implanted. The platform enabled to study the materials' potential to induce migration and vascularization, which are two crucial processes in the early phase of bone regeneration.

Another challenge for tissue engineering of *in vitro* human bone models is the transition from mono-cultures to co-cultures. Bone has multiple mechanical and metabolic functions that are maintained through lifelong remodeling by bone-resorbing osteoclasts, bone-forming osteoblasts, and regulating osteocytes. Pathological bone remodeling is characterized by imbalanced resorption and formation. Thus, to study healthy and pathological bone remodeling, *in vitro* models should at least include a co-culture of osteoclasts and osteoblasts. To perform these co-cultures, each lab develops their own protocol for the cell-culture and analyses methodology. As a consequence, current *in vitro* remodeling models face reproducibility and translational issues. To address this problem, we identified all *in vitro* bone remodeling models that have been described in literature before 2020 in Chapter 5. From these studies, differences in cell-culture methods and resorption/formation analyses methods were mapped systematically. For example, we identified the controversial fetal bovine serum (FBS) as common standard for these co-cultures. In Chapter 6, we therefore investigated whether FBS could be replaced by human platelet lysate (hPL) as a more physiologically relevant and xenogeneic-free medium supplement for *in vitro* human bone remodeling models. We found that hPL supported both osteoclasts and osteoblasts and when co-cultured, remodeling could be balanced by the hPL concentration. As such, we successfully found a xenogeneic-free replacement for FBS to increase the compliance of our *in vitro* model to the 3Rs. Another limitation of current *in vitro* bone remodeling models identified in Chapter 5 is the lack of functional (*i.e.*, resorption and formation) outcome measures, and their spatiotemporal organization. Inspired by collagen mineralization techniques, we developed a mineralized silk fibroin scaffold in Chapter 7. As a remodeling template, this scaffold facilitated the spatiotemporal investigation of both resorption by osteoclasts and formation by osteoblasts. In Chapter 8, we utilized the model described in Chapter 7 to address the reproducibility and translational issues identified in Chapter 5. A design of experiments set-up was used to study the influence of base medium, cell-ratio, hPL concentration, mechanical loading, osteogenic medium supplements, osteoclast medium supplements, and vitamin D3 on osteoclast-osteoblast co-cultures. With this study, we characterized the effect of these culture conditions on the remodeling balance and therefore also identified an optimal protocol for healthy balanced *in vitro* bone remodeling.

To conclude, in this thesis the tissue engineering paradigm has been extended to *in vitro* human bone models. Methods to improve biomimicry of the produced or to-be remodeled ECM as well as the cell-culture environment were refined. As a result, this thesis presents functionally validated *in vitro* models for the evaluation of crucial aspects of material-driven human bone regeneration and human bone remodeling, helping to advance preclinical *in vitro* bone treatment development while contributing to the 3Rs.

Publiekssamenvatting

Tissue engineering (vrij vertaald: het opbouwen van weefsels in het laboratorium) wordt sinds de jaren 90 toegepast voor de regeneratieve geneeskunde. Deze regeneratieve geneeskunde richt zich op het ontwikkelen van behandelmethodes (onder andere implantaten) gebruikmakend van het herstellend vermogen van ons lichaam. Weefsels kunnen in het laboratorium opgebouwd worden door gebruik te maken van stamcellen en materialen die fungeren als stijger (scaffold), gestimuleerd door een juiste toediening van biochemische “voeding” (toegediend via het kweekmedium) en biomechanische belasting (toegediend met een bioreactor). Door het toepassen van deze methode hebben onderzoekers levensechte botimplantaten ontwikkeld voor de regeneratie van botdefecten. Ondanks de vooruitgang in de ontwikkeling van ‘tissue engineered botimplantaten’, zijn de implantaten nog niet geschikt voor grootschalig gebruik in de kliniek. Door het gebruik van diermodellen in de ontwikkeling van deze implantaten is de vertaling naar de uiteindelijke toepassing voor het menselijk lichaam vaak niet succesvol. Dit komt waarschijnlijk door de genetisch verschillen tussen mensen en de (proef)dieren. De laatste jaren wordt de tissue engineering methode steeds vaker toegepast voor het ontwikkelen van kweekmodellen voor menselijk bot. Met kweekmodellen kan het menselijk botweefsel in het lab worden nagebootst, wat als voordeel heeft dat we behandelingen, naast reguliere dierproeven, ook direct kunnen testen op menselijke weefsels. Naast de ethische voordelen, bijdragend aan het vervangen, verminderen en verfijnen van dierproeven, kunnen deze menselijke kweekmodellen bijdragen aan een betere vertaling naar de toepassing voor het menselijk lichaam. De verandering in de toepassing van tissue engineering van botimplantaten voor regeneratie naar kweekmodellen voor de ontwikkeling van behandelmethodes, heeft uitdagingen met zich meegebracht, waarvan een aantal zijn beschreven en onderzocht in dit proefschrift.

Eén van deze uitdagingen is het nabootsen van de structuur van botweefsel. Botweefsel bestaat voornamelijk uit het eiwit collageen type I en het mineraal hydroxyapatiet (calcium en fosfaat) welke anisotroop georganiseerd en in elkaar verweven zijn en daarmee zorgen voor de stevigheid van bot. Voor botregeneratie is de gekweekte botstructuur minder belangrijk door het herstellend vermogen van het menselijk lichaam na implantatie. Hierbij wordt het geïmplanteerde bot door lichaamseigen cellen omgezet in functioneel bot. Afwijkingen in de botstructuur zijn vaak een kenmerk van botaandoeningen zoals voor bijvoorbeeld botontkalking (osteoporose). Wanneer kweekmodellen worden ingezet voor de ontwikkeling van behandelmethodes voor deze botaandoeningen, dan moeten deze kweekmodellen de botstructuur en afwijkingen

daarin kunnen nabootsen. Het nabootsen van deze typische botstructuur in kweekmodellen is tot op heden nog niet gelukt. Met name het stimuleren van de cellen om een collageen netwerk te vormen met anisotrope eigenschappen blijkt lastig. In dit onderzoek hebben we daarom onder andere gekeken naar twee mogelijke manieren om cellen te stimuleren en daarmee een anisotroop collageen netwerk te vormen: curvatuur en gerichte vloeistofstroom. Dit hebben we onderzocht door gebruik te maken van een scaffold met een cilindervormig kanaal in een bioreactor welke een vloeistofstroom kan toedienen. Dit cilindervormig kanaal bootste een kritisch botdefect na: een botdefect dat (zonder ingreep) niet kan dichtgroeien. Humane mesenchymale stamcellen, welke kunnen specialiseren in de bot vormende cellen (osteoblasten), werden gezaaid op deze scaffolds en gekweekt met of zonder vloeistofstroom voor een periode van twee, vier of zes weken. Het bleek dat vloeistofstroom de geproduceerde collageen hoeveelheid kan stimuleren, maar niet de anisotropie van het netwerk kan verbeteren. De cellen lijken zich meer te richten naar de curvatuur van het kanaal, al bleef een duidelijk effect uit. Over een periode van zes weken bleef regeneratie, oftewel het dichtn van het kanaal, inderdaad uit. Daarom hebben we dit kweekmodel verder uitgebreid om botregeneratie met behulp van implantaten te kunnen bestuderen buiten het menselijk lichaam en/of proefdier. De implantaten waarop dit onderzoek zich richtte bestaan uit slimme materialen welke een regeneratieve reactie van het menselijk lichaam kunnen stimuleren. Een uitdaging voor botregeneratie met behulp van deze materialen is de ingroei van bloedvaten, welke nodig zijn voor de toevoer van cellen, zuurstof en voedingsstoffen naar het nieuw te vormen botweefsel. Om deze reden hebben we naast humane mesenchymale stamcellen ook humane endotheel cellen, welke betrokken zijn bij de ontwikkeling van bloedvaten, gezaaid op de scaffolds met defecten. Het kweekmodel werd na vier weken, waarin botachtig weefsel en bloedvaat-achtige structuren gevormd waren, gebruikt voor het implanteren en evalueren van materialen. Na implantatie werd de verplaatsing van cellen naar, en de vorming van bloedvaten en weefsel rondom en in de materialen bestudeerd. Met het kweekmodel voor het bestuderen van materiaal-gedreven regeneratie konden we de potentie van materialen om botregeneratie te stimuleren bestuderen waarbij verschillende aspecten van botregeneratie werden nagebootst.

Een andere uitdaging in het gebruik van tissue engineering voor kweekmodellen is de transitie van simpele mono-celkweken (met één type cel) naar meer complexe celkweken (met twee of meer celtypes). In ons lichaam wordt botweefsel onderhouden door botremodellering. Botremodellering bestaat uit de afbraak van oud bot door osteoclasten en de aanmaak nieuw bot door osteoblasten. Een disbalans in botremodellering is een kenmerk voor verschillende botaandoeningen. Een veelvoorkomend voorbeeld is botontkalking (osteoporose), waarbij er meer botaafbraak



plaatsvind dan botaanmaak. Om deze reden dienen kweekmodellen voor botremodellering in ieder geval te bestaan uit een co-celkweek van de botafbrekende osteoclasten en de botvormende osteoblasten. Om deze cellen samen te kunnen kweken, ontwikkelen alle onderzoekers kweekmethoden welke soms niet nauwkeurig beschreven worden of niet herhaald worden door andere onderzoekers. Dit maakt de reproduceerbaarheid en de vertaalbaarheid van deze onderzoeken lastig. Om deze reden hebben we op een systematische manier alle bestaande co-celkweken geïdentificeerd welke als doel hadden een kweekmodel te ontwikkelen voor botremodellering. De methodes die door deze onderzoeken zijn gebruikt om cellen te co-kweken en om botremodellering te analyseren hebben we in kaart gebracht als basis voor vervolgstudies naar kweekmodellen voor botremodellering. Hieruit kwam naar voren dat veel kweekmodellen nog gebruik maken van foetaal runderserum als bron van groeifactoren in het kweekmedium voor de cellen. Dit serum is controversieel doordat het gewonnen wordt bij een volgroeide maar ongeboorte runderfoetus. Daarnaast is het gebruik van foetaal runderserum een belangrijke oorzaak voor beperkte reproduceerbaarheid binnen het onderzoek door de verschillen in samenstelling afhankelijk van de afkomst van het serum. Om deze reden hebben we een alternatief onderzocht voor het gebruik bij kweekmodellen van botremodellering: humaan bloedplaatjeslysaat. In bloedplaatjes zitten veel groeifactoren opgeslagen welke vrijkomen bij het lyseren (kapot maken van het membraan). In dit onderzoek merkten we dat de toevoeging van bloedplaatjeslysaat aan het kweekmedium de functies van osteoclasten en osteoblasten ondersteunden. Wanneer deze celtypen samen gekweekt werden kon botremodellering gebalanceerd worden door de gebruikte bloedplaatjeslysaat concentratie. Hiermee hebben we een alternatief gevonden voor foetaal runderserum voor ons kweekmodel.

Een andere beperking van de huidige kweekmodellen voor botremodellering is het gebrek aan functionele uitkomstmaten, namelijk het direct kunnen meten en lokaliseren van botaanmaak en botafbraak. De oorzaak hiervan is dat veel kweekmodellen in 2D zijn uitgevoerd of geen gebruik maken van botachtige materialen die afgebroken kunnen worden door osteoclasten. Om deze reden hebben we een materiaal ontwikkeld in de vorm van een scaffold, welke kenmerken heeft van botweefsel. Door wekelijks de kweekmodellen te scannen met de μ CT, konden we de botafbraak en -opbouw kwantificeren en lokaliseren. Het ontwikkelde materiaal stimuleerde botafbraak door osteoclasten en botaanmaak (met name mineralisatie) door osteoblasten. Vervolgens hebben we dit kweekmodel gebruikt om de invloed van de verschillende kweekmethoden zoals beschreven in de literatuur te kunnen bestuderen. Hierbij hebben we gekeken naar de invloed van het kweekmedium, de ratio tussen osteoclasten en osteoblasten, mechanische belasting, de gebruikte bloedplaatjes lyasaat concentratie, en

het gebruik van verschillende groeifactoren voor osteoblasten en osteoclasten. Met deze studie hebben we de invloeden van deze factoren op de balans tussen botafbraak en botaanmaak in kaart gebracht, waarbij werd gestreefd naar een balans tussen afbraak en aanmaak, kenmerkend voor gezond botweefsel.

In dit proefschrift is de tissue engineering methode uitgebreid voor de toepassing bij de ontwikkeling van kweekmodellen van bot. Hierbij hebben we methodes geëvalueerd om de structuur en eigenschappen van het aangemaakte botweefsel en de gebruikte scaffold te verbeteren. Daarnaast hebben we de invloed van de biochemische en biomechanische kweekomgeving op botaanmaak en botafbraak bestudeerd en verbeterd. Dit proefschrift presenteert daarbij twee kweekmodellen welke aspecten van (materiaal-gedreven) botregeneratie en botremodellering kunnen nabootsen. Het onderzoek kan daardoor bijdragen aan het verbeteren van de preklinische evaluatie van behandelmethodes en het vervangen, verminderen en verfijnen van dierproeven.

Curriculum vitae



Bregje W.M. de Wildt was born on the 11th of November 1992 in Nijmegen, The Netherlands. In 2015 she obtained her bachelor's degree in Physiotherapy at Fontys University of Applied Sciences in Eindhoven, with the distinction cum laude. Besides working as a physiotherapist, she continued her studies at the Vrije Universiteit in Amsterdam where she obtained her master's degree in Human Movement Sciences (research master) in 2018. During her master's graduation project, she evaluated the regenerative potential of notochordal cell-derived matrix hydrogel for degenerated intervertebral discs, in collaboration with associate prof. Marco Helder, prof. Theo Smit and prof. Keita Ito at

Amsterdam University Medical Centers and Eindhoven University of Technology. In November 2018 she joined the Orthopaedic Biomechanics group at the Biomedical Engineering department of Eindhoven University of Technology as a PhD Candidate. In her research, she worked under supervision of associate prof. Sandra Hofmann and prof. Keita Ito on the development of *in vitro* human bone models. In 2020, she was an awardee of the Materials Driven Regeneration Young Talent Incentives program, which allowed her to collaborate with associate prof. Debby Gawlitta and visit the lab of prof. Laoise McNamara at the National University of Ireland Galway in the summer of 2021. The results of her PhD research are presented in this dissertation.

Scientific output

Journal publications

Bregje W.M. de Wildt, Sana Ansari, Nico A.J.M. Sommerdijk, Keita Ito, Anat Akiva, Sandra Hofmann. From bone regeneration to three-dimensional *in vitro* models: tissue engineering of organized bone extracellular matrix. *Current Opinion in Biomedical Engineering* (2019), 10:107115. Doi: 10.1016/j.cobme.2019.05.005

Sana Ansari[†], **Bregje W.M. de Wildt**[†], Michelle A.M. Vis, Caroline E. de Korte, Keita Ito, Sandra Hofmann, Yuana Yuana. Matrix vesicles: role in bone mineralization and potential use as therapeutics, *Pharmaceuticals* (2021), 14:289. Doi: 10.3390/ph14040289

Stefan J.A. Remmers, **Bregje W.M. de Wildt**[†], Michelle A.M. Vis[†], Eva S.R. Spaander, Rob B.M. de Vries, Keita Ito, Sandra Hofmann. Osteoblast-osteoclast co-cultures: A systematic review and map of available literature. *PLoS ONE* (2021), 16(11):e0257724. Doi: 10.1371/journal.pone.0257724

Bregje W.M. de Wildt, Keita Ito, Sandra Hofmann. Human platelet lysate as alternative of fetal bovine serum for enhanced human *in vitro* bone resorption and remodeling. *Frontiers in Immunology* (2022), 13:915277. Doi: 10.3389/fimmu.2022.915277

Bregje W.M. de Wildt, Robin van der Meijden, Paul A.A. Bartels, Nico A.J.M. Sommerdijk, Anat Akiva, Keita Ito, Sandra Hofmann. Bioinspired silk fibroin mineralization for advanced *in vitro* bone remodeling models. *Advanced Functional Materials* (2022), 2206992. Doi: 10.1002/adfm.202206992

Bregje W.M. de Wildt, Feihu Zhao, Iris Lauwers, Bert van Rietbergen, Keita Ito, Sandra Hofmann. Characterization of three-dimensional bone-like tissue growth and organization under influence of curvature and directional fluid flow. (submitted) Preprint available at BioRxiv. Doi: 10.1101/2022.08.18.504382

Bregje W.M. de Wildt, Esther E.A. Cramer, Leanne S. de Silva, Keita Ito, Debby Gawlitta, Sandra Hofmann. Evaluating material-driven regeneration in a tissue engineered human *in vitro* bone defect model. (submitted) Preprint available at BioRxiv. Doi: 10.1101/2022.08.05.502914

Stefan J.A. Remmers, Freek C. van der Heijden, **Bregje W.M. de Wildt**, Keita Ito, Sandra Hofmann. Tuning the resorption-formation balance in an *in vitro* three-dimensional osteoblast-osteoclast co-culture model of bone. (submitted) Preprint available at BioRxiv. Doi: 10.1101/2022.08.04.502780

Michelle A.M. Vis, **Bregje W.M. de Wildt**, Keita Ito, Sandra Hofmann. A dialysis medium refreshment cell culture set-up for an osteoblast-osteoclast coculture. (submitted) Preprint available at BioRxiv. Doi: 10.1101/2022.09.15.508113

Bregje W.M. de Wildt, Lizzy A.B. Cuypers, Esther E.A. Cramer, Annelieke S. Wentzel, Keita Ito, Sandra Hofmann. The impact of culture variables on human *in vitro* bone remodeling; a design of experiments approach. (in preparation)

†Authors contributed equally

Conference contributions

Bregje W.M. de Wildt, Vivian H.M. van Hooijdonk - Mouser, Stefan A.H. de Vries, Christine M.E. Rustenburg, Kaj S. Emanuel, Theodoor H. Smit, Marco N. Helder, Keita Ito. Notochordal cell-derived matrix hydrogel to restore biomechanics of the degenerated intervertebral disc, ESBiomech, July 2019, *oral presentation*

Bregje W.M. de Wildt, Anat Akiva, Nico A.J.M. Sommerdijk, Keita Ito, Sandra Hofmann. Poly-aspartic acid improves mineralization of silk fibroin scaffolds for bone tissue engineering, NBTE, November 2019, *oral presentation*

Bregje W.M. de Wildt, Anat Akiva, Nico A.J.M. Sommerdijk, Keita Ito, Sandra Hofmann. Poly-aspartic acid improves mineralization of silk fibroin scaffolds for bone tissue engineering, MDR annual meeting, December 2019, *poster presentation*

Bregje W.M. de Wildt, Anat Akiva, Nico A.J.M. Sommerdijk, Keita Ito, Sandra Hofmann. Biomimetic mineralization of silk fibroin scaffolds for bone tissue engineering, TERMIS-EU, June 2020, *accepted for poster presentation*

Bregje W.M. de Wildt, Keita Ito, Sandra Hofmann. Human platelet lysate defeats fetal bovine serum for human osteoclast formation and resorption, MDR annual meeting, November 2020, *poster presentation*

Bregje W.M. de Wildt, Keita Ito, Sandra Hofmann. Human platelet lysate defeats fetal bovine serum for human osteoclast formation and resorption, NBTE, November 2020, *oral presentation*

Bregje W.M. de Wildt, Feihu Zhao, Iris Lauwers, Keita Ito, Sandra Hofmann. Characterization of directional fluid flow induced tissue growth in a 3D *in vitro* human bone defect model, ESBiomech, July 2021, *oral presentation*

Bregje W.M. de Wildt, Keita Ito, Sandra Hofmann. Human platelet lysate as a xenogeneic-free alternative of fetal bovine serum for human *in vitro* bone remodeling models, TERMIS-World, November 2021, *oral presentation*

Bregje W.M. de Wildt, Anat Akiva, Nico A.J.M. Sommerdijk, Keita Ito, Sandra Hofmann. A bioinspired template for advanced *in vitro* bone remodeling models, TERMIS-World, November 2021, *oral presentation*

Bregje W.M. de Wildt, Esther E.C. Cramer, L.S. de Silva, Keita Ito, D. Gawlitta, Sandra Hofmann. Towards an *in vitro* platform to evaluate material-driven human bone regeneration, NBTE, April 2022, *poster presentation*

Bregje W.M. de Wildt, Towards an *in vitro* platform to evaluate material-driven human bone regeneration, MDR annual meeting, May 2022, *oral presentation*

Bregje W.M. de Wildt, Esther E.C. Cramer, L.S. de Silva, Keita Ito, D. Gawlitta, Sandra Hofmann. Towards an *in vitro* platform to evaluate material-driven human bone regeneration, IBEC EMBL winter conference, June 2022, *poster presentation*

Bregje W.M. de Wildt, Lizzy A.B. Cuypers, Keita Ito, Sandra Hofmann. A design of experiments set-up to assess the influence of culture conditions on bone remodeling balance in a human three-dimensional *in vitro* model, ESBiomech, June 2022, *oral presentation*

Outreach

Bregje W.M. de Wildt, The development of a human mini-bone in the lab to reduce animal experiments, Famelab, pitch finalist, April 2020

Bregje W.M. de Wildt, A tissue engineering approach to create three-dimensional *in vitro* human bone models, Invited presentation at a seminar of the Regenerative Biomaterials group at Raboud University Medical Center Nijmegen, September 2021

Grant

Bregje W.M. de Wildt, Towards an *in vitro* platform to evaluate materials-driven human bone regeneration. Awardee of the Materials Driven Regeneration Young Talent Incentives Program, June 2020, € 10.000,-.

Dankwoord (Acknowledgement)

Na bijna vier jaar gewerkt te hebben aan de voorgaande pagina's van dit proefschrift, mag ik nu eindelijk het meest gelezen onderdeel schrijven. Met veel plezier kijk ik terug naar de leuke en leerzame jaren bij de TU/e. Iedereen die een bijdrage heeft geleverd aan dit proefschrift, direct of indirect, wil ik bij deze bedanken.

First, I would like to thank my promotors for their support the last four years. **Sandra**, as my first promotor you were a great and truly inspirational mentor. You gave me freedom and trust to perform my research, helped me to gain confidence, set my boundaries, and taught me many aspects of being a scientist. Your energy and enthusiasm during our meetings motivated me and I liked that personal matters were also discussed. Your door was always open for a short chat about results or requests for permission to buy another expensive assay or antibody. You are being missed at TU/e and I wish you the best for your future career. Visiting you and swimming in the Bern river was an amazing experience! **Keita**, a bit more than five years ago you gave me the opportunity to perform my master graduation project with you, although the space in your group was limited. I am still grateful you gave me this opportunity, as well as for your support in the transition towards my PhD (and potentially postdoc). I am often impressed by the questions you ask and your intelligence. The discussions during our meetings and your suggestions for my manuscripts really helped me to improve. I appreciate the friendly atmosphere within the Orthopaedic Biomechanics group.

I would like to thank the members of my defense committee. I am honored that **prof. dr. Gwendolen Reilly**, **prof. dr. ir. Sander Leeuwenburgh**, **prof. dr. Carlijn Bouten**, **dr. Astrid Bakker** and **dr. ir. Debby Gawlitta** spent their valuable time on evaluating the thesis manuscript, and grateful for their kind participation in my defense ceremony. **Carlijn Bouten**, as an alumna of the VU University Human Movement Sciences master, I saw you as my role model, which motivated me to apply for a graduation internship and PhD project at TU/e. **Astrid Bakker**, you motivated me during my master studies with your inspiring lectures for bone (remodeling). **Gwendolen Reilly**, the review on *in vitro* models of bone remodeling was published right before the start of my PhD trajectory and was a huge inspiration for my research. **Debby Gawlitta**, thank you for the nice collaboration we had on the MDR young talent incentives award. Thank you for your enthusiasm and great contribution to the final study.

I also would like to thank all excellent researchers with whom I have collaborated over the past 4 years. **Feihu**, thank you for all computational simulations you provided to support my work. Although we sometimes spoke a different (scientific) language, we

always came to a shared conclusion and action list. Especially in the last phase of my PhD you were very supportive which allowed me to finish everything in time, thank you for that. **Bert**, jij stond altijd voor mij klaar wanneer ik tegen problemen aanliep met de μ CT en je hebt op het einde nog een waardevolle bijdrage gegeven aan de studie met Feihu. Ik heb ook genoten van de “Bone Cell and Tissue Mechanics” cursus in Udine en het gezellige etentje daar, bedankt voor alles! **Leanne**, thank you for providing the cartilage spheres for the MDR study, for teaching me how to work with them, and for your extensive input on the manuscript. I wish you all the best for your PhD! **Yuana**, ik ben zo trots om een publicatie te hebben samen met de lab-manager. Je hebt me veel geleerd over extracellular vesicles en ik wil je daar erg voor bedanken. Ik heb respect voor hoe je onderzoek combineerde met je werk als lab-manager. **Nico** and **Anat**, thank you for your great input on two studies of this thesis. **Robin**, met jou achter de raman microscoop zitten in Nijmegen was mega leuk. Bedankt voor je raman lessen en je bijdrage aan de silk fibroin mineralisatie publicatie. **Paul**, bedankt voor jouw spoedcursus XPS en je bijdrage aan de silk fibroin mineralisatie publicatie.

Then I would like to thank the Materials Driven Regeneration program for providing me with the opportunity to visit the lab of **prof. Laoise McNamara**. Laoise McNamara, thank you for giving me a warm welcome to Galway despite the Covid-restrictions. Thank you for showing me the research that is being performed in your group and for the opportunity to learn working with the compression-perfusion bioreactor at your lab. **Masooma** and **Vatsal**, thank you for dedicating your time to teach me to work with the bioreactor.

I had the most amazing colleagues and friends in the Bioengineering Bone group. **Johanna**, thank you for giving me a crash course in bone tissue engineering during the busiest time of your PhD. **Stefan**, bedankt voor jouw expertise in osteoclasten en de uitgebreide systematic review waar we samen met Michelle en Eva aan hebben gewerkt. Then, the bone girls: **Sana**, **Michelle** and **Esther**, we have such a nice group together and I am happy that **Annelieke** also joined recently. I am grateful to have worked with you for almost 4 years. Our time in Udine with one day in Venice was AMAZING! We had the best cappuccini, burrata, pizza, tiramisu and gelati from the Accademia del Getalo (I was glad Esther could also eat endless gelati). The PhD journey was much easier and more fun with you around. When starting at 7:00 AM in the lab, there was often another bone girl present already which cheered me up! Thank you, **Sana**, for your help with the first review study, for letting us experience the Iranian kitchen, and your always enthusiastic greetings. **Annelieke**, bedankt voor je hulp bij het pipetteren van minimaal 30 96-wells assayplaten in de laatste 2 maanden voor mijn proefschrift deadline. Dan mijn twee paranimfen **Michelle** en **Esther**, het was heerlijk om mijn



frustraties bij jullie kwijt te kunnen en met jullie samen te werken! **Michelle**, ik was super blij dat jij na een half jaar op hetzelfde project kwam. Ik heb bewondering voor hoe jij zoveel verschillende chips en een dialysekweekstelsel hebt ontwikkeld binnen jouw project en de lange adem die je daarvoor nodig hebt. Gelukkig gaat het nu de goede kant op! Bedankt ook voor de leuke sportmomenten buiten het werk om. Jij motiveert me altijd om te gaan hardlopen en (voorheen) te gaan zwemmen. Ik hoop dat je dat kunt blijven doen als ik hier weg ben. Ik heb ook genoten van de microscopie cursus in York samen! **Esther**, als geluk (voor mij) bij een ongeluk kwam jij op het *ex vivo* remodeling project terecht en ik heb onwijs veel van jou geleerd! Jij was altijd in het lab te vinden en was altijd top gezelschap tijdens het pipetteren of achter de microscoop wanneer je even kwam buurten en plaatjes kwam kijken. Onze gedeelde liefde voor mooie plaatjes leefde helemaal op tijdens het MDR project waarbij jij heel veel hebt geholpen. Dit project samen met jou heeft me helemaal uit de PhD-dip getrokken, bedankt hiervoor! Ik vind het knap hoe jullie beiden zo gedisciplineerd zijn in de sport naast jullie werk en ik heb bewondering voor hoe jullie omgaan met de vele studenten op jullie projecten. Ik ben trots en blij dat jullie mij bij willen staan tijdens mijn verdediging!

Then I would like to thank all members of the Orthopaedic Biomechanics group. Thank you all for the nice atmosphere we have in our group and the great section retreats we had. So cool that **we won the Meerkamp** last year, I am super proud of our team! Een extra dankjewel voor **Rienk**, die mij 5 jaar geleden heeft geleerd om cellen te passeren en mij hielp met taart bakken voor mijn verjaardagstraktatie. **Elias**, jij maakt mij altijd vrolijk, bedankt voor je motiverende woorden om toch verder te gaan in het onderzoek en het doorsturen van alle postdoc en grant opties. Het lijkt me super om nog eens met jou samen te werken in de toekomst maar dan vanuit een ander lab?! **Celien**, sinds ons masterproject ben je een steun en stabiele factor voor mij. Superleuk dat we onze PhD hebben kunnen starten en eindigen op de ESBiomech conferenties samen. **Evelien**, bedankt voor je het plannen en verzetten van alle meetings, ook bedankt voor je hulp bij het plannen van mijn verdediging. **Jurgen**, bedankt voor al je briljante oplossingen voor de problemen met onze bioreactoren!

Dan wil ik graag alle studenten die ik heb mogen begeleiden bedanken. Een speciaal dankjewel voor **Iris**. Bedankt voor je inzet in het groeiemodel project. Het was geen makkelijke periode voor jou maar toch heeft het geresulteerd in een mooi hoofdstuk en manuscript. **Freek**, bedankt voor je bijdrage aan het kwantificeren van de resorptieplaten. **Lizzy**, door de coronapandemie kon je helaas niet naar Barcelona. Voor mij kwam dit goed uit, want je zocht daardoor een alternatief (online) project bij Sandra. Je hebt voor mij alles uitgezocht over “design of experiments” en kwam met een goed

proposal wat inmiddels heeft geresulteerd in een hoofdstuk in dit proefschrift. Superleuk dat je me hebt uitgenodigd voor een presentatie tijdens jullie seminar vorig jaar. Ik wens je het beste voor je PhD! **Eva Spaander**, bedankt voor je bijdrage aan de systematic review. **Kim Geelink**, bedankt voor je inzet bij het ontwikkelen van een protocol voor MSC-isolatie uit bloed. **Kim en Graaf en Eva Burgers**, blij dat ik jullie heb mogen begeleiden het laatste jaar en dat jullie aan de slag zijn gegaan met het remodeleringsmodel. Het zat niet altijd mee, maar jullie hebben beiden superhard gewerkt en ik kijk uit naar jullie verdediging!

Tommaso, thank you for your advice and motivational words on the continuation of my academic career. **Suzanne**, bedankt voor al je advies rondom het afronden van mijn PhD. Het document dat jij hebt gemaakt zal nog minstens 5 jaar rondgaan verwacht ik!

De afgelopen jaren heb ik veel tijd doorgebracht in het lab. Ik heb dit altijd als leuk ervaren; fijn om te werken aan je resultaten, praktische afleiding te hebben, maar vooral fijn om omringt te zijn door zoveel gezellige mensen. Ik ben het **tech-team** dankbaar voor het draaiende houden van het lab, wat niet gemakkelijk is geweest de afgelopen jaren tijdens de pandemie. Ondanks alle beperkingen hebben jullie hard gewerkt om het praktisch onderzoek door te kunnen laten gaan. Bedankt voor jullie inzet en geduld!

I would also like to thank all (former) members of **office 4.09**. Thanks for the coffee's, lunches, dinner parties and foosball games we had together. Great that we visited Barcelona with a small group last summer for a conference. Een speciaal dankjewel voor mijn beste buurmaatje **Dewy**, superleuk om mineralisatie met jou te bediscussiëren vanuit een ander perspectief. De koffietjes met jou zijn altijd gezellig. Fijn dat we elkaar konden helpen met raman en μ CT.

Lieve **Floor, Tessa, Renée, Merlijn en Joleen**, altijd fijn om met jullie af te spreken! De afgelopen tijd was het wat lastiger door de werk-reisjes en het afronden van mijn proefschrift, maar ik vond het heerlijk om het inlevermoment met jullie te vieren op onze partyboot! **Floor**, met jou kon ik altijd makkelijk alles over werk bespreken. Ik ben je ook dankbaar voor alle sportmomenten samen en onze deelname aan de adventure race, ooit gaan we er weer voor! De bakfiets voor **Tessa** moet dan misschien wel uitgebreid worden nu ze zelf ook een kleintje krijgt, superleuk! **Renée**, gaaf dat je een tastbare bijdrage hebt geleverd aan dit proefschrift. Ik ben blij met en trots op het ontwerp dat je hebt gemaakt (met een lekker hoog zuurstokgehalte, perfect voor mij), bedankt hiervoor!

Dan mijn lieve familie, bedankt voor alles! Wat ben ik trots op mijn **papa en mama**. Ik heb onwijs veel bewondering voor jullie inzet voor het dorp en de gemeente. Dat jullie ook nog vrije tijd over hebben om zoveel te fietsen, waardoor ik afgelopen jaar in het



wiel van mama het fietsweekend doorkwam, is onvoorstelbaar. Jullie staan altijd voor mij en mijn broers klaar (verhuizen, klussen, nog eens verhuizen en nog meer klussen), weten van aanpakken en doen altijd of dat allemaal maar normaal is. Dit heeft ook mij gevormd tot de persoon wie ik nu ben en daar ben ik jullie dankbaar voor. **Sjoerd**, bedankt dat je mij hebt geïnspireerd naar Eindhoven te gaan 12 jaar geleden. Wat een eer dat ik jullie bruidstaart mocht maken vorig jaar! **Rick**, ik ben trots dat ik jou heb kunnen inspireren om ook te gaan roeien. Het is altijd weer fijn om met het gezin bij elkaar te komen, spelletjes te spelen en lekker samen te fietsen.

Schoonfamilie, **Jos** en **Lidwine**, ook jullie bedankt voor de afgelopen jaren. Ook bij jullie voelt het als thuiskomen en jullie interesse, betrokkenheid en waardering voor mijn onderzoek vind ik fijn.

Stef, al meer dan 11 jaar ben ik gelukkig met jou. Jij was mijn slag en in mijn dromen gaf ik je elke haal een kusje. Na de degradatie van een 8+ naar een 4+ moest ik een half jaar lang 5 keer per week natte kleren verdragen voor je mij ook echt zag zitten, maar het was het waard. Bedankt voor je onvoorwaardelijke steun. Ik ben trots op wat we samen hebben opgebouwd en ons paleisje in Nuenen. We weten wat we aan elkaar hebben en zijn een echt topteam; ik zorg dat we aan het werk beginnen en jij maakt het af. Tja, dit boekje moest ik echt helemaal zelf schrijven, al had ik jouw hulp een paar uur voor de deadline toch nog even nodig. Bedankt voor alles en ik kijk uit naar de toekomst met jou!

